THE UNIVERSITY OF CHICAGO

ION TRANSPORT IN NANOSCALE POLYMER PATHWAYS

A DISSERTATION SUBMITTED TO
THE FACULTY OF THE PRITZKER SCHOOL OF MOLECULAR ENGINEERING
IN CANDIDACY FOR THE DEGREE OF
DOCTOR OF PHILOSOPHY

BY
YU KAMBE

CHICAGO, ILLINOIS
AUGUST 2019

To my loving family, to my dear friends, to all of my amazing mentors who believed in me.

For Yosuke-kun and Jose.

TABLE OF CONTENTS

LIST OF FIGURES

LIST OF TABLES

ACKNOWLEDGMENTS

An undertaking like a PhD cannot be done alone. I have had the sincere privilege and honor of being supported by excellent mentors and colleagues. First and foremost, I thank my adviser Professor Paul F. Nealey for accepting me into his research group and having the wisdom and the patience necessary to expand out the electrochemistry research currently done in the Nealey Group. I thank Professor Juan de Pablo, Professor Shrayesh N. Patel, Professor Bozhi Tian, Professor Seth Darling, and Professor Matthew Tirrell for being on my Defense Committee or my Candidacy Committee, for supporting me as a candidate, and for being excellent mentors.

Additional thanks go the the present and past members of the Nealey Group. A special thank you to Professor Christopher G. Arges who gave me the confidence to continue my research here at the PME and for letting me into the electrochemistry community, to Dr. John Colson for becoming such an important friend and mentor through research as well as through entrepreneurship, to Veronica Burnett who contributed tireless hours to the ion conduction pathway work, to Satya Krishnan who is a gifted researcher, to James Lettow who showed generosity in his knowledge and friendship, to Dr. Xiao Li for all of her kind words, and to Dr.James Dolan who has become a treasured friend and confidant. Todah to the current and past electrochemistry team including, Veronica Burnett, Peter Bennington, Professor Chris G. Arges, Dr. Daniel Sharon, Dr. Ban Dong, James Lettow, Satya Krishnan, and Kai Wang. Thank you to Jiaxing Ren, Xuanxuan Chen for welcoming me into the group. Thank you to Moshe Dolejsi and Jiajing Li for being my comrades and for being my rivals.

Thank you to the members of the staff at the University of Chicago who helped make my research possible including but not limited to, Paul Julson, Diana Morgan, Kimberly McGee, and Dr. Phil Griffin.

Thank you to the members of the staff at Argonne National Laboratory who invested countless hours to collaborate on the work including but limited to, Dr. Dave Czplewski and Dr. Leonidas Ocola.

Through my time here, I have cried and laughed with excellent friends and colleagues. Thank you to Zack, Viktor, Elyse, Arin, Marissa, Sanja. The time at the PME was that much better because of each and every one of you.

Final thanks go to parents, Dr.Nobuyuki Kambe, Misako Kambe, my fiance Christine M. McIntosh, and to my soon to be family Michael McIntosh and Suzanne McIntosh.

ABSTRACT

Ion conducting block copolymers (BCEs) have emerged as a promising solution to overcome the inverse relationship between high ionic conductivity and high mechanical robustness required for safer and cheaper electrochemical devices (e.g. batteries, fuel cells, desalination membranes). To date, many studies have investigated the structure and electrochemical property relationship at the membrane scale ($> 100\ \mu m$) which is orders of magnitude larger in comparison to the natural periodicity of BCEs ($< 100\ nm$). This results in a mismatch in the resolution of information that is extracted from AC impedance spectroscopy (EIS) and structure characterization methods. In comparison to the collected structure information, EIS probes the complex impedance response of charge conduction pathways as a function of perturbation frequency. This granularity of the information extracted from EIS to date is far superior to the resolution achieved through thick film structure characterization methods.

Our objective is to control and characterize deterministic structure of ion conduction pathways to fully extract information out of electrochemical characterization methods such as AC impedance spectroscopy. The approach is as follows. First, we will study our system in the thin film ($< 100\ nm$). With the use of thin film self-assembly techniques and directed self-assembly techniques such as chemoepitaxy and graphoepitaxy, the morphology of the BCEs can be structured so that the morphology on the free surface is projected throughout the thin film. This enables simple top down characterization techniques such as scanning electron microscopy and atomic force microscopy to probe deterministic structure. Second, we will study the thin films on top of interdigitated electrodes (IDEs) that enable thin films to be characterized for both structure and complex electrochemical behavior. Third, the IDEs are fully fabricated using semiconductor manufacturing process compliant methods that are compatible with nanoscale fabrication methods such as electron beam lithography used to control morphology of BCEs, therefore IDEs can be customized with nanoscale features enabling us to control morphologies on top of the IDEs.

CHAPTER 1

INTRODUCTION

1.1 Abstract

In this introduction, I will provide justification for studying structure function relationships in block copolymer electrolytes and the challenges it solves in the community. I will begin with a statement of the benefits and challenges of using block copolymer electrolytes in today's electrochemical systems and provide a thermodynamic overview of methods to engineer the morphology of the system. I will define the common methods used to extract the structure function relationships in BCE film thicknesses commonly studied and explain the shortcoming of the methods to extract deterministic properties and justify the reasons for my research approach.

This introductory chapter was adapted with permission from The Electrochemical Society Interface 26.1 (2017): 61-67.[1] Copyright 2017, The Electrochemical Society.

1.2 Introduction

Ion conducting polymers are attractive electrolytes for electrochemical devices because of their superior safety in comparison to liquid electrolytes (e.g., lower flammability, prevention of dendrite shorting, and reduction of the crossover of unwanted species), compact cell design (e.g., as 10 μm thick membrane separators), and the ease of their integration in solid-state cells. For device integration, the ion conducting polymer must also exhibit high ionic conductivity and robust mechanical properties over a wide range of thermal, electrochemical, and chemical conditions, while satisfying cost and scalability requirements. At the molecular-level, there are two classes of ion conducting polymers: neutral polymers with dissolved salts enabling both cation and anion conduction (e.g., polyethylene oxide with dissolved LiTFSI for lithium ion batteries) or polymers that contain ionic moieties tethered to the polymer backbone with oppositely charged mobile counterions (e.g., sulfonated polystyrene for electrodialysis, fuel cells, and redox flow batteries). One key material challenge for ion conducting polymers is the inverse correlation between ion conductivity and mechanical properties. For example, Fenton et al.[2] demonstrated in 1973 the ability of poly(ethylene oxide) (PEO) to dissolve salts into its amorphous matrix and conduct ions. The conductivity of the salt was found to improve with increasing segmental mobility of the PEO chains (often achieved by heating PEO above its glass transition temperature T_g) and the elimination of crystallinity. However, these changes at the molecular-level diminished the mechanical properties of the material (e.g., often reported in terms of elastic modulus [3, 4]) leading to a soft film. The inverse relationship can be observed in the work by Snyder et al, [5] where solvent free electrolytes were fabricated by dissolving Li salts into a crosslinked polymer mixture comprised of ethylene gylcol and one to four vinyl ester groups. 1.1 Similarly, ion conducting polymers with tethered ionic groups experienced a higher ionic conductivity with increased ionic loadings, but excessive swelling due to water uptake at high loadings compromised the mechanical properties of the membranes.[6]

In recent years, block copolymer electrolytes (BCE), a sub-class of ion conducting polymers, have generated considerable attention from the electrochemical community as a means to bypass this tradeoff in the conductivity and mechanical properties. Block copolymers with the simplest molecular architecture consist of two chemically distinct polymer chains that microphase separate into periodic morphologies with sizes ranging from 3 to 100 nm (see Figure 1.2a).[7, 8] The chemically distinct nanoscale domains facilitate the expression of the properties of the individual constituents, such that two or more disadvantageously correlated properties may be independently expressed in a single material. Therefore, BCEs may be designed from the molecular-level to have one domain that is an ion conductor while the other domain maintains the mechanical structure of the overall material. Functionalization of the ion conducting domain can be accomplished either before or after the BCP is self-assembled into its nanoscale architecture; although functionalization before mi-

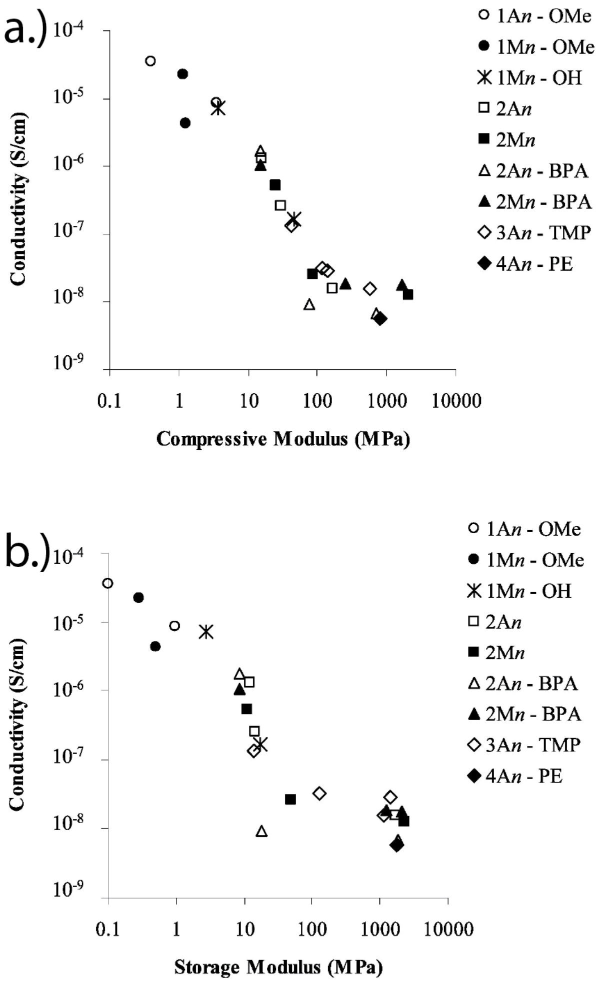

Figure 1.1: Conductivity and modulus for the materials with varying salt, PEG, and vinyl ester groups prior to cross linking. Adapted with permission from Chemistry of Materials [5]. Copyright 2007 American Chemical Society.

crophase separation enables a wider variety of chemistries, introduction of the ionic components, post self-assembly may simplify the thermodynamic driving forces for microphase separation and enable standardized processing.[9–13] To date, diverse BCEs have been synthesized with an ion conducting block (e.g., a Li salt dissolved in poly(ethylene oxide), sulfonated poly(styrene), or poly(n-methyl pyridinium iodide)) and a neutral polymer block (e.g., poly(styrene), poly(methyl butylene), or poly(ethylene)) selected to optimize the ion conductivity and mechanical response of the material, respectively.[13–15]

Although BCEs offer the prospect for high ionic conductivity with the desired mechanical properties, achieving conductivities comparable to their homopolymer counterparts has remained elusive. An ideal BCE would exhibit ion conducting and mechanical domains that span the entire thickness of the membrane providing continuous and percolating pathways for ion conduction. However, this idealized structure does not commonly occur in real block copolymer systems. As illustrated in Figure 1.2b-d, the mechanically stiff domain is not functionalized with ion conductors, consequently insulating one of the domains and introducing nanoscale barriers to ion transport. When these barriers are not controlled, they can block the ideal pathways for ion conduction and increase the length and tortuosity of the available transport pathways, thereby reducing the ion conductivity of the bulk film. Elabd and Hickner[16] suggested in a notable review that future research priorities for BCEs should aim at understanding how nuanced attributes of the self-assembled morphology (e.g., grain boundaries and local defects in the microstructure that arise during self-assembly) influence the ion transport behavior.

1.3 Engineering the Block Copolymer Morphology

1.3.1 Thermodynamics of Block Copolymer Phase Separation

BCPs are comprised of two or more chemically distinct homopolymers that are covalently bonded to each other from end to end. BCPs, ion conducting or not, can undergo microphase

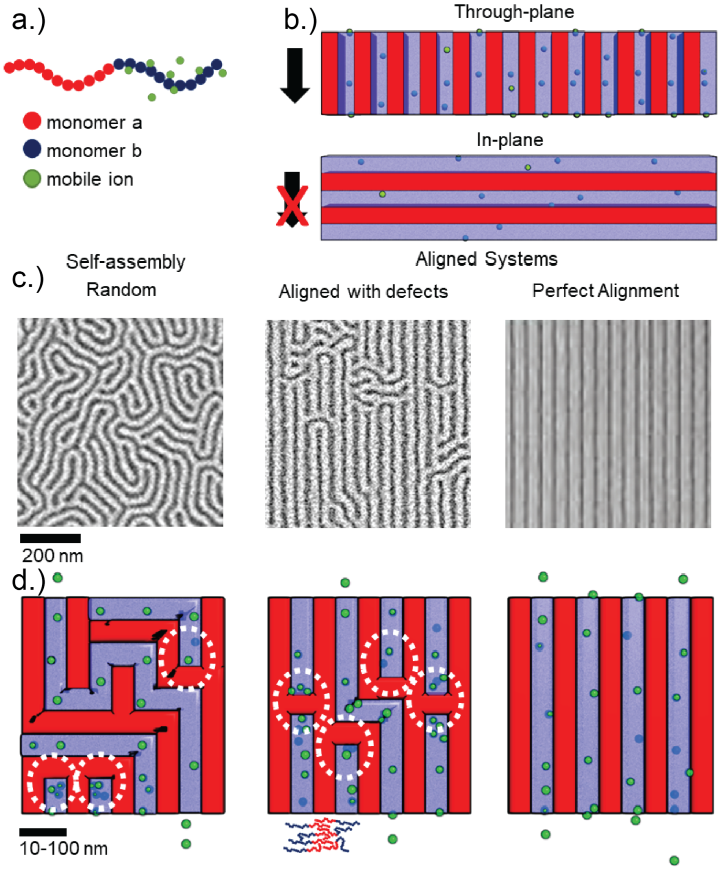

Figure 1.2: Schematic showcasing the morphologies formed via block copolymer self-assembly and alignment. a. The molecular structure of block copolymers where the red domain is a neutral block while the blue domain is an ion conducting block. b. (top) Through-plane alignment that provides mechanical structure allows transport of the ions throughout the membrane, while the in-plane alignment (bottome) restricts transport through the thickness direction of the film. c. Scanning electron micrographs at different extents of BCP alignment showing thin-film defects and d. a simplified schematic of aligned BCEs showing how an ion may travel from the top to bottom in each system. White circles highlight a few positions in the film where ions are unable to traverse the film.

separation through the de-mixing of dissimilar polymer segments into periodic nanoscale structures. The physical connection of the chemically dissimilar segments restricts the phase separation length scales similar to the radius of gyration. The morphologies that are formed by the microphase separation can be controlled by manipulating a number of variables including: the volume fraction of the segments, the chemical dissimilarity of the domains, and additional external fields.

First, the effect of volume fraction of the segments of the BCE are shown in Figure 1.3. In a diblock copolymer for an examples, ϕ_A=1- ϕ_B, where ϕ is the volume fraction of the blocks A and B, as ϕ_A increases in volume and ϕ_B decreases, a sequence of morphologies is encountered stating with cubic packed spheres of block A, to hexagonally packed cylinders of block A, to bicontinuous two phased gyroids, to lamellae morphology, then back to cubic packed spheres of block B. Second, phase separation of the BCP and the morphology of the resulting film is dictated by the chemical dissimilarity of the two domains defined as the Flory Huggins Parameter (χ) and the molecular weight of the BCP (N). As shown in Figure 1.3b, the morphology can change with χ_N even if the volume of the film remains constant. There is also a point at low χ_N at which phase separation ceases to occur. This point can be reached by decreasing N, or by changing the χ. χ can change by changing the segment chemistries, but also with temperature. At a critical temperature, the chemical difference of the two domains becomes masked increasing the miscibility of the two domains to a point where phase separation ceases to occur. This point is commonly called the order-disorder temperature (TODT). Above TODT, the BCP film is isotropic, disordered, and in a melt like state. Third, in addition to the inherent chemical property difference of the domains, external fields can be employed to engineer the domains to form high levels of anisotropy. The methods reported in literature include: mechanical shear alignment, electric field alignment, and magnetic field alignment. The methods of alignment are discussed in detail below.

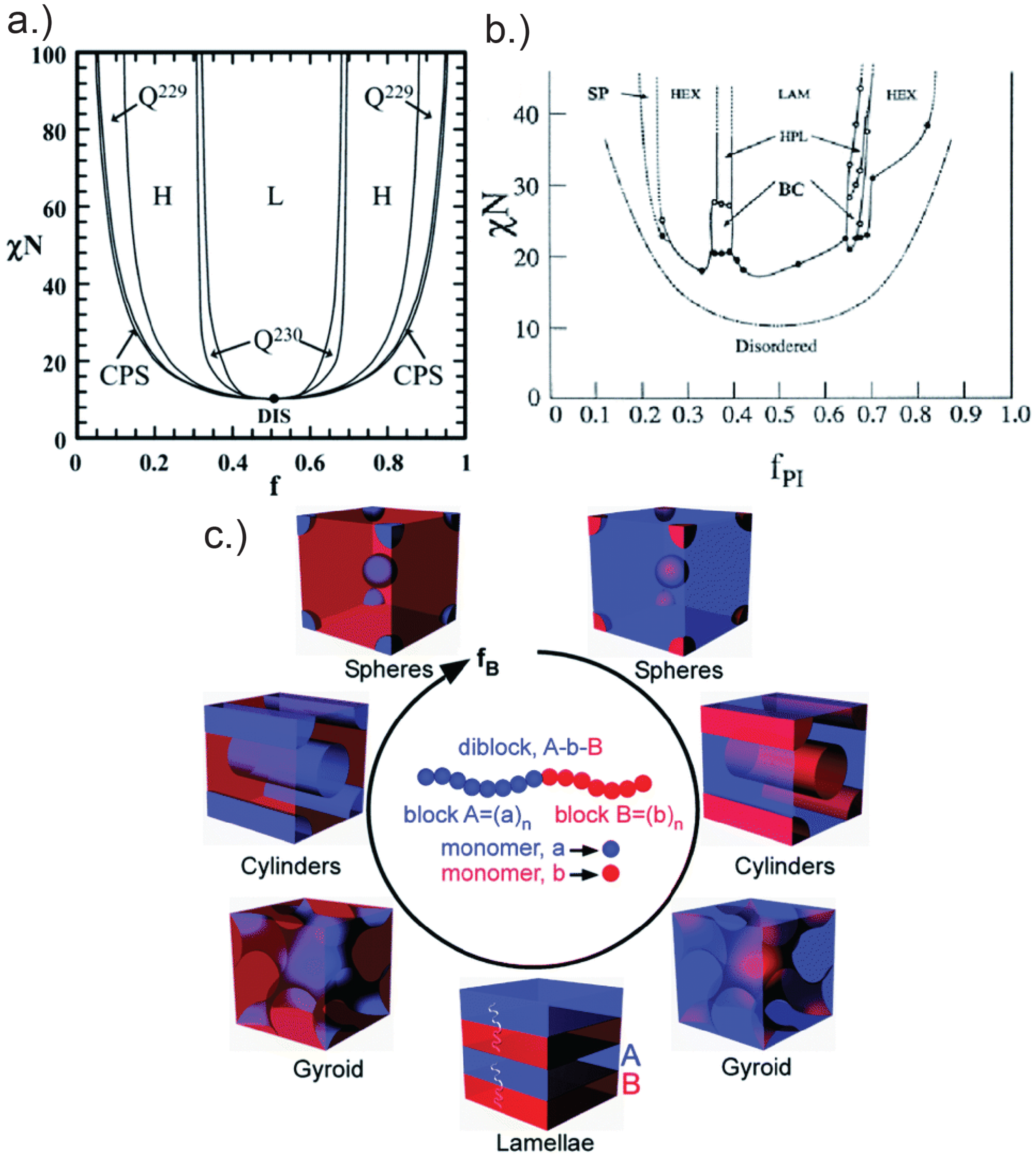

Figure 1.3: Diblock copolymer melt state phase behavior. a.) Theoretical predictions by self-consistent field theory where N is the degree of polymerization, χ is the Flory interaction parameter, f is volume fraction of one of the blocks. CPS: close packed spheres, H: hexagonally packed cylinders, $Q229$: body centered spheres, $Q230$: double-gyroid, L: lamellae and DIS: disordered. b.) Experimental results for PS-b-PI. c.) Schematic illustration of microstructures of diblock A-b-B (where block A is consists of monomers ‘a’ while B is made of monomers ‘b’) on increasing the volume fraction of the B block. Phase diagrams adapted with permission from Macromolecules.[17],[18] Copyright (1995,1996) American Chemical Society. Base diagram adapted with permission of The Royal Society of Chemistry.[19]

1.4 Bicontinuous Structures

In certain morphologies, both the ion conducting and mechanically supporting domains can achieve macroscale continuity without any long-range order. These bicontinuous morphologies are of significant interest because they can achieve a high degree of connectivity in a film without any sophisticated post-processing (e.g. Mangetic field alignment). Notable bicontinuous structures reported for BCEs include BCEs undergoing spinodal decomposition, polymerization induced phase separation, and gyroids. [20–22]

1.4.1 Spinodal Decomposition

A common method of forming a bicontinuous film is to prevent full phase separation from occurring in a BCP. For an example, Chintapalli et al [20] demonstrated an increase in conductivity by flash freezing a lamellae forming Poly(styrene)-block-Poly(ethylene oxide) with LiTFSI and slowly increasing the temperature of the film while the grain size and the conductivity of the film were characterized. When the conductivity was normalized for temperature, they were ale to determine that when the grain boundaries were at the scale of the natural periodicity of the BCE (20 nm), the ion conductivity was higher than when the grains were at micron scales. When the grain size is near the periodicity of the film, it is indicative of a partial phase separation similar to a film that is undergoing spinodal decomposition. Such a film achieved a higher conductivity through the nanostructure due to the lack of defined grain boundaries.

1.4.2 Polymerization Induced Phase Separation

While films that undergo spinodal decomposition are bicontinuous, the structure can still undergo phase separation. To prevent any further change in morphology, Lodge and Hillmeyer have reported on a method for forming, phase separating, and crosslinking a BCE in a single process. The process, called polymerization induced phase separation, is a synthesis process in which the reaction for forming the BCE also microphase separates the morphology. By stopping the synthesis and crosslinking the mechanical domain of the BCE, the morphology of the film can be suspended in such a way to resemble a film undergoing spinodal decomposition. The conductivities of such morphologies reported by Chopade et al [23, 24] are within a factor of five of the homopolymer conductivity.

1.4.3 Gyroids

Of the original morphologies reported in Figure 1.3, the only bicontinuous morphology reported is the gyroid morphology. The gyroid morphology also can form grains and consequently grain boundaries. However, due to the nature of the morphology, the grain boundaries are well connected and do not form ion conduction blockades. A well phase separated film like this have been reported by Kim et al.[22] In this study, the (BCE) was reported to exhibit ion conductivity values within a factor of two of the homopolymer counterpart.

1.5 Engineered Grain Boundaries

In addition to developing morphologies with inherently bicontinuous structures, grain boundaries can also be engineered in non-bicontinuous structures to form lower resistance grain boundaries. For an example, Hoarfrost et al [25] introduced ionic liquids (ILs) into a lamellae forming PS-b-P2VP and phase separated the film. The film was fully phase separated into a lamellae structure but the conductivity of the film was shown to collapse within experimental error onto percolation theory. In addition, it has been reported previously by Stoykovich et al,[26] that small molecules will selectively move into grain boundaries and defect sites to reduce the free energy in the system.

1.6 Anisotropic Alignment of Morphology

One approach to achieving continuous domains throughout BCEs is to introduce external fields to align the self-assembled nanoarchitecture. Using external field alignment techniques, microphase separated domains of the BCE can be aligned parallel to the desired transport direction (e.g., with through-plane alignment in membranes) and can be connected from one side of the BCE to the other by eliminating all of the barriers in the percolating pathways in the ion conducting domain. Figure 1.2b demonstrates how through-plane alignment is preferred to the alignment orthogonal to the thickness direction (i.e., in-plane alignment) because most electrochemical devices are sandwich type cells; in addition, in fuel cells and flow batteries, through-plane aligned membranes also provides the isolation of the liquid or gaseous reactants. In response, significant research has been focused on aligning the ionic domains of microphase separated BCEs to improve material function and characterize transport behavior.[14, 27–30] Recent advances in aligning BCEs are highlighted below to emphasize the role of the microphase separated structure and domain alignment on the ion conducting pathways. Although the constituent ion conducting polymer and the selection of ion conducting materials are critical for such applications, such considerations are only briefly discussed here and the reader is instead directed to other reviews on BCEs and ion conducting polymers.[16, 31, 32]

1.6.1 Mechanical Alignment

Mechanical alignment is considered one of the most versatile thick film alignment techniques due to its applicability to a diverse set of BCPs. To date, BCP films have been aligned through methods such as mechanical shear,[33, 34] compression,[14] extrusion,[35, 36] and roll casting.[37] The degree of alignment can be controlled by manipulating variables such as the molecular weight, volume ratio of polymer segments, viscoelastic properties of each polymer component, shear rate (or shear frequency for dynamic shearing), force amplitude, and force direction.[33, 34, 38–41] In one example, Albalak et al.[37] reported a roll-casting technique to align poly(styrene-block-butadiene-block-styrene) in the through-plane direction using constant shear. Shear and compression alignment techniques were also successfully applied to the BCE poly(styrenesulfonate-block-methylbutelyne) by Park et al.[14] Although the origin of assembly in mechanical alignment is known to be related to the differences in mechanical properties of each domain, the explicit theory behind the mechanism is still debated.

1.6.2 Electric Field Alignment

Electric field alignment is attractive because of its strong effect on non-charge carrying materials and the inverse relationship of field strength on the electrode separation distance. This uniquely enables electric fields to align a wide range of materials more effectively than other methods through thicknesses attractive for many membrane applications. The extent of alignment of a lamellar-forming block copolymer is proportional to the local energy (δg) of the interface of the BCP in relation to the electric field:

$$\delta g = \frac{\delta\epsilon^2}{\epsilon} E^2 (q_{Efield} \cdot q_{AB})^2 \tag{1.1}$$

where $\delta\epsilon$ is the difference in the dielectric constant of the two polymer domains, $\langle\epsilon\rangle >$ is the space averaged dielectric constant, E is the strength of the electric field, and $(qEfield \cdot qAB)$ is the dot product of the vectors between the applied electric field and the normal to the polymer domain interface, respectively.[42–45] As the system approaches full alignment, the driving force behind alignment decreases significantly thus requiring a BCP with a large dielectric difference or the application of a large electric field. Both direct and alternating electric fields have successfully been applied to orient BCP domains.[46] Alternating field alignment is particularly useful for domains with mobile ions that may accumulate and otherwise form a counter field in a direct field setup. Amundson et al.[44] was the first to align poly(styrene-block-methylmethacrylate) BCPs under an electric field. More recently, Park et al.[14] achieved alignment of the proton conducting BCE poly(styrenesulfonate-block-methylbutylene) using an electric field. In an attempt to scale up the process, electric field alignment systems have been integrated into roll-to-roll manufacturing.[47] However, the need to kinetically trap the aligned structure prior to removing the electric field and the dielectric breakdown limits of polymer materials remain challenges to large-scale implementation of such processing methods.

1.6.3 Magnetic Field Alignment

Exposure to magnetic fields is another promising technique for the alignment of BCPs, in part because it eliminates the need for direct material contact and therefore is more amenable to roll-to-roll and other scalable manufacturing processes in comparison to other alignment methods. Additionally, due to the lack of a dielectric breakdown, a large magnetic field can be applied to align the system. The alignment occurs when $\delta\epsilon_m V\ kT$ where V is the volume of a BCP domain and:

$$\delta\epsilon_m = \frac{\delta\psi B^2}{2\mu_0}\frac{3Cos(90-\theta)^2}{2} \tag{1.2}$$

$$\delta\psi = \frac{(\psi_A - \psi_B)^2}{\frac{\psi_A}{\phi_A} + \frac{\psi_B}{\phi_B}} \tag{1.3}$$

where B is the magnitude of the magnetic field, μ_0 is the permittivity constant, ψ_A and ψ_B are the magnetic susceptibilities of the two polymer domains, and θ is the angle between the magnetic field and the normal to the domain interfaces in the BCP.[48] Similar to the electric field alignment method, magnetic field strength and the BCP permittivity differences can be increased to counter balance the reduction in energetic driving force for alignment as alignment is achieved. Osuji et al.[29, 30, 48–52] successfully employed large magnetic fields ($3\ T$) to align BCEs with the aid of LC or crystalline moieties with large

Method of Alignment	Mechanical Segment	Conductive Segment	BCE Type	ϕ_c	Alignment	Conductivity (mS/cm)	T (\circ C)	RH (%)	Ref
Mechanical	PMB	PSS (20 mol % sulfonated)	SI	0.465	A	31	25	98	Park et al. \cite{Park2010}
					I	34			
					AA	45			
Electric	PMB	PSS (20 mol % sulfonated)	SI	0.465	A	28	25	98	Park et al. \cite{Park2010}
					I	35			
					AA	35			
Magnetic	PLA/CB	PEO/$LiClO_4$ (1:120)	DS	0.23	A	3E-4	25	–	Majewski et al. \cite{Majewski2010}
					I	3E-5			
					AA	4E-7			

Table 1.1: Ion conductivities reported in the literature as a function of alignment method for BCEs. The BCEs have been examined when aligned in the channel direction (A), without alignment (I), and in an anti-aligned directions (AA). Single ion conductors (SI) and neutral polymers with dissolved salts (DS) are represented.

$\delta\psi$. A recent report has also shown high extents of alignment using LC-free BCPs such as poly(styrene-block-4-vinylpyridine) with a strong magnetic fields (6 T).[49]

It is important to note that is only a cursory survey that disregards effect to the phase separation due to effects such as crystallinity, lower critical solution temperature, lyotropic ordering, effects of conformational asymmetry, and non-Gaussian statistics.

1.7 Equivalent Medium Theory

In light of the numerous methods for forming nanoarchitectures that promote efficient shuttling of ions from one electrode to the other, a common metric has emerged to report the efficiency of transport as a function of the morphology of the BCE. Here, I will call this common method of disseminating the effect of ion transport in BCEs by the morphology as the Equivalent Medium Theory, or EMT. The EMT was first proposed in the paper by Sax and Ottino [53] in 1983 and popularized in the BCE community by Balsara et al [54] in 2014. Structure-function relationships in BCEs are challenging to derive because the periodic domain structure of BCEs formed through self-assembly are well-ordered only locally, at the sub-micron scale, but transport properties are typically measured over macroscopic dimensions, on the scale of tens to hundreds of microns. At this device scale, the materials can be described as consisting of multiple grains. The implications of this structure are that regardless of the local BCE morphology, the materials have the potential to conduct in three dimensions, the conduction pathways are likely to be highly tortuous, and mechanisms of transport across grain boundaries and defects must be considered. EMT[16] is a methodology to characterize the dependence of ion transport on morphology and is written in its simplest form as:

$$\sigma_{BCE} = f\phi_{cond}\sigma_h \tag{1.4}$$

where σ_{BCE} is the conductivity of the BCE, σ_h is the conductivity of the homopolymer that is chemically identical to the conducting block of the BCE, ϕ_{cond} is the volume fraction of the conducting block, and f is a tortuosity factor. Theoretical values of f have been determined by Sax and Ottino[53] for multi-grained films that are comprised of grains of periodic nanoscale BCP morphologies that form charge transport defects at grain boundaries. The transport defects result in increased tortuosity of ion transport paths and a lower conductivity for multi-grained films. Sax and Ottino have determined f to be 1 for bicontinuous morphologies such as gyroids, 1 for sphere-forming BCEs where the majority phase is ion conducting, 0.66 for lamellae forming systems, 0.33 for cylinder-forming BCEs where the minority phase is ion conducting, and 0 for sphere-forming BCEs where the minority phase is ion conducting.

1.8 Characterization of Deterministic Structure

In most of the literature, the morphology of BCPs have been characterized by complementary methods that provide information on the average structure, such as small angle x-ray scattering (SAXS) and birefringence, in combination with higher resolution and real-space approaches such as electron microscopy to access local structural information. Figure 1.4 highlights the structural characterization of BCE films aligned using the methods discussed in the previous section. In-situ birefringence and two-dimensional SAXS data were collected for the aligned samples to show the degree of increase in alignment in the through-plane direction. Bulk scattering techniques, such as SAXS in particular, are attractive due to the large cross-sectional areas (i.e., mm scale) that can be characterized allowing acquisition of statistical structural information including the degree of alignment. In Figures 1.4b and c, TEM micrographs and finite Fourier transform (FFT) analysis of the micrographs are shown that were also used to characterize the morphology orthogonal to the through-plane direction. Cross sectional AFM may also be used to visualize the BCP structure, as shown in Figure 1.4c, enabling the direct characterization of the nanoscale structure, confirm alignment, and to identify defects.

In Figure 1.4a Chopade et al [21] characterized the structure of the morphology of the polymerization induced phase separation reaction with a PEO conducting domain using SAXS, TEM, and SEM. The SAXS showed a single broach scattering peak that increased as a function of increasing Li salt concentration that is indicative of a microphase separated bicontinuous film. The phase separation is confirmed by the TEM image where the dark areas are stained PS domains and the SEM image where the bright sections are the remaining PS domains following an HCl etch. Using the evidence in Figure 1.4b and c, Park et al.[14] demonstrated alignment of poly(styrenesulfonate-block-methylbutylene) (PSS-block-PMB) using mechanical shear (Figure 1.4b) and electric field (Figure 1.4d). Comparing the birefringence data, the mechanical shear alignment yielded a degree of alignment four times better than the electric field. The surface TEM probing the structure orthogonal to the through-plane direction showed perpendicular orientation of the domains in both mechanical and electric field alignment samples, suggesting successful alignment through the film. In Figure 1.4d, Feng et al.[50] demonstrated alignment of poly(ethylene oxide-block-6-(4-cyanobiphenyl-4-yloxy)-hexyl methacrylate) (PEO-block-PLA/CB) with dissolved $LiClO_4$ using a large magnetic field. Here, the birefringence has a higher signal contrast and the two-dimensional SAXS shows a narrow set of points on the horizontal axes indicating a high degree of alignment in comparison to the electric field and shear alignment. The cross-sectional AFM also can be visually inspected for defects and, at lower degrees of alignment, provide evidence that a fraction of the domains is now percolated.

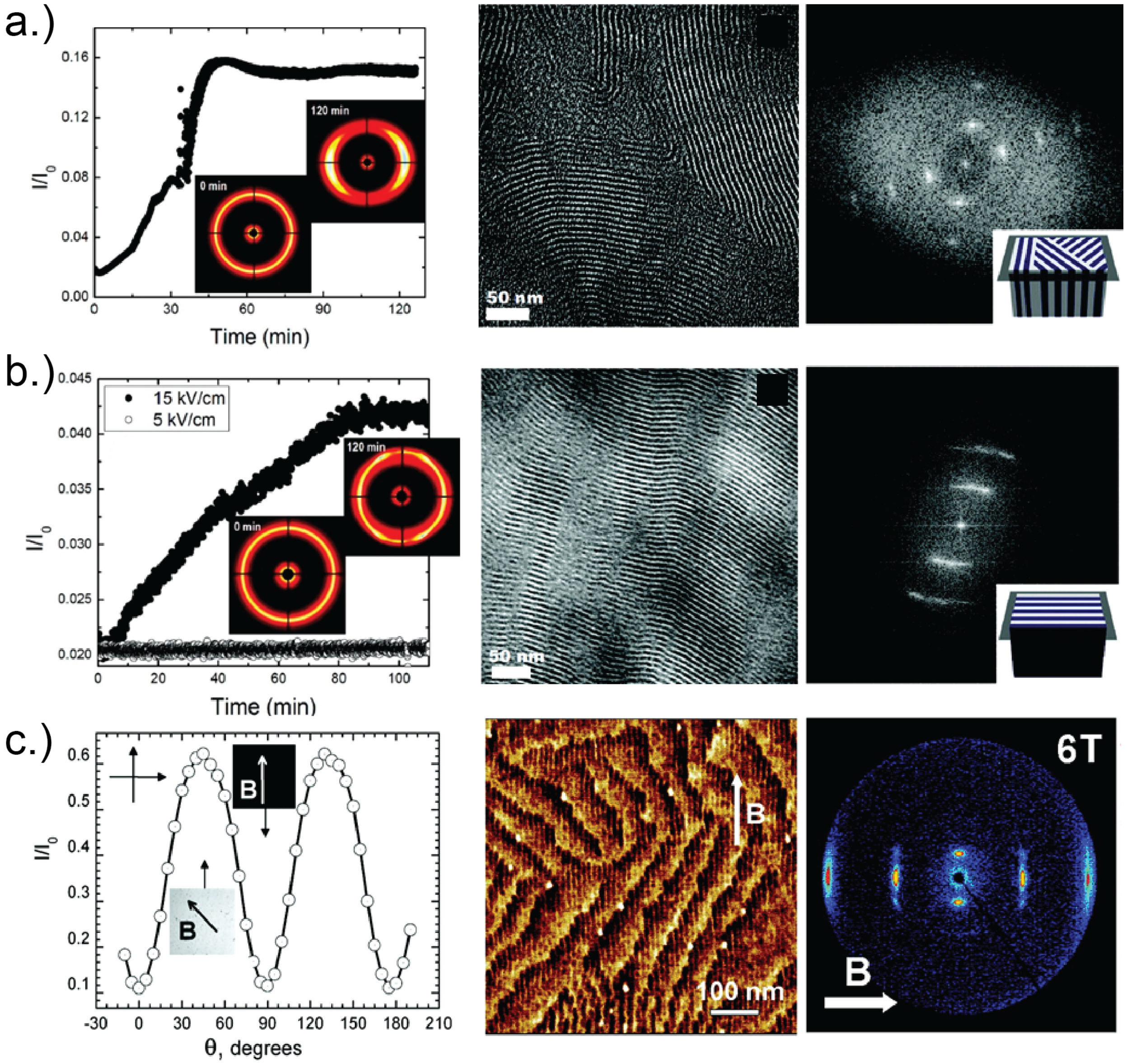

Figure 1.4: Characterization of alignment of block copolymer domains using complementary real-spacing imaging and scattering methods. Birefringence, SAXS, and cross-section TEM (from left to right) of poly(styrenesulfonate-block-methylbutylene) aligned through-plane using a. mechanical shear and b. electric fields. [Adapted with permission from Ref. [14]. Copyright 2010 American Chemical Society.] c. Birefringence, cross sectional AFM, and SAXS (from left to right) of a through-plane magnetic field aligned poly(ethylene oxide-block-6-(4'-cyanobiphenyl-4-yloxy)-hexyl methacrylate) with $LiClO_4$ dissolved in the poly(ethylene oxide) layer. Adapted with permission from Ref. [29]. Copyright 2010 American Chemical Society.

1.9 Conclusion

As demonstrated above, the average structure and the morphology of the BCE film can be determined using methods such as SAXS, TEM, SEM, AFM, and birefringence. However the individual nanoscale conduction pathways are near impossible to characterize due to the number of nanoscale pathways per film. Consequently, the structure function relationship reported by this method can only provide a statistical understanding of the transport efficiencies and little can be extracted about ion transport behavior at the molecular scale. BCEs inherently introduce a high number of interfaces due to the nanoscale periodicity of the film, and there is a significant opportunity to engineer this interface to surpass the efficiencies of the homopolymer conductors. For this to occur however, there is still a need to understand how ion transport and more pragmatically, AC impedance response, is affected by both the morphology and molecular deviations from the homopolymer (i.e. crystallinity, anisotropy in segmental configurations). To do so, there is a need to take a drastically different approach to deriving structure function relationships in BCE systems.

In my work, I report on the use of thin film BCP directed assembly techniques to control morphologies on top of interdigitated electrodes. The approach in its multitudes have yielded successful ways to characterize both deterministic structure and AC impedance responses. The suite of solutions have enabled the decoupling of the morphology and molecular contributions to deviations to the EMT and can provide insights into why specific morphologies have reported f values that were significantly smaller than EMT predictions and others have reported close correlations. Furthermore, the morphology contributions on deviation from EMT was further isolated by forming ion conduction pathways by patterning insulator material into nanoscale trenches, confining ion conducting homopolymers into controlled ion conduction pathways, and studying the impedance response as a function of the pathways. Finally, the molecular contribution on deviation from EMT was further isolated by studying ion transport in the BCE as a function of water content and proximity to Tg. The resulting insight informs the governing principles behind ion transport in heterogeneous nanostructures and how future BCE systems can be engineered to match, if not surpass the transport performance of homoplymer systems.

1.10 References

[1] Y. Kambe, C. G. Arges, S. Patel, M. P. Stoykovish, and P. F. Nealey, The Electrochemical Society Interface **26**, 61 (2017).

[2] D. E. Fenton, J. M. Parker, and P. V. Wright, Polymer **4**, 6272 (1973).

[3] L. D. McIntosh, T. Kubo, and T. P. Lodge, Macromolecules **47**, 1090 (2014), ISSN 00249297.

[4] M. W. Schulze, L. D. McIntosh, M. A. Hillmyer, and T. P. Lodge, Nano Letters **14**, 122 (2014), ISSN 15306984.

[5] J. F. Snyder, R. H. Carter, and E. D. Wetzel, Chemistry of materials **19**, 3793 (2007).

[6] B. Smitha, S. Sridhar, and A. A. Khan, Journal of Membrane Science **225**, 63 (2003), ISSN 03767388.

[7] S. Ji, L. Wan, C. C. Liu, and P. F. Nealey, Progress in Polymer Science **54-55**, 76 (2016), ISSN 00796700.

[8] C. Sinturel, F. S. Bates, and M. A. Hillmyer, ACS Macro Letters **4**, 1044 (2015), ISSN 2161-1653.

[9] Q. Peng, Y. C. Tseng, S. B. Darling, and J. W. Elam, ACS Nano **5**, 4600 (2011), ISSN 19360851.

[10] C. Cummins, T. Ghoshal, J. D. Holmes, and M. A. Morris, Advanced Materials pp. 5586–5618 (2016), ISSN 15214095.

[11] J. Kamcev, D. S. Germack, D. Nykypanchuk, R. B. Grubbs, C. Y. Nam, and C. T. Black, ACS Nano **7**, 339 (2013), ISSN 19360851.

[12] M. Biswas, J. A. Libera, and S. B. Darling, Chemistry of Materials **26**, 6135 (2014).

[13] C. G. Arges, Y. Kambe, H. S. Suh, L. E. Ocola, and P. F. Nealey, Chemistry of Materials **28**, 1377 (2015), ISSN 0897-4756.

[14] M. J. Park and N. P. Balsara, Macromolecules **43**, 292 (2010), ISSN 00249297.

[15] M. Singh, O. Odusanya, G. M. Wilmes, H. B. Eitouni, E. D. Gomez, a. J. Patel, V. L. Chen, M. J. Park, P. Fragouli, H. Iatrou, et al., Macromolecules **40**, 4578 (2007), ISSN 0024-9297.

[16] Y. a. Elabd and M. a. Hickner, Macromolecules **44**, 1 (2011), ISSN 00249297.

[17] M. W. Matsen and F. S. Bates, Macromolecules **29**, 1091 (1996).

[18] A. K. Khandpur, S. Foerster, F. S. Bates, I. W. Hamley, A. J. Ryan, W. Bras, K. Almdal, and K. Mortensen, Macromolecules **28**, 8796 (1995).

[19] H. Hu, M. Gopinadhan, and C. O. Osuji, Soft matter **10**, 3867 (2014), ISSN 1744-6848.

[20] M. Chintapalli, X. C. Chen, J. L. Thelen, A. A. Teran, X. Wang, B. A. Garetz, and N. P. Balsara, Macromolecules **47**, 5424 (2014), ISSN 15205835.

[21] S. A. Chopade, J. G. Au, Z. Li, P. W. Schmidt, M. A. Hillmyer, and T. P. Lodge, ACS Applied Materials and Interfaces **9**, 14561 (2017), ISSN 19448252, `arXiv:1408.1149`.

[22] O. Kim, S. Y. Kim, J. Lee, and M. J. Park, Chemistry of Materials **28**, 318 (2016), ISSN 15205002.

[23] S. A. Chopade, J. G. Au, Z. Li, P. W. Schmidt, M. A. Hillmyer, and T. P. Lodge, ACS Applied Materials and Interfaces **9**, 14561 (2017).

[24] S. A. Chopade, S. So, M. A. Hillmyer, and T. P. Lodge, ACS applied materials & interfaces **8**, 6200 (2016), ISSN 1944-8252.

[25] M. L. Hoarfrost and R. A. Segalman, Macromolecules **44**, 5281 (2011), ISSN 21611653.

[26] M. P. Stoykovich, M. Muller, S. O. Kim, H. H. Solak, E. W. Edwards, J. J. de Pablo, and P. F. Nealey, Science **308**, 1442 (2005), ISSN 0036-8075.

[27] J. Li, K. Kamata, M. Komura, T. Yamada, H. Yoshida, and T. Iyoda, The Journal of Asian Studies **52**, 107 (1993), ISSN 0021-9118.

[28] R. Mäki-Ontto, K. De Moel, E. Polushkin, G. Van Alberda Ekenstein, G. Ten Brinke, and O. Ikkala, Advanced Materials **14**, 357 (2002), ISSN 09359648.

[29] P. W. Majewski, M. Gopinadhan, W.-S. S. Jang, J. L. Lutkenhaus, and C. O. Osuji, Journal of the American Chemical Society **40**, 17516 (2010), ISSN 1520-5126.

[30] P. W. Majewski, M. Gopinadhan, and C. O. Osuji, Soft Matter **9**, 7106 (2013), ISSN 1744-683X.

[31] N. Li and M. D. Guiver, Macromolecules **47**, 2175 (2014), ISSN 15205835.

[32] W. S. Young, W. F. Kuan, and T. H. Epps, Journal of Polymer Science, Part B: Polymer Physics **52**, 1 (2014), ISSN 08876266.

[33] V. K. Gupta, R. Krishnamoorti, J. A. Kornfield, and S. D. Smith, Macromolecules **28**, 4464 (1996).

[34] V. K. Gupta, R. Krishnamoorti, Z.-r. Chen, J. A. Kornfield, S. D. Smith, M. M. Satkowski, and J. T. Grothaus, Macromolecules **29**, 875 (1996).

[35] W. S. Young and T. H. Epps, Macromolecules **45**, 4689 (2012), ISSN 00249297.

[36] A. Keller, E. Pedemonte, and F. M. Willmouth, Colloid & Polymer Science **238**, 385 (1970), ISSN 0303402X.

[37] R. J. Albalak and E. L. Thomas, Journal of Polymer Science, Part B: Polymer Physics **32**, 341 (1994), ISSN 08876266.

[38] C. Oelschlaeger, J. S. Gutmann, M. Wolkenhauer, H. W. Spiess, K. Knoll, and M. Wilhelm, Macromolecular Chemistry and Physics **208**, 1719 (2007), ISSN 10221352.

[39] D. E. Angelescu, J. H. Waller, D. H. Adamson, P. Deshpande, S. Y. Chou, R. A. Register, and P. M. Chaikin, Advanced Materials **16**, 1736 (2004), ISSN 09359648.

[40] G. H. Fredrickson, Journal of Rheology **38**, 1045 (1994), ISSN 01486055.

[41] S. S. Patel, R. G. Larson, K. I. Winey, and H. Watanabe, Macromolecules **28**, 4313 (1995), ISSN 0024-9297.

[42] K. Amundson, E. Helfand, X. Quan, S. D. Hudson, and S. D. Smith, Macromolecules **27**, 6559 (1994), ISSN 0024-9297.

[43] K. Amundson, E. Helfand, X. Quan, T. B. Laboratories, M. Hill, and S. D. Smith, Macromolecules **26**, 2698 (1993).

[44] K. Amundson, Macromolecules **24**, 6546 (1991).

[45] Y. Tsori, Reviews of Modern Physics **81**, 1471 (2009), ISSN 00346861, `0912.1736`.

[46] S. A. Mullin, G. M. Stone, A. A. Teran, D. T. Hallinan, A. Hexemer, and N. P. Balsara, Nano Letters **12**, 464 (2012), ISSN 15306984.

[47] J. Y. Lee, J. H. Lee, S. Ryu, S. H. Yun, and S. H. Moon, Journal of Membrane Science **478**, 19 (2015), ISSN 18733123.

[48] P. W. Majewski, M. Gopinadhan, and C. O. Osuji, Journal of Polymer Science, Part B: Polymer Physics **50**, 2 (2012), ISSN 08876266.

[49] Y. Rokhlenko, M. Gopinadhan, C. O. Osuji, K. Zhang, C. S. O'Hern, S. R. Larson, P. Gopalan, P. W. Majewski, and K. G. Yager, Physical Review Letters **115**, 2 (2015), ISSN 10797114, `1509.01292`.

[50] X. Feng, M. E. Tousley, M. G. Cowan, B. R. Wiesenauer, S. Nejati, Y. Choo, R. D. Noble, M. Elimelech, D. L. Gin, and C. O. Osuji, ACS Nano **8**, 11977 (2014).

[51] M. Gopinadhan, P. W. Majewski, and C. O. Osuji, Macromolecules **43**, 3286 (2010), ISSN 00249297.

[52] P. Deshmukh, M. Gopinadhan, Y. Choo, S. K. Ahn, P. W. Majewski, S. Y. Yoon, O. Bakajin, M. Elimelech, C. O. Osuji, and R. M. Kasi, ACS Macro Letters **3**, 462 (2014), ISSN 21611653.

[53] J. Sax and J. M. Ottino, Polymer Engineering and Science **23**, 165 (1983), ISSN 0032-3888.

[54] D. T. Hallinan Jr. and N. P. Balsara, Annual Review of Materials Research **43**, 503 (2013), ISSN 1531-7331.

CHAPTER 2

FUNDAMENTALS

2.1 Abstract

In this chapter, I will detail the experimental techniques and designs used throughout my research projects. Each section will include a brief introduction of the approach and common use of the techniques in literature. In the proceeding chapters, the techniques are modified to meet the needs of the experiment. These modifications will be reported in the relevant chapters. This section can act as a primer for those interested in employing the given techniques in their own experiments.

2.2 Approach in the Dissertation

In Chapter 1, I introduced the motivation and base approach for disseminating structure function relationships from BCE nanoarchitectures without making assumptions about the ion conduction paths used in the film. In my work, thin film nanoscale ion conduction pathways (e.g. BCE thin films) are assembled on top of interdigitated electrodes and characterized using 1) AC electrochemical impedance spectroscopy for the transport behavior in the system and 2) scanning electron microscopy and atomic force microscopy for the deterministic structure properties. By using IDEs, both electrochemical and structural information can be extracted from the same film, further reducing error generated from experiments. Each proceeding chapter will add functionality to the approach and provide insight into how BCE structure influences impedance response. It is important to note that many of the studies also employed simulations that were completed by collaborators in the de Pablo research group as well as in the Srinivasen group. The approaches used by the two groups will be described in the relevant chapters.

2.3 AC Electrochemical Spectroscopy

By far, the most commonly employed method of characterization of ion conductivity is AC Electrochemical Impedance Spectroscopy (EIS). [1] To perform EIS, an AC potential is applied to the sample through the electrodes into the polymer and the current response is measured. Figure 2.1 demonstrates a number of potential response cases plotting the probing potential and the sensed current. In Figure 2.1a, the potential perturbation sees an immediate response in current. This overlapping case is when the polymer exhibits a completely resistive response. The perturbation receives an immediate response in current without any delay from the sample. This would occur in cases where the polymer is a highly conductive electron conductor. In Figure 2.1b, we see a delayed response in the current. This shift in peak is called a phase shift and the degree of shift between the perturbation and current can provide information about the imaginary impedance of the system. A larger peak to peak offset indicates a higher capacitive nature and a lower resistive nature of the polymer. In ion conducting polymer such as our systems, this response is more common.

2.3.1 Lissajous Analysis

In Figure 2.2, the current and potential are plotted as the x and y axis respectively. Figure 2.2a, plots the data shown in Figure 2.1a and Figure 2.2b plots the data shown in Figure 2.1b. In Lissajous analysis, the impedance is calculated by taking the peak potential and current response (i.e. the red circle values) and calculating impedance with the equation:

$$Z = \frac{V}{I} \tag{2.1}$$

Where Z is the complex impedance, V is the perturbation potential, and I is the response current. The phase shift is extracted by taking the equation:

$$\phi = Sin^{-1}(Y/B) \tag{2.2}$$

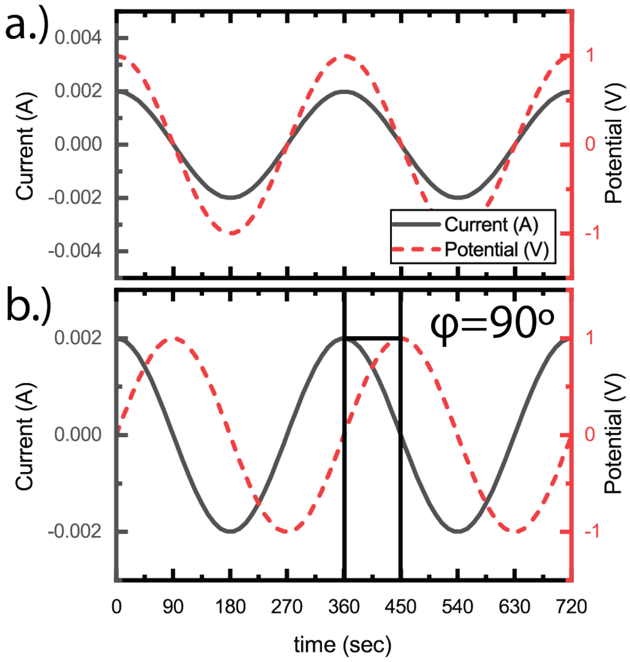

Figure 2.1: Perturbation potential and current response plot for a.) a perfect resistor and b.) perfect capacitor

Where Y is the potential based off of the green circles and B is the potential based off of the blue circles. In EIS, this process is done through a range of frequencies. In our case, the perturbation frequency commonly ranges from 1 MHz to 0.1 Hz.

2.3.2 Bode Plot

Figure 2.3 shows the impedance response and the phase shift as a function of frequency. This depiction of the data is known as a Bode plot. The Bode plot in is useful because it provides the impedance information as a function of both the phase shift and the frequency of perturbation. Bode plots are shown in Figure 2.3a, b, c, and d for common charge conduction systems such as a perfect resistor, a perfect capacitor, a slow and lossy charge conductor (e.g. semiconductor), and an ion conductor (e.g. polymer electrolyte) respectively. Inspection of Figure 2.3a demonstrates that the phase shift is at zero throughout the entire range of frequencies. This is an indicator that the system is resistive, and the behavior of the film is identical to a film probed under direct current (DC) conditions. In Figure 2.3b,

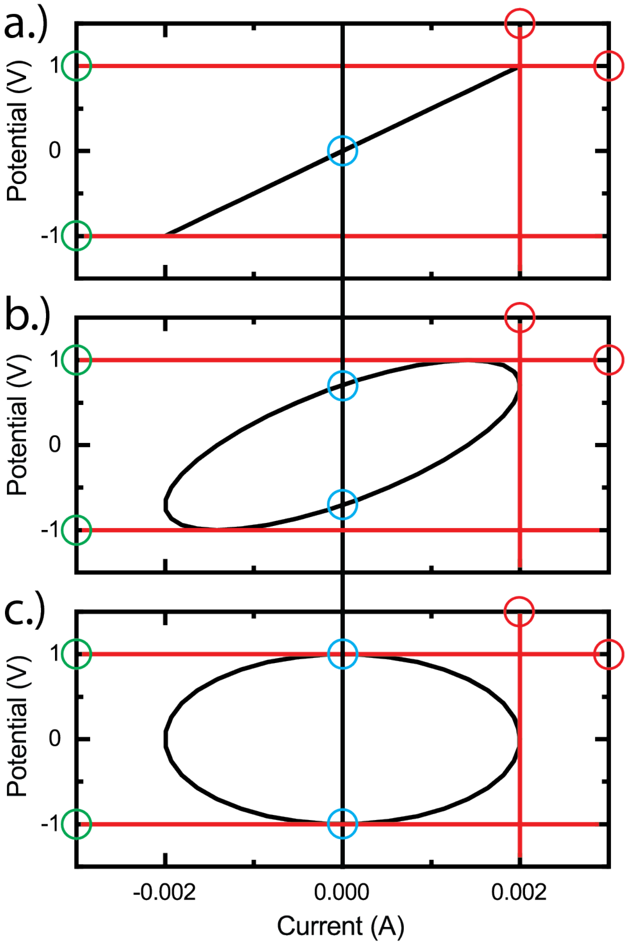

Figure 2.2: Lissajous response of a.) a perfect resistor, b.) a partial capacitor, and c.) a perfect capacitor. Red circles indicate values used to calculate the impedance, blue circles indicate values used to calculate B, and the blue circles indicate values used to calculate C.

the impedance increases at lower frequencies while the phase shift remains at 90 ° signifying that ion transport is capacitive and there is no singificant transport of charge going on in the film. From inspection of Figure 2.3c, at higher frequencies (1 MHz to 100 kHz), the impedance is small, and the phase shift decreases until it reaches 0 while the impedance becomes independent of frequency. This plateau location is indicative of the cross over point where there is no more delay in the current response due to dielectric and charge polarization. Figure 2.3d exhibits a similar behavior to Figure 2.3c, however the phase shift does not go to zero and rather increases at lower frequencies. This global minimum in the phase shift is accompanied by a constant impedance across a range of frequencies prior to increasing again. This behavior is indicative of a charge conductor where the charge concentration is finite. For an example, an ion conducting electrolyte measured with non-redox active electrodes (blocking electrode) can exhibit a resistance that may be probed at certain frequencies but at a critical point, the slow timescale begins to form depletion regions the local environment is not charge neutral and a concentration of ions at interfaces begin to form charge repelling double layers. In a DC system, such a film would exhibit a current close to zero due to the lack of replenishing charges.

2.3.3 Nyquist Plot

To understand the data further, the impedance and the phase shift information can be combined into a Nyquist Plot. To plot a Nyquist one begins with a complex representation of the ohm's law.

$$V_0 exp(i\omega) = Z I_0 exp(i\omega + \phi) \tag{2.3}$$

Where V_0 is the maximum amplitude potential, Z is the complex impedance, I_0 is the maximum amplitude current and ϕ is the phase shift of the film. Solving for Z, we simplify

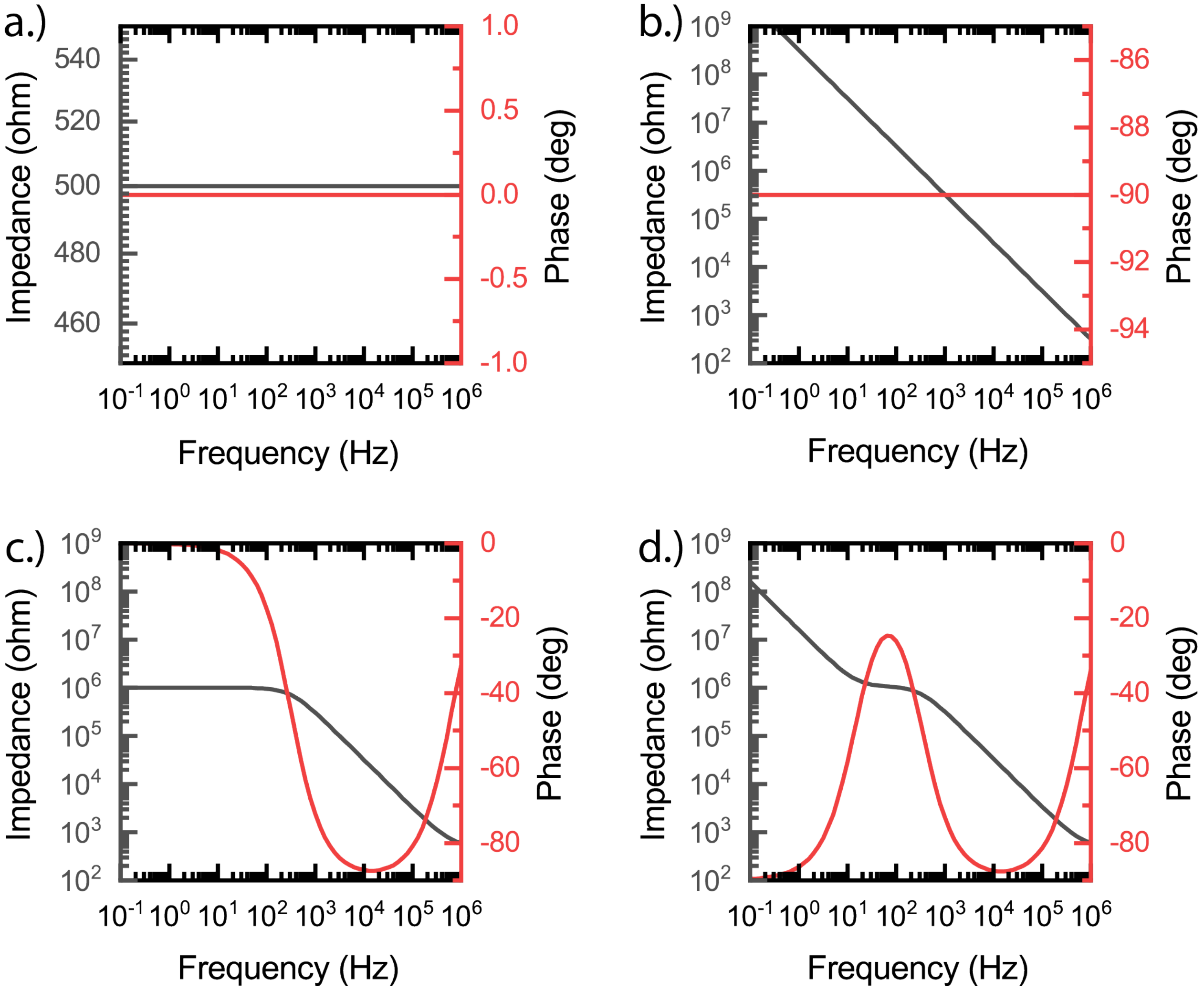

Figure 2.3: Bode plots of a.) a perfect resistor, b.) a perfect capacitor, c.) a randles cell, and d.) a charge conductor with a blocking electrode.

the equation to

$$Z = \frac{V_o}{I_o} exp(-i + \phi) \tag{2.4}$$

With Euler's Approximation, the exponent is simplified to:

$$Z = \frac{V_o}{I_o}(sin(\phi) - icos(\phi)) = Z_o(sin(\phi) - icos(\phi)) \tag{2.5}$$

The impedance vales are depicted in Figure 2.4 as the real impedance component on the x axis and the imaginary component on the y axis. Each data point in this Nyquist plot corresponds to a frequency dependent impedance and phase shift. Consequently, the Nyquist plot obscures frequency dependence of the impedance, however provides the researcher with a unique view of the impedance response that is visually easier to interpret for equivalent circuit modeling. The shape of a perfect resistor, a perfect capacitor, a slow and lossy charge conductor (e.g. semiconductor), and an ion conductor (e.g. polymer electrolyte) are again shown in Figure 2.4a, b, c, and d respectively to demonstrate the differences in shapes formed. Resistance of the film in Figure 2.4c and d can be estimated by taking the diameter of the hemisphere. In Figure 2.4d, the hemisphere does not fully touch back down to Zimag value of zero. This is due to the emergence of double layer capacitance contributions to impedance at lower frequencies. In such cases, the resistance can still be approximated by projecting the location where the hemisphere would touch down to the Zreal axis.

2.3.4 Equivalent Circuit Modeling

When the measured system is homogeneous like an ion conducting homopolymer, a simple diameter extraction is sufficient to obtain resistance and capactiance data. But in heterogeneous structures, the spectra collected using EIS will contain complex impedance response that can be harder to interpret. In such complex imepdance systems, equivalent circuit modeling (ECM) can be used to fit and extract resistance and dielectric properties of the measured film from the impedance data. ECM utilizes circuit elements arranged in certain

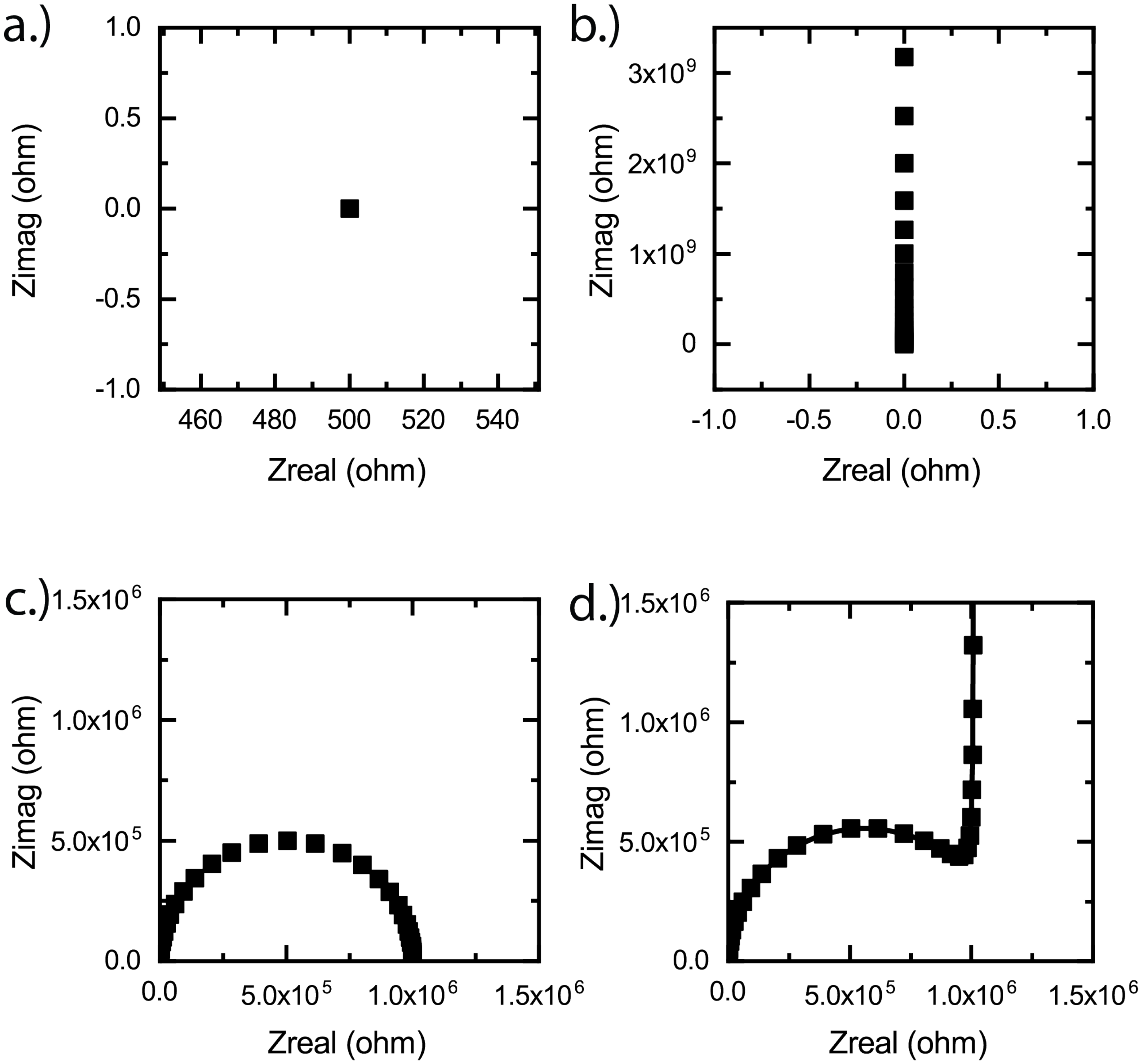

Figure 2.4: Nyquist plots of a.) a perfect resistor, b.) a perfect capacitor, c.) a randles cell, and d.) a charge conductor with a blocking electrode.

orientations (e.g. parallel or series) to form a circuit equivalent model of charge transport in the film. In addition to a resistors and capacitors commonly seen in circuits, additional elements are introduced to model elements of diffusion and "leaky" capacitors. In this section, I will provide a brief introduction to ECM along with justifications for its use in typical EIS setup that will enable the reader to understand my decisions to use specific ECM elements in later chapters. For further reading, the reader is referred to additional work from our group.[2]

We revisit a common Nyquist plot response that is collected from an interdigitated electrode with a thin film of ion conducting homopolymer on top and an overlay of the circuit elements on top of a common charge transport pathway in an interdigitated electrode. It can be seen that the film contains four shape features: 1) a delay in the beginning of the hemisphere at about 200 ohms, 2) the hemisphere at lower impedance values, 3) a transitionary linear curve as impedance increases, 4) and a long linear tail. We will explore each of these features in reference to an ion conduction pathway. It is important to note, that previously, we stated that a simple projection of the diameter of the hemisphere can provide relatively accurate information about the resistance. This section will provide discussion in respect to this system to show complimentary methods of extracting transport information out of impedance data.

First, the impedance data does not begin exactly at zero here due to the existence of resistance in the wires and the interdigitated electrodes prior to the perturbation of the polymer itself. This is commonly modeled in the ECM as a simple resistor placed in parallel to the rest of the impedance models. Resistance is related to the impedance as:

$$Z = R \tag{2.6}$$

Where R is resistance.

Second, there is a hemisphere at lower impedance values that can be used to extract out the polymer's resistance and capacitance that is due to ion transport. In a hemisphere such as the one seen here, the diameter of the radius measured in the x-axis (real impedance response) from the beginning of the hemisphere to the projected point that it touches back down as shown in Figure 2.5 represents the AC resistance value from the polymer. In the case that the projected end of the hemisphere is difficult to determine, an ECM of a resistor and a capacitor can be placed in parallel to form a hemisphere. This circuit element is commonly called a Randle's cell. The impedance relationship to capacitance is as follows:

$$Z = \frac{1}{j\omega C} \tag{2.7}$$

Where C is the capacitance.

In practice, it is more common to substitute the capacitor in the Randle's cell with a constant phase element (CPE). The CPE is a two-factor fit that enables the modeling of an imperfect capacitor. It is commonly used by the BCE community due to the heterogeneity of the interface between the electrodes and the polymer. CPE is related to impedance as the function:

$$Z = \frac{1}{Q_0(j\omega)^{\alpha}} \tag{2.8}$$

Where Q_0 and α are the CPE fitting parameters with the units $Siemen * s^{\alpha}$ and unitless respectively. The exponent α is a value that ranges from 1 $<\alpha<$0. It is important to understand the relationship between the capacitance and CPE. When α approaches 1, the impedance relationship of the CPE simplifies to equation 2.7. When α is not 1, the capacitance of the film can be calculated when the CPE is in a Randles Cell through the relationship:

$$C = \frac{(Q_0 R)^{1/\alpha}}{R} \tag{2.9}$$

Where R is the resistance extracted from the resistance in parallel to the CPE in the Randles Cell.

When all of the elements of the model have been defined, the model is converted into a impedance equation and fit to the Nyquist (or Bode) plot using a multivariable fitting process such as the Simplex method. For impedance elements in series, the relationship is simply:

$$Z_{total} = Z_1 + Z_2 + Z_3 + \tag{2.10}$$

While the impedance relationship for elements in parallel are:

$$1/Z_{total} = 1/Z_1 + 1/Z_2 + 1/Z_3 + \tag{2.11}$$

When the impedance of the R_{film} and CPE_{film} are combined into an impedance value, the equation becomes:

$$Z = \frac{R_{film}}{j\omega C^{\alpha} R_{film} + 1} + R_e \tag{2.12}$$

Third, prior to the hemisphere touching down to an imaginary impedance of zero, the impedance begins to increase again. This slope is notably less steep compared to the linear section at higher impedance values and the presence of this transition section can be interpreted as a diffusion process of charge in the polymer film. At faster perturbation frequencies, the impedance signal from diffusion is low because the ions do not travel far. Conversely, at slower perturbation frequencies, the ions are able to move further resulting in a larger impedance contribution. This can be modeled by the Bounded Warburg element that relates to impedance as:

$$Z = \frac{1}{Y_0\sqrt{j\omega}} tanh(B\sqrt{j\omega}) \tag{2.13}$$

Where Y_0 and B are the Warburg fitting parameters with the units $siemens * s^{1/2}$ and $s^{1/2}$ respectively, ω is the radial frequency in the unit of s^{-1} and j is the imaginary constant.

B is depicted as:

$$B = \frac{\sigma}{\sqrt{D}} \tag{2.14}$$

Where σ is the Nernst Diffusion layer constant with the unit in cm and D is the diffusion constant in cm^2/s.

Fourth, at the high real and imaginary impedance values of the spectrum, the impedance increases as a line that is a steeper slope in comparison to the Warburg element. This linear impedance response can be correlated to the formation of the double layer at the interface of the polymer and the electrode. This double layer formation occurs due to the inability for charge transfer of electrons in the electrode into ion carriers due to the lack of a redox reaction. This capacitive tail can be modeled as a capacitor or a CPE. In our case, the CPE is commonly used.

When the circuit elements discussed above are combined for our ion conducting system, the final impedance equation becomes:

$$Z = \frac{tanh(B\sqrt{j\omega})}{j\omega C_{dl}^{\alpha} tanh(B\sqrt{j\omega}) + Y_0\sqrt{j\omega}} + \frac{R_{film}}{j\omega C^{\alpha} R_{film} + 1} + R_e \tag{2.15}$$

The fit of this specific model to the data is shown in Figure 2.5d as the solid line and the values extracted are shown in Table 2.1. From this table, the R_{film}, Q_{film}, and α_{film} are of particular interest for calculating the conductivity and dielectric parameters. To calculate the material parameters, there is a need to first understand the geometry of the thin film on top of the measurement device called an interdigitated electrode.

2.4 Interdigitated Electrodes

One characterization challenge of thin film polymers is the low current response that results from the nanoscale geometry of one dimension paired with the macro scale of the other dimensions. For an example, an impedance response from a 100 mS/cm polymer film (i.e.

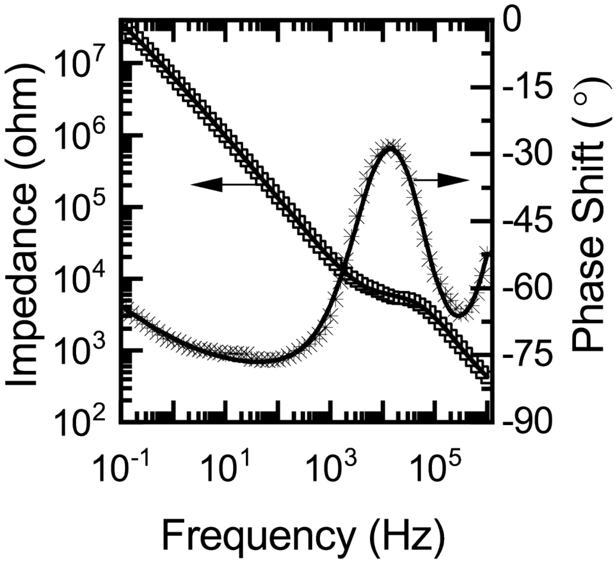

Figure 2.5: Bode plot (scatter) and model (line) fit of an ion conductor on top of an IDE.

Model Variable	Value	Units
R_e	200	ohm
R_{film}	5000	ohm
Q_{film}	715E-12	$S \cdot s^{\alpha}$
α_{film}	0.980	-
Q_{dl}	23.23E-9	$S \cdot s^{\alpha}$
α_{dl}	0.889	-
Y_0	16.51E-9	$S \cdot s^{1/2}$
B	874.8	$\sqrt{sec}$

Table 2.1: Extracted parameter values from an ion conducor on top of an IDE.

sulfonated polystyrene at 25 °C and 95 %RH) that is measured across the thin film thickness of 50 nm with a cross sectional area of 1 cm^2 in a parallel plate configuration. This setup would result in EIS measuring an impedance response of 50 $\mu ohms$. Considering the parasitic resistance in the setup (electrode and wire resistances) can be as high as 300 $ohms$, it becomes impractical to measure films in this geometry because the signal from the sample would be lost in the noise. To achieve a reasonable resistance difference of the electrode and film, the resistance should be at the least 1 $kohms$. To reach this value with this ion conductor, the cross-sectional area would have to be $5 \cdot 10^{-8}$ cm^2. This is highly impractical due to challenges in alignment of the two electrodes and the need to achieve sufficient current from such a small surface area.

Interdigitated electrodes (IDEs) can resolve this challenge by measuring the in-plane impedance where the thin film becomes a cross sectional area (A) dimension rather than the distance between electrodes (d). An example IDE can be seen in Figure 2.6. IDEs are comprised of a large number of thin metallic teeth that are arranged periodically with alternating counter electrodes.

An important feature of the IDE is the ability to control the dimension of the electrodes to optimize the response from the polymer film or the specific phenomenon that is of interest (e.g. electrode polymer interface double layer). For an example, Sharon *etal* recently observed that the quality of the hemisphere used for extraction of the film resistance and capacitance was affected by the thickness of the thin film.[2] As the film became thinner, a Warburg diffusion element contributed to an impedance response at higher frequencies making a model fit less accurate for the resistance and capacitance elements. To extract higher quality R_{film} and CPE_{film} values for the calculating conductivity or dielectric properties, a thicker film may be coated to shift the Warburg Diffusion element to lower frequencies. Alternatively, it is also a possibility to extract higher quality Warburg parameters by coating a thinner film to increase the signal from this element. The conductivity of the film measured using an IDE can be calculated using the equation:

$$\sigma_{film} = \frac{d}{R_{film}tl(N-1)} \tag{2.16}$$

Where d is the distance between the periodic electrodes, t is the thickness of the polymer film, l is the overlay of individual electrode, and N is the total number of electrode teeth. Note that the thickness of the thin film is now in the denominator of the equation and can be compensated by simply increasing the l or N.

Additionally, the dielectric constant can also be calculated using the equation:

$$\epsilon_{film} = \frac{Cd}{\epsilon_0 tl(N-1)} \tag{2.17}$$

Where ϵ_{film} is the relative permittivity of the film and ϵ_0 is the vacuum permittivity.

In addition to the ability to probe thin films and extract practical values, the IDE is a versatile platform for controlling morphologies because the process of fabrication of the IDEs is compatible with microfabrication processes used in the polymer physics community to control thin film block copolymer morphologies. For an example, chemical treatments of the surface of the IDE can also change the wetting behaviors of the IDE enabling BCE domains to be aligned perpendicular or parallel to the surface of the device. Examples of this approach are showcased in Chapters 3 and 7. By forming periodic nanoscale trenches with dielectric materials on top of the IDEs, the BCP morphology can be manipulated so that the domains are aligned in relation to the electrodes. Examples of this control are demonstrated in Chapter 4. Additional customization of the IDEs for isolating specific structure-impedance relationships are shown in Chapters 5 and 6.

2.5 Structure Characterization of Thin Film Morphologies on IDEs

Different Structure characterization techniques were used throughout the work to cater to different morphologies and orientations of thin films. There are two orientations of thin

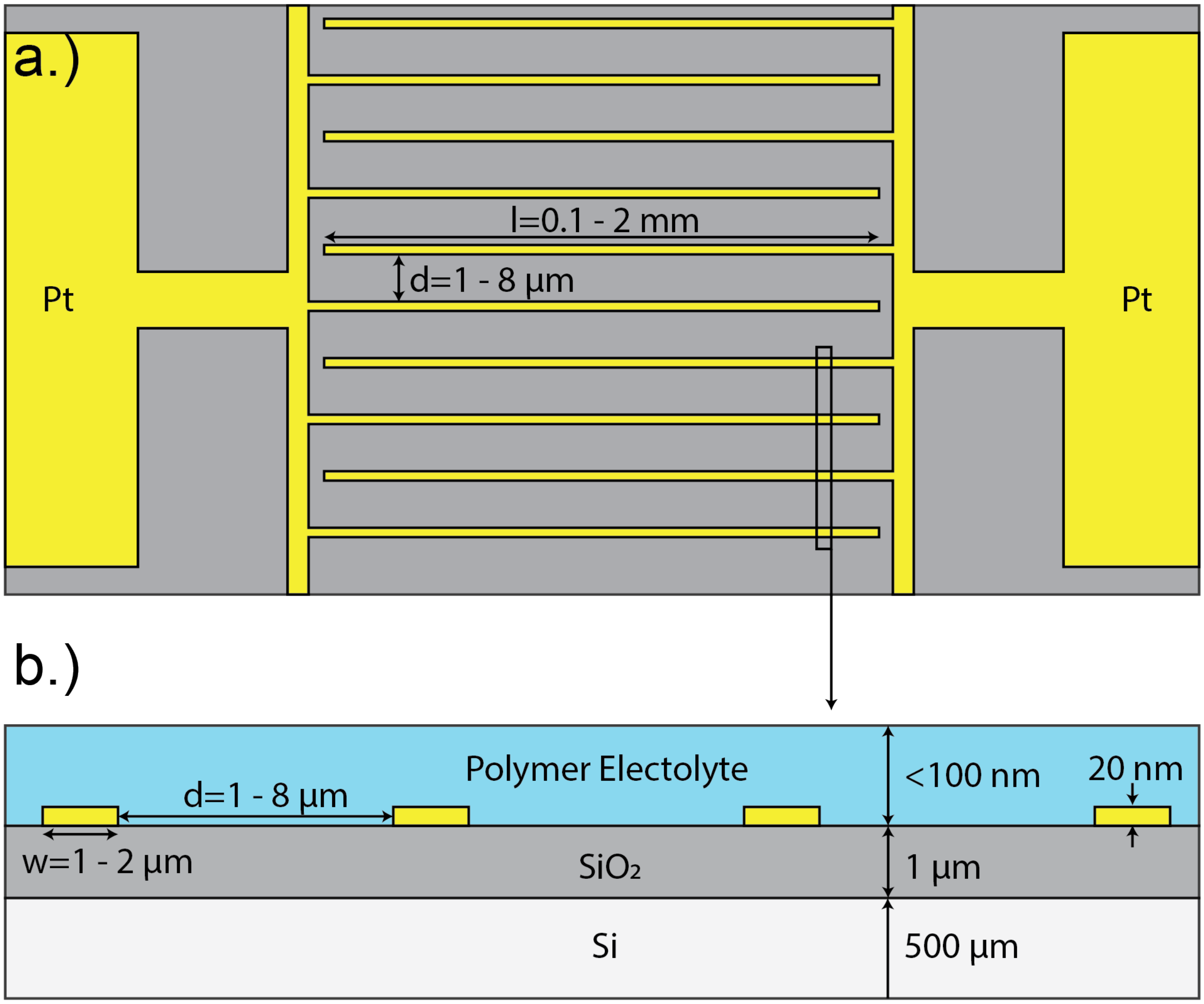

Figure 2.6: Schematic demonstrating the design of an IDE from a.) the top and b.) the cross section.

film morphologies relative to the substrate surface of the IDE, 1) where the two domains simultaneously interface the IDE substrate and the free surface forming domains that can be characterized from the top view and 2) where a specific domain preferentially interfaces the IDE substrate surface and the free interface forming domains that are parallel to the substrate.

First, when the morphology of the film is orthogonal to the surface of the IDE, scanning electron microscopy and atomic force microscopy are sufficient to provide deterministic structure for the film. Examples of the micrographs can be seen in Figure 2.7a The morphology through the thin film direction has been characterized throughout literature with notable work done by Segal-Peretz et al where TEM tomography was used to probe the 3-dimensional structure of the film to show that the lamellae morphology was consistent through the thin film direction. [3–6]

Second, when the domains are parallel to the substrate, it is difficult to characterize the structure using top down surface metrology techniques. In this scenario, a method called hole-island tests are employed to determine the morphology of the film. An example of a hole-island test is shown in Figure 2.7. Each BCP has a natural periodicity in its domain size that dictates the thickness at which a film forms a perfect parallel orientation. When the coated film thickness is commensurate with this periodicity and the correct domain can wet the IDE substrate or the free interface, no topology should be seen on the surface of the IDE. The topology can be characterized by using AFM and a rough characterization of surface topology can be done using an optical microscope. Conversely, when the film is incommensurate with the periodicity of the film, the film can either take material from parts of the film to reach a commensurate thickness or push material on top. When the material is taken from regions to increase the thickness in others, this is a suggestion that the film is incommensurate thickness and resembles ”holes”. When excess material is pushed above the film to minimize surface energy, the film resembles a flat surface with ”islands” of BCP. Assuming the film is at least the thickness of a half periodicity, either a smooth film or a hole-island morphology will appear on the surface.[7] This enables the simple use of AFM and optical microscopy to determine the deterministic morphology of parallel morphologies.

2.6 References

[1] M. E. Orazem and B. Tribollet, *Electrochemical impedance spectroscopy*, vol. 48 (John Wiley and Sons, 2011).

[2] D. Sharon, P. Bennington, C. Liu, Y. Kambe, B. X. Dong, V. F. Burnett, M. Dolejsi, G. Grocke, S. N. Patel, and P. F. Nealey, Journal of The Electrochemical Society **165**, H1028 (2018), ISSN 0013-4651.

[3] T. Segal-Peretz, J. Winterstein, J. Ren, M. Biswas, J. A. Liddle, J. W. Elam, N. Zaluzec, and P. F. Nealey, in *Metrology, Inspection, and Process Control for Microlithography XXIX*, edited by J. P. Cain and M. I. Sanchez (2015), vol. 9424, p. 94240U.

[4] T. Segal-Peretz, J. Ren, S. Xiong, G. Khaira, A. Bowen, L. E. Ocola, R. Divan, M. Doxastakis, N. J. Ferrier, J. de Pablo, et al., ACS Nano **11**, 1307 (2017), ISSN 1936-0851.

[5] T. Segal-Peretz, J. Winterstein, J. Ren, M. Biswas, J. A. Liddle, J. W. Elam, L. E. Ocola, R. N. Divan, N. Zaluzec, and P. F. Nealey, in *Metrology, Inspection, and Process Control for Microlithography XXIX* (International Society for Optics and Photonics, 2015), vol. 9424, p. 94240U.

[6] J. Ren, L. E. Ocola, R. Divan, D. A. Czaplewski, T. Segal-Peretz, S. Xiong, R. J. Kline, C. G. Arges, and P. F. Nealey, Nanotechnology **27**, 435303 (2016), ISSN 0957-4484.

[7] J. N. L. Albert and T. H. Epps, *Self-assembly of block copolymer thin films* (2010).

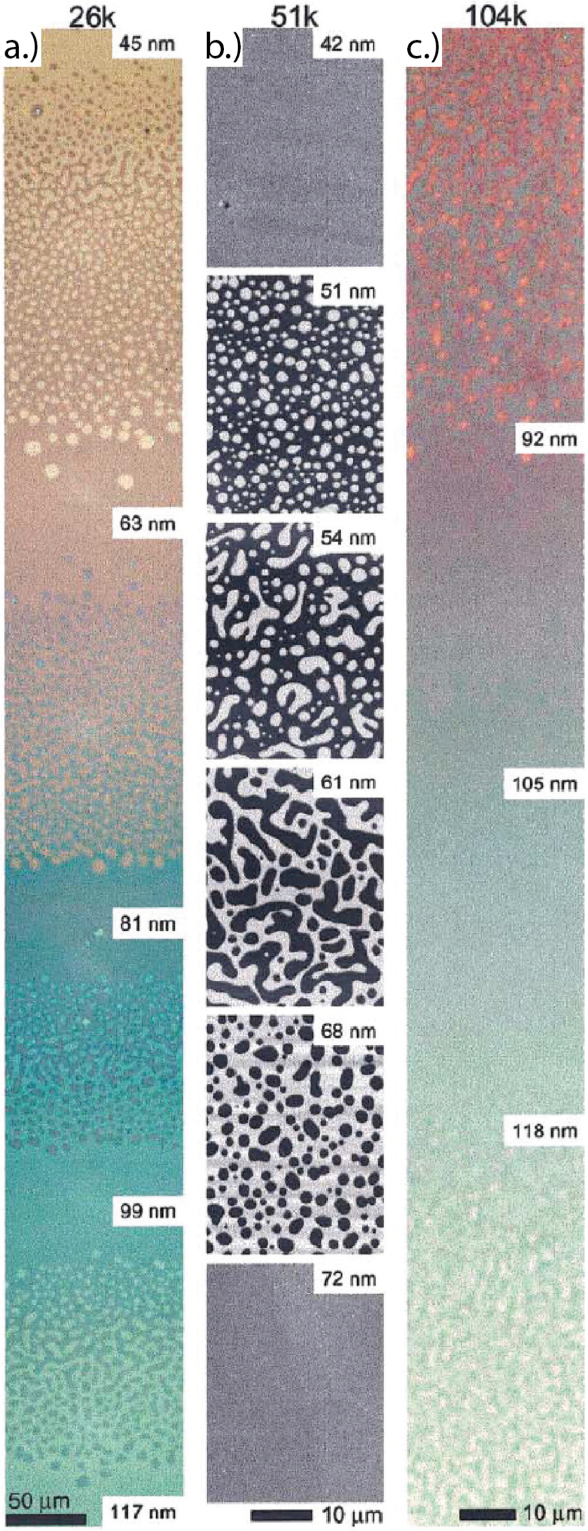

Figure 2.7: Optical microscope results of the hole island test of PS-b-PMMA BCP of different MW and thickness. Figure reproduced with permission of Elsevier.[7]

CHAPTER 3

PERPENDICULARLY ALIGNED, ANION CONDUCTING NANOCHANNELS IN BLOCK COPOLYMER ELECTROLYTE FILMS

3.1 Abstract

Connecting structure and morphology to bulk transport properties, like ionic conductivity, in nanostructured polymer electrolyte materials is a difficult proposition because of the challenge to precisely and accurately control order and the orientation of the ionic domains in such polymeric films. In this work, poly(styrene-block-2-vinyl pyridine) (PS-b-P2VP) block copolymers were assembled perpendicularly to a substrate surface over large areas through chemical surface modification at the substrate and utilizing a versatile solvent vapor annealing (SVA) technique. After block copolymer assembly, a novel chemical vapor infiltration reaction (CVIR) technique selectively converted the 2-vinyl pyridine block to 2-vinyl n-methyl pyridinium (NMP+ X-) groups – which are anion charge carriers. The prepared block copolymer electrolytes maintained their orientation and ordered nanostructure upon the selective introduction of ion moieties into the P2VP block and post ion-exchange to other counterion forms (X- = chloride, hydroxide, etc.). The prepared block copolymer electrolyte films demonstrated high chloride ion conductivities – 45 $mS\ cm^{-1}$ at 20 $^{\circ}C$ in deionized water - the highest chloride ion conductivity for anion conducting polymer electrolyte films. Additionally, straight-line lamellae of block copolymer electrolytes were realized using chemoepitaxy and density multiplication. The devised scheme allowed for precise and accurate control of orientation of ionic domains in nanostructured polymer electrolyte films and enables a platform for future studies that examines the relationship between polymer electrolyte structure and ion transport. This chapter was adapted with permission from Chemistry of Materials [1]. Copyright 2015 American Chemical Society.

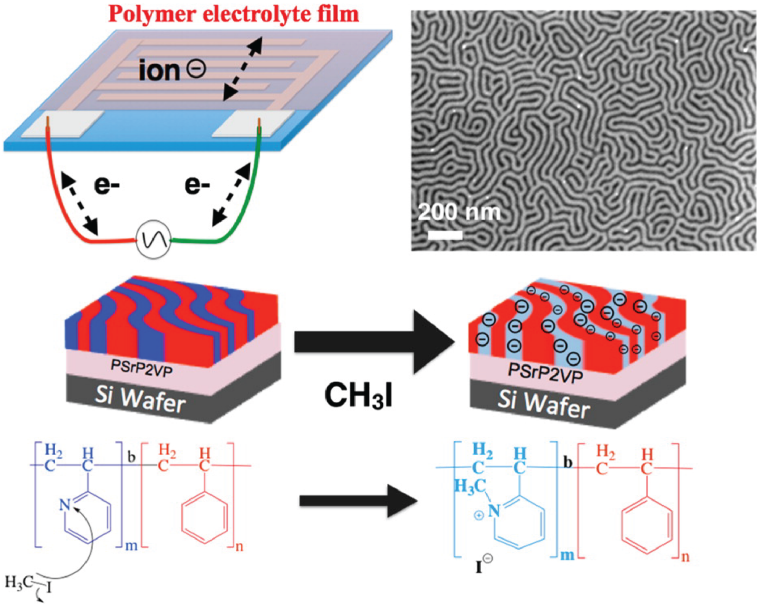

Figure 3.1: Summary of the experiment.

3.2 Introduction

In this work, the self-assembly (SA) process was adopted to achieve perpendicular alignment of poly(styrene-block-2-vinyl pyridine/n-methyl pyrdinium) (PS-b-P2VP/NMP+ I-) in sub-50 *nm* thin films.[2–4] This is the first report, to the best of our knowledge, utilizing the processes of chemically assisted SA of thin film block copolymers to align ionic domains in BCEs. Herein, we oriented the block copolymer prior to introduction of ionic groups. After assembling the perpendicular lamellae, a chemical vapor infiltration reaction (CVIR) technique introduced fixed quaternary ammonium iodide (i.e., n-methyl pyridinium iodide (NMP+ I-)) groups into the PS-b-P2VP film. The CVIR process performs a Menshutkin reaction between the nitrogen in the pyridine groups and methyliodide vapor. Controlling the nanostructure and orientation of ionic domains in BCEs is a challenging task due to the strong segregation between the ionic and non-ionic blocks often resulting in aggregated, micellar structures when trying to prepare polymer electrolyte film from a dissolved polymer solution.[5] Although external fields have proven mildly successful in alignment of ionic domains in BCE films/membranes,[6–9] an alternative method, such as the SA process, was pursued. The process is elegant and robust for creating ordered perpendicular orientation of block copolymers for a variety of technological applications (e.g., advanced lithography for semiconductor manufacturing targeted for data processing and storage).[3, 10, 11]

The oriented SA of PSbP2VP/NMP+ X- in thin-films may have application for miniaturized electrochemical systems (such as micro-batteries,[12] electrochemical sensors,[13] and micro-electrochemical supercapacitors [14, 15]). Furthermore, the assembled thin-films may serve as an ideal platform for understanding ion transport in polymer electrolyte films at a more fundamental level (e.g, the role of grain size, grain boundaries, and connectivity and their influence on ion transport and how thin film polymer electrolyte films covering electro-catalytic surfaces alter redox reaction rates).[16] Understanding how ion transport proceeds in thin-films has attracted recent attention[17–19] because confining a polymer electrolyte, like Nafion, into a thin-film alters its self-assembly behavior disrupting the network that facilitates facile ion transport. Hence, examining ion conductivity in polymer electrolyte films and understanding relationships between structure/morphology to transport properties is paramount for the rational design of new, functional polymer electrolyte materials.

3.3 Methods

3.3.1 Materials

All block copolymers - PS-b-P2VP diblock (40.5k-41k) and P2VP-b-PS-b-P2VP (12k-23k-12k) triblock and monohydroxy terminated polymers - poly(2-vinyl pyridine) (P2VP-OH Mn: 6.2k), and polystyrene (PS-OH Mn: 1.2k) were received from Polymer Source Inc. and used as is. The random terpolymer brush, poly(styrene-random-2-vinvyl pyridine-random-hydroxyl ethyl methacrylate) (PS-r-P2VP-r-PHEMA), was synthesized and evaluated as a brush for the SA of PS-b-P2VP in a previous report.[20] All other chemicals (acetone, methyliodide, toluene, n-methyl-2-pyrrolidone (NMP), N,N-dimethyformamide (DMF), sulfuric acid,[21] *wt*% hydrogen peroxide, and sodium salts) were received from Sigma-Aldrich or Fisher Scientific and used without further purification. Low electrical resistance, polished silicon wafers doped with arsenic (resistance 0.001 to 0.004 $ohms$) were received from WRS materials. Silica coated silicon wafers with interdigitated platinum electrodes (IDEs) were purchased from the Electronics Design Center at Case Western University. The specifics of the IDEs were: N=22 electrodes, 8 mm x 8 mm substrate, 4.5 mm length in electrodes, 100 μn spacing between electrodes, and 200 nm thick platinum electrodes with a 5 nm titanium adhesion layer beneath the platinum. Deionized water collected from a Millipore water filtration system (water resistance 18.2 $M\omega$) was used to: i.) rinse wafers after piranha cleaning, ii.) prepare salt solutions for the ion-exchange process, and iii.) carry out ionic conductivity experiments.

3.3.2 Preparation of Self-assembled Samples

Silicon wafers without interdigitated electrodes were cleaned with piranha solution (70:30 volume mixture of concentrated sulfuric acid with 35 $wt\%$ of hydrogen peroxide) for 30 minutes at 130 $^{\circ}C$. The polished silica wafers and the interdigitated electrode substrates were then exposed to oxygen plasma (O_2=100 $mTorr$) in a Reactive Ion Etcher (RIE-2000 from South Bay Technologies) for 12 seconds at 50 W to introduce more surface functional groups (e.g., silanol and SiO_2) for the grafting of polymer brushes.

The SA of PS-b-P2VP diblock copolymer samples was achieved by first preparing a 1 $wt\%$ solution of the polymer brush PS-r-P2VP-r-PHEMA containing 61 % styrene (by weight) in toluene and spin coating the polymer solution on the oxygenated wafer substrates and interdigitated substrates at 4000 RPM for 45 seconds. The polymer brush was then grafted at 250 $^{\circ}C$ for 5 minutes in a nitrogen filled glove box (¡0.2 ppm of water and ¡1.0 ppm of oxygen). The excess brush was removed by soaking the substrates in an excess amount of DMF:toluene (50:50 mixture by volume) for one hour at 80 $^{\circ}C$. The sample was placed in a fresh mixture of DMF:toluene and sonicated for 5 minutes. The sonication rinse step was repeated two more times with a fresh mixture of DMF:toluene for each repeat. The brush layer thickness was 10 nm. A 2 $wt\%$ solution of diblock copolymer (PSbP2VP Mn: 40.5k-41k) in DMF was prepared and spin coated on to the substrates with the grafted brush at 4000 RPM for 45 seconds. The block copolymer was annealed using a solvent vapor annealing (SVA) flow chamber. The film thickness was 30 nm. See the Figure 3.2 for details describing the SVA flow chamber.

The samples were annealed at 20 $^{\circ}C$ in a flow chamber that consisted of a mixture of saturated acetone vapor in nitrogen at 44.9 $sccm$ mixed with a pure nitrogen stream at 5.9 $sccm$ for 2 hours. Afterwards, the saturated acetone vapor stream was discontinued and the pure nitrogen stream flow rate was increased to 156.2 $sccm$ for 5 minutes. The samples were then removed from the flow chamber. Placing the samples in a 150 mL jar containing an opened 2 mL vial filled with methyliodide formed the NMP+ I- groups. The 150 mL jar was sealed during the Menshutkin reaction and the exposure time to methyliodide vapor dictated the extent of the reaction.

3.3.3 Ion-exchange Procedure

Substrates with the BCE film were immersed in 0.5 M NaX (X= Cl, F, Br, and HCO_3) aqueous solutions for 12 hours. The substrates were then removed from the 0.5 M NaX solutions and then subsequently immersed in DI water for 3 hours. During the 3 hour rinse period, the DI water was exchanged several times to ensure complete removal of excess salt. The substrates containing the BCEs were dried in a fume hood. Note: The ion-exchange process with 0.5 M $NaOH$ slightly differed. To prevent damaging the wafer, the substrates with the BCE film were immersed in 0.5 M $NaOH$ solution for 2 hours followed by an identical rinse procedure.

3.3.4 Chemical Characterization of Materials

Fourier Transform infrared spectra (FTIR) on thin film samples were collected on a Perkin Elmer Frontier FT-IR spectrometer in the range of 4000 cm^{-1} to 400 cm^{-1} with 10 scans

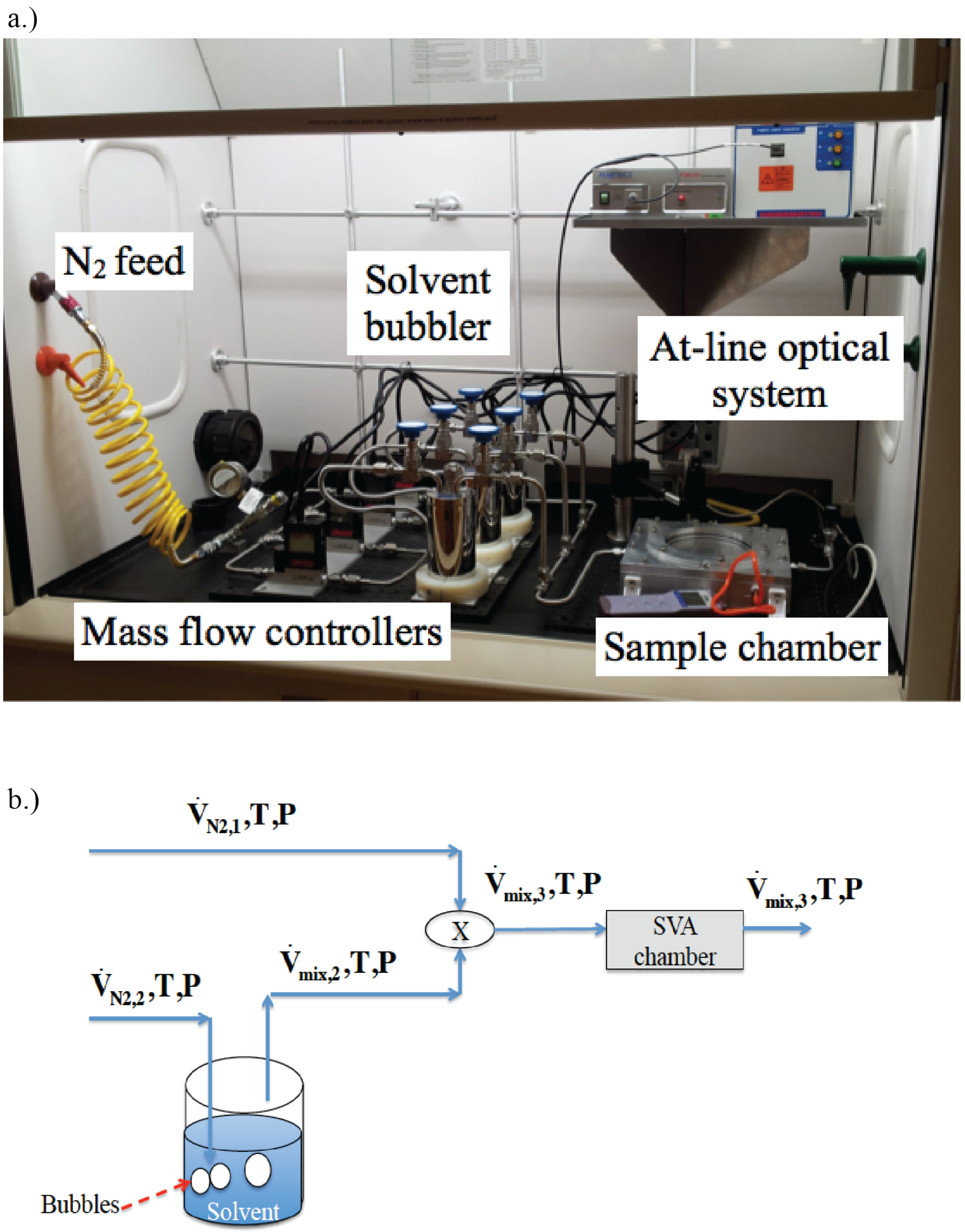

Figure 3.2: a.) Picture of the solvent vapor annealing flow chamber. Above the sample chamber, an at-line Filmetrics optical detector is positioned to monitor film thickness during solvent vapor annealing. b.) A process flow diagram of the solvent vapor annealing flow chamber. Computer controlled flow controllers set the volumetric flow rates of the nitrogen carrier and dilution gases.

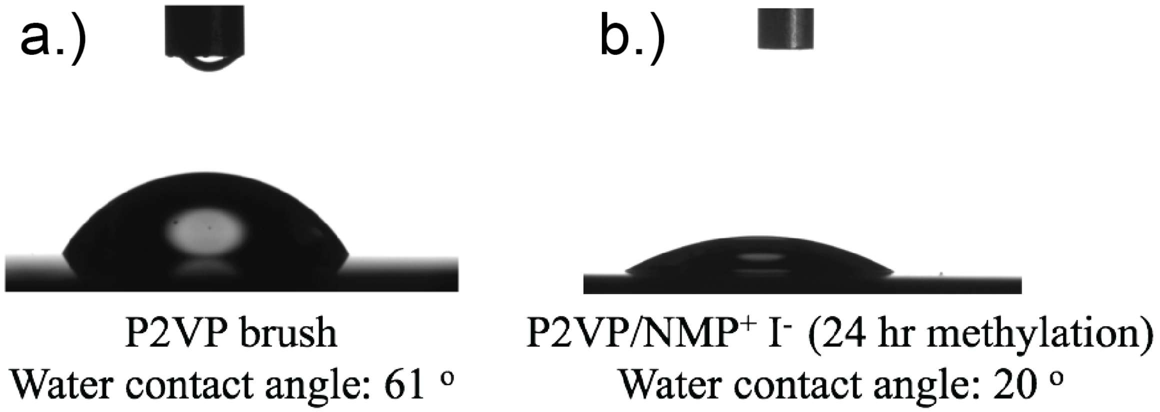

Figure 3.3: Water contact angle images of a.) P2VP brushes (no methylation) and b.) P2VP/NMP+ I- after 24 hour exposure to methyliodide vapor.

using a attenuated total reflectance (ATR) accessory. Note: The substrates for the FTIR measurements were gold-coated silicon wafers (100 *nm* of gold coating) from Sigma-Aldrich. Gold-coated silicon wafer substrates were employed because of their excellent reflectance. X-ray photoelectron spectra (XPS) were acquired on a Kratos Axis 165 with an aluminum filament operated at 12 *kV* and 10 *mA*.

3.3.5 Film Thickness and Water Contact Angle Determination

The film thicknesses of the underlying polymer brushes and block copolymer films were determined using J.A. Woollam Co., Inc. Ellipsometer. An optical contact angle measurement apparatus by Future Digital Scientific Corporation measured the water contact angle values. The water contact angle results are shown in 3.3.

3.3.6 Structural Characterization of Materials

Top down images of the SA block copolymers and BCEs were taken with a field emission scanning electron microscope (SEM - Carl Zeiss Merlin) and an atomic force microscope (AFM – Asylum MFP3D). The accelerating voltage for the SEM was 1.0 *kV* with a working distance of 3 to 4 *mm* using an in-lens detector. AFM images were collected in tapping mode using silicon cantilever tips with 300 kHz resonance frequency and a 40 Nm^{-1} spring constant.

Grazing Incidence Small Angle X-ray Scattering (GISAXS) was conducted on the PS-b-P2VP and PS-b-P2VP/NMP+ X- (24 hour exposure to methyliodide vapor) at the 8-ID-E beamline at the Advanced Photon Source (APS), Argonne National Laboratory using x-rays with a wavelength of l = 1.6868 A and a beam size of 100 μm (horizontal) x 15 μm (vertical). A 2D PILATUS 1M-F detector was used to capture the scattering patterns and was located at 2165 mm from samples. The incident angle varied from 0.14 $\circ$ to 0.20$\circ$. The qy line cuts were obtained from the horizontal line cuts from collected GISAXS scattering patterns along Yoneda peaks where the intensity of X-ray scattering peaks corresponding to the lateral structures in a sample are dramatically enhanced.

3.3.7 Ionic Conductivity Characterization of Materials

The IDE samples with the PS-b-P2VP/NMP+ X- BCE were immersed in deionized water at room temperature (20 $\circ C$). The BCE over the electrode pads on the IDE substrate were scraped away to make electrical connections. The polymer film resistance was determined using electrochemical impedance spectroscopy (EIS) carried out in galvanostatic mode. The Gamry 600Ref Potentiostat/Galvanostat with a frequency response analyzer executed the EIS experiments. The frequency range for EIS was set from 100,000 to 0.1 Hz with a 10 mA amplitude. An electric circuit equivalent (ECE) model presented in the ESI interpreted the impedance data and calculated the block copolymer film resistance. The ionic conductivity was determined from the block copolymer film resistance.

Figure 3.4 and 3.5 demonstrates the appropriate ECE models, model fits, and equations.

To extract the BCE film resistance (RFILM) from the galvanostatic EIS measurements, an equivalent circuit design was fitted to the Nyquist plot. Figure 3.4a shows a cross sectional diagram of the interdigitated electrode (IDE) that depicts the interdigitated electrode with the brush layer and the block copolymer electrolyte film. The equivalent circuit model utilized resistor, capacitor, and constant phase element components.

$$Z_R = R \tag{3.1}$$

Shows the relationship between resistance and the impedance element where R is resistance.

$$Z_C = \frac{1}{i\omega C} \tag{3.2}$$

The relationship between the capacity and the impedance element where ω is the frequency of the measurement and i is the imaginary number operator.

$$Z_{CPE} = \frac{1}{(i\omega C)^{\alpha}} \tag{3.3}$$

The α value is assigned a value between 0 and 1 and accounts for the ideality of the capacitor.

In the model given above, the BCE path was modeled as a resistor and a capacitor in parallel connected in series to another resistor and capacitor in parallel. The two parallel elements were models for the polymer electrolyte brush and the BCE. The two elements were in series because the charge carrier inevitably crosses through the brush prior to passing through the BCE. This sequence is effectively represented in a Nyquist plot as two semi-circles of varying radii. The employed equivalent circuit model is shown in Figure 3.4b.

The model fit prioritized the smaller semi-circle in the Nyquist plot when fitting because that semi-circle represented the BCE film resistance in the system. The model was designed and fitted using the SimpleX damped least squares method available on the ECHEM analysis tool by Gamry Inc. The optimization of the fit on average took 20 iterations. The extracted resistance was used to calculate the ionic conductivity using the equation:

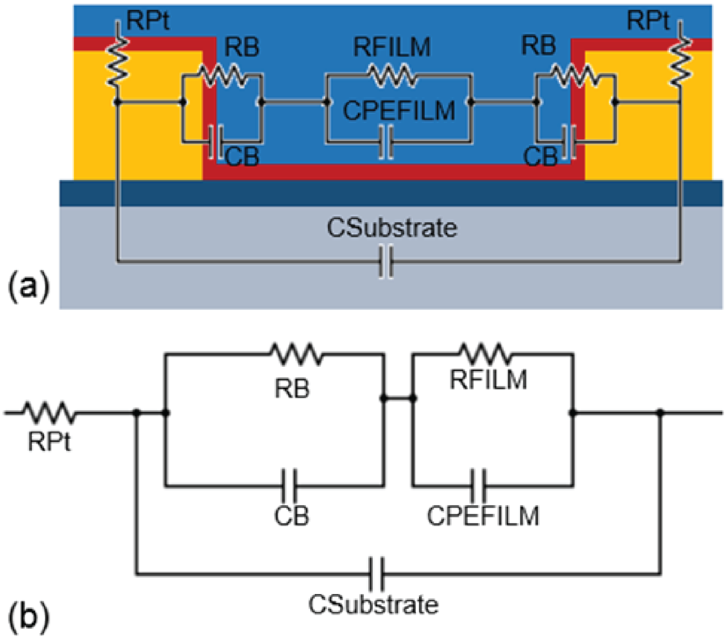

Figure 3.4: a.) Cross sectional diagram of the teeth in the interdigitated electrodes and b.) the equivalent circuit model that was used for the modeling of the system.

$$\sigma_{film} = \frac{d}{R_{film} * t * l * (N-1)} \tag{3.4}$$

The film ionic conductivity σ_{film} was calculated with the modeled film resistivity R_film, the spacing between the interdigitated electrode teeth ($d = 100\mu m$), the length of the teeth ($l = 0.45cm$), thickness of the BCE film ($t = 28nm$) and the number of electrodes ($N = 22$).

3.4 Results and Discussion

3.4.1 Process Scheme

Figure 3.6 illustrates the process flow diagram for making perpendicular aligned PS-b-P2VP/NMP+ I- BCEs. In this process, a random copolymer brush of PS-r-P2VP-r-PHEMA containing 61 % styrene was grafted to the piranha cleaned silicon wafer. The PS-b-P2VP block copolymer solution was spincoated on top of the wafer containing the grafted ran-

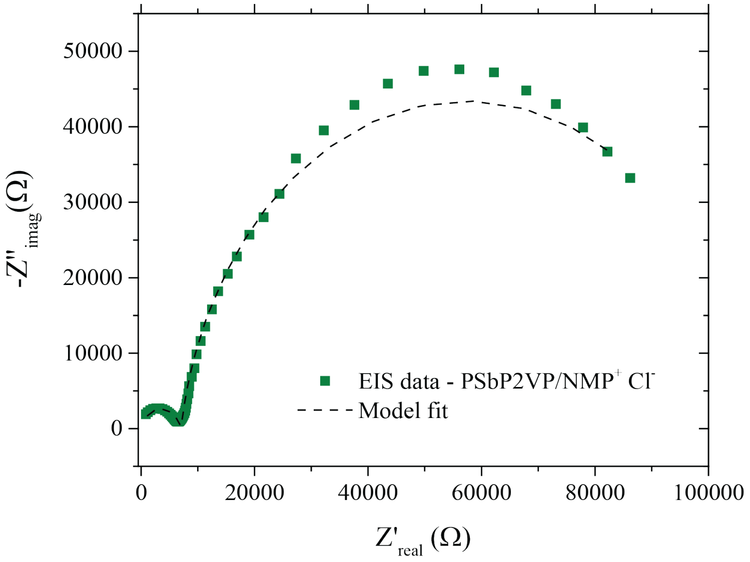

Figure 3.5: Representative model fit of the equivalent circuit model for the PS-b-P2VP/NMP+ Cl- block copolymer electrolyte with 48 hours exposure to methyliodide vapor.

dom copolymer brush. Solvent vapor annealing with acetone created the micro-phase separated, perpendicular aligned lamella of the PS-b-P2VP block copolymer. This particular process was developed for the self-assembly and directed self-assembly of PS-b-P2VP block copolymers.[21]

The two critical parameters governing perpendicular lamellae registration of PS-b-P2VP block copolymers was: i.) controlling the interfacial surface energy at the substrate surface interface and the free surface interface (i.e., surface above the block copolymer film) and ii.) annealing the block copolymer above the glass transition temperature to enable polymer chain mobility. During the annealing step, the different polymer blocks aggregate into periodic, micro-phase separated nanostructured domains and the tuned interfacial surface energies align the self-assembled blocks perpendicularly to the substrate surface. Minimizing the free energy in the system drives the self-assembly process. Most annealing processes utilize a thermal process that heats the block copolymer above its glass transition temperature. But, this method necessitates a neutral boundary condition at the free surface and

PS-b-P2VP is not neutral at the free surface under nitrogen or vacuum at elevated temperatures. Hence, thermal annealing is not an option for achieving perpendicular alignment of PS-b-P2VP block copolymers.

Alternatively, solvent vapor annealing (SVA) is an effective, versatile method for inducing neutral boundary conditions when annealing block copolymers. The SVA process passes a solvent vapor (either a single solvent or a mixture of solvents) that i.) penetrates and plasticizes the block copolymer to depress its glass transition temperature below the operating temperature in the SVA chamber, ii.) induces a neutral condition for the different blocks at the free surface interface, iii.) allows for micro-phase separation into periodic microdomains even when the solvent swells the polymer blocks, and iv.) allows for the solvated PS-b-P2VP block copolymer to recognize the underlying substrate surface chemistry to achieve perpendicular alignment. After annealing the block copolymer for a period of time, the system terminates the flow of solvent vapor and subsequently passes a dry nitrogen stream at a high flow rate to vitrify the self-assembled PS-b-P2VP block copolymer. Figure 3.2 illustrate the process for solvent vapor annealing using a custom-built flow chamber.

Figure 3.6 depicts the chemical reaction of PS-b-P2VP to PS-b-P2VP/NMP+ I- - an anion conducting BCE and the chemical structure of PS-r-P2VP-r-PHEMA random copolymer (61% PS and 2 % PHEMA by weight) that is grafted to the wafer surface to induce a neutral boundary condition for the SA of PS-b-P2VP. Storing the self-assembled PS-b-P2VP sample in a sealed jar containing an open 2 mL vial filled with liquid methyliodide converted the block copolymer into an anion conducting BCE. The exposure time to methyliodide vapor dictated the conversion of pyridine groups to NMP+ I-.

The BCEs were prepared using a newly developed reaction scheme that entails the use of methyliodide vapor infiltrating into the polymer film and reacting with the pyridine group in the P2VP block to form NMP+ I- groups. We define this process as a chemical vapor infiltration reaction (CVIR). The use of methyliodide to alkylate organic amines (i.e., a Menshutkin reaction) is well established [22, 23] but to the best of our knowledge, this is the first report performing this reaction with methyliodide vapor on thin block copolymer films or grafted polymer brushes containing tertiary amine functionalities. When initially developing the reaction scheme, we immersed the substrates with the self-assembled PS-b-P2VP film in methyliodide liquid, but the morphology of the polymer film was destroyed. Altering the reaction scheme by exposing the block copolymer film to methyliodide vapor allowed for the conversion of pyridine to anion charge carriers without distorting the morphology. To examine this chemical reaction further, we studied the change in the water contact angle before and after methylation of chemically grafted mono-hydroxyl terminated poly(2-vinyl pyridine) polymer brushes. After exposing to methyliodide vapor for 24 hours, the water contact angle of the polymer brushes changed from 62 ° to 20°. See Figure 3.3. The reduction in water contact angle supported the introduction of hydrophilic NMP+ I- into the polymer brushes. Spectroscopic techniques, XPS and FTIR, also confirmed the success of the reaction. Finally, we wish to point out that this reaction scheme can be extended for creating anion conducting charge carriers in block copolymer thin-films containing poly(4-vinyl pyridine) (P4VP) blocks rather than P2VP blocks.

3.4.2 Structural Characterization

Figure 3.12 provides SEM images of the PS-b-P2VP (Figure 3.12a) and PS-b-P2VP/NMP+ I- samples (Figures 3.12b to e). Figures 3.12b through e represent images for samples exposed to methyliodide vapor for different periods of time. These images convey no changes to the fingerprint lamellae structure when compared Figure 3.12a (pristine PS-b-P2VP), but the contrast between the two blocks for Figures 3.12b to e increased with longer methylation times. Figure 3.13 shows the finger print lamellae morphology for PS-b-P2VP/NMP+ I- (methylated for 48 hours) over 42 μm^2 demonstrating excellent, perpendicular registration of the BCE over large areas. Note: Figures 3.7,3.8,3.9,and 3.10 provide the SEM images of the fingerprint lamellae of the PS-b-P2VP and PS-b-P2VP/NMP+ I- for different methylation times over large areas. The calculated periods of the PS-b-P2VP and PS-b-P2VP/NMP+

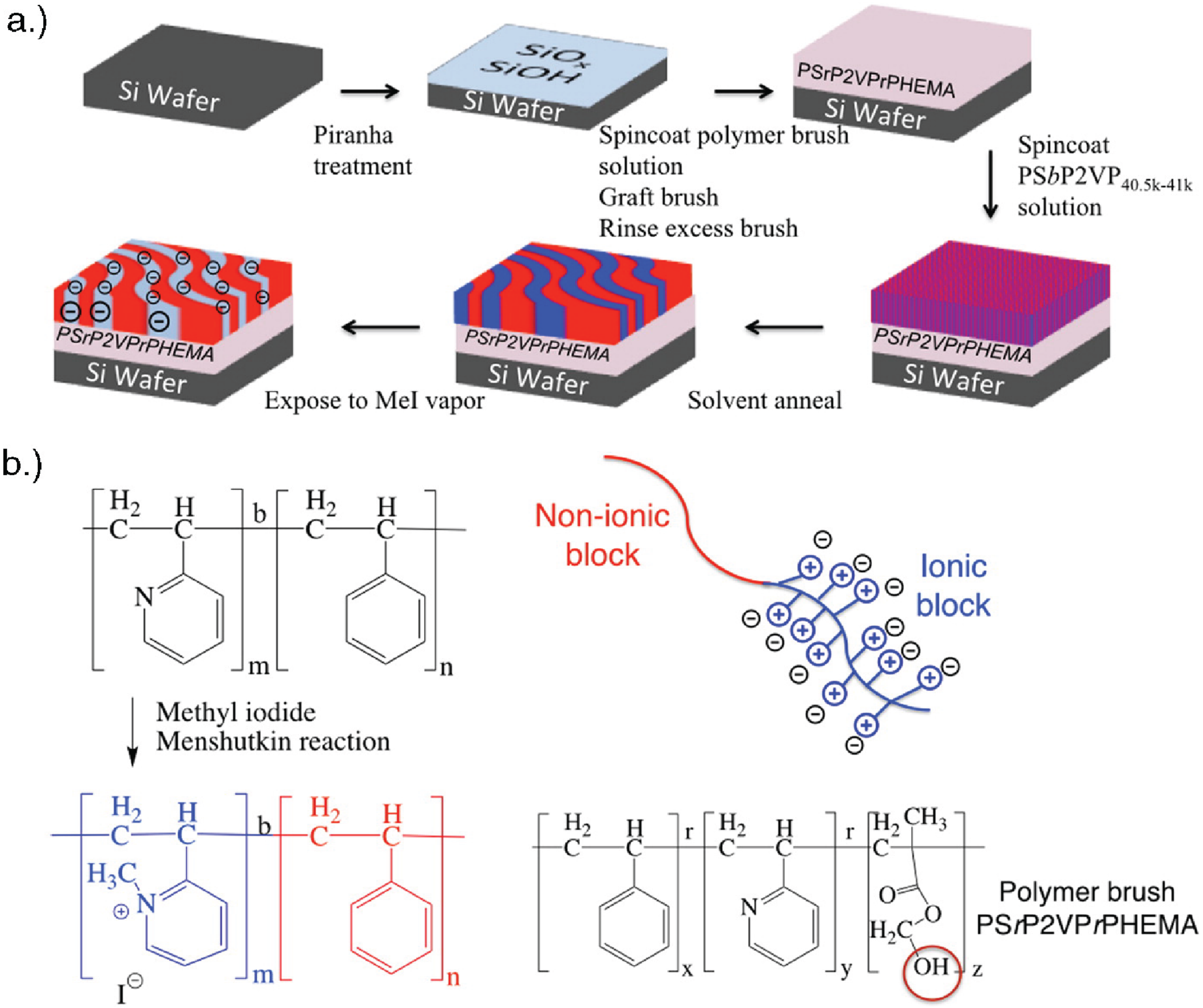

Figure 3.6: a.) Process flow scheme for the preparation of SA PS-b-P2VP/NMP+ I- block copolymer electrolytes. b.) Chemical reaction of PSbP2VP with methyliodide to prepare PS-b-P2VP/NMP+ I- block copolymer electrolytes and the chemical structure of PS-r-P2VP-r-PHEMA. The red circle in the PS-r-P2VP-r-PHEMA chemical structure draws attention to the alcohol moiety used for grafting the polymer brush to the substrate surface.

nm.

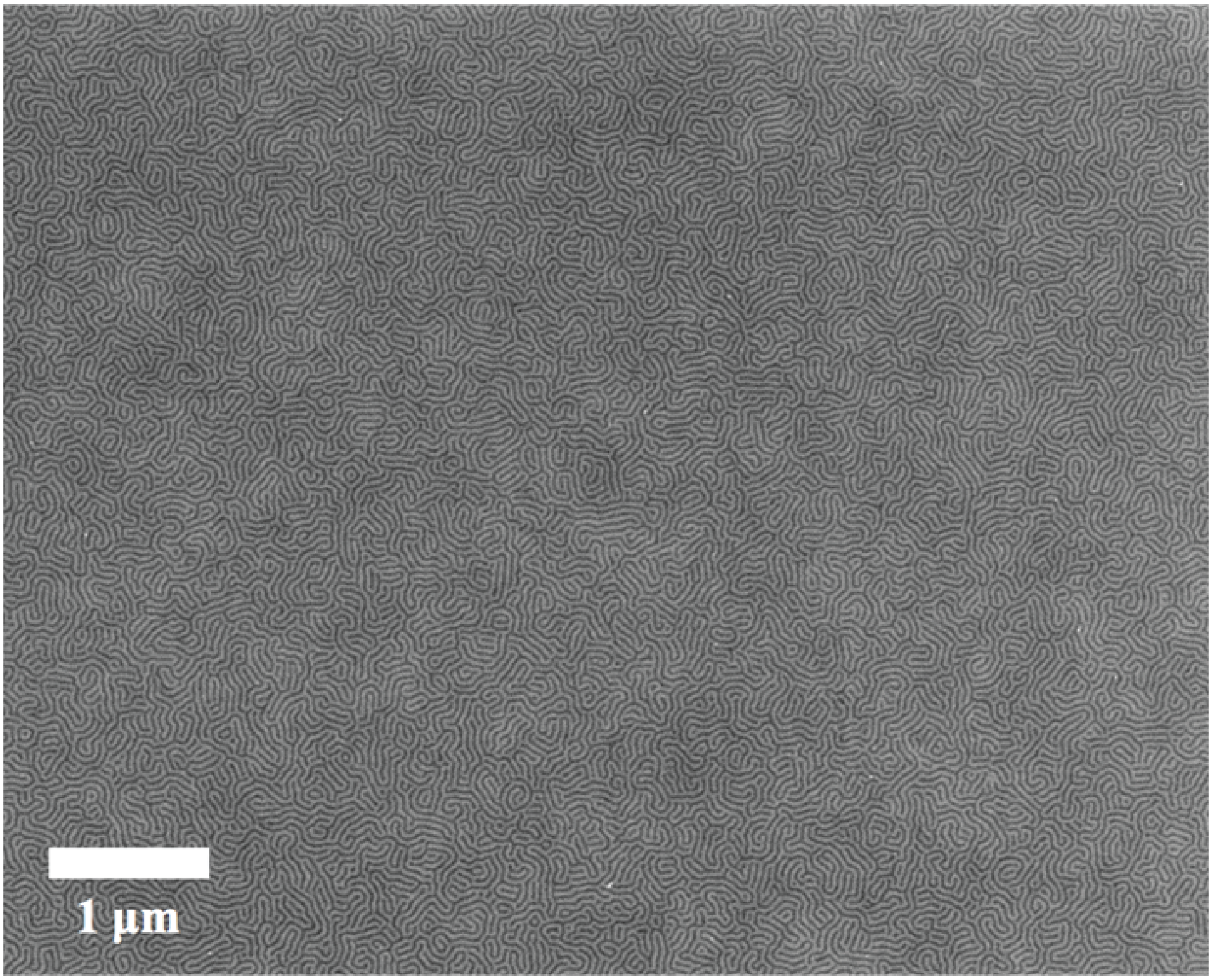

Figure 3.7: SEM image of fingerprint lamellae of PS-b-P2VP (no methylation). Area size over 42 μm^2.

I- samples with different degrees of the methylation remained relatively unchanged – in the range of 44 to 46 nm (determined by the Finite Fourier Transform (FFT) of the SEM images). Atomic force micrographs (AFM) of PS-b-P2VP and PS-b-P2VP/NMP+ I- are given in Figures 3.14a to e. Figures 3.14b to e represent the PS-b-P2VP/NMP+ I- samples corresponding to different methyliodide vapor exposure times. Figure 3.14f provides representative 1D height profiles from each of the micrographs. The height difference between the blocks, regardless of length of time of exposure to methyliodide vapor, was no more than 2 nm.

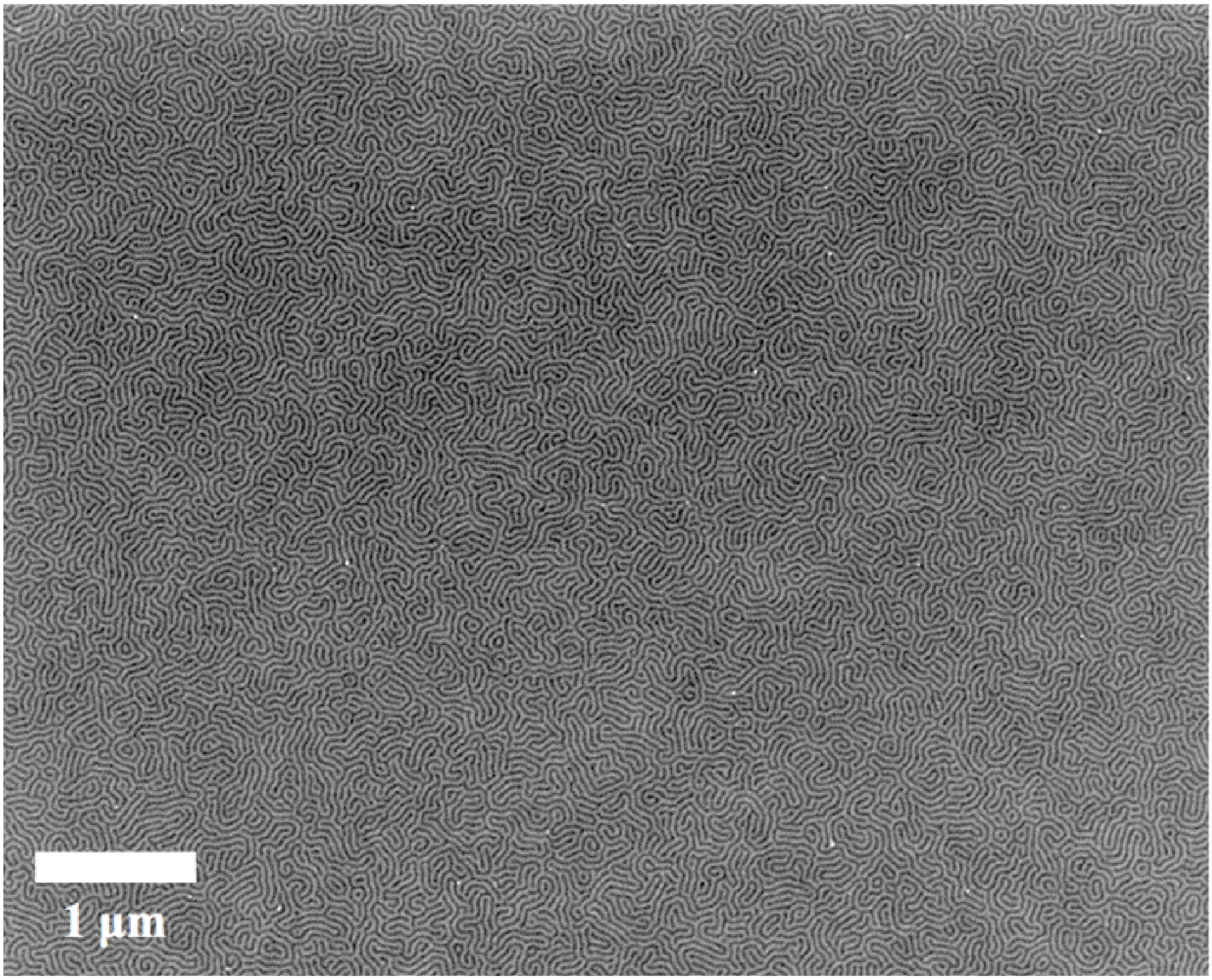

Figure 3.8: SEM image of fingerprint lamellae of PS-b-P2VP (methylated for 2 hours). Area size over 42 μm^2.

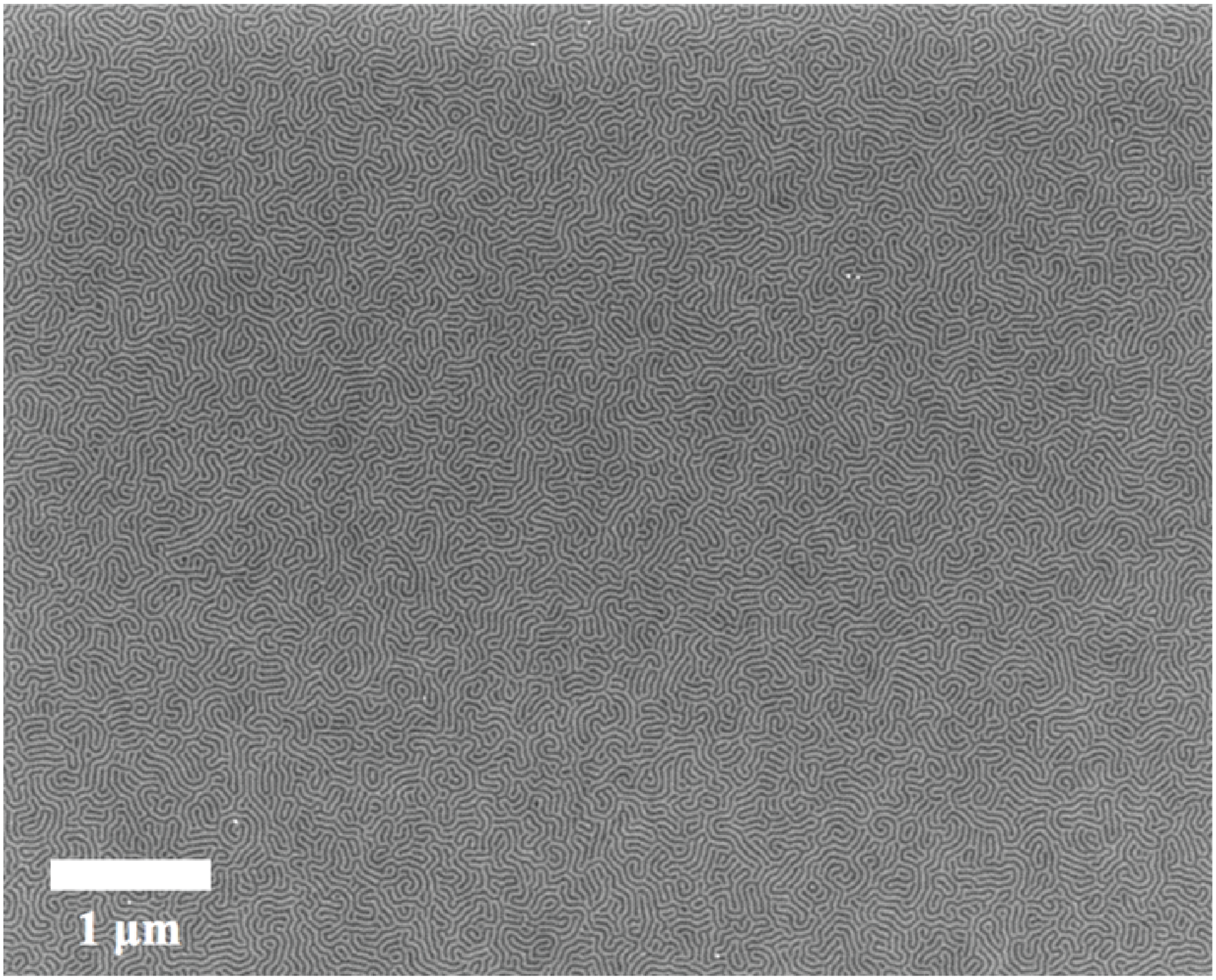

Figure 3.9: SEM image of fingerprint lamellae of PS-b-P2VP (methylated for 4 hours). Area size over 42 μm^2.

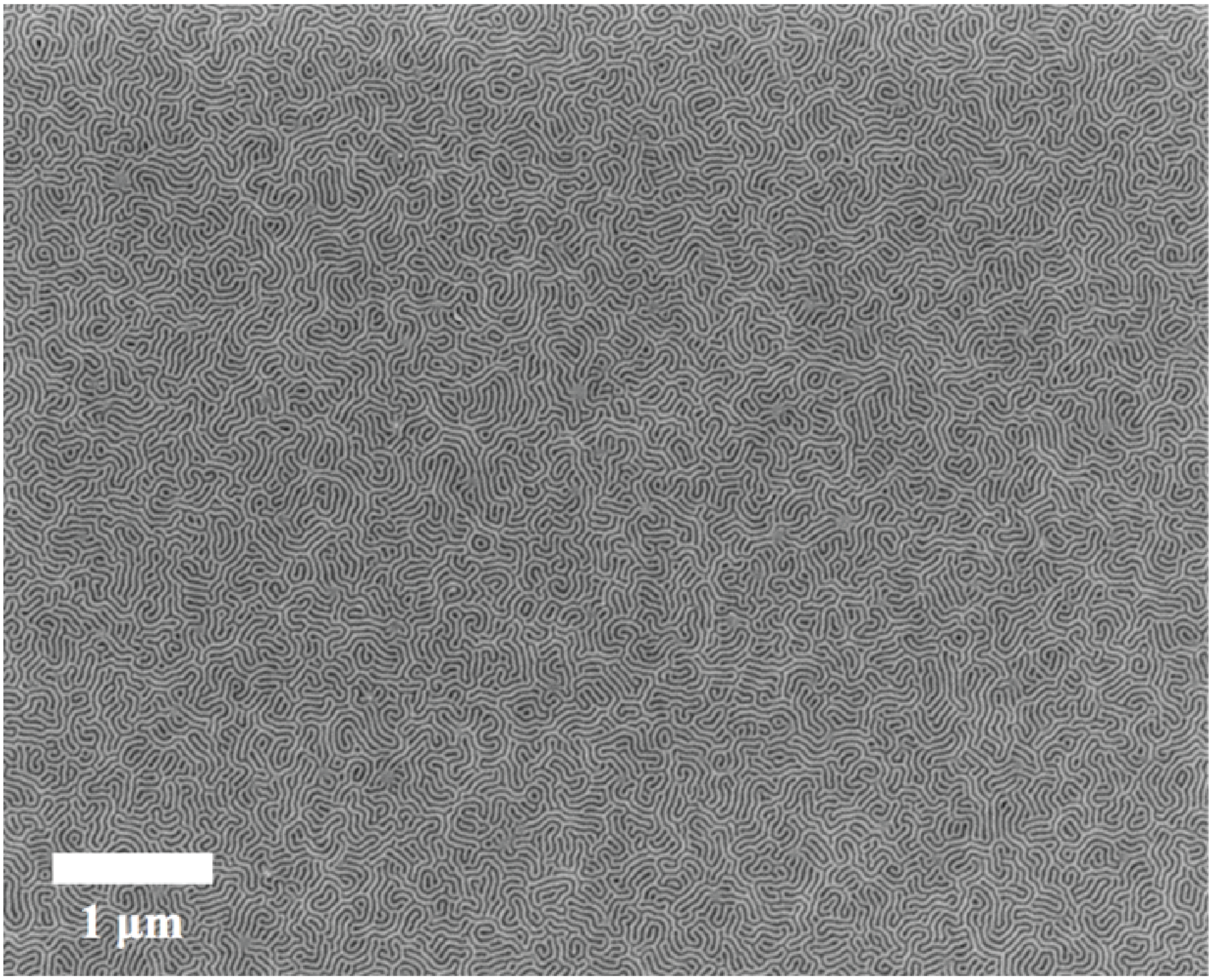

Figure 3.10: SEM image of fingerprint lamellae of PS-b-P2VP (methylated for 24 hours). Area size over 42 μm^2.

Figures 3.15a,b, and c provide the GI-SAXS data of PS-b-P2VP (dotted line) and PS-b-P2VP/NMP+ I- (solid line) for different incident angle values (θ). PS-b-P2VP displayed a strong first order peak (q) and weak second and third peaks with $3q$ and $5q$ spacing indicating symmetric lamellae morphology. The PS-b-P2VP/NMP+ I- sample, exposed to methyliodide vapor for 24 hours, yielded 5 intense ordered peaks with $2q$, $3q$, $4q$, and $5q$ spacing after the first order peak (q). The domain size (D) was calculated by $D = \frac{2\pi}{q_y}$, where q_y is the first-order in-plane scattering distance in reciprocal space relative to the non-scattered beam. The average values for each θ were calculated by fitting each peak with a Gaussian fit to determine the position of peak. The values of peak positions were divided by their order peak integers and averaged for Table 3.1. No statistical difference existed between the block copolymer period before and after the CVIR reaction for 24 hours (see Table 3.1). A qualitative inspection of each incidence angle scan shows an emergence of a 2nd and 4th order peak following the 24 hour CVIR. Note: The raw 2D GI-SAXS patterns are provided in the ESI under Figure 3.11.

In this work, the CVIR technique selectively introduced the ionic groups into one block of the block copolymer without disrupting the assembled morphological structure. As previously mentioned, controlling the orientation of the ionic domains in BCEs is a difficult proposition because of the strong segregation between the ionic block and non-ionic block. Additionally, the iodide counterions in the pyridinium iodide group provided greater contrast for imaging. Hence, the PS-b-P2VP/NMP+ I- samples did not require iodine staining for contrast between the two blocks. Like the SEM images, the AFM images also supported no changes to the morphology after introduction of ionic groups. The GI-SAXS also supported no changes to the morphology and period of the PS-b-P2VP block copolymer when exposed to methyliodide vapor. Interestingly, the presence of the 2nd and 4th order peaks in the GI-SAXS patterns at the different incidence angle values indicated a shift in the form factor - from a symmetric lamellae to an asymmetric lamellae). The absence of a period change, but a change in the symmetry, suggested slight compression of the PS domains and a slight

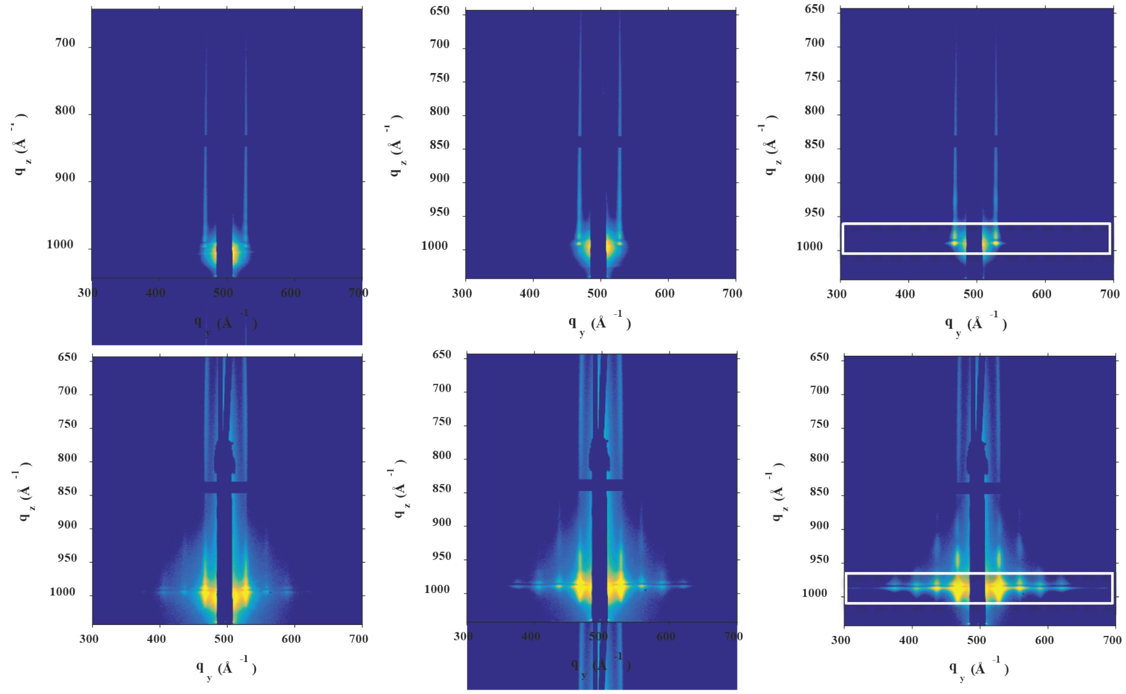

Figure 3.11: GISAXS data pre (top) and post (bottom) CVIR with incident angles from 0.14 (left) 0.18(middle) to 0.20 (right). Horizontal line cut of the Yoneda peak is shown by the dotted line.

expansion of the P2VP domain after the CVIR. Also, the presence of these peaks at the different incidence angle supported that the CVIR occurred across the thickness of the film (i.e., the CVIR does not only take place at the surface). Overall, the CVIR allows introduction of ionic moieties without disrupting the morphology of self-assembled PS-b-P2VP block copolymers in thin-films.

3.4.3 Chemical Characterization

Figures 3.16a and b give the XPS spectra for PS-b-P2VP and PS-b-P2VP/NMP+ I- for different methylation times. Figure 3.16a focuses on the binding energy for iodine 3d (I 3d) and an increase in methylation time yielded a subsequent increase in I 3d signals at 615 eV (I 3d5/2) and 627 eV (I 3d3/2). The signals observed in Figure 3.16a were attributed to the iodide counterion. Figure 3.16b zooms in on the binding energy associated with nitrogen 1s (N 1s). Two peaks were identified in Figure 3.16b – 396 eV associated with the nitrogen in the tertiary amine (i.e., pyridine) and 399 eV associated with the nitrogen in the quaternary ammonium (i.e., pyridinium) iodide group. An increase in methylation time saw a loss in intensity at 396 eV with a subsequent increase in signal at 399 eV demonstrating that longer exposure times to methyliodide vapor resulted in greater conversion of pyridine to NMP+ I-.

Figure 3.17a provides a series of zoomed in FTIR traces for PS-b-P2VP and PS-b-P2VP/NMP+ I- for different methylation times in the range of 1480 to 1750 cm^{-1}. Figure 3.17a depicts the evolution of the different peak signals associated with C-N and C-N+ stretching. In the PS-b-2VP trace, C-N stretching was observed in the range of 1570 cm^{-1} and 1590 cm^{-1}, while the C-N+ signal intensity was displayed at 1630 cm^{-1} and this signal increased with prolonged exposure time to methyliodide vapor. Figure 3.17b gives the FTIR spectra of PS-b-P2VP and PS-b-P2VP/NMP+ I- for different methylation times in the range of 2000 cm^{-1} to 4000 cm^{-1}. The broad signal present at 3500 cm^{-1} for the PS-b-P2VP/NMP+ I- samples in Figure 3.17b corresponded to O-H stretching. The O-H

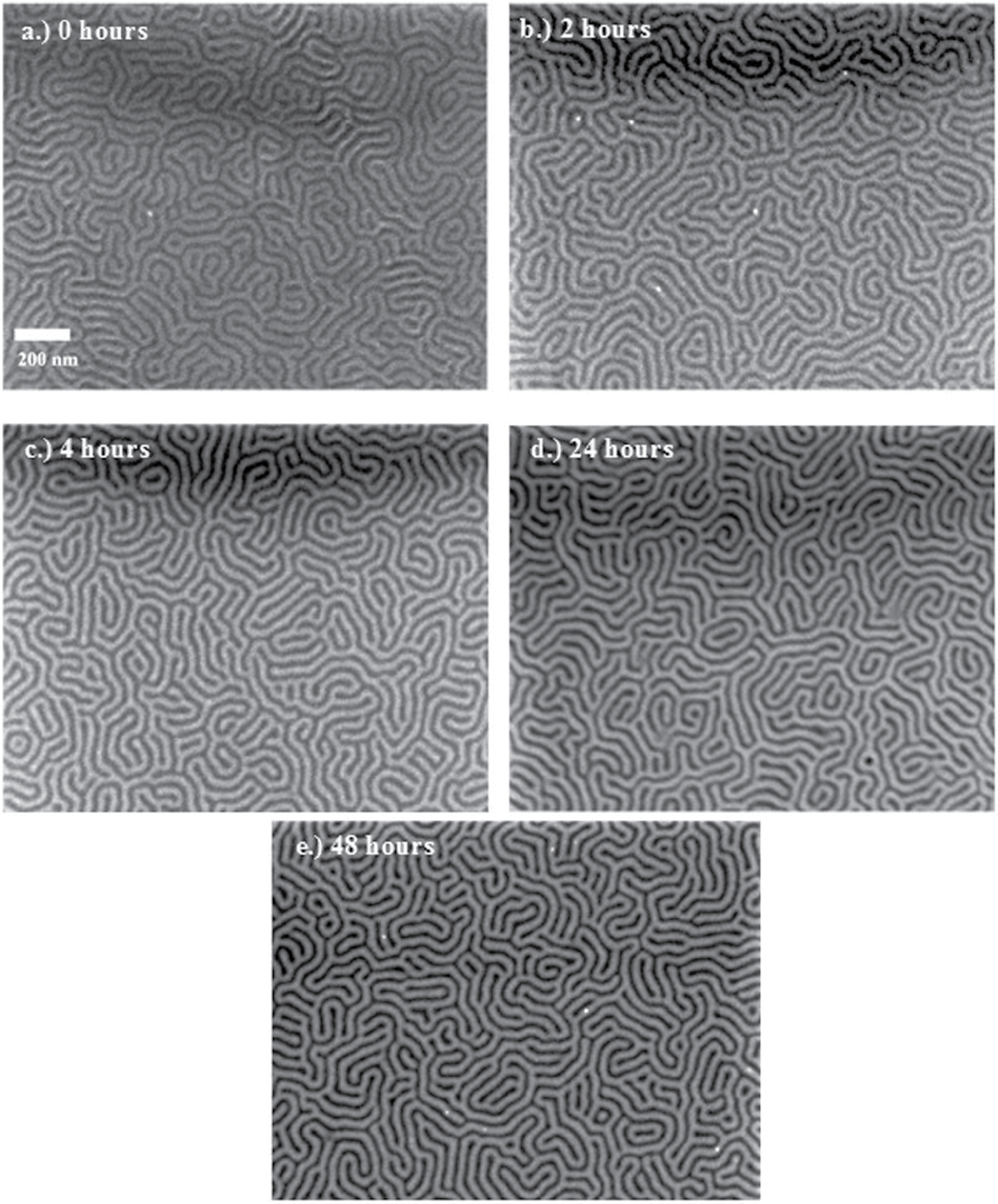

Figure 3.12: SEM images of: a.) PS-b-P2VP (stained with iodine), b.) PS-b-P2VP/NMP+ I- (methylated for 2 hours), c.) PS-b-P2VP/NMP+ I- (methylated for 4 hours), d.) PS-b-P2VP/NMP+ I- (methylated for 24 hours), and e.) PS-b-P2VP/NMP+ I- (methylated for 48 hours). Scale bar (200 *nm*) is located in a.

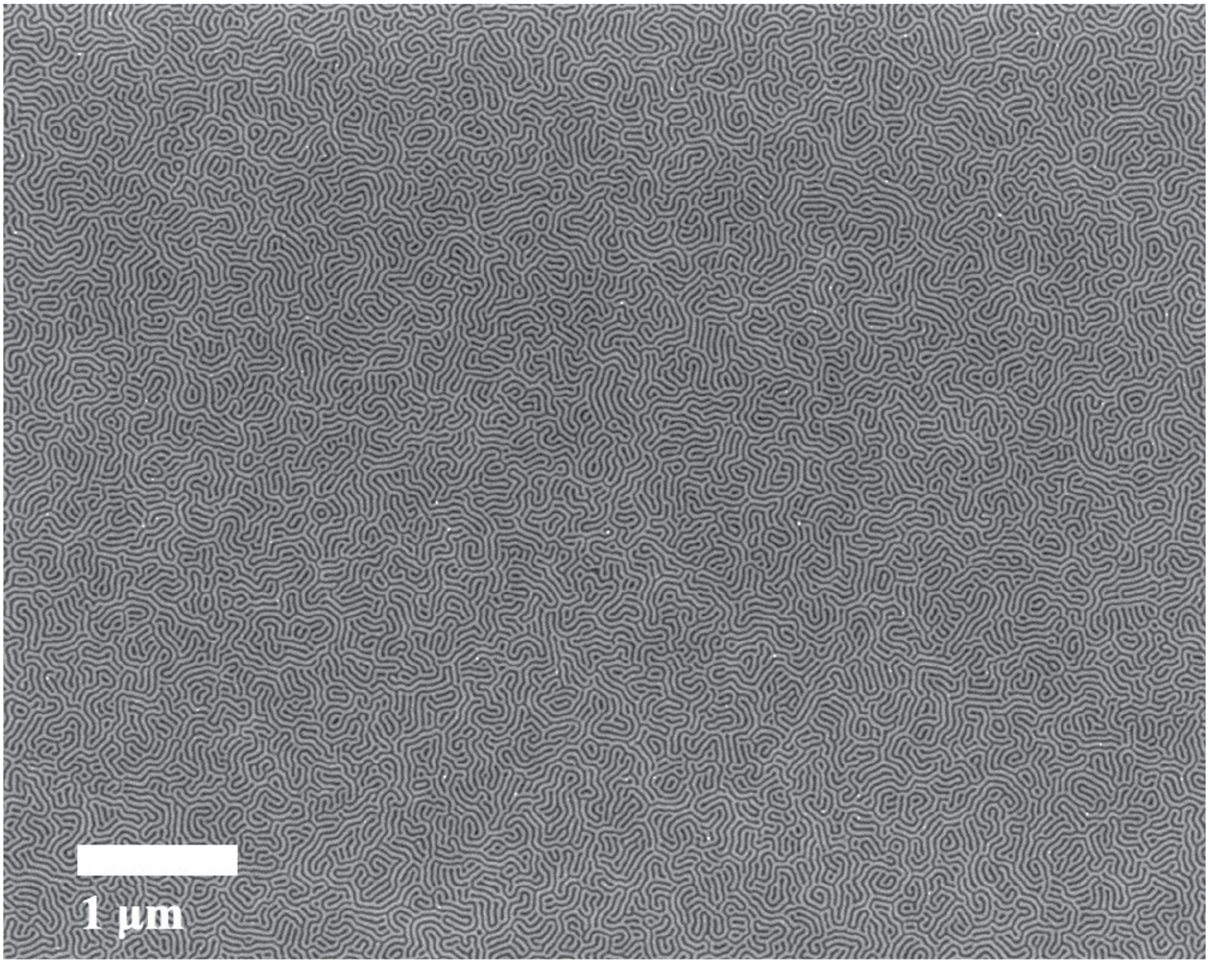

Figure 3.13: SEM image of fingerprint lamellae of PSbP2VP/NMP+ I- (methylated for 48 hours). Area size over 42 μm^2.

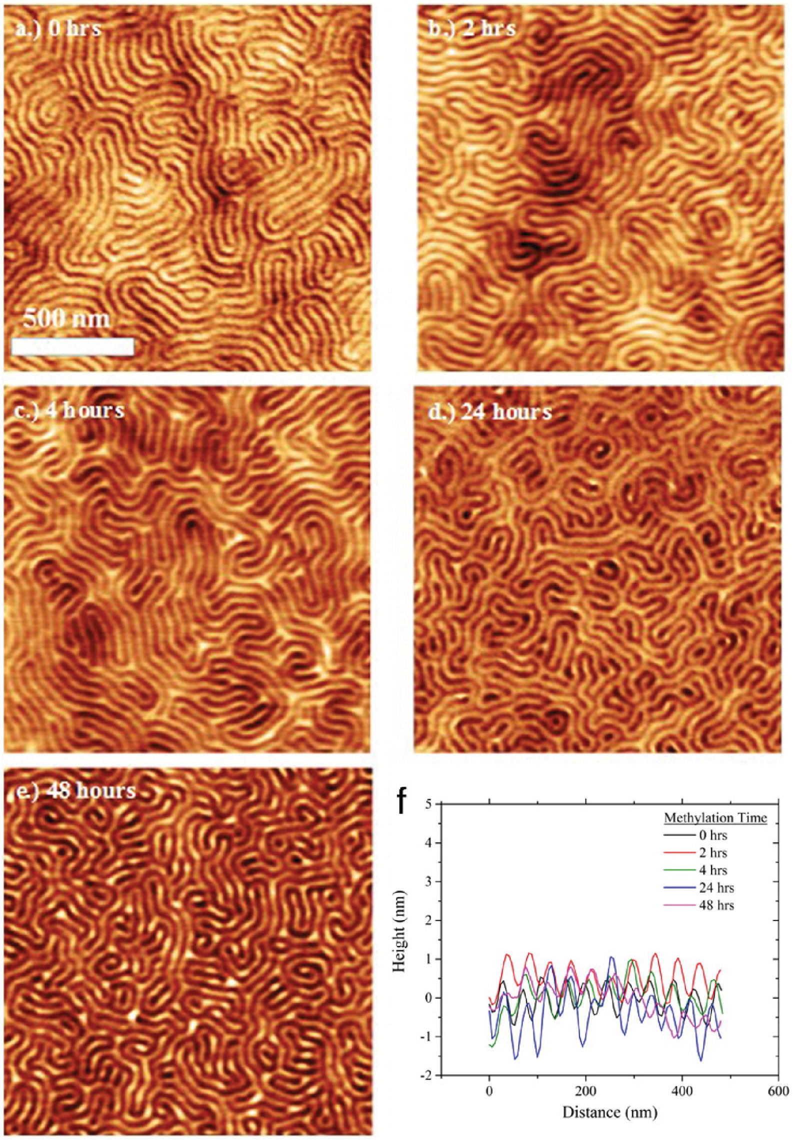

Figure 3.14: AFM height micrographs of a.) PS-b-P2VP, b.) PS-b-P2VP/NMP+ I- (methylated for 2 hours), c.) PS-b-P2VP/NMP+ I- (methylated for 4 hours), d.) PS-b-P2VP/NMP+ I- (methylated for 24 hours), and e.) PS-b-P2VP/NMP+ I- (methylated for 48 hours). f.) Representative height profile for PS-b-P2VP and PS-b-P2VP/NMP+ I- exposed to methyliodide vapor for different times. Scale bar (500 *nm*) is located in a.)

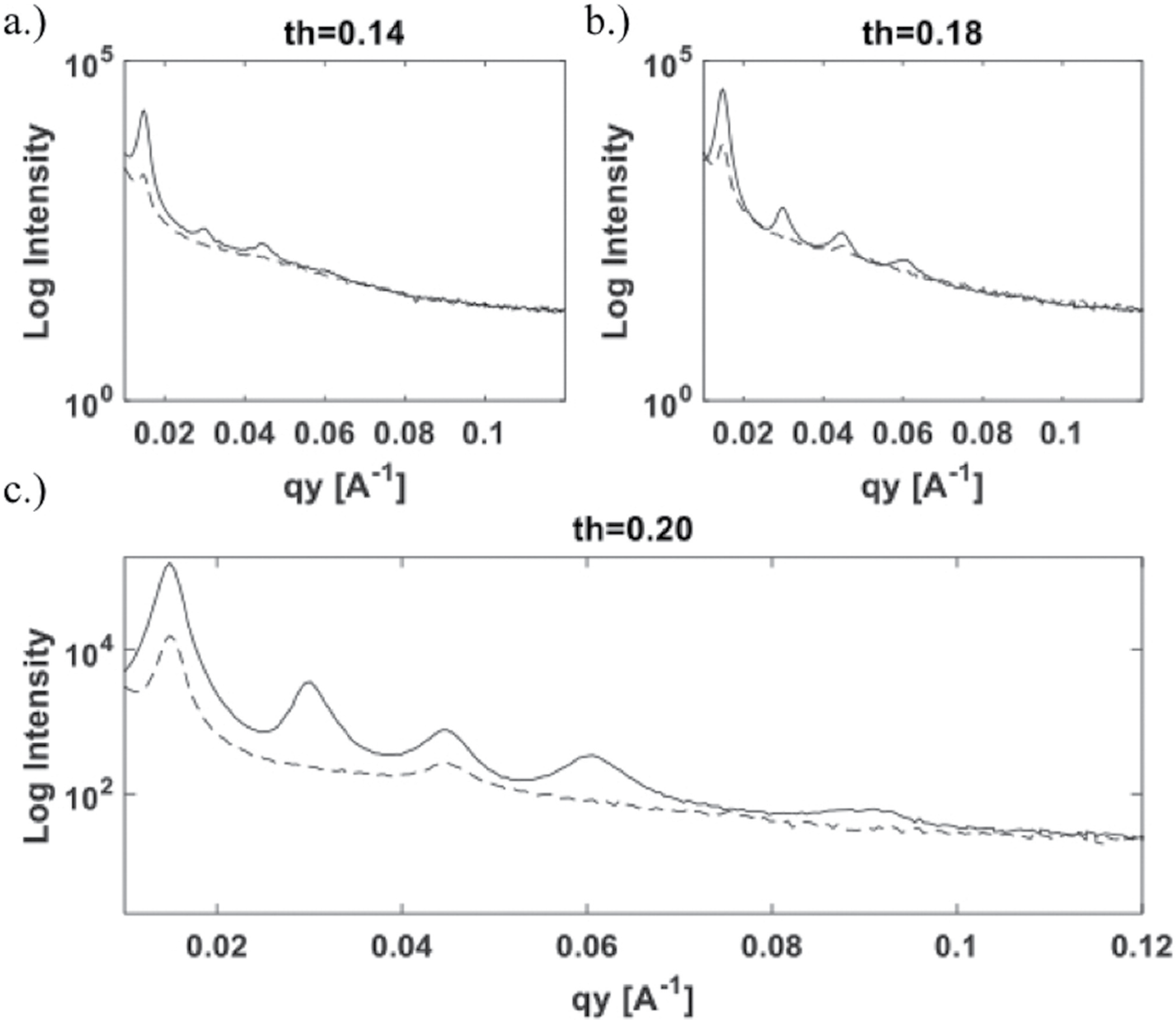

Figure 3.15: Horizontal linecuts along Yoneda peak from GISAXS scattering patterns of PS-b-P2VP (dotted) and PS-b-P2VP/NMP+ I- (24 hr CVIR) (solid) samples at different incidence angles a.) $\theta = 0.14 \circ$, b.) $\theta = 0.18 \circ$, and c.) $\theta = 0.20 \circ$ degree incident beam angles.

Sample	**Incidence Angle (θ)**	**Domain Spacing (D)**
PS-b-P2VP	0.14, 0,18, 0.20	42.93 + 0.70 *nm*
PS-b-P2VP/NMP+ I-	0.14, 0,18, 0.20	42.66 + 0.84 *nm*

Table 3.1: Domain spacing determined from GI-SAXS experiemnts

Methylation Time *hrs*	Frac of NMP+ I- in the P2VP block	MW of the P2VP block $g\ mol^{-1}$	IEC $mmol\ g^{-1}$
0	0	41000	0
2	0.164	50090	0.707
4	0.208	52492	0.871
24	0.368	61354	1.41
48	0.371	61509	1.42

Table 3.2: Calculated MW of the P2VP block and ion-exchange capacity (IEC) of PS-b-P2VP and PS-b-P2VP/NMP+ I- from integrated FTIR data

stretching derived from the bound water to the hydrophilic NMP+ I- groups. Finally, Figure 3.18 plots the fraction of pyridine converted to NMP+ I- as a function of methylation time for different integration strategies of the XPS data and integration of the FTIR data. In one XPS integration strategy, the integrated value associated with iodide versus the total nitrogen was determined (red trace). The second XPS integration strategy compared the integrated area for the signal at 399 *eV* over the summed areas for signals at 399 *eV* and at 396 *eV* (black trace). The third integration compared the integrated peaks of C-N+ stretching at 1630 cm^{-1} to the sum of integrated peaks of C-N+ and C-N (stretching at 1570 to 1590 cm^{-1}). Table 3.2 reports the change in the molecular weight of the P2VP block with increasing methylation and the calculated ion-exchange capacity value for PS-b-P2VP/NMP+ I-. The values in Table 3.2 were based off the integrated FTIR data. Overall, each integration strategy of the XPS and FTIR gave the same qualitative trend of the extent of reaction of pyridine to pyridinium iodide.

The confirmation of ionic groups present within the thin block copolymer films post CVIR was verified using the two complementary techniques: XPS and FTIR. FTIR provided full film analysis, while XPS probed only 5 *nm* into the film. Based on Figures 3.16 and 3.17, XPS and FTIR both confirmed the conversion of pyridine to NMP+ I- groups for the CVIR because a.) the iodide counterion was detected in the XPS spectra (Figure 3.16a), b.) the XPS spectra saw the formation of N+ at 399 eV (Figure 3.16b), and c.) the FTIR spectra also saw the formation of C-N+ stretching at 1630 cm^{-1} (Figure 3.17a) and the increased O-H stretching at 3500 cm^{-1} (Figure 3.17b) – indicative of water bound to the hydrophilic salt groups. The extent of the reaction monitored over time was evaluated by both XPS and FTIR. Both techniques, as well as the different integration strategies of the XPS data, yielded the same qualitative trend of the pyridine conversion to pyridinium iodide. Because the integrated FTIR data reflected the same trend as the XPS data, we inferred that the CVIR takes place within the film with a reasonable degree of homogeneity. This conclusion agrees with GI-SAXS data, which also confirmed that reaction was taking place throughout the thickness of the film.

3.4.4 Ion-exchange Capability

Figures 3.20a, b, and c provide the XPS spectra of the PS-b-P2VP/NMP+ I- (exposed to 48 hours of methyliodide vapor) ion-exchanged to the fluoride form (F 1s) (Figure 3.20a), chloride form (Cl 2p) (Figure 3.20b), and bromide form (Br 3.20d) (Figure 3.20c). Figure 3.20d is the XPS spectra of PS-b-P2VP/NMP+ I- ion-exchanged to the hydroxide form then ion-exchanged to the chloride form (Cl 2p). The subsequent ion-exchange of PS-b-P2VP/NMP+ OH- to PS-b-P2VP/NMP+ Cl- form was made for two reasons: i.) the sample rinsed and dried in the hydroxide form would have a considerable amount (if not all) of its hydroxide ions converted to the bicarbonate and/or the carbonate form [24] (because of exposure to air containing carbon dioxide (CO_2)) and ii.) the remaining hydroxide ions present in the film, poorly hydrated, could potentially degrade the NMP+ groups.[25] Hence, our goal was to see if the NMP+ groups could be ion-exchanged to the hydroxide form without degrading NMP+ groups. After the hydroxide ion-exchange, we rinsed the sample in deionized water excessively and immediately exchanged to the chloride form. The presence of chloride an-

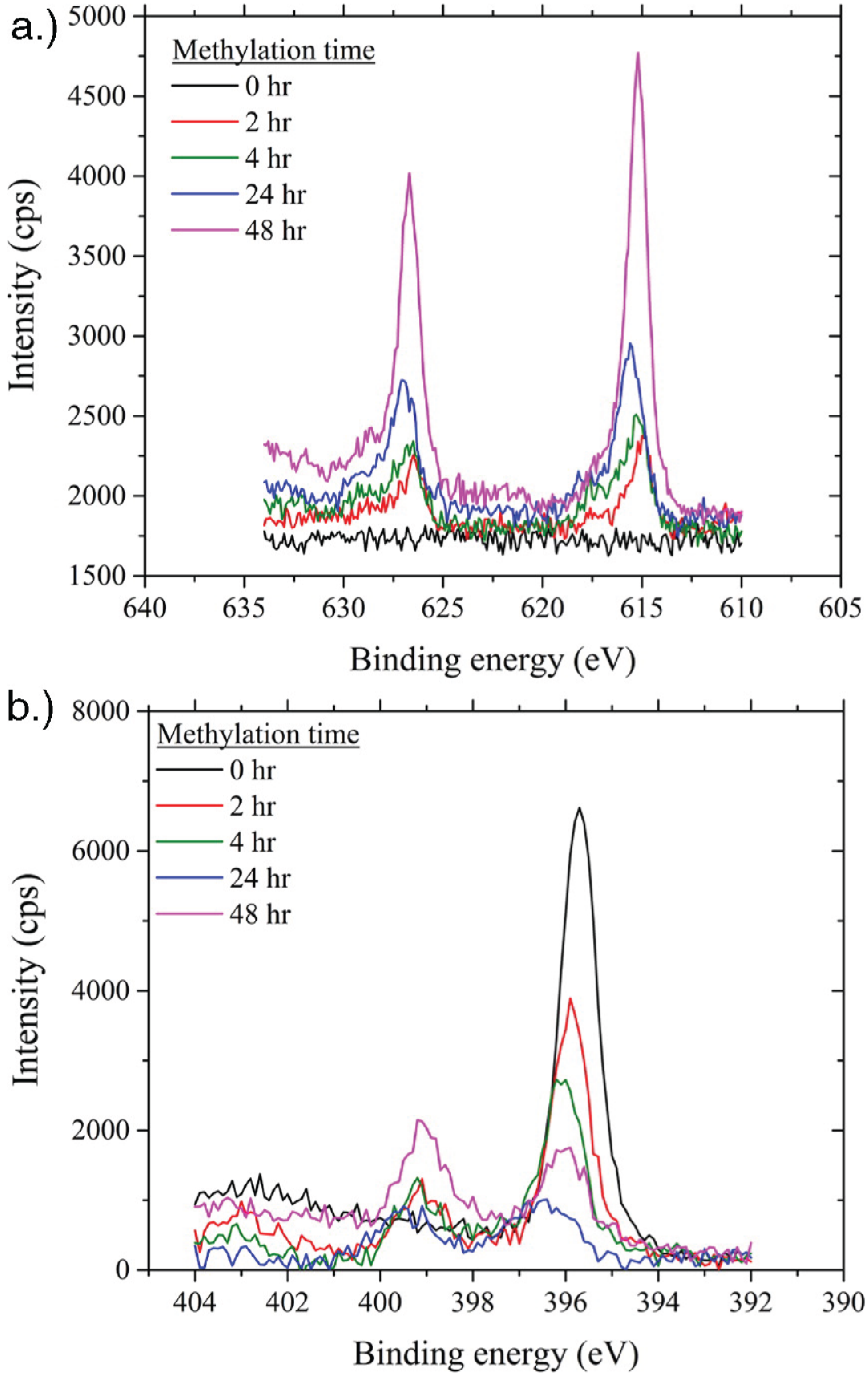

Figure 3.16: XPS spectra for PS-b-P2VP and PS-b-P2VP/NMP+ I- for different methylation times: a.) I 3d binding energy and b.) N 1s binding energy.

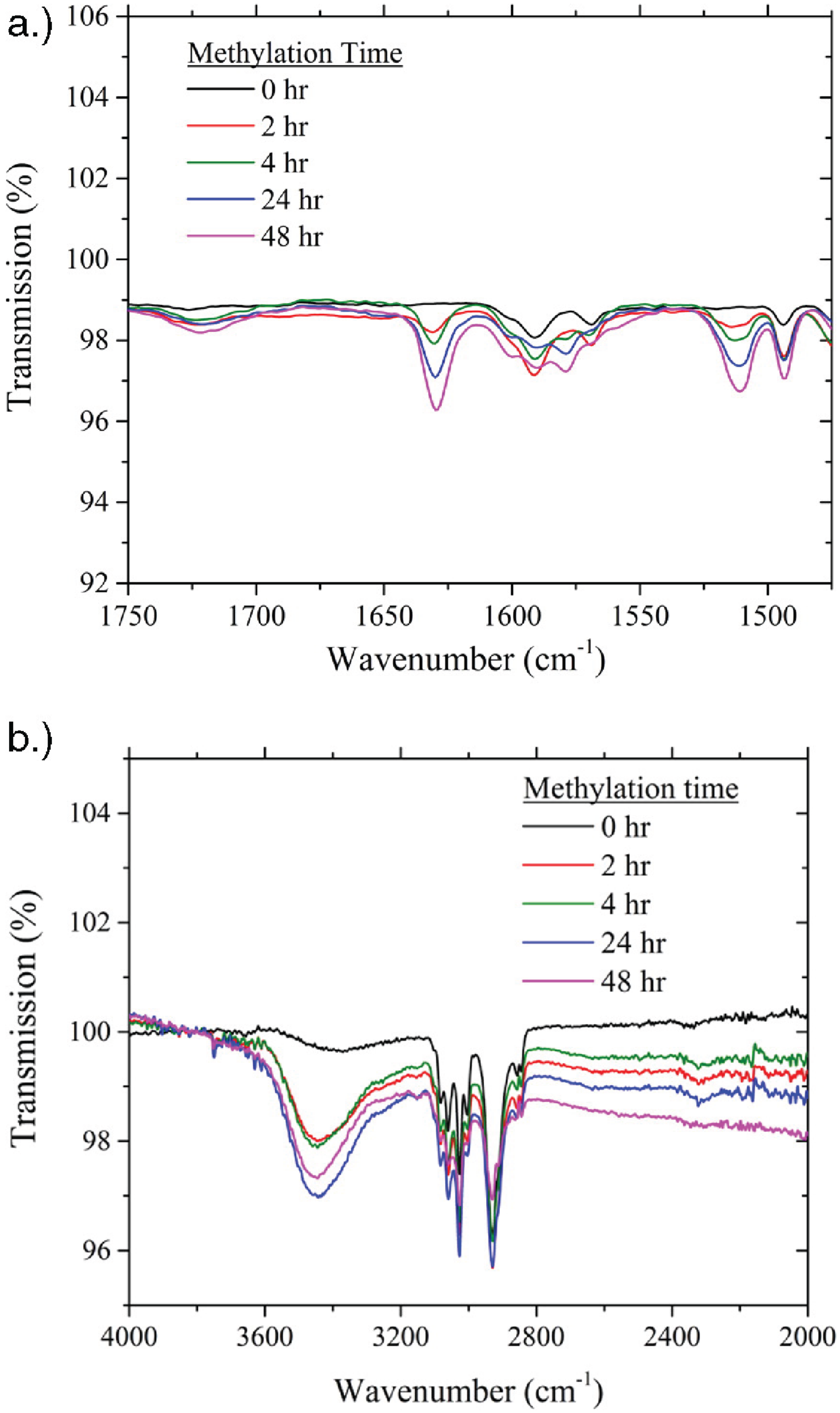

Figure 3.17: a.) FTIR spectra for PS-b-P2VP and PS-b-P2VP/NMP+ I- for different methylation times in the range of 1520 cm^{-1} to 1735 cm^{-1} and b.) FTIR spectra for PS-b-P2VP and PS-b-P2VP/NMP+ I- for different methylation times in the range of 2000 cm^{-1} to 4000 cm^{-1}

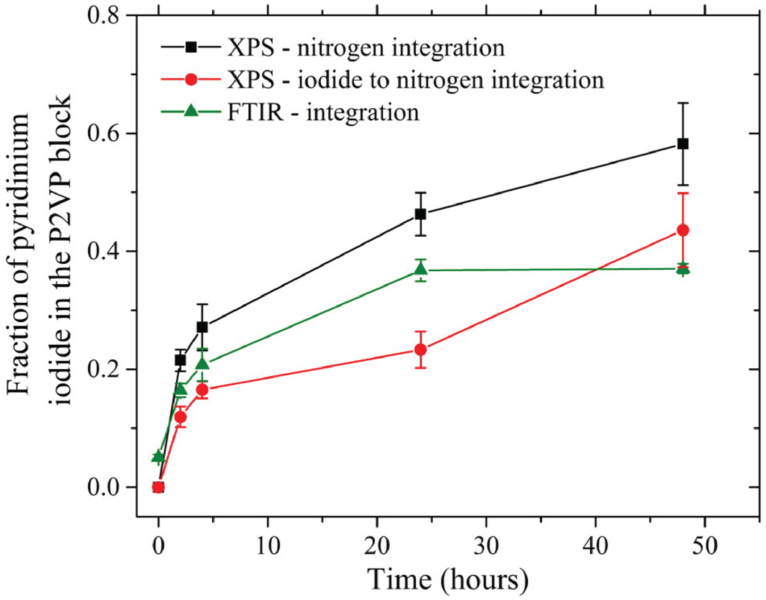

Figure 3.18: Fraction of NMP+ I- groups in the P2VP block in PS-b-P2VP/NMP+ I- films exposed to varying times of methyliodide vapor. The different traces resulted from differing integration strategies of data from XPS or from FTIR data. Note: error bars are the standard error for n = 3 samples.

ions in the XPS spectrum (Figure 3.20d) supported the integrity of NMP+ groups because they facilitated the initial ion-exchange from the iodide form to the hydroxide form and then the subsequent exchange to the chloride form. Hydroxide ion conducting polymer electrolytes are important to alkaline electrochemical devices (e.g., alkaline fuel cells and water electrolyzers)[26–28]. Figure 3.19 reports the XPS spectra for I 3d for PS-b-P2VP/NMP+ I- samples (methylated for 48 hours) before and after the ion-exchange process. This validates the removal of iodide species during the ion-exchange process. Figure 3.21 presents the N 1s XPS spectra for the ion-exchanged samples (including the sample exchanged to the bicarbonate form). For each sample ion-exchanged, the presence of the quaternary ammonium group at 399 eV was present. The ratio of quaternary ammonium signal at 399 eV to tertiary amine signal at 396 eV remained the same for the ion-exchange samples when compared to their original iodide form. Figures 3.22a to e are the corresponding SEM images of the aforementioned ion-exchange samples (Figure 3.20a to e). The fingerprint lamellae morphology remained intact for all the samples except PS-b-P2VP/NMP+ exchanged to the

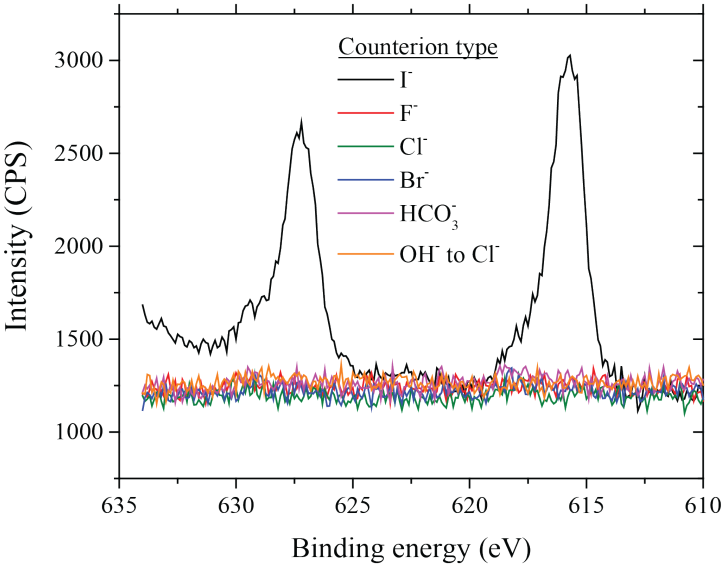

Figure 3.19: XPS I 3d spectra of PS-b-P2VP/NMP+ I- (exposed to methyliodide vapor for 48 hours) a.) before ion-exchange and after ion-exchange to the F- form b.) Cl- form c.) Br- d.) HCO3- e.) and OH- to Cl-.

fluoride form (Figure 3.22a).

XPS has the added capability to not only detect the change from pyridine to pyridinium through observation of the binding energy associated with nitrogen, but it can also pick up the binding energy signal associated with the counteranion (e.g., iodide, chloride, etc.). Thus, XPS also verified the ion-exchange capability of the PS-b-P2VP/NMP+ I-. We ascribed the unchanged morphology for most ion-exchanged samples (Figures 3.21a to e) to the hydrophobic, glassy styrene that anchored the BCE morphology during the ion-exchange process. However, the hydrophilic character of the P2VP/NMP+ allowed some swelling of the P2VP domain in the ion-exchanged samples, but the calculated period (via FFT of the SEM images) of the ion-exchanged samples (excluding the fluoride form) and the non-ion-exchange samples were similar. The SEM images of the ion-exchanged samples (minus the fluoride ion-exchanged sample) demonstrated an expansion of P2VP/NMP+ domain accompanied by a slight shrinkage in the PS domains resulting in the calculated period of the BCE to be not that different from the PS-b-P2VP/NMP+ samples not ion-exchanged. As for the changed morphology observed in PS-b-2VP/NMP+ F- (seen in Figure 3.21a), we assigned that the P2VP/NMP+ and PS blocks in PS-b-2VP/NMP+ F- merged together during the ion-exchange process. We contend that the electron rich fluoride anion was fully associated (i.e., condensed) with the NMP+ cations pulling the P2VP/NMP+ and PS blocks together – but future investigation of this effect is warranted. To summarize this section, we unequivocally demonstrated the ion-exchange capability of PS-b-2VP/NMP+ X-. Furthermore, this section also established that the morphology of fingerprint lamellae remained intact for ion-exchange processes involving 0.5 *M* NaCl, NaBr, NaHCO3, and NaOH.

3.4.5 Ionic Conductivity Results

Figure 3.23a illustrates the process and substrates used for making ionic conductivity measurements of self-assembled BCE films. Figure 3.23b represents an SEM image of the BCE (PS-b-P2VP/NMP+ I- methylated for 48 hours) at the platinum electrode and silicon wafer interface, while Figure 3.23c presents the AFM images at this interface. Fingerprint lamellae was observed in the SEM and AFM phase images seen in Figures 3.23b and c, but it was difficult to observe the fingerprint lamellae in the AFM height image because of the 200 *nm* height difference between the platinum electrode and silicon substrate.

Figure 3.24a depicts Nyquist plots of self-assembled PS-b-P2VP/NMP+ I- for samples exposed to methyliodide vapor for different times, while Figure 3.24b shows the calculated in-plane ionic conductivity of the BCE film. Figure 3.24a displays a progressive reduction in the first (i.e., impedance at higher frequencies) and smaller semi-circle diameter, proximal to the origin, with increasing methyliodide exposure time. In addition to iodide ionic conductivity, the ionic conductivity of the chloride ion and hydroxide ion forms were assessed because ion transport of these counterions in polymer electrolytes are applicable to water treatment and alkaline electrochemical applications.[26] Figure 3.25compares the Nyquist plot of the PS-b-P2VP/NMP+ X- samples methylated for 48 hours (X= I-, Cl-, and OH-).

The ionic conductivity experiments examined two different relationships: i.) the influ-

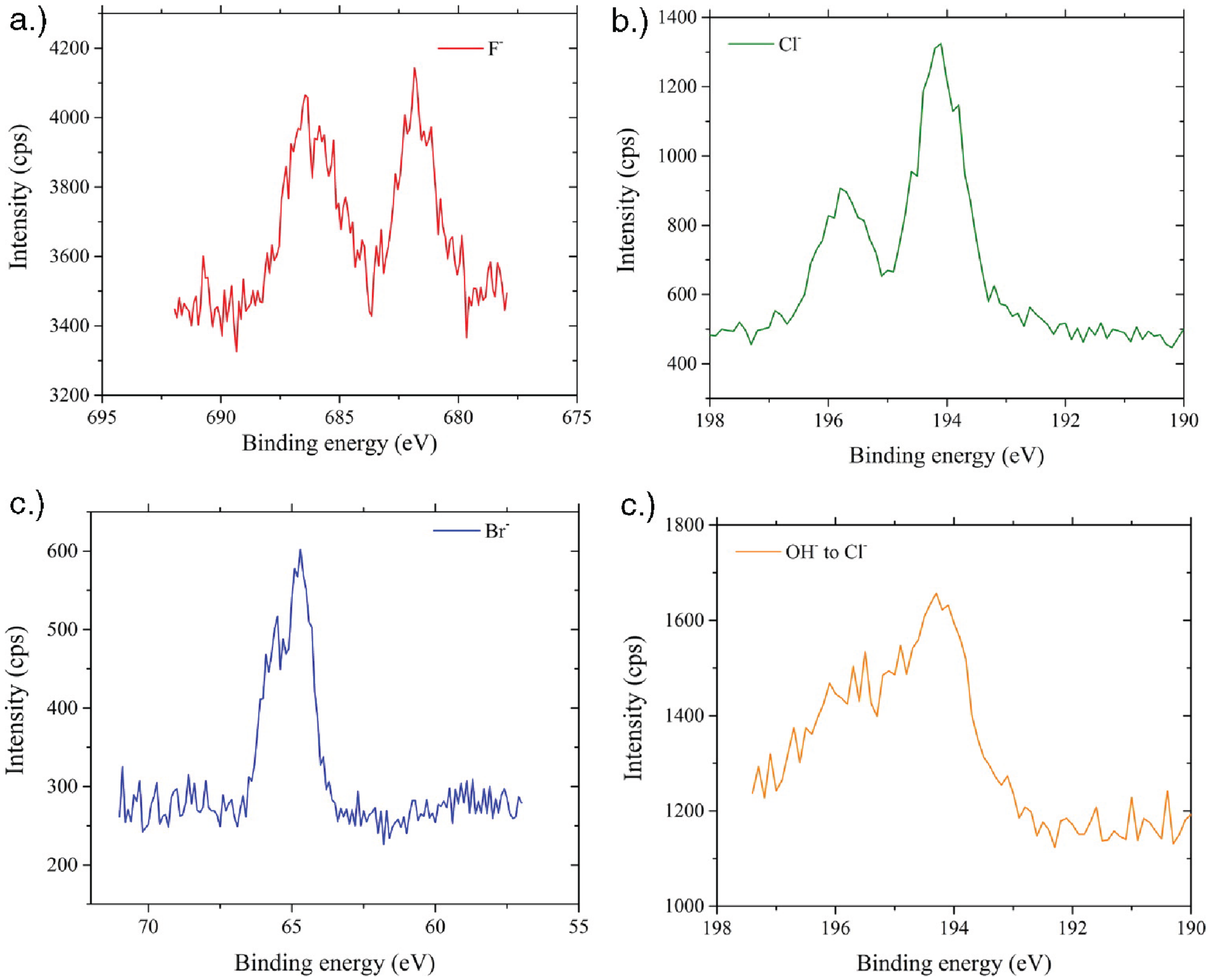

Figure 3.20: XPS spectra of PS-b-P2VP/NMP+ X- after the ion-exchange process. PS-b-P2VP was exposed to methyliodide vapor for 48 hours. X- = a.) F- (F 1s) b.) Cl- (Cl 2p) c.) Br- (Br 3d) and d.) OH- to Cl- (Cl 2p) sample was ion-exchanged to hydroxide ion form followed by an ion-exchange to the chloride ion.

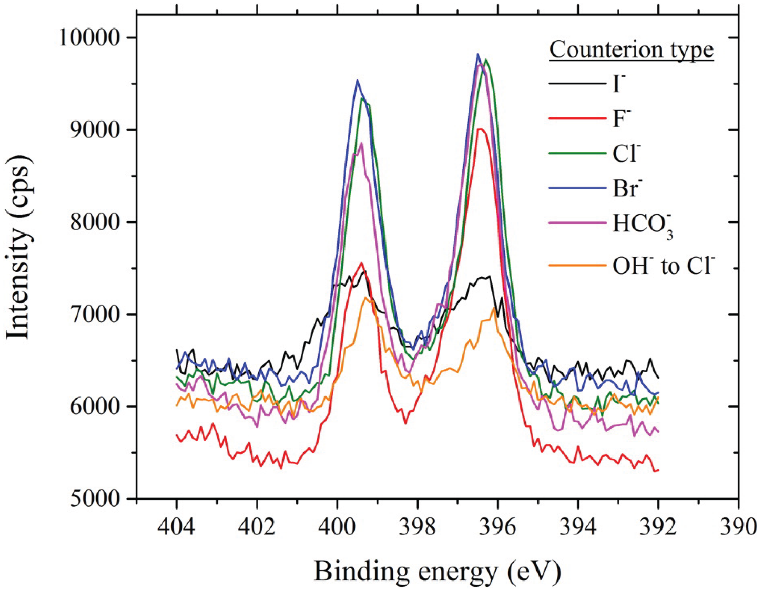

Figure 3.21: XPS N 1s spectra of PS-b-P2VP/NMP+ X- before and after ion-exchange. PS-b-P2VP/NMP+ I- was exposed to methyliodide vapor for 48 hours. X- = a.) I- (before ion-exchange), b.) F-, c.) Cl-, d.) Br- e.) HCO3-, and f.) OH- to Cl- (sample was ion-exchanged to hydroxide ion form followed by an ion-exchange to the chloride ion).

ence of sample exposure time to methyliodide vapor and its effect on iodide ion conductivity and ii.) the ionic conductivity PS-b-P2VP/NMP+ X- with different counterions (I-, Cl-, and OH-). Prior to elaborating on these two relationships, it is important to understand the process for interpreting the Nyquist plots to determine the ionic conductivity. The smaller, first semi-circle in the Nyquist plots shown in Figure 3.24a was ascribed to BCE film resistance, while the second, larger semi-circle corresponded to the resistance of the PS-r-P2VP-r-PHEMA brush layer grafted to the interdigitated electrode substrate. Note: The PS-b-P2VP with no methylation only displayed a single semi-circle because of its overall large impedance of PS-b-P2VP and the second semi-circle in the Nyquist plots also displayed a reduction in resistance during the CVIR supporting that the methyliodide diffuses through the film and reacts with underlying grafted brush layer. The ESI details the electric circuit equivalent model used to extract the PS-b-2VP/NMP+ I- film resistance from the acquired EIS data. The film resistance was an input for calculating the ionic conductivity. The subsequent increase in PS-b-P2VP/NMP+ I- film ionic conductivity with larger methyliodide

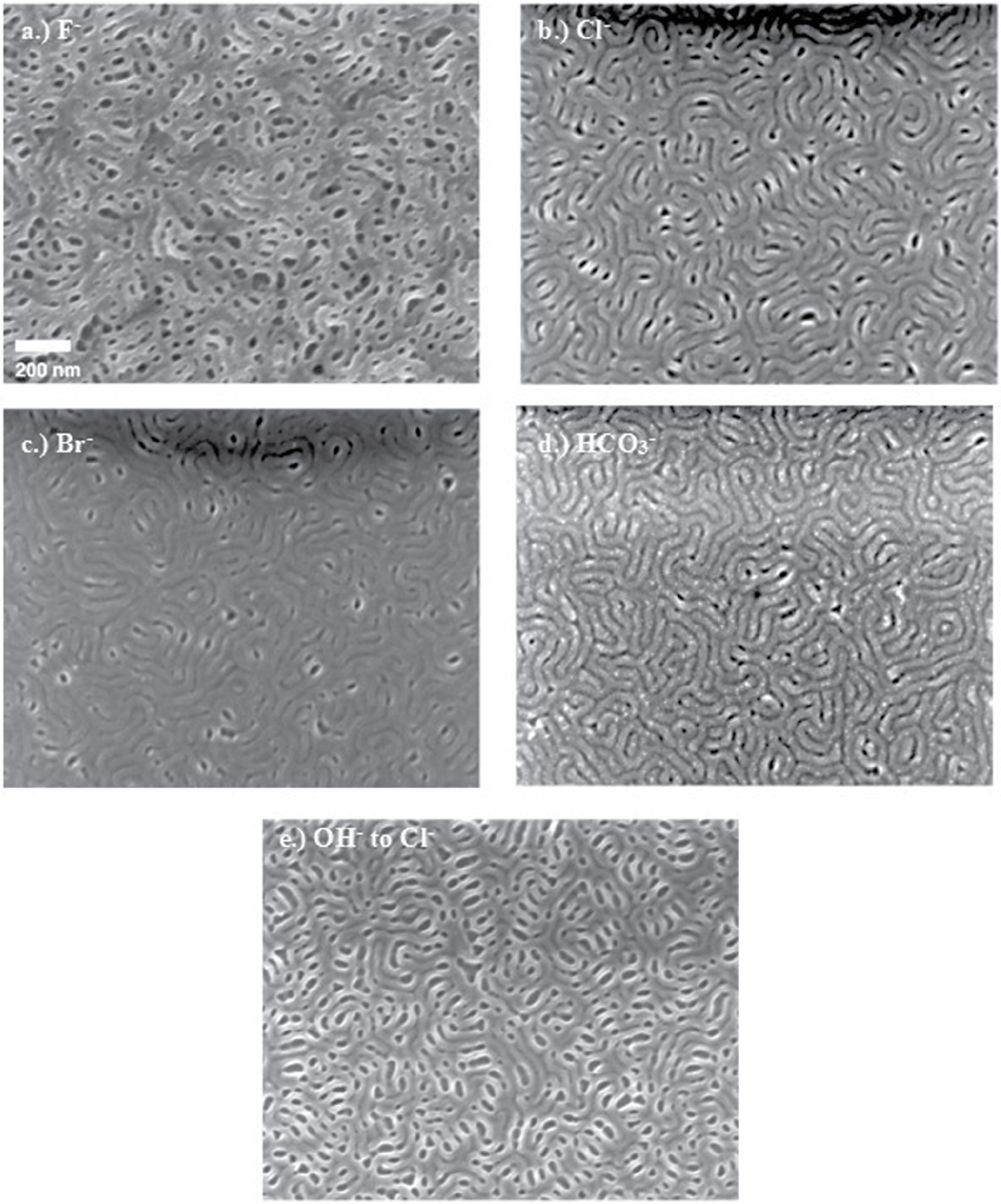

Figure 3.22: SEM images of ion-exchanged PS-b-P2VP/NMP+ X- (scale bare in image a.)). PS-b-P2VP/NMP+ I- was exposed to methyliodide vapor for 48 hours. X- = a.) F-, b.) Cl-, c.) Br-, d.) HCO3-, and e.) OH- to Cl- (sample was ion-exchanged to hydroxide ion form followed by an ion-exchange to the chloride ion).

vapor exposure times resulted from the larger concentration of fixed ionic carriers within the thin film – as substantiated from the XPS and FTIR data. Generally, ionic conductivity scales linearly with the amount fixed ionic carriers in ideal, liquid electrolytes.[29] But, solid-state electrolytes, like polymer electrolyte films, display a more complex relationship with regard to concentration of ionic groups because of synergistic effects arising from water hydration, structural morphology,[30] counterion condensation,[31] and non-ideality (e.g, activity coefficients, etc.).[32]

For PS-b-P2VP/NMP+ X-, the Nyquist trace for the chloride form (X=Cl-) showed a drastic reduction in the diameter of the first semi-circle indicating a substantial drop in the BCE film resistance. The resultant ionic conductivity of PS-b-P2VP/NMP+ Cl- was 46.01 + 4.00 $mS\ cm^{-1}$ at 20 $\circ C$ in deionized water and is the highest chloride ion conductivity value, to the best of our knowledge, for anion conducting polymer electrolyte membranes.[33] The increase in the ionic conductivity of the chloride form over the iodide form was attributed to the higher ionic mobility of the chloride anion in contrast to the iodide anion. Interestingly, the second semi-circle of PS-b-P2VP/NMP+ Cl- in Figure 3.25 was larger when compared to the iodide form indicating that the charger transfer resistance from the brush layer to the BCE film increased. We ascribed this increase in the impedance to larger charge transfer resistance between the brush layer and the BCE film due to the ion-exchange process (i.e., swelling of the brush or film), which disrupted the intimate contact between the film and brush layer. The Nyquist plot trace of PS-b-P2VP/NMP+ OH- gave slightly higher impedance values for the first and second semi-circles when compared to PS-b-P2VP/NMP+ I-. Although the ionic mobility of the hydroxide ion is higher than the iodide ion, the hydroxide ion can react readily with available CO_2 to form carbonate and bicarbonate anions – both of which have lower ionic mobility values than the hydroxide ion.[26] Furthermore, the carbonate anion has a -2 valence and it can form ionic crosslinks within the PS-b-P2VP/NMP+ X- hindering ionic conductivity. Another possibility explaining the lower ionic conductivity is assigned to the potential degradation of the NMP+ cation groups by attack of the hydroxide ion.[34] However, XPS data revealed the integrity of the quaternary ammonium moiety in the NMP+ cation groups when ion-exchanged to the hydroxide ion. Therefore, the slightly higher impedance of PS-b-P2VP/NMP+ X- ion-exchanged to the hydroxide ion form was assigned solely to the carbonation of the BCE by ambient CO_2.

3.5 Conclusion

In this work, we prepared block copolymer electrolyte films with their ionic blocks oriented perpendicularly to the substrate surface over large areas. The process disseminated herein first assembled the non-ionic block copolymer variant and then utilized a simple CVIR to selectively introduce fixed ion carriers into the P2VP block of the PS-b-P2VP copolymer film without disrupting its morphology and orientation - this is the first report, to the best of our knowledge, that effectively engineers block copolymer electrolytes with a self-assembled, desired orientation in thin films. Complementary spectroscopic (XPS and FTIR) and structural characterization (SEM and AFM) tools substantiated the introductions of ionic groups within BCE film while maintaining its oriented nanostructure. The prepared BCE films demonstrated excellent ionic conductivity (e.g., chloride ion conductivity over 45 $mScm^{-1}$ at 20 $\circ C$ in deionized water) in several different counterion forms. Furthermore, the SA BCE electrolyte could be ion-exchanged to chloride, bicarbonate, bromide, and hydroxide counter ions without change to its lamellae morphology. This work also demonstrated that introducing more fixed ionic carriers within the film yielded higher ionic conductivity values. Overall, we envision this scheme as an effective analytical platform for understanding how the salient structure features of block copolymer electrolytes (e.g., connectivity, tortuosity, grain size, etc.) influence ion transport processes.

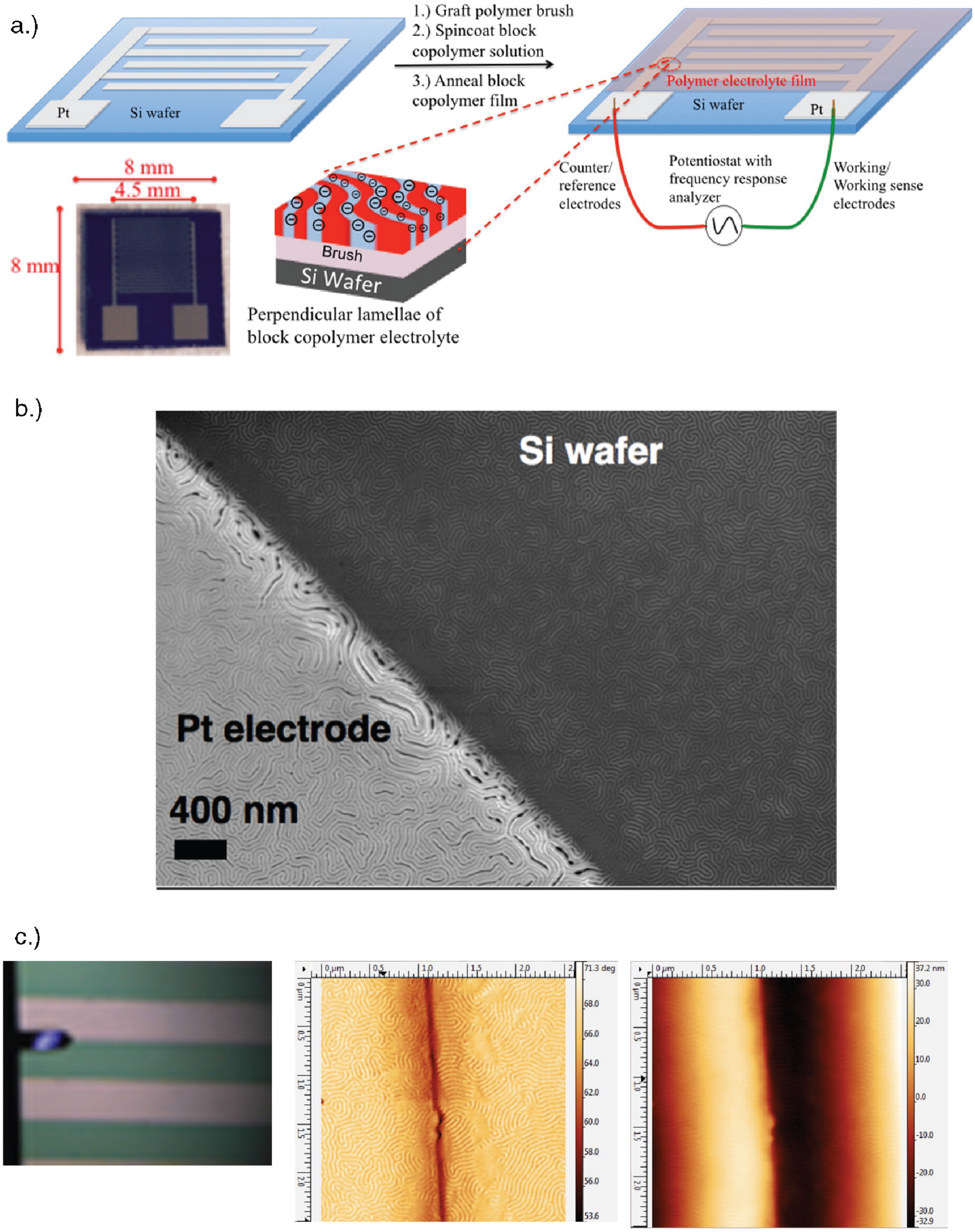

Figure 3.23: a.) Process scheme for the SA of BCE film on to interdigitated electrode substrates. b.) SEM image and c.) AFM images (phase and then height) at the interface of the platinum electrode and silicon wafer with BCE film on top.

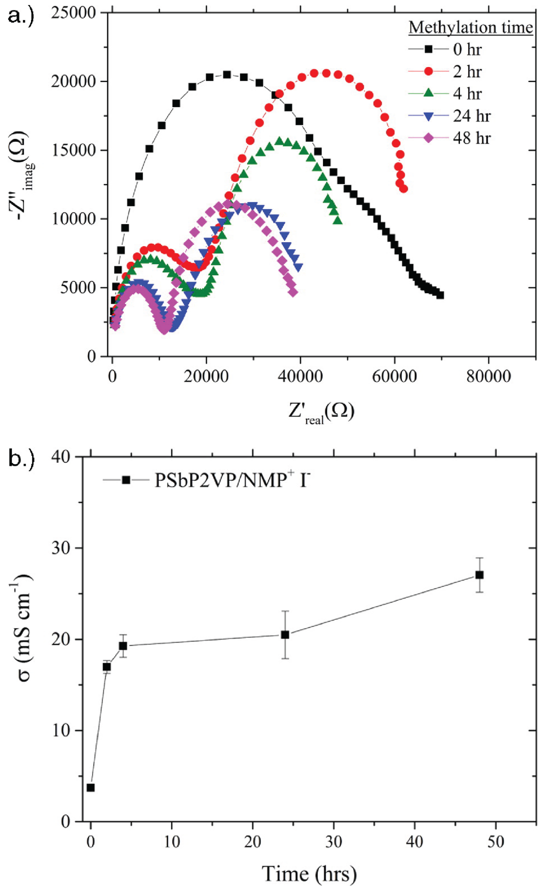

Figure 3.24: a.) Nyquist plots of PS-b-P2VP and PS-b-P2VP/NMP+ I- samples with varying exposure times to methyliodide vapor b.) Calculated in-plane iodide ion conductivity using the extracted BCE film resistance from the Nyquist plots. Note: error bars are the standard error for n = 3 samples.

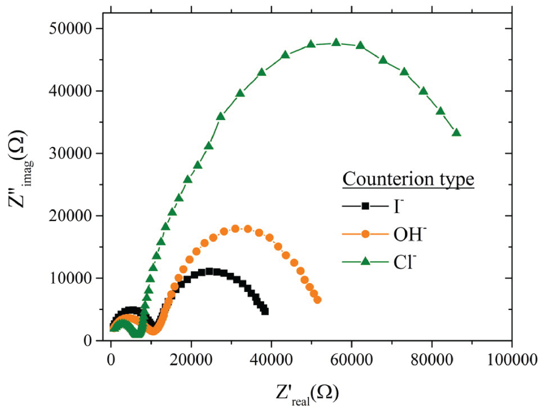

Figure 3.25: The Nyquist plots of PS-b-P2VP/NMP+ I- (exposed to methyliodide vapor for 48 hours) in different counterion forms iodide, hydroxide, and chloride ions. Additionally, the calculated in-plane ion conductivity values for PS-b-P2VP/NMP+ I- are provided. Note: error bars are the standard error for n = 3 samples.

3.6 References

[1] C. G. Arges, Y. Kambe, H. S. Suh, L. E. Ocola, and P. F. Nealey, Chemistry of Materials **28**, 1377 (2016).

[2] M. P. Stoykovich, M. Muller, S. O. Kim, H. H. Solak, E. W. Edwards, J. J. de Pablo, and P. F. Nealey, Science **308**, 1442 (2005), ISSN 0036-8075.

[3] R. Ruiz, H. Kang, F. A. Detcheverry, E. Dobisz, D. S. Kercher, T. R. Albrecht, J. J. de Pablo, and P. F. Nealey, Science **321**, 936 (2008), ISSN 0036-8075.

[4] M. P. Stoykovich and P. F. Nealey, Materials Today **9**, 20 (2006).

[5] X. Chen, B. B. Wayland, M. Fryd, K. I. Winey, and R. J. Composto, Macromolecules **39**, 6063 (2006), ISSN 00249297.

[6] P. W. Majewski, M. Gopinadhan, W.-S. S. Jang, J. L. Lutkenhaus, and C. O. Osuji, Journal of the American Chemical Society **40**, 17516 (2010), ISSN 1520-5126.

[7] M. J. Park and N. P. Balsara, Macromolecules **43**, 292 (2010), ISSN 00249297.

[8] P. W. Majewski, M. Gopinadhan, and C. O. Osuji, Soft Matter **9**, 7106 (2013), ISSN 1744-683X.

[9] X. Feng, M. E. Tousley, M. G. Cowan, B. R. Wiesenauer, S. Nejati, Y. Choo, R. D. Noble, M. Elimelech, D. L. Gin, and C. O. Osuji, ACS Nano **8**, 11977 (2014).

[10] S. J. Jeong, J. Y. Kim, B. H. Kim, H. S. Moon, and S. O. Kim, Materials Today **16**, 468 (2013), ISSN 13697021.

[11] M. P. Stoykovich, H. Kang, K. C. Daoulas, G. Liu, C. C. Liu, J. J. De Pablo, M. Müller, and P. F. Nealey, ACS Nano **1**, 168 (2007), ISSN 19360851.

[12] J. H. Pikul, H. Gang Zhang, J. Cho, P. V. Braun, and W. P. King, Nature communications **4**, 1732 (2013), ISSN 2041-1723.

[13] F. Opekar and K. Štulík, in *Analytica Chimica Acta* (1999), vol. 385, pp. 151–162, ISSN 00032670.

[14] M. F. El-Kady and R. B. Kaner, Nature communications **4**, 1475 (2013), ISSN 2041-1723.

[15] Y. G. Majid Beidaghi, Energy & Environmental Science **7**, 867 (2014), ISSN 1754-5692.

[16] Y. a. Elabd and M. a. Hickner, Macromolecules **44**, 1 (2011), ISSN 00249297.

[17] M. a. Modestino, D. K. Paul, S. Dishari, S. a. Petrina, F. I. Allen, M. a. Hickner, K. Karan, R. a. Segalman, and A. Z. Weber, Macromolecules **46**, 867 (2013), ISSN 00249297.

[18] A. Kusoglu, D. Kushner, D. K. Paul, K. Karan, M. a. Hickner, and A. Z. Weber, Advanced Functional Materials **24**, 4763 (2014), ISSN 16163028.

[19] D. K. Paul, R. McCreery, and K. Karan, Journal of the Electrochemical Society **161**, F1395 (2014), ISSN 0013-4651.

[20] S. Ji, C.-C. Liu, J. G. Son, K. Gotrik, G. S. W. Craig, P. Gopalan, F. J. Himpsel, K. Char, and P. F. Nealey, Macromolecules **41**, 9098 (2008), ISSN 0024-9297.

[21] P. F. Nealey and L. Wan, *Solvent Annealing block copolymers on patterned substrates* (2012).

[22] J. Rao, H. Ma, J. Baettig, S. Woo, M. C. Stuparu, J. Bang, and A. Khan, Soft matter **10**, 5755 (2014), ISSN 1744-6848.

[23] Streitwieser, A. H., Clayton H. Kosower, Edward M., *Introduction to Organic Chemistry. 4th Edition* (Macmillian Publishing, New York, NY, 1992).

[24] S. Watanabe, K. Fukuta, and H. Yanagi, in *ECS Transactions* (The Electrochemical Society, 2010), vol. 33, pp. 1837–1845, ISSN 1938-6737.

[25] S. Chempath, B. R. Einsla, L. R. Pratt, C. S. Macomber, J. M. Boncella, J. A. Rau, and B. S. Pivovar, Journal of Physical Chemistry C **112**, 3179 (2008), ISSN 19327447.

[26] J. R. Varcoe, P. Atanassov, D. R. Dekel, A. M. Herring, M. A. Hickner, P. A. Kohl, A. R. Kucernak, W. E. Mustain, K. Nijmeijer, K. Scott, et al., Energy & Environmental Science **7**, 3135 (2014), ISSN 1754-5692.

[27] C. G. Arges, L. Wang, J. Parrondo, and V. Ramani, Journal of The Electrochemical Society **160**, F1258 (2013), ISSN 0013-4651.

[28] J. Parrondo, C. G. Arges, M. Niedzwiecki, E. B. Anderson, K. E. Ayers, and V. Ramani, RSC Advances **4**, 9875 (2014), ISSN 20462069.

[29] H. Strathmann, *Ion-Exchange Membrane Separation Processes*, vol. 9 (Elsevier Science, 2004), ISBN 9780444502360.

[30] I. Villaluenga, X. C. Chen, D. Devaux, D. T. Hallinan, and N. P. Balsara, Macromolecules **48**, 358 (2015), ISSN 0024-9297.

[31] K. M. Beers, D. T. Hallinan, X. Wang, J. a. Pople, and N. P. Balsara, Macromolecules **44**, 8866 (2011), ISSN 00249297.

[32] K. N. Grew, D. Chu, and W. K. S. Chiu, Journal of The Electrochemical Society **157**, B1024 (2010), ISSN 00134651.

[33] G. Merle, M. Wessling, and K. Nijmeijer, *Anion exchange membranes for alkaline fuel cells: A review* (2011).

[34] V. Neagu, I. Bunia, and I. Plesca, Polymer Degradation and Stability **70**, 463 (2000), ISSN 01413910.

CHAPTER 4

ROLE OF DEFECTS IN ION TRANSPORT IN BLOCK COPOLYMER ELECTROLYTES

4.1 Abstract

Ion conducting block copolymers can overcome traditional limitations of homopolymer electrolytes by phase separating into nanoarchitectures that can be simultaneously optimized for two or more orthogonal material properties such as high ion conductivity and mechanical stability. A key challenge in understanding ion transport properties of these materials is the difficulty of extracting structure-function relationships without having complete knowledge of all nanoscale transport pathways in bulk samples. Here we demonstrate a method for deriving structure-transport relationships for ion conducting block copolymers using thin films and interdigitated electrodes. Well-defined and directly imaged structure in films of poly(styrene)-block-poly(2-vinyl pyridine) is controlled using techniques of directed self-assembly then the poly(2-vinyl pyridine) is selectively converted into an ion conductor. The ion conductivity is found to be directly proportional to the total number of connected paths between electrodes and the path length. A single defect such as a dislocation anywhere in the path of an ion conducting route disconnects and precludes that pathway from contributing to the conductivity and results in an increase in the capacitance of the film. When all the ion conduction pathways are blocked between electrodes, the conductivity is negligible, four orders of magnitude lower compared to a completely connected morphology and the capacitance increases by a factor of 50. These results have profound implications for the interpretation, design, and processing of block copolymer electrolytes for applications as ion conducting membranes.

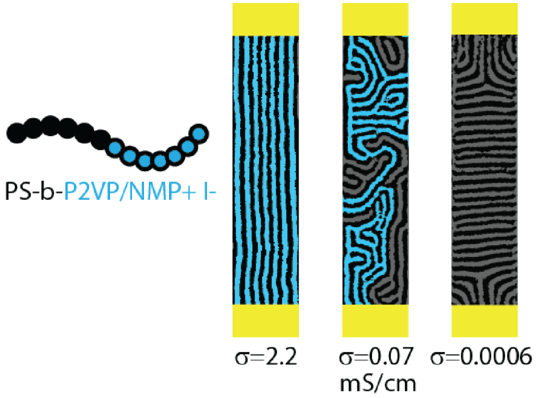

Figure 4.1: Summary of the experiment.

4.2 Introduction

Ion conducting polymer membranes play a central role in the development of safer and more efficient electrochemical devices such as fuel cells,[1] electrolyzers,[2] and redox flow batteries.[3–8] Membranes composed of a single component often suffer from trade-offs between high ionic conductivity and mechanical robustness.[9] Block copolymer electrolytes (BCEs) are promising candidates as membrane materials because of the opportunity to simultaneously optimize two (or more) orthogonal properties.[10, 11] The two components of a diblock BCE, for example, can be optimized for both ion conductivity and mechanical properties. The blocks can then self-assemble into a structure of nanoscale ion conducting channels that are periodically distributed amongst mechanically rigid but ion insulating domains. Morphologies commonly formed by BCEs include gyroid networks,[12] lamellae,[13] and hexagonally-packed cylinders,[14] ostensibly offering transport in three, two, and one dimensions, respectively.

Structure-property relationships in BCEs are challenging to derive because the periodic domain structure of BCEs formed through self-assembly are well-ordered only locally, at the sub-micron scale, but transport properties are typically measured over macroscopic dimensions, on the scale of tens to thousands of microns. At this device scale, the materials can be described as consisting of multiple grains. The implications of this structure are that, regardless of the local BCE morphology, the materials have the potential to conduct in three dimensions, the conduction pathways are likely to be tortuous, and mechanisms of transport across grain boundaries and defects must be considered. Effective Medium Theory (EMT) [15] is a methodology to characterize the dependence of ion transport on morphology and is written in its simplest form as:

$$\sigma_{BCE} = f\phi\sigma_{HOMO} \tag{4.1}$$

where σ_{BCE} is the conductivity of the BCE, σ_{HOMO} is the conductivity of the homopolymer that is chemically identical to the conducting block of the BCE, ϕ is the volume fraction of the conducting block, and f is a tortuosity factor. The value of f for each grain in a BCP morphology is uncomplicated: f equals one for gyroids and for sphere-forming BCPs with majority phase conducting in all directions, while f equals one for lamellae and cylinders in the directions parallel to the domains, and zero in the transverse directions. Theoretical values of f have been determined by Sax and Ottino[15] for multi-grained BCP films assuming no impediments to transport across defects and grain boundaries. They determined transport to be isotropic in the bulk, and f to be 1 for bicontinuous morphologies such as gyroids, 1 for sphere-forming BCES where the majority phase is ion conducing, 0.33 for cylinder-forming BCEs where the minority is ion conducting, and 0.66 for lamellae forming BCE, of primary interest in this work. Hallinan and Balsara[16] have reviewed the conductivities of many different bulk and multigrain BCE systems with varying morphologies and tabulated or calculated the values of f. In the review and cited literature, the values of f reported for lamellae systems range from as low as 0.01 to within error of the theoretical value of 0.66. The majority of the reported material systems exhibited conductivities of the BCE that were not consistent with an EMT description. These included high molecular weight, lamella-forming BCPs such as polystyrene-block-poly(ethylene oxide) (PS-b-PEO) that have f values as low as 0.015 [17] and lamellae forming BCEs that were aligned using external fields, in an attempt to mitigate the effect of tortuosity described above, that have f

values below 0.1.[14] In the few studies where the reported values of f were within an order of magnitude of the values predicted for multi-grained samples: 1) the materials systems were either lamellae forming BCPs with small grain sizes, at the scale of the lamellar period itself, such as PS-b-PEO that reach an f value of 0.2,[18, 19] or 2) fully microphase-separated, lamellae-forming BCPs with high volume fractions of low molecular weight ionic liquids (ILs) with f values approaching the theoretical value of 0.66.[20] As noted by many researchers, the information required to build a unifying, fundamental understanding of transport in BCE systems is a measurement of the structure-conductivity relationship under conditions in which the structure of the material is known quantitatively, especially as it relates to the role of transport across defects and grain boundaries. However, characterization of the structure at the scale of individual domains or conduction pathways, on the scale of 10-20 nm, throughout the entire volume at the device scale, e.g., a membrane of 100 microns in thickness, is difficult or impossible.[21–23]

Here we report the measurement of structure–electrochemical property relationships in lamellae-forming BCEs using thin films and interdigitated electrodes. The use of thin films enables quantitative structural characterization, and the use of interdigitated electrodes results in measurements with high signal-to-noise ratios in electrochemical impedance spectroscopy. Fabrication of connected, partially connected, and unconnected morphologies between electrodes is achieved by rudimentary implementation of the techniques of directed self-assembly, and these structural motifs are analogous to grain boundary and defect structures found in the bulk. Conductivity is found to be directly proportional to the number and length of domains of the BCE that are connected from one electrode to the other. Any conducting domain within the film with even a single impeding defect (e.g., a dislocation) does not contribute to the conductivity and increases the capacitance of the material. Films with no connecting pathways exhibit conductivities more than four orders of magnitude lower and a capacitance that is an order of magnitude higher than the connected film. These results signify that defects and grain boundaries play a central role in determining the electrochemical properties of self-assembling nanostructured electrolytes and are key parameters to understand and control in the design and processing of these materials.

4.3 Methods

4.3.1 Materials

The block copolymer PS-b-P2VP (Mn of 25 $kgmol^{-1}$ PS, 22 $kgmol^{-1}$ P2VP) was received from Polymer Source and used as is. The mono-hydroxy terminated random copolymer brush (P(S-r-2VP)-OH) was synthesized as described in the electronic supporting information of this work. The neutral preference surface was formed using the P(S-r-2VP)-OH brush with 69 % of the repeat units comprising of PS while the weakly preferential surface was formed using the P(S-r-2VP)-OH with 48% of the repeat units comprising of PS. All other chemicals (methyl iodide, toluene, N,N-dimethyformamide (DMF), methyl isobutyl ketone (MIBK), tetrahydrofuran (THF), acetone, and 2-propoanol (IPA)) were received from Sigma-Aldrich or Fisher Scientific and used without further purification. The gold interdigitated electrodes with HSQ guiding stripes were fabricated on semiconducting polished silicon wafers (1 μm – thermally grown oxide layer) obtained from WRS materials. PMMA 950 k MW and MMA 6.5 photoresists were obtained from MicroChem Corporation and used as is for photolithography fabrication of the gold electrode layer. The HSQ photoresist FOX22 used for the guiding stripe layer was obtained from Du Pont Chemicals and diluted to 1:2 (v:v FOX22:MIBK) prior to use to control the thickness of the final film. Fabrication of interdigitated electrodes with nanoscale trenches. Silicon wafers with a 1 μm thick, thermally grown oxide was cleaned with piranha solution (70:30 v:v mixture of concentrated sulfuric acid and 35 wt% hydrogen peroxide) for 30 mins at 130 $^{\circ}C$. The wafer was dehydrated on a hotplate at 80 $^{\circ}C$ for 15 $mins$ prior to being spun coat with a bilayer photoresist of MMA 6.5 (120 nm) and PMMA 950A (140 nm). The device pattern was written using the NFD JEOL JBX-9300FS electron beam lithography system with an acceleration voltage of 100

kV and a dose of 1200 $\mu C/cm^2$, and was developed with 1:3 v:v MIBK:IPA solution for 30 s, rinsed in IPA and blown dry with N_2. The sample was then subject to 8 s of O_2 plasma to descum the lithographic features prior to evaporation of 10 nm of a titanium adhesion layer followed by a 90 nm gold layer using the AJA ATC-Orion electron beam evaporation chamber. The wafer was soaked in N-methyl-2-pyrrolidone at 80 $^{\circ}C$ for 15 $mins$ under subtle agitation for liftoff. The HSQ trench pattern was written using the NFD JEOL JBX-9300FS electron beam lithography system with an acceleration voltage of 100 kV and a dose of 1400 $\mu C/cm^2$, and was developed with CD26 for 3 $mins$, rinsed in DI water and blown dry with N_2. Alignment marks were used to orient the topographic features in HSQ relative to the interdigitated electrodes.

PS-r-P2VP with mono-hydroxide end group functionalization was synthesized by varying compositions of styrene and 2-vinylpyridine via nitroxide-mediated controlled radical polymerization (NMP). A representative polymerization procedure is described for the synthesis of copolymer as follows: A mixture of OH-modified initiator, styrene and 2-vinylpyridine was degassed through three freeze-thaw cycles. The mixture was heated at 160 $\circ C$ for 72 hours under a N_2 atmosphere. Conversion of both styrene and 2vinylpyridine in the random copolymerization was determined to be greater than 95 % in all cases. The resulting copolymers were dissolved in THF and precipitated in hexanes. The Mn of the terminal-OH copolymers were in the range of 2000-7500 $gmol^{-1}$, with a polydispersity index values of 1.2-1.6. The fraction of PS was determined by 1H NMR spectroscopy.

4.3.2 Device Fabrication

The schematic for the fabrication of devices is shown in Figure 4.2. Gold interdigitated electrodes (IDEs) were fabricated on top of a silicon wafer with a 1 μm thick thermally grown oxide. 90 nm thick gold with a 10 nm Ti adhesion layer were deposited and patterned using ebeam lithography and liftoff techniques. The resulting IDE features 1 μm wide electrode teeth that overlap counter electrodes by 20 μm with a 1 μm separation distance. The teeth

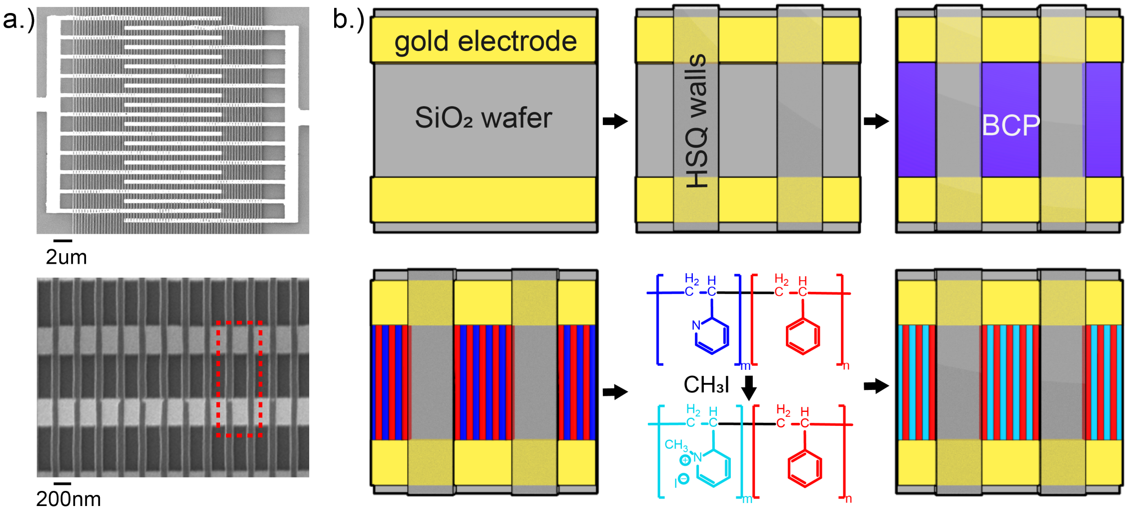

Figure 4.2: Schematic and results showing the fabrication and assembly processes for the graphoepitaxy interdigitated electrodes and the BCE. a.) SEM micrographs of the interdigitated electrodes with the gold electrodes appearing as the bright horizontal bars and the HSQ guiding topography as vertical stripes that form 200 nm by 1 μm trenches (single trench highlighted by a red box). b.) Fabrication schematic where the device is fabricated on a 1 μm thick SiO_2 substrate (top to bottom, left to right).

are arranged in an alternating sequence with each electrode going to one of the large contact pads for a total of 40 electrode teeth per pole. Following the fabrication of the IDE, 80 nm thick hydrogen silsesquioxane (HSQ) resist was cast on top of the IDE and patterned using electron beam (ebeam) lithography. The resulting HSQ structure formed rectangular grating structures perpendicular to the electrode axis consisting of 200 nm trenches on a 400 nm pitch as shown in Figure 4.2a. The HSQ grating and the gold electrodes formed elevated walls creating 200 nm by 1 μm isolating trenches where the polymer could be confined and manipulated into different morphologies. Precisely 3950 identical trenches were fabricated on each IDE for polymer confinement.

The substrate, HSQ features, and electrodes were modified with polymer brushes at different stages during the fabrication process to induce the formation of three distinct BCE structures. Next, a film of lamellar-forming polystyrene-block-poly(2-vinyl pyridine) (PS-b-P2VP) was spin coated onto the IDEs, solvent annealed in acetone, and dried such that all the polymer in the device area was confined in the trenches formed by the gold and the HSQ walls. The phase separated BCP film was then functionalized to become a BCE by exposing the film to methyl iodide (MeI) vapor for 24 h. As reported previously under these conditions, approximately 50 % of the P2VP repeat units were functionalized with a fixed quaternary ammonium cation (NMP+) and a free iodide anion (I-). The BCE film was subsequently equilibrated in an environment with 95 % relative humidity (95 %RH) at 25 $^{\circ}C$ for 6 hrs. The absorbed water dissociates the iodide from the cation and plasticizes the P2VP/NMP+ I- domain such that the Tg of the conducting blocks are below room temperature. The samples were characterized using AC Electrochemical Impedance Spectroscopy (EIS) with a range of frequencies from 1 MHz to 0.1 Hz with a perturbation voltage of 10 mV.

Control of morphology in the nanoscale trenches. The substrate, HSQ features, and the gold electrodes were grafted or physiosorbed with hydroxyl-terminated (P(S-r-2VP)-OH) brushes. The brushes were deposited by spin coating a film of P(S-r-2VP)-OH (1 wt% dissolved in Toluene), annealing at 200 $^{\circ}C$ for 2 h, rinsing away the excess by soaking in a Toluene bath at 60 $^{\circ}C$ with periodic stirring by hand, rinsed in IPA, then blown dry with N_2.[24]

The morphology of the BCE films after deposition, annealing, and functionalization on the device depended on the engineered boundary conditions of the trenches within the IDEs. The SiO_2 substrate, the HSQ side walls, and the gold surfaces [25] without chemical modification are all preferentially wet by one block of the BCP. PS preferentially wetted the HSQ and the gold surfaces, while P2VP preferentially wetted the bare SiO_2 substrate. The substrate, HSQ walls, and the gold surfaces were chemically modified at different stages of the fabrication process to be non-preferential in wetting towards the BCP by grafting or physisorbing hydroxyl-terminated poly(styrene-rand-2-vinyl pyridine) (P(S-r-2VP)-OH) brushes.[24] Under conditions in which a P(S-r-2VP)-OH brush was deposited onto the substrate prior to the fabrication of the HSQ guiding lines, and the monomeric mole fraction of PS in the brush was 0.685, graphoepitaxial assembly of the BCP occurred in the trenches with preferential wetting of the HSQ sidewalls, neutral (SiO_2-brush) bottom surfaces, and neutral (gold) sidewalls. With these boundary conditions, the BCP domains assembled perpendicular to the substrate and uniformly parallel to the HSQ walls, with each domain forming a straight and continuous pathway between pairs of electrodes (Figure 4.3a). In this morphology, 7 natural periodicities of PS-b-P2VP/NMP+ I- were assembled parallel to the HSQ walls. In our previous work,[26] we extracted the periodicity of the BCP to be 28 nm. Therefore, in an unconfined film, the 7 periods in parallel would result in a film width of 196 nm, which is consistent with the separation distance between the two HSQ walls. This morphology will be referred to as the 'connected' structure. Second, samples were fabricated after depositing a different P(S-r-2VP)-OH brush that was weakly preferential to P2VP (monomeric mole fraction of PS in the brush equal to 0.48) on all surfaces of the devices after the HSQ fabrication. Under these conditions, the BCP domains assembled perpendicular to the substrate but in a fingerprint pattern in the plane of the film (Figure 4.3b). This morphology will be referred to as the 'partially connected' structure. Finally, when the neutral P(S-r-2VP)-OH brush was deposited after the HSQ fabrication, all surfaces of the confining trenches were non-preferential in wetting towards the copolymer. Under these boundary conditions, the BCP domains assembled perpendicular to the substrate, perpendicular to the gold electrodes, and perpendicular to the HSQ walls. Due to the aspect ratio, there was a section in the middle of the trenches over which the lamellae spanned from one HSQ wall to the other, with no domains forming pathways between electrodes (see Figure 4.3c). This morphology will be referred to as the 'unconnected' structure. Representative SEM images are shown in Figure 4.3d and connected domains from one electrode (top to bottom) to another in the images are identified and labeled in blue.

Two additional types of samples were prepared to compare and contrast with the results of the controlled morphologies. For the first sample, a P2VP homopolymer of comparable molecular weight to the P2VP block of the BCP (Mn = 22,000 $gmol^{-1}$) was deposited on the IDE with the HSQ features, annealed, and functionalized under identical protocols to

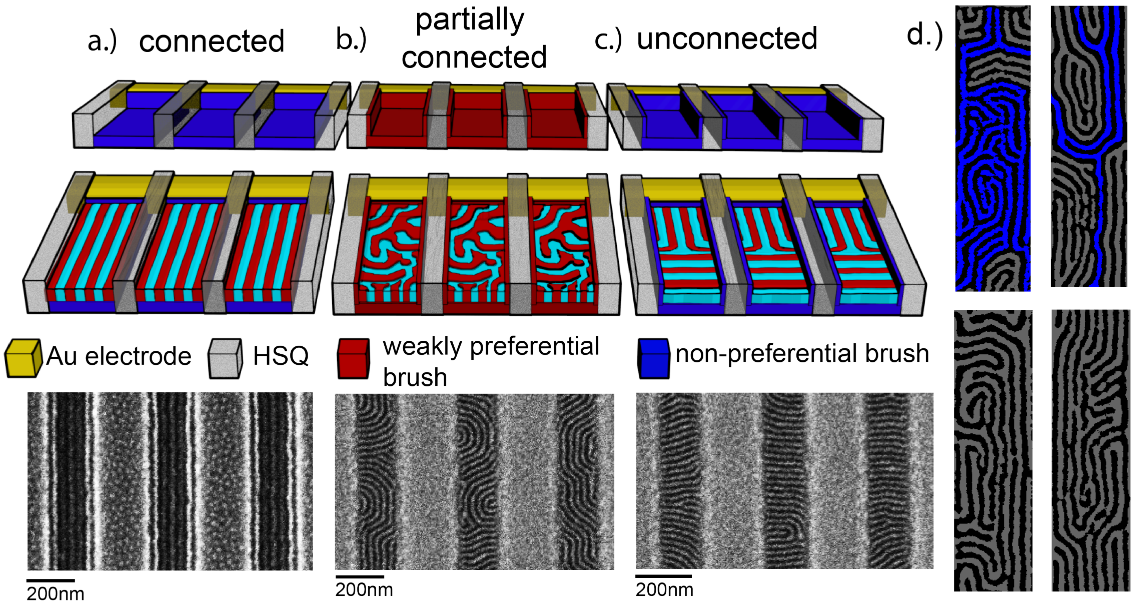

Figure 4.3: Orientation of the PS-b-P2VP domains relative to the HSQ guiding stripes and the electrodes that form the individual trenches. Schematic and SEM micrograph of a.) connected structure b.) partially connected, c.) unconnected orientation. d.) Partially connected morphology SEM micrographs after image flattening and path identification where disconnected paths are labeled grey and the connected domains are labeled blue.

the BCE. This sample will be referred as the 'homopolymer' sample. For the second sample, the HSQ grating features were not fabricated on top of the IDE. P(S-r-2VP)-OH brush was deposited over the entire surface to form a uniformly non-preferential substrate. Then the BCP was deposited, annealed, and functionalized to form a morphology that will be referred to as the 'fingerprint' structure.

4.3.3 Thickness Change

The thickness change of the BCP thickness was determined by spin coating a 42 nm thick BCP film on top of a Si wafer. The film was annealed inside of a nitrogen glove box at 250 $\circ C$ for 10 $mins$. The resulting film was placed inside of a jar with MeI solution and functionalized for 24 hours. The resulting film was placed in a vacuum desiccator for 2 days prior to being immediately measured on the ellipsometer. The same film was then placed inside of the relative humidity chamber and conditioned at 25 $\circ C$ and 95 $\% RH$ for 24 hour prior to being taken out and immediately measured via ellipsometer. The PS-b-P2VP annealed film was measured at 42 nm, the methylated PS-b-P2VP/NMP+ I- at 0 $\%RH$ condition was measured to be 47.75 nm, and the fully hydrated film was measured to be 49.81 nm. The volume fraction of the hydrated film was determined by taking the equation below:

$$volfraction = \frac{t - t_{PS}}{t} \tag{4.2}$$

Where t is the measured thickness and t_PS is the thickness of the PS domain, determined to be 21 nm. The resulting hydrated thickness is determined to be approximately 58 $vol\%$. This volume change has also been observed through SEM in perpendicular lamellae films of the PS-b-P2VP/NMP+ I- in our previous work.[26]

4.3.4 Solvent Vapor Annealing

Solvent vapor annealing (SVA) in acetone was used to phase separate the PS-b-P2VP BCP prior to the conversion of the P2VP domain into P2VP/NMP+ I-. SVA was chosen in particular for this application because PS-b-P2VP can easily form thin film morphologies where the domains align perpendicular to the substrate surface as well as the free interface (e.g. interface that is exposed to the environment). The Nitrogen flows from the house nitrogen inlet through the lettered sections in sequence. The samples are placed in the main chamber e and closed. The sample is conditioned under 93 $sccm$ of dry N_2 for 10 mins prior to swelling. 31 $sccm$ of acetone saturated N_2 gas and 62 $sccm$ of dry nitrogen are flown together into the film for 5 $mins$, then 62 $sccm$ of actone vapor and 31 $sccm$ of dry for 5 min, then 90 $sccm$ of acetone vapor and 3 $sccm$ of dry N_2 for 2 hrs. At the end of 2 hrs, the system is immediately purged with 390 $sccm$ of dry N_2 to vitrify the assembled morphology. The sample is kept under 390 $sccm$ for 15 $mins$ prior to removing the sample.

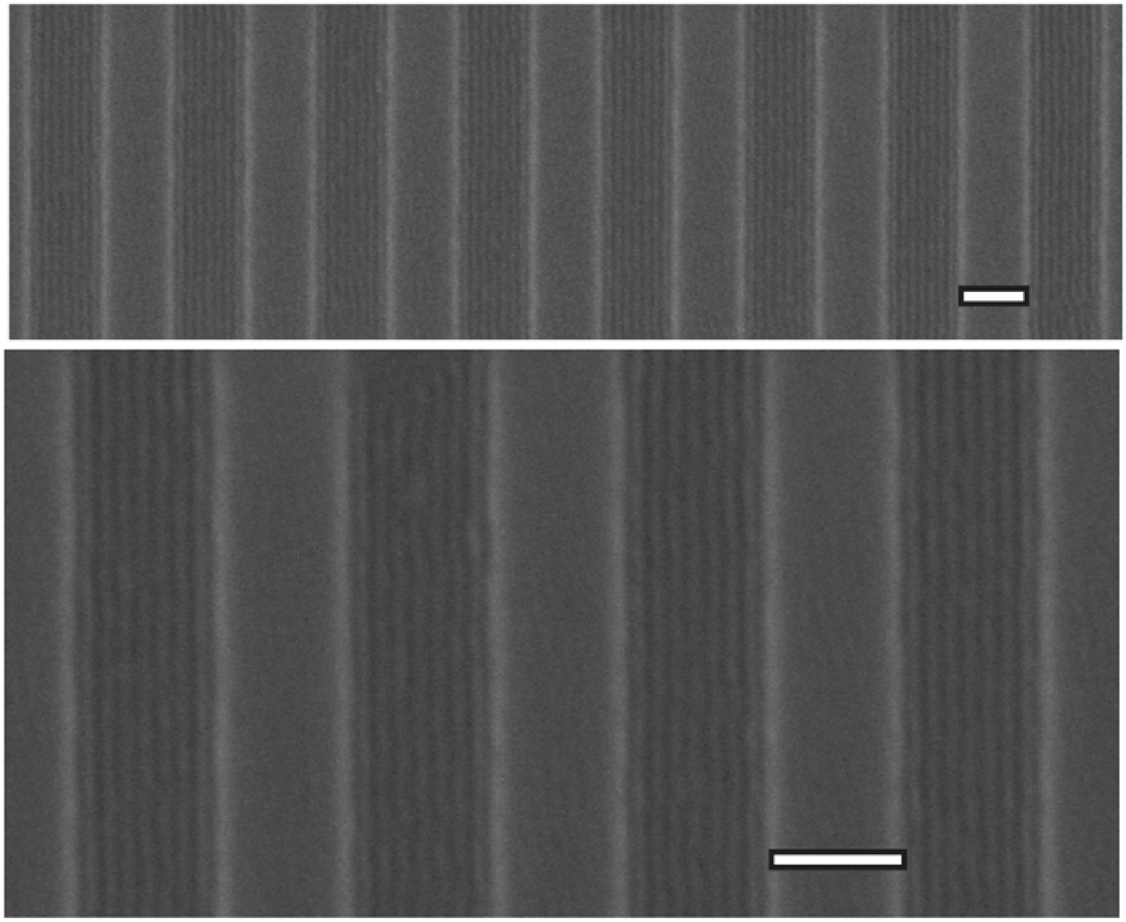

Figure 4.4: SEM image of the DSA. Scale is 200 nm.

4.3.5 Characterization

Top-down SEM images of the self-assembled BCE films were taken with the Carl Zeiss - Merlin field emission scanning electron microscope. The acceleration voltage was 1.0 kV with a working distance of 3 to 4 mm using an in-lens detector. 1 nm of Pt/Pd was sputtered onto the surface of the device using the Cressington 108 Auto Sputter Coater to reduce electron beam charging and improve the image quality. The unprocessed connected SEM image is shown in Figure 4.4.

Image processing of the lamellar structure was done via a visual Python analysis code in Figure 4.5. Raw SEM images were processed in python using the SciPy toolkit.[27] The original image is imported into a 2D array and the SEM metadata read to retrieve scale. The image can then be manually cropped or automatically cropped to isolate the active device area. Once cropped the image is denoised with a total variation algorithm as implemented in Scikit Image, which preserves edge information while removing most of the imaging noise.[28] This image is than locally thresholded to create a binary image of PS and P2VP domains. Any cluster of white (1) or black (0) pixels smaller than ten pixels is then identified and flipped to remove any remaining noise that may be present. This removal of small objects was often found not to be necessary but was kept across all images for consistency. At this point each separate foreground (white) domain is identified and. If an index of a domain exists at both the top and bottom of the active device area than it is considered a connected domain. Each pixel which matches the label of one of these connected domains is then colored blue to create the final image.

The electrochemical properties of the samples were probed using the Gamry reference 600 potentiostat AC electrochemical impedance spectroscopy (EIS). EIS measurements were made from 1 MHz to 1 Hz [29–31] by connecting the IDEs to larger 2-probe contact pads wired to the potentiostat/galvanostat. The measurements were made in a chamber with controlled temperature (25 $°C$) and relative humidity (95$\%RH$) after an equilibration period of at least 24 h. Humidity-controlled testing at 25 $°C$ and 95$\%RH$ eliminates undesired condensation of water at the interfaces but hydrates the P2VP/NMP+ I-) domains, enabling iodide transport at a common device operating condition. The resulting raw data is plotted in Figure 4.6

An equivalent circuit model with the elements representing material and device properties to capture the essential physics of the system was used to derive the resistance and capacitance values related to the transport of ions in the polymer films from the EIS data. Recently Sharon et al[32] reported on the conditions and system parameters for which the IDEs and circuit model yield quantitative material transport properties for ion conducting polymer films. The model is comprised only of circuit elements that have physical manifestations in the charge transport in the IDE configuration. In this study, the model consists of

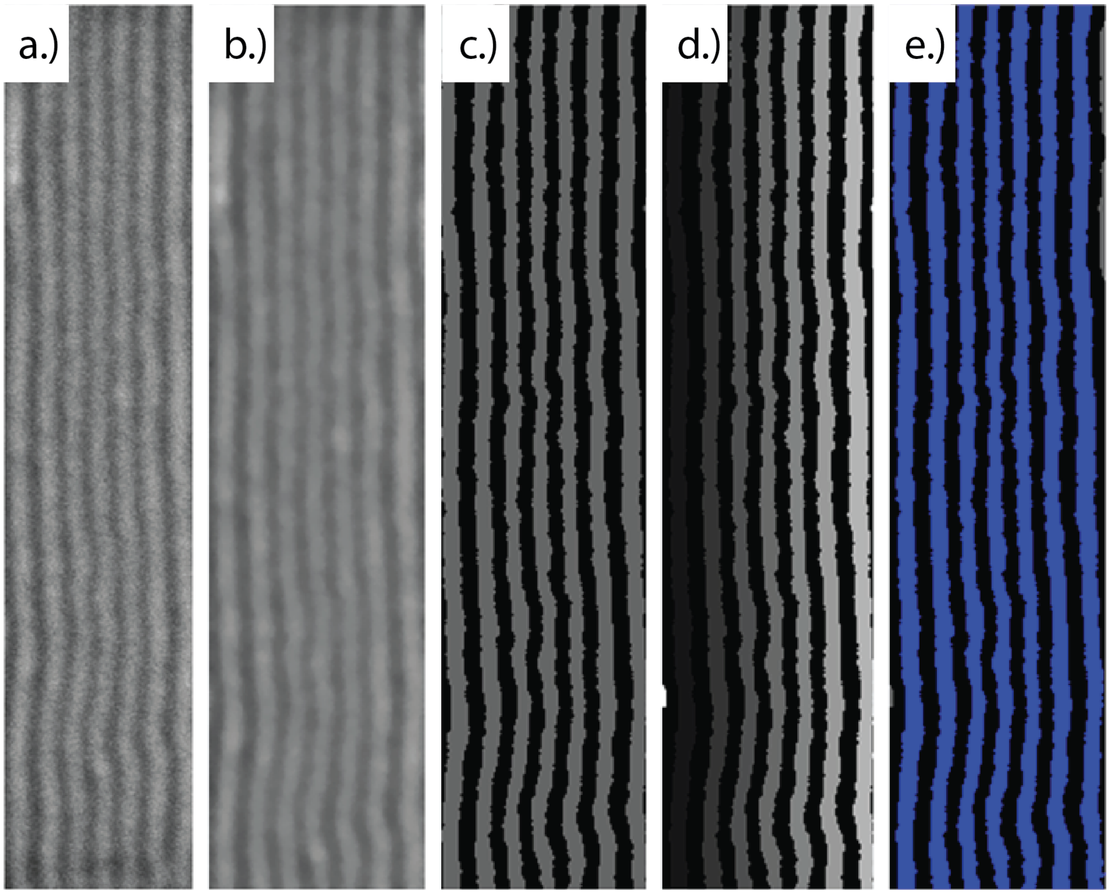

Figure 4.5: Quantification of structure parameters. a.) original SEM image b.) denoised image c.) threshold image d.) labeled image e.) interconnected domains which span from one electrode to the other.

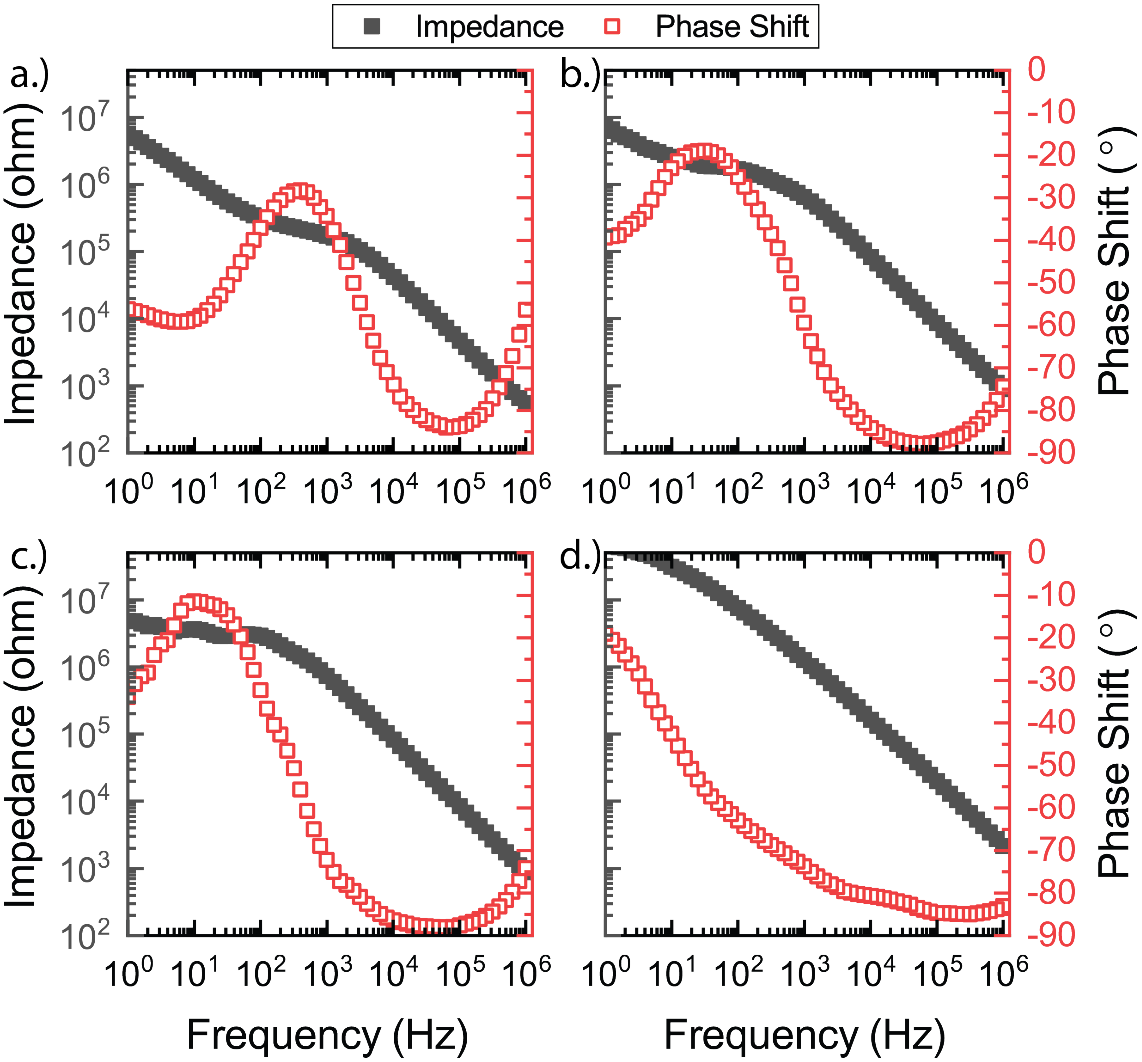

Figure 4.6: Bode plots for a.) connected b.) partially connected c.) fingerprint and d.) unconnected.

resistors (R) and constant phase elements (CPE) in the setup shown in Figure 4.7a: $Rfilm$ and $CPEfilm$ capture the resistance and capacitance behavior of the polymeric material between the electrodes, respectively, $CPEdl$ models the ion depletion double-layer capacitances at the polymer-electrode interface, $CPESiO2$ represents the capacitance of the $SiO2$ substrate, and $Relectrode$ models the electrode resistance. Conductivity (σ) of the polymer was calculated using from the value of $Rfilm$ using the following equation:

$$\sigma = \frac{d}{R_{film}Lt(N-1)} \tag{4.3}$$

where N is the number of electrode teeth in the interdigitated array, t is the film thickness of the polymer in the trench, d is the separation distance between the edges of electrodes, and L is the length of overlap between adjacent electrodes for the polymer, not including the areas occupied by the HSQ. The capacitance (C) of the polymer film was calculated from the values of the CPE_{film} by using the following equation:

$$C = \frac{(R_{film}Q^{-1})^{1/a}}{R_{film}} \tag{4.4}$$

where Q and a are the fitting parameters of the CPE_{film}. The unit of the Q is $S * s^{\alpha}$. Note that CPE_s are used instead of pure capacitance elements in the circuit model to improve the fit to the data. However, all values of a from modeling the EIS data were above 0.8, indicating that CPE_{film} was behaving as, and can be interpreted as, a near pure capacitor element. Figure 4.7a provides representative electrochemical data (scatter plot) in the form of a Nyquist plot and the fit (solid line) for the BCE with the partially connected structure. The values used for the calculation of the σ and C are tabulated in Table 4.1.

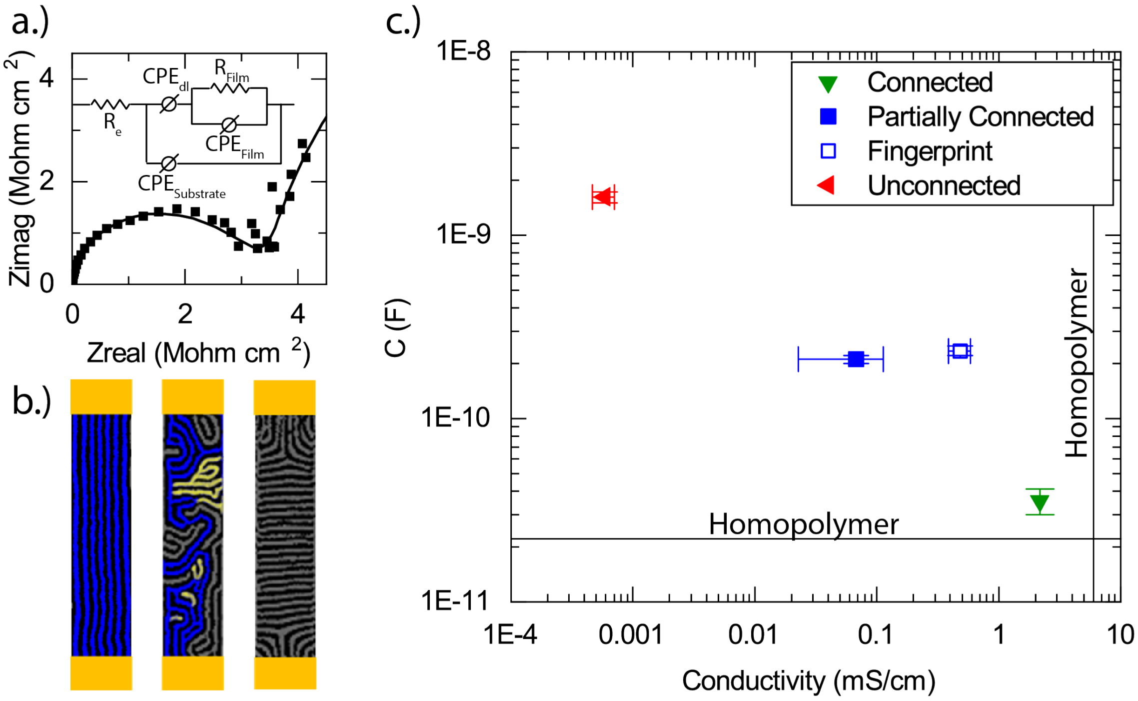

Figure 4.7: SEM and EIS results correlating the ion conduction pathways to electrochemical behavior. a.) Multivariable fit of EIS data for the connected structure using a custom equivalent circuit diagram to simulate the charge transport pathway. b.) Analyzed SEM micrographs of ion conduction pathways (percolated paths labeled in blue with non-participating sections in yellow) in segmented HSQ trenches showing (left to right) connected, partially connected (confined), and disconnected orientations. c.) Calculated capacitance and conductivity for each structure orientation with performance limitations for the PS-b-P2VP/NMP+ I- system (solid lines) calculated from the homopolymer conductivity and capacity values.

	Units	Connected	Partially Connected	Fingerprint	Unconfined
R_e	ohm	191.4	200	5.78E-01	4.11E-03
Q_{DL}	Ss^{α} $[Siemenssec^{\alpha}]$	6.36E-09	2.75E-08	4.87E-08	4.16E-10
α_{DL}	-	6.94E-01	9.66E-01	6.85E-01	9.00E-01
Q_{FILM}	Ss^{α} $[Siemenssec^{\alpha}]$	3.57E-11	2.30E-10	2.34E-10	1.27E-09
α_{FILM}	ohm	1	9.86E-01	1	8.97E-01
R_{FILM}	ohm	2.63E+05	5.33E+06	1.57E+06	6.32E+09
$Q_{Substrate}$	Ss^{α} $[Siemenssec^{\alpha}]$	1.63E-10	5.36E-08	4.81E-12	1.05E-08
$\alpha_{Substrate}$	-	1	1.65E-01	1	1.86E-01
Thickness (t)	nm	20	16	34	33

Table 4.1: Values extracted from the bode and Nyquist plots.

4.4 Results and Discussion

4.4.1 Conductivity and C Dependence on Morphology

The electrochemical behavior of BCEs in the EIS experiments showed marked differences as a function of structure. A log-log plot of the values of σ and C derived from the EIS data for the connected, disconnected, and partially connected BCE structures is shown in Figure 4.7c and the values used in the Figure are shown in Table 4.2. The solid lines also shown in Figure 4.7c are the σ_{homo} and C_{homo} values for the homopolymer that correspond to the electrochemically active block of the BCEs. Several features in the log-log plot stand out. First, the σ of the homopolymer and the connected structure are relatively high, 2 to 6 mS/cm, and C of the homopolymer and the connected structure are relatively low, $3x10^{-11}$ F. For comparison, hydrated Nafion 117 has a conductivity of 79 mS/cm and a capacitance of $9x10^{-10}$ F when conditioned at 25 $^{\circ}C$ and 95 $\%RH$.[33] Second, σ_{BCE} of the unconnected structure was four orders of magnitude smaller than σ_{BCE} of the connected structure or σ_{homo}, so it was negligible in comparison. The fact that there is no conductivity when there are no domains connecting the electrodes highlights the integrity of the samples and experimental procedures. There are no unanticipated or unwanted pathways for conduction in the samples, such as through a layer of swollen polymer on the surface, through a layer

	Conductivity (mS/cm)	Capacitance (pF)
Connected	2.2 (±0.2)	36 (±6)
Fingerprint	0.5 (±0.1)	234 (±14)
Partially Connected	0.07 (±0.05)	210 (±10)
Unconnected	0.0006 (±0.0001)	1613 (±113)
Homopolymer	6 (±1)	25 (±5)

Table 4.2: Calculated conductivity and capacitance data.

of condensation of the surface, through the brush materials, or through the underlying substrate. Third, the capacitance of the unconnected structure was a factor of 50 higher than the connected structure, indicating the presence of trapped charge. Fourth, the values of the σ_{BCE} and the C of the partially connected structure were intermediate between the connected and unconnected structures, suggesting that σ_{BCE} is proportional to the number of connected domains, and that C was proportional to the number of isolated domains, dead ends, or ion trapping defects. Fifth, the σ_{BCE} value of the fingerprint structure was a factor 7 larger than the partially connected film while the C stayed about the same. This suggests that there are more conduction pathways in the fingerprint structure, but there is still a significant volume of 'dead' paths. The electrochemical structure-transport properties of the BCE films are discussed in quantitative fashion below.

It is important to note that the absolute conductivity and capacitance values of the connected morphology are close but not equal to the values of the homopolymer. The ability to probe a fully connected structure allows us to decouple and independently characterize the parameters f and ϕ_{cond} in the EMT (Equation 1). Using experimental values of σ_{homo} and σ_{BCE} equal to 6 mS/cm and 2.2 mS/cm (see Table 4.2), and $f = 1$ in Equation 1, ϕ_{cond} of the connected structure is calculated to be 0.37, a value substantially lower than the estimated volume fraction of the hydrated P2VP/NMP+ I- in the BCE of 0.58. Unlike the P2VP/NMP+ I- homopolymer, the PS-b-P2VP/NMP+ I- BCE contains domain interfaces with PS over which the P2VP/NMP+ I- and PS are mixed over the length scale of a few nanometers.[34] P2VP/NMP+ I- in the interfacial regions does not likely contribute to conductivity due to the presence of even small concentrations of PS. The mechanisms by which PS may reduce the conductivity when mixed with P2VP/NMP+ I- include: 1) a reduction of local charge carrier concentration due to the hydrophobic PS lowering the local hydration levels, 2) a reduction in ionic mobility due to slower segmental dynamics of P2VP/NMP+ I- near the interface with glassy PS, or 3) a reduction in ion hopping probability due to the dilution of active sites by the PS. The mechanisms for reduced conductivity near the interface of conducting rubbery and non-conducting glassy domains have been reported previously for the PS-b-PEO system.[35, 36]

The volume fraction of the conducting domain is related to the conductivity of the BCE and the homopolymer through EMT Equation:

$$\sigma_{BCE} = f\phi_{COND}\sigma_{homopolymer} \tag{4.5}$$

Where σ_{BCE} is the conductivity of the BCE, f is the structure factor associated to tortuosity, ϕ_{COND} is the conducting volume fraction of the BCE, and $\sigma_{homopolymer}$ is the conductivity of the homopolymer.

In the connected film, the ion conduction pathway is direct and fully connected, hence f=1. When f=1, Equation 4.5 can be rearranged into the form:

$$\phi_{COND} = \frac{\sigma_{BCE}}{\sigma_{HOMO}} \tag{4.6}$$

Using the values 2.2 mS/cm and 6 mS/cm for σ_{BCE} and σ_{COND} respectively, ϕ_{COND} is calculated to be 0.37. The width of the P2VP/NMP+ I- domain normal to the interface not contributing to ion transport (w) with the unit of nm was calculated by taking the difference in the P2VP/NMP+ I- fraction assessed using SEM micrographs and ϕ_{COND} and multiplying the difference by the periodicity of the BCE. The equation is shown as below:

$$w = \phi_r L_0 - \phi_{COND} L_0 \tag{4.7}$$

Where ϕ_r is the volume fraction of the P2VP/NMP+ I- domain determined from direct observation to be 0.58, and L_0 is the domain width of the PS-b-P2VP/NMP+ I- previously determined to be 28 nm,[26] and ϕ_r assumes that the P2VP/NMP+ I- domain is not affected by the PS concentration. Using the values stated, the w value is calculated to be 3 nm, a value consistent with the width of the interface in block copolymer theory calculated using the Flory Huggins interaction parameter χ. Additionally, the value of the capacitance derived from the EIS data for the connected film (2.83 nF) is close to that of the homopolymer (2.5 nF) but slightly higher. We attribute this increased capacitance to impeded transport of ions near domain interfaces where the P2VP/NMP+ I- is non-conductive.

4.4.2 Conductivity Dependence on Number of Connected Domains and Length of Path

A comparison between defect-free connected and defect containing partially connected structures allows for analysis of the role of defects and grain boundaries on BCE transport properties. Because the state of the hydrated P2VP/NMP+ I- domains of fully microphase-separated BCE films are all equivalent at the same temperature and relative humidity, quantitative comparisons of conductivities and structure are possible between all of our samples with fully formed lamellae morphologies. σ_{BCE} of the BCE with a connected structure was 31-fold higher than σ_{BCE} of the BCE with a confined, partially connected morphology (2.2 versus 0.07 mS/cm). The lower σ_{BCE} observed in the partially connected BCE films could be fully accounted for by taking into account two structural differences between the samples: 1) the number of P2VP/NMP+ I- domains that are connected from one electrode to the other, and 2) the tortuosity (distance traveled between electrodes) of the connected domains.

The quantitative analysis was made using the equation:

$$\sigma_{pc,eff} = \frac{m_{pc}}{m_c}\frac{l_c}{l_{pc}}\sigma_c \tag{4.8}$$

Where $\sigma_{pc,eff}$ is the estimated effective conductivity of the partially connected morphology based on the assumptions above, σ_c is the conductivity of the connected morphology, m_{pc} is the total number of connected paths for the partially connected morphology, m_c is the total number of connected paths for the connected morphology, l_{pc} is the average length of the conduction path for the partially connected morphology and l_c is the average length of the conduction path for the connected morphology. Note: the derivation of Equation 4.8 is shown in the following sub-section.

The values of m_{pc}, m_c, l_{pc}, and l_c were determined by inspecting and performing image analysis on scanning electron micrographs of 1000 trenches in selected samples and counting and averaging the total number of connected pathways and the increase in the transport pathlength due to increased tortuosity. The statistics for the analysis are recorded in Figure 4.8. We determined m_c to be 27650 connected paths by counting a total of 7 connected paths per trench and multiplying by 3950, the total number of trenches. Next, m_{pc} was determined by identifying and counting the connected paths in 1000 randomly selected trenches. Image analysis showed only 300 of 1000 trenches had connected pathways, and the vast majority of the 300 trenches contained only a single connected path. The trenches with zero connected paths were similar in morphology, but every P2VP/NMP+ I- channel was blocked by at least one PS domain barrier. The analysis of one trench shown in Figure 4.7d illustrates by example how we determined the number of pathways per trench if a connection existed. The number of connected pathways per trench was determined at the bottleneck where the ion transport would be gated. For an example, the partially connected BCE structure analyzed in Figure 4.7d had seven separate ion conduction paths that make contact with the electrode. However, at the cross section with the smallest number of connected channels (i.e., the middle of the film), only a single channel is highlighted in blue. Therefore, this trench was determined to contain only one connected path out of seven. Additional examples of partially

	Units	Connected	Partially Connected	Unconnected
m	-	27650	1185	0
l	μm	1	1.4	-
s	mS/cm	2.2	0.067	0

connected morphologies are shown in Figure 4.3d and the compiled count of trenches with specific number of connected domains is shown in Figure 4.8a. The m_{pc} value of 1185 was calculated by multiplying the fraction of connected trenches (300/1000) by the total number of trenches (3950) where each trench contained only one connected path. The conduction pathlengths l_{pc} and l_c were determined by tracing the shortest connected path from one electrode to the other on the SEM image and determining the length of the traced line using ImageJ graphic analysis software. The conduction pathways identified in the partially connected structure were more tortuous in comparison to the connected structure. The distribution of trenches with specific lengths of connected paths are shown in Figure 4.8b. Due to the higher tortuosity, the connected pathways in the partially connected morphology were measured to have a l_{pc} of 1.4 μm. l_c the connected morphology is simply the separation distance of the electrodes in the IDE, namely 1 μm. Using the values of m_{pc}, m_c, l_{pc}, and l_c in equation 4, and testing the hypothesis that σ is proportional to the number of paths and inversely proportional to the path length, we estimate σ_{pc} to be 0.067 mS/cm, a value that compares very favorably with the experimentally determined value of 0.07 ± 0.05 mS/cm. The values are tabulated in Table 1. Using Equation 4.8, the unconnected morphology would have an m value of zero, resulting in a calculated conductivity of zero.

4.4.3 Derivation of Equation 4.8 - Linear Scaling of Conductivity and Number of Connected Paths

In the discussion, we successfully use structure arguments alone to predict the ion conductivity of the partially connected morphology. In this calculation, we make an assumption that the conductance linearly scales with the total number of ion-conducting domains. We can verify this approximation by first considering each independent ion conduction path as a resistor. Each connected path begins at one electrode and ends at the counter electrode, hence the ion conduction paths can be considered to be ion conduction pathways in parallel. The overall resistance of the film therefore can be calculated by taking the equation:

$$\frac{1}{R_{film}} = \frac{1}{R_{singlepath,1}} + \frac{1}{R_{singlepath,2}} + \frac{1}{R_{singlepath,3}} + = \sum_{n=1}^{n=n_total} \frac{1}{R_{singlepath,n}} \tag{4.9}$$

Where the R_{film} is the total resistance of the measured film and $R_{singlepath,n}$ is the resistance of each specific pathway.

We will now take the model of the connected morphology. If we assume that the resistance of each domain is the same, then the equation simplifies to:

$$1/R_{film} = n/R_{singlepath} \tag{4.10}$$

Where n is the total number of connected pathways. Without taking into account the changes in ion conduction path, it is possible to consider that the inverse resistance of the partially connected path scales linearly to the number of connected pathways. The prediction of the partially connected pathway was done with conductivity values because conductance is inversely related to resistance. Therefore, the conductance of the film is related to the conductance of individual paths and the total number of connected paths through the modification of the above equation into:

$$G_{film} = nG_{singlepath} \tag{4.11}$$

Where G_{film} is the conductance of the total film and $G_{singlepath}$ is the conductance of an individual conduction path. This form is modified to take into account that each path is not the same conduction due to variations in path length.

$$G_{film} = \sum_{n=1}^{n=n_{total}} G_{singlepath,n} \tag{4.12}$$

In the partially connected film, the conductance value of a single path is lower in comparison to the conductance of the single path of the connected morphology due to the due to the increased path length. Assuming conductivity scales linearly with the path length regardless of tortuosity, the $G_{singlepath,pc}$, i.e. the conductivity of the single path of a partially connected film, can be calculated by using the equation:

$$G_{singlepath,pc} = \frac{l_c}{l_{pc}} G_{singlepath,c} \tag{4.13}$$

Where $G_{singlepath,c}$ is the conductance of a single path in the connected film, l_c is the length of the path in the connected film, and l_{pc} is the length of the connected path of the partially connected film. Therefore the conductance of the partially connected film is related to $G_{singlepath,c}$ by the equation:

$$G_{pc} = \sum_{n=1}^{n=n_{total}} \frac{l_c}{l_{pc}} G_{singlepath,c} \tag{4.14}$$

Where G_{pc} is the conductance of the partially connected film. To simplify the input parameters for this work, the equation is simplified by 1.) replacing $G_{singlepath,c}$ with $\frac{G_c}{m_c}$ and 2.) assuming that all of the connected pathways of the partially connected film have a similar length. With these assumptions, the equation becomes:

$$G_{pc} = m_{pc} \frac{l_c}{l_{pc}} \frac{G_c}{m_c} \tag{4.15}$$

Where m_c is the number of connected domains in the connected film and m_{pc} is the number of connected domains in the partially connected film. Rearranging the equation, one arrives at:

$$G_{pc} = \frac{m_{pc}}{m_c}\frac{l_c}{l_{pc}}G_c \tag{4.16}$$

Conductivity is calculated from conductance using the equation:

$$\sigma = \frac{Gd}{A} \tag{4.17}$$

Where d is the distance between electrodes and A is the cross-sectional area of the film. Assuming these geometric parameters are identical for the connected and partially connected films, the conductivity of the partially connected film σ_{pc} can be calculated from the conductivity of the connected film σ_c using the equation:

$$\sigma_{pc} = \frac{m_{pc}}{m_c}\frac{l_c}{l_{pc}}\sigma_c \tag{4.18}$$

4.4.4 Capacitance

The capacitance value from the equivalent circuit model can provide valuable structural information that is complementary to that derived from the conductivity analysis. Whereas the connected structure has very small differences in capacitance from that of the homopolymer, the partially connected morphology has a capacitance that is higher by an order of magnitude. This suggests that substantial charge accumulation occurs in the defective structures of the partially connected films. Defect structures that exist in the partially connected domains include 1) dead ends of connected ion conduction paths (colorized yellow in Figure 4.7b) and 2) disconnected ion conduction pathways (colorized grey in Figure 4.7b). Furthermore, the value of the capacitance for the unconnected morphology, with the highest number of disconnected domains, was higher by an order of magnitude compared to the partially connected morphology. From this comparison, we can speculate that values of the capacitance derived from the EIS data are a measure of the relative volume fractions of material that are 'dead' to transport due to defects and grain boundaries. In this sense, reporting the capacitance and

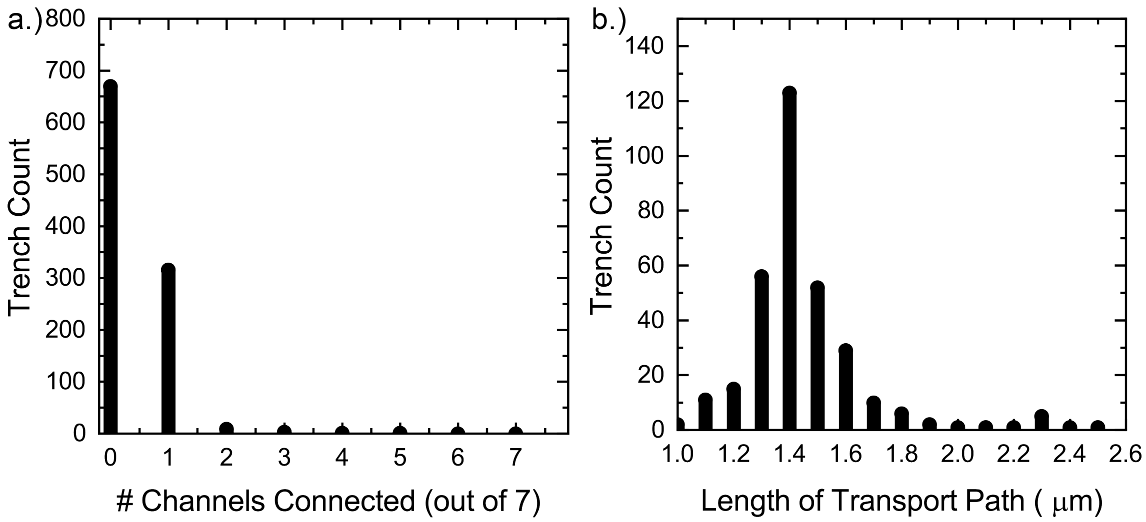

Figure 4.8: Extracted structure data of the partially connected morphology using visual analysis software showing a.) the total number of connected conduction paths where the total number of conduction channels is at a bottleneck, and b.) the total number of trenches as a function of the length of the conduction pathway.

looking for order of magnitude differences between homopolymer and nanostructured samples may be a useful tool to estimate the relative magnitude that structure and processing is playing in bulk measurements for which structure cannot be determined independently.

4.4.5 Understanding Three Dimensional Defects Using Thin Film Morphologies

To further explore the properties of defect structures, and to take a small step from the confined two-dimensional structures presented above towards more three-dimensional structures, (or at least unconfined two-dimensional structures) we also investigated BCE films with fingerprint lamella patterns on the IDEs without the confining HSQ guiding topography. The σ_{BCE} of the fingerprint structure was found to be a factor of 7 higher than the σ_{BCE} of the partially connected structure (0.5 versus 0.07 mS/cm), whereas the capacitance remained almost constant. The 7-fold increase in σ_{BCE} suggests that the fingerprint structure without the guiding topography provided more connected pathways between the electrodes, perhaps with longer more tortuous routes than were possible when confined by the HSQ guides. The σ_{BCE} of the fingerprint structure was also only an order of magnitude lower than σBCE (0.5 versus 6 mS/cm), and this difference is expected to decrease further upon moving to a fully three-dimensional domain structure for which there are additional pathways to circumvent defects. The fact that the capacitance was equivalent between the two samples, and much higher than the capacitance of the connected structure or homopolymer, suggests that despite more pathways, there is still a significant fraction of the fingerprint films that did not contribute to the σ_{BCE}. An analogous observation has been reported by Diederichsen et al[37] who studied electron transport in fingerprint BCP morphology templated gold nanowires. A discrete fraction of disconnected domains can reduce the conductivity by increasing tortuosity of connected paths and limiting the conductive volume.

4.5 Conclusion

In conclusion, the use of thin films and IDEs allowed for quantitative determination of structure property relationships in BCEs. Defects and grain boundaries often create dead ends for pathways of the conducting component, with the net result of reduced conductivity as substantial volume fractions of material are no longer active in transport processes. The results of this study complement the past literature and improve our understanding of the use, potential caveats, and shortcomings of Equation 1 and EMT to analyze transport in these materials. Whereas f is usually considered to account for structural information and has been used as a basis for comparison of differences in structure, in practice it is often better described as an empirical efficiency factor. Lumped into f is tortuosity, the impact of defects and grain boundaries, an effective volume fraction of conducting material, and perhaps even the possibility that the pure conducting material in the nanostructured confinement does not have the same conductivity of the pure conducting material in the bulk. Of these factors, only defects and grain boundaries can potentially reduce σ_{BCE} by an order of magnitude or more compared to the σ_{homo}; the reduction in conductivity due to tortuosity or an effective ϕ_{COND} is likely maximized at a factor of two or three. Finally, there is opportunity to combine thin film experiments and analysis as described here with bulk measurements on the same material; the complimentary information may yield the fundamental understanding necessary for the design of materials and strategies for processing to realize selective and highly conducting membranes for electrochemical applications.

4.6 References

[1] Y. a. Elabd and M. a. Hickner, Macromolecules **44**, 1 (2011), ISSN 00249297.

[2] J. Parrondo and V. Ramani, Journal of The Electrochemical Society **161**, F1015 (2014), ISSN 0013-4651, 1945-7111.

[3] A. Panday, S. Mullin, E. D. Gomez, N. Wanakule, V. L. Chen, A. Hexemer, J. Pople, and N. P. Balsara, Macromolecules **42**, 4632 (2009), ISSN 0024-9297.

[4] J. Sun, G. M. Stone, N. P. Balsara, and R. N. Zuckermann, Macromolecules **45**, 5151 (2012), ISSN 00249297.

[5] R. P. Doyle, X. Chen, M. Macrae, A. Srungavarapu, L. J. Smith, M. Gopinadhan, C. O. Osuji, and S. Granados-Focil, Macromolecules **47**, 3401 (2014), ISSN 15205835.

[6] D. T. Hallinan, S. a. Mullin, G. M. Stone, and N. P. Balsara, J. Electrochem. Soc. **160**, A464 (2013), ISSN 0013-4651.

[7] P. E. Trapa, B. Huang, Y.-Y. Won, D. R. Sadoway, and A. M. Mayes, Electrochemical and Solid-State Letters **5**, A85 (2002), ISSN 10990062.

[8] A.-V. G. Ruzette, P. P. Soo, D. R. Sadoway, and A. M. Mayes, Journal of The Electrochemical Society **148**, A537 (2001), ISSN 00134651.

[9] M. Singh, O. Odusanya, G. M. Wilmes, H. B. Eitouni, E. D. Gomez, a. J. Patel, V. L. Chen, M. J. Park, P. Fragouli, H. Iatrou, et al., Macromolecules **40**, 4578 (2007), ISSN 0024-9297.

[10] O. Buriez, Y. B. Han, J. Hou, J. B. Kerr, J. Qiao, S. E. Sloop, M. Tian, and S. Wang, Journal of Power Sources **89**, 149 (2000), ISSN 03787753.

[11] X. Wang, M. Goswami, R. Kumar, B. G. Sumpter, and J. Mays, Soft Matter **8**, 3036 (2012), ISSN 1744-683X.

[12] W. S. Young and T. H. Epps, Macromolecules **45**, 4689 (2012), ISSN 00249297.

[13] X. C. Chen, D. T. Wong, S. Yakovlev, K. M. Beers, K. H. Downing, and N. P. Balsara, Nano Letters **14**, 4058 (2014), ISSN 15306992.

[14] P. W. Majewski, M. Gopinadhan, W.-S. S. Jang, J. L. Lutkenhaus, and C. O. Osuji, Journal of the American Chemical Society **40**, 17516 (2010), ISSN 1520-5126.

[15] J. Sax and J. M. Ottino, Polymer Engineering and Science **23**, 165 (1983), ISSN 0032-3888.

[16] D. T. Hallinan Jr. and N. P. Balsara, Annual Review of Materials Research **43**, 503 (2013), ISSN 1531-7331.

[17] M. T. Irwin, R. J. Hickey, S. Xie, S. So, F. S. Bates, and T. P. Lodge, Macromolecules p. acs.macromol.6b01553 (2016), ISSN 0024-9297.

[18] M. Chintapalli, X. C. Chen, J. L. Thelen, A. A. Teran, X. Wang, B. A. Garetz, and N. P. Balsara, Macromolecules **47**, 5424 (2014), ISSN 15205835.

[19] M. Chintapalli, T. N. P. Le, N. R. Venkatesan, N. G. Mackay, A. A. Rojas, J. L. Thelen, X. C. Chen, D. Devaux, and N. P. Balsara, Macromolecules **49**, 1770 (2016), ISSN 15205835.

[20] M. L. Hoarfrost and R. A. Segalman, Macromolecules **44**, 5281 (2011), ISSN 21611653.

[21] P. W. Majewski, M. Gopinadhan, and C. O. Osuji, Soft Matter **9**, 7106 (2013), ISSN 1744-683X.

[22] Y. Kambe, C. G. Arges, S. Patel, M. P. Stoykovich, and P. F. Nealey, The Electrochemical Society Interface **26**, 61 (2017).

[23] M. Chintapalli, K. Higa, X. C. Chen, V. Srinivasan, and N. P. Balsara, Polymer Physics **55**, 266 (2017).

[24] S. Ji, C.-C. Liu, J. G. Son, K. Gotrik, G. S. W. Craig, P. Gopalan, F. J. Himpsel, K. Char, and P. F. Nealey, Macromolecules **41**, 9098 (2008), ISSN 0024-9297.

[25] E. Han, H. Kang, C. C. Liu, P. F. Nealey, and P. Gopalan, Advanced Materials **22**, 4325 (2010), ISSN 09359648.

[26] C. G. Arges, Y. Kambe, H. S. Suh, L. E. Ocola, and P. F. Nealey, Chemistry of Materials **28**, 1377 (2015), ISSN 0897-4756.

[27] E. Jones, E. Oliphant, and P. Peterson, *SciPy: Open Source Scientific tools for Python* (2001), URL `http://www.scipy.org/`.

[28] S. van der Walt, J. L. Schönberger, J. Nunez-Iglesias, F. Boulogne, J. D. Warner, N. Yager, E. Gouillart, and T. Yu, PeerJ **2**, e453 (2014), ISSN 2167-8359, URL `https://peerj.com/articles/453`.

[29] B. Scrosati, F. Croce, L. Persi, J. E. Soc, B. Scrosati, F. Croce, and L. Persi, Journal of The Electrochemical Society **147**, 1718 (2000).

[30] M. E. Orazem, B. Tribollet, B.-Y. Chang, and S.-M. Park, Annual review of analytical chemistry **3**, 207 (2010), ISSN 19361335, `arXiv:1011.1669v3`.

[31] D. K. Paul, R. McCreery, and K. Karan, Journal of the Electrochemical Society **161**, F1395 (2014), ISSN 0013-4651.

[32] D. Sharon, P. Bennington, C. Liu, Y. Kambe, B. X. Dong, V. F. Burnett, M. Dolejsi, G. Grocke, S. N. Patel, and P. F. Nealey, Journal of The Electrochemical Society **165**, H1028 (2018).

[33] R. Yadav and P. S. Fedkiw, Journal of the Electrochemical Society **159**, B340 (2012), ISSN 0013-4651.

[34] A. N. Semenov, Tech. Rep. (1993).

[35] D. M. Pesko, M. A. Webb, Y. Jung, Q. Zheng, T. F. Miller, G. W. Coates, and N. P. Balsara, Macromolecules **49**, 5244 (2016), ISSN 15205835.

[36] M. A. Webb, Y. Jung, D. M. Pesko, B. M. Savoie, U. Yamamoto, G. W. Coates, N. P. Balsara, Z. G. Wang, and T. F. Miller, ACS Central Science **1**, 198 (2015), ISSN 23747951.

[37] K. M. Diederichsen, R. R. Brow, and M. P. Stoykovich, ACS nano **9**, 2465 (2015), ISSN 1936-086X.

CHAPTER 5

QUANTITATIVE ANALYSIS OF CONNECTIVITY ON ION TRANSPORT IN POLYMER ELECTROLYTES

5.1 Abstract

Nanoscale defects within polymer electrolyte systems have a significant impact on the ionic conductivity. In this chapter we design devices of precisely patterned nanoscale defects in ion conduction pathways in order to quantify the impact of pathway connectivity between electrodes. Interdigitated electrode devices were fabricated with periodic insulating walls of SiO_2 on top, forming channels where ion conducting polymers were flowed in to form ion conduction pathways and characterized by AC electrochemical impedance spectroscopy (EIS). Each device was designed with a different ratio of connected to disconnected pathways. For devices comprised entirely of one type of ion conduction pathway, a simple equivalent circuit model was used to extract the resistance and capacitance of the individual connected and disconnected pathways. This model was expanded to include both connected and disconnected circuits into one model in order to predict the EIS spectra of devices containing both types of pathway. The expanded model fit the full experimental data well for both dry and hydrated materials poly(ethylene oxide) and sulfonated poly(styrene) respectively. The resistance from the connected pathways manifested as a high frequency peak on the Bode plots while the disconnected pathway resistance appeared as a low frequency peak.

5.2 Introduction

In Chapters 3 and 4, we formed deterministic morphologies of the poly(styrene)-block-poly(2-vinylpyridine) (PS-b-P2VP) block copolymers (BCP) on top of interdigitates electrodes (IDEs) and electrochemically characterized the films as a function of structure.[1] Through the comparison of the conductivity value, we demonstrated that complex ion conduction pathways can be predicted if the number and length of the connected domain is known. Even when the ion conduction path was connected without a single grain boundary, the homopolymer conductivity and the morphology information was not sufficient to justify the difference. This discrepancy was postulated to be due to molecular effects at the interface of the two domains. It became clear, even in a perfectly controlled structure, it is difficult to decouple the impedance responses due to the morphology and molecular effects near the interfaces.

Here we demonstrate a platform that can isolate the structural contributions to impedance. Thin film ion conducting homopolymers are confined in nanoscale trenches formed with insulating SiO_2 walls on top of IDEs to emulate BCP electrolyte (BCE) morphologies and are characterized via electrochemical impedance spectroscopy (EIS). The influence of the number of connected and disconnected trenches, or pathways, is compared across devices with the same number of pathways but different ratios of connectivity. This effect is studied across two material systems: poly(ethylene oxide) (PEO) with lithium salt, a high ionic conductivity polymer electrolyte for solid state lithium batteries, and poly(styrene-rand-styrene sulfonate) (PSS), a proton-conducting membrane material for fuel cell applications capable of operating in various humidity conditions. Equivalent circuit models (ECM) were made to extract the resistance and ionic conductivity from these experiments. A simple ECM was employed for devices of one type of pathway, connected or disconnected, and an expanded ECM was used for devices of both pathway types. Our ECMs fit the data well for both material systems proving their widespread accuracy. Following this, a simple peak analysis of the data indicated that the simplest interpretations of EIS data will yield the resistance of the connected pathways only. These findings may have profound implications for any BCE group measuring films without deterministic knowledge of the charge transport pathways and finding that their calculated conductivities are lower than expected.

5.3 Methods

5.3.1 Materials

The polyelectrolyte PSS (Mn 24.7 kg/mol with 88 % of sulfonated PS repeat units) was received from Polymer Source and used as is. The polyelectrolyte poly(ethylene oxide) (PEO, Mn 20 kg/mol with dimethyl-terminated end groups) and LiTFSI salt (lithium bis(trifluoromethanesulfonyl) imide) were received from Polymer Source and dried for 24 hours at 60 $^{\circ}C$ under vacuum in an inert glovebox antechamber before being transferred into the glovebox. Solutions of PEO in DMF N,N-dimethylformamide (DMF) and LiTFSI in DMF both with concentrations of 20 mg/mL were prepared and placed on a shaker in the glovebox for 24 hours before combining in a ratio of Li cation to EO units in PEO of $r = 0.05$, which was subsequently shook for an additional 24 hours prior to sample preparation. The poly(styrene) (PS) (Mn 25 kg/mol) was received from Polymer source and used as is. All other chemicals (DMF, Acetone, 2-propanol (IPA), and Anisole) were received from Sigma-Aldrich or Fisher Scientific and used without further purification. The Pt interdigitated electrodes with dielectric walls were fabricated on semiconducting polished silicon wafers (1 μm thermally grown oxide) obtained from WRS materials. The spin-on-glass was received from Desert Silicon and used with no further filtration. GL2000 ebeam resist was received from MicroChem Corporation and diluted 1:1 by volume in anisole prior to spin coating. The poly(dimethoxysiloxane) (PDMS) mix kit (Sylgard 184) was purchased from Sigma Aldrich and used as instructed. 10:1 by weight of the base and crosslinker, respectively, were mixed and poured on top of a petri dish with a taped down Si wafer. After degassing, the PDMS was crosslinked at 75 $^{\circ}C$ for 4 hours.

5.3.2 Fabrication of the Interdigitated Electrodes

Figure 5.1 shows the fabrication process of the IDE with nanoscale dielectric trenches on top. Interdigitated electrodes made of a 5 nm Titanium (Ti) adhesion layer followed by 20

nm thick of platinum (Pt) were fabricated using conventional photolithography on top of a silicon (Si) wafer with 1 μm of thermal oxide grown on the surface. The IDE contained a total of 200 electrodes that were separated from each counter electrode by 8 μm, the overlap between counter electrodes was 2 mm, and each of the electrode teeth was 2 μm wide. 120 nm of spin-on-glass (SOG) was spin coated on top of the IDEs, annealed at 95 $^{\circ}C$ for 1 min, 115 $^{\circ}C$ for 1 min, then 180 $^{\circ}C$ for 15 $mins$ to create a layer of SiO_2 on top of the IDE. The device was treated with an O_2 plasma descum process (50 W) and spin coated with 205 nm of GL2000 ebeam resist and baked on a hotplate at 180 $^{\circ}C$ for 3 $mins$. The ebeam resist was patterned using the JEOL 9500 electron beam writer with an effective ebeam dosage of 350 $\mu C/cm^2$. The film was then developed in Amyl Acetate without agitation for 45 sec, quenched in IPA, and dried with Nitrogen. The devices were etched using a Fluorine etcher. Following the Fluorine etch, the excess ebeam resist was removed using an O_2 plasma etch (50 W forward bias, 50 $sccm$ O_2) for 2 $mins$ in the same chamber without any prior conditioning. The resulting film was removed from the Fluorine etcher and placed inside the YES downstream asher and exposed to an oxygen descum process. The resulting IDEs had periodic 200 nm wide and 120 nm high walls that, when multiple walls were placed in parallel, formed trenches that spanned from one electrode to the other.

5.3.3 Polymer Sample Preparation on IDEs

One hydrated and one anhydrous polyelectrolyte were studied for different applications. First, the 24.7 k MW poly(styrene-rand-styrenesulfonate) (PSS) with 80 % of the repeat units functionalized was studied under humidified conditions. When in humid conditions, the water infiltrates the film, dissociates the protons from the static sulfonate groups, and forms a water conduction path for proton transport. The higher polarizability of the water is known to increase the dielectric permittivity of the PSS film. [2, 3] Following an oxygen plasma functionalization, PSS was uniformly deposited on top of the IDEs via spin coating. PDMS cubes with surfaces cured on top of the atomically flat Si wafer were placed on top of the IDE with the PSS coated on top then annealed at 155 °*C*. The annealing process thermally reflowed the PSS into the trenches and the PDMS reacted with the hydroxyl groups on the dielectric walls forming a hydrophobic coating of PDMS on top of the trenches when the PDMS was peeled off. The thickness of the polymer films in the trenches was determined by AFM of the bare IDE then of the IDE after the PSS was reflowed into the film and the PDMS removed. The identical PSS polymer was also deposited onto the control IDE via spin coating. The thickness was determined by ellipsometry on a witness wafer to be 28 *nm* and 56 *nm*.

Second, the 20k MW PEO with LiTFSI (PEO/LiTFSI) was studied in anhydrous conditions at 90 °*C*. Following an oxygen plasma functionalization, a solution of PEO/LiTFSI in DMF ([Li:EO] = r = 0.05) was uniformly deposited by spincoating on top of the IDEs. Samples were heated at 100 °*C* for 5 hours to thermally reflow most of the PEO/LiTFSI into the trenches. Samples were heated at 120 °*C* for 20 minutes before PDMS was used to press remaining PEO on top of trench walls into trenches. PDMS was peeled off then AC impedance measurements were made using a setup within the inert glovebox conditions. The identical PEO solution was also deposited onto a witness wafer via spin coating. The thickness was determined by ellipsometry and confirmed by scratch test and AFM to be 46 *nm*. Note: the PEO thickness in the trench is subject to a higher degree of error when characterized in the trench using AFM at ambient conditions due to the extremely hygroscopic nature of PEO. Therefore, the thickness of the PEO in the trench was estimated to be double the spin coat thickness at 92 *nm*. This is a reasonable value considering the PSS reflow also doubled the spin coat thickness.

5.3.4 Structure Characterization

Top-down images of the dielectric trenches were taken with the Carl Zeiss – Merlin field emission scanning electron microscope. The acceleration voltage was 1.0 *kV* with a working distance of 4 *mm* using an in-lens detector. 1 *nm* of Pt/Pd was sputtered onto the surface

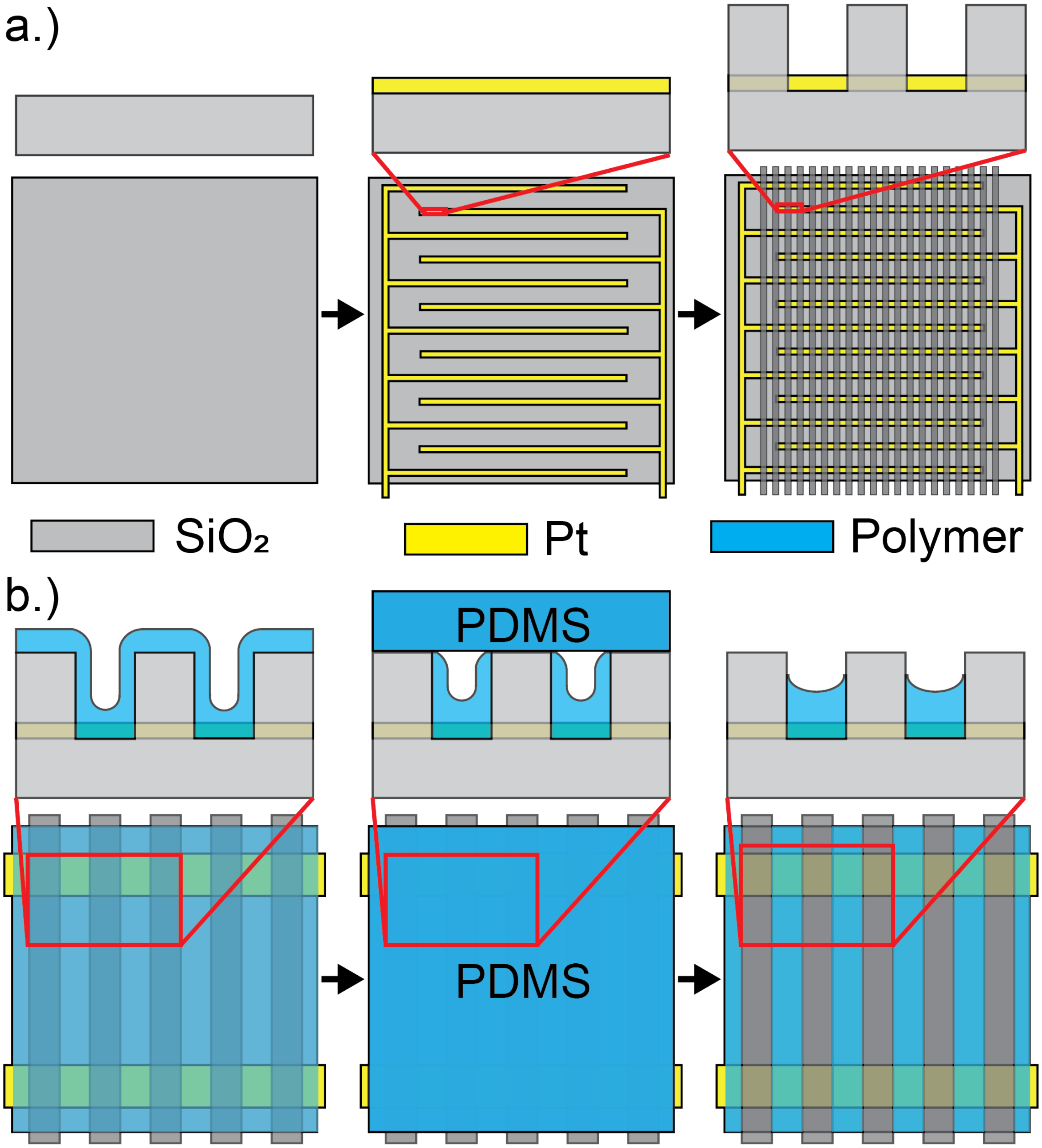

Figure 5.1: Fabrication schematic of the a.) Pt interdigitated electrodes fabricated via photolithography and the dielectric trenches patterned using ebeam lithography and b.) the ion conducting polymer reflow process using PDMS and thermal reflow.

of the device using the Cressington 108 Auto Sputter Coater to reduce charging due to the electron beam. Topography of the film was characterized by the Bruker Atomic Force Microscope.

5.3.5 Controlling Ion Conduction Pathways

Figure 5.2 shows the different dielectric topologies that were patterned on top of the IDEs using ebeam lithography. The SEM and AFM micrographs shown are taken after all of the polymer sample preparation and electrochemical characterization was completed.

Ion conduction pathways were designed as periodic trenches that were 200 *nm* wide by 8 *μm* long and oriented orthogonal to the electrodes, resulting in the shortest and most direct path. The width of the wall between trenches was also 200 *nm* wide. A trench that spans from one electrode to the other is referred to as the "connected path", as shown by all of the paths in Figure 5.2a. A trench patterned with dielectric walls blocking the pathway between electrodes is referred to as the "disconnected path", as shown by half of the paths in Figure 5.2b and all of the paths in Figure 5.2c. The "block" was 2.6 *μm* long and comprised several periodic dielectric walls and square pockets each 200 *nm* wide. The pockets prevent accumulation of polymer on top of the dielectric walls during thermal reflow in order to eliminate any unintended charge transport over the block. The blocks were introduced uniformly throughout the film by breaking up local connected structures in to a unit set of 4 and blocking a fraction of the pathways in each device set. The total number of pathways were blocked by 0, 25, 50, 75, and 100 percent resulting in a total of 995000, 746250, 497500, 248750, and 0 connected pathways respectively on each set of devices. Devices with all or none of the pathways blocked were considered devices of one type of pathway, disconnected or connected, respectively. The other three sets still contained 995000 pathways total but with different ratios of connected to disconnected pathway types.

5.3.6 Electrochemical Characterization

The AC impedance measurements for the PSS samples were made under humidified and controlled temperature conditions. After the devices with PSS were prepared, the samples were placed inside of the relative humidity chamber and conditioned at 25 $°C$ 25 $\%RH$ for 6 hours prior to measurement. The samples were then measured from 1 MHz to 0.1 Hz with a perturbation voltage of 10 mV. After all the devices were measured, the relative humidity was raised to the next value and the devices were conditioned for a minimum of 3 hrs. In this study, the samples were measured at 25, 35, 45, 65, and 95 $\%RH$ all at 25 $°C$.

The AC impedance measurements for the PEO samples with LiTFSI were made under inert conditions with temperature control. Samples were placed on the heated stage of the probe station for 10 $mins$ before making AC impedance measurements from 1 MHz to 1 Hz with a perturbation voltage of 100 mV. Each sample was measured at 90 $°C$, well above the melt temperature of 20k MW PEO (70 $°C$).

5.4 Results and Discussion

5.4.1 Effect of Nanoscale Confinement on Conductivity

Our devices were designed to model nanoscale structure within phase separating polymer electrolyte materials. The goal was to simplify the system as much as possible since these systems are highly complex and have many interrelated factors affecting ion transport properties. By isolating structural effects from all other factors, we aimed to shed light on how individual structure feature contributes to changes on ion transport. We began our simplification with studying materials in the thin film thickness range (< 100 nm) in order to limit transport to two dimensions instead of three. Previous work in our group has shown that 2D ion transport in thin films behaves similarly to 3D transport in bulk films for the PEO/LiTFSI system with the same salt concentration ($r = 0.05$) [4]. Therefore we started with our IDE design to measure thin film polymers. As an additional control study, we

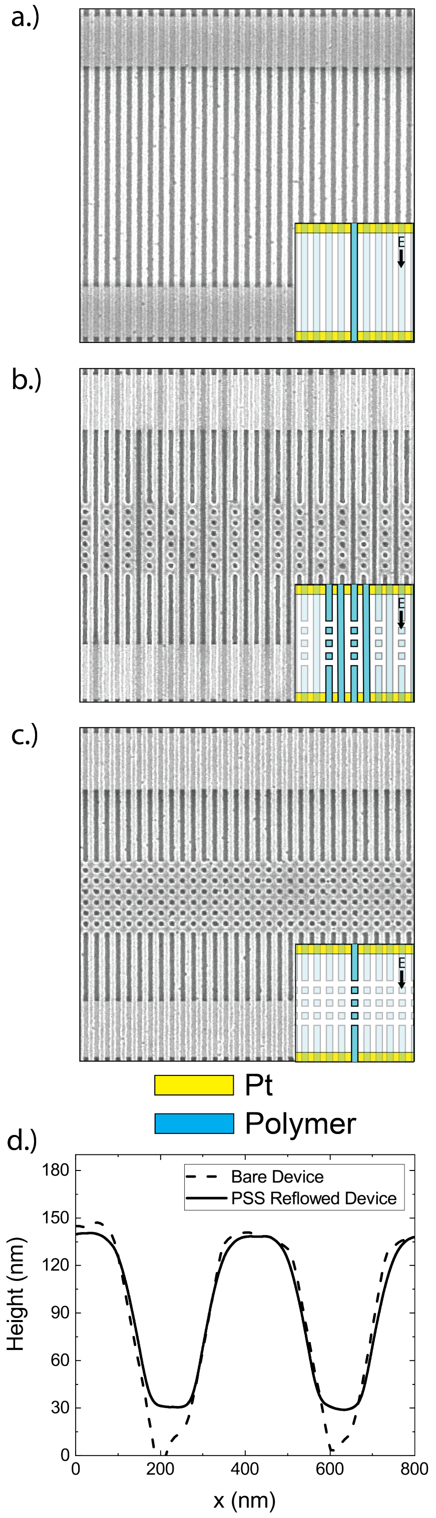

Figure 5.2: Micrographs of the fabricated trenches with reflowed PSS homopolymer. Top down SEM micrographs of the device with a. 955000 connected paths (0 % disconnected), b. 477500 connected paths (50 % disconnected), and c. 0 connected paths (100 % disconnected). d. AFM cross section topological trace of two trenches before (dotted line) and after (solid line) the deposition and reflow of homopolymer.

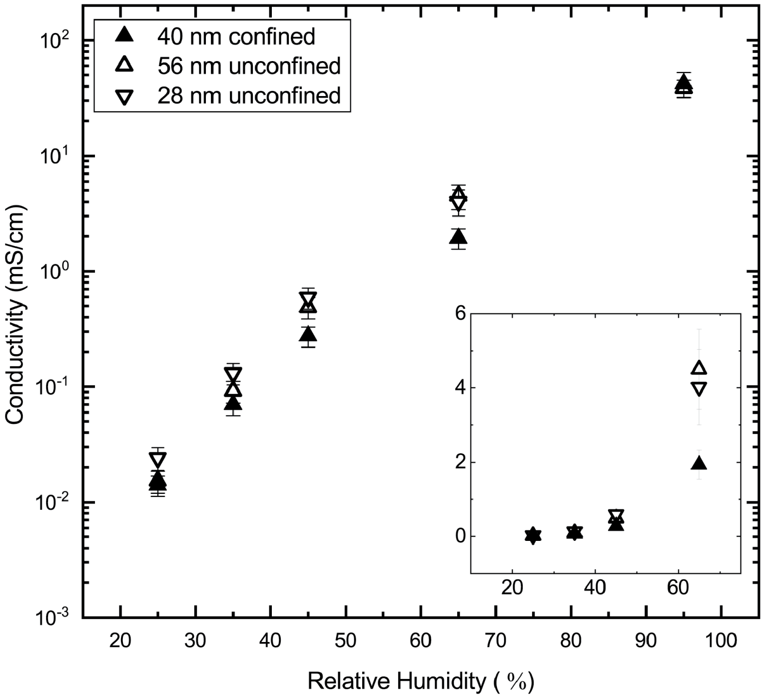

Figure 5.3: Conductivity of the unconfined and confined PSS homopolymer films as a function of the RH. Linear inset zooms in on the conductivity between 25 to 65 $\%RH$.

compared the conductivity of a thin film of PSS on an IDE with no insulator trenches to the conductivity of PSS on the IDE with fully connected pathways in insulating trenches. The conductivity of the PSS film confined in the insulting nanoscale trenches were calculated assuming the cross section of only the PSS material without the insulating trenches. The resulting conductivity values are compared in Figure 5.3. The conductivity decreased incrementally for the PSS on the IDE with trenches reaching the largest deviation around 65 $\%RH$. This confirmed that further confinement from thin film polymer to thin film polymer with dielectric trenches had only a minor impact on overall conductivity, even when accounting for geometric differences.

5.4.2 Device Design Approach

Next, we designed nanoscale conduction pathways similar to those that exist in phase separating systems such as BCPs. In these systems, two materials with vastly different mechanical properties and ionic conductivity are covalently linked to phase separate into periodic domains possessing the properties of one of the materials alongside domains of the other material. For example lamellar forming PS-b-PEO with equal volume fractions of each block would contain percolating regions of flexible, ion-conducting PEO alongside regions of mechanically rigid, insulating PS. This forms pathways of PEO where ions could conduct, but only qualitative assumptions can be made about the amount of nanoscale pathways that fully percolate through an entire film integrated into a device, typically several microns or millimeters thick.

The interface between domains also adds complexity to the system by being diffuse and sometime trapping ions, leading to additional decrease in overall ionic conductivity. We chose SiO_2 as the insulator material to mimic the mechanically rigid, insulating domains of PS, due to its similar properties as well as ease of incorporating into fabrication. Lithographic patterning can be easily transferred to SiO_2 by common etch processes, giving us the ability to use electron beam lithography with nanoscale precision to pattern our pathways. By using dimethyl-terminated PEO, we chose the same ion conducting material for this region that would not graft to the SiO_2 wall in order to create a clear, non-diffuse interface between the PEO and SiO_2. Since this system is most commonly studied for lithium ion conductivity, which requires dehumidified, inert conditions, we chose PSS to study a humidified system similar to those used as fuel cell membranes such as Nafion. Thus, our devices provided a platform to study any ion conducting material, dry or humidified, in confined nanoscale pathways similar to structures in phase separating materials, with no interfacial effects between domains and complete control over the structure of the pathway.

With the goal of quantifying ionic conductivity effects from specific pathway structures, we examined the effect of connectivity of pathways. It should be noted that this fabrication process could potentially be used to design any pathway geometry between electrodes on IDEs in order to study individual structural effects. For this study, we hypothesized that connected pathways contributed to overall ionic conductivity measured by AC EIS, but disconnected pathways did not. By preparing sets of devices with five different ratios of connected to disconnected pathways, we were able to track changes across each set of EIS data to analyze the impact of nanoscale variations in structure.

5.4.3 Mixed Structures Contain Two Peaks, One for Connected and One for Disconnected

Figure 5.4 shows EIS data for the 0, 25, 50, 75, and 100 % blocked structures for a) the PEO system measured at 90 $^{\circ}C$ and b) the PSS system at 25 $^{\circ}C$ 95 $\%RH$ depicted as Bode plots that overlay impedance and phase shift response as a function of perturbation frequency. The resistance is determined on a Bode plot as the point where the impedance curve plateaus, which corresponds to a peak in the phase shift curve.

Upon inspection of Figure 5.4 it is evident that a transition in the data occurs for devices with both types of conduction pathways in both materials systems. There are three transition curves between these that represent devices with 25, 50, and 75 % of pathways disconnected. From here on, these structures will be referred to as "mixed structures". At higher RH for the PSS and at 90 $\circ C$ for PEO, a secondary peak in the phase shift can be observed to grow at lower frequencies as the fraction of disconnected domains increased. This peak is interpreted to correspond to the impedance signal from the disconnected paths. This can be seen in Figure 5.5c and d where the secondary peak grows and drifts to a lower frequency value. The peak appeared for the PEO at 90 $^{\circ}C$ and for the PSS at 95 and 65 $\%RH$ but not for the lower RH values due to an insufficient degree of hydration for an ion conduction to occur across the barrier. At the lower RH values, where the impedance is significantly higher, the response is beyond the frequency and impedance values probed, resulting in a single hemisphere spectrum. In practice, spectra with only a single inflection point are more representative of impedance data commonly observed when probing nanostructured ion conductors at the membrane scale. [5] Conversely, the presence of the residual ion conduction of the disconnected path enabled us to demonstrate that EIS is probing the entire film.

It has been previously demonstrated,[6] that when probing a dielectric, the impedance response is a representation of all of the conduction pathways, including the disconnected pathways, therefore it is not particularly surprising that a second lower frequency peak emerges in mixed structures that are comparable in frequency to the impedance response of the fully disconnected film. However, the scaling relationship of the impedance, relative to the fraction of connected and disconnected pathways, has only been speculated to be linear. Due to the definitive control of geometry achieved through our approach, we used this experimental platform to demonstrate the linear relationship of the impedance peaks to the total fraction of connected and disconnected pathways.

5.4.4 Expanded ECM for Mixed Types of Conduction Pathways

Evidenced by the qualitative observation of the peaks in the Bode plot of the mixed structures, we hypothesize that the collective two-peak impedance of the mixed structures scale linearly with the total number of connected and disconnected domains. To demonstrate this hypothesis, 1.) the resistance and capacitance values associated with a connected or disconnected path were calculated from model fits of the fully connected or fully disconnected film impedance, 2.) the single channel values were used with the total number of connected and disconnected pathway, 3) the rescaled values were placed in the expanded ECM, and 4.) the model impedance and phase shift were calculated and overlaid on top of the mixed structure impedance response.

In order to directly correlate changes in EIS data to structural differences, it is important to justify the equivalent circuit used to model the system. AC EIS is the most common tool for measuring material conductivity properties, but there is much debate over which equivalent circuit model elements are necessary to calculating an accurate resistance, which is then used to determine conductivity. Often, more circuit elements are added to a model to better fit the data. However as more elements are added, each one has less of a direct correlation to a physical electrochemical process taking place in the material. Therefore it

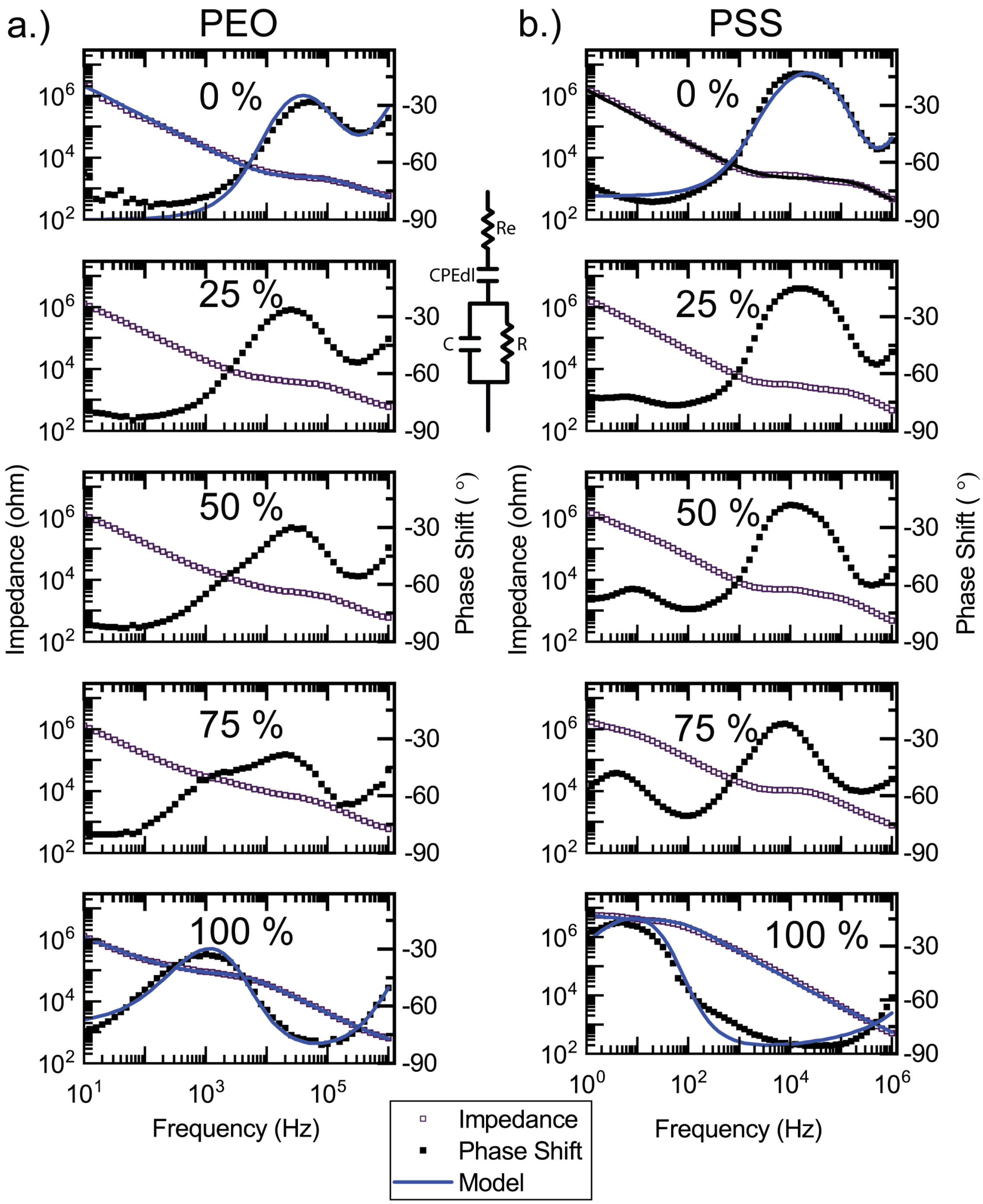

Figure 5.4: Complex impedance response from the connected, mixed, and disconnected structures for a.) PEO measured at 90 $°C$ and b.) PSS measured at 25 $°C$ and 95 $\%RH$. The equivalent circuit fit to the impedance data of the 0 % and 100 % blocked structures are shown in the middle.

is important to design an equivalent circuit model that fits the captured data well, but with as simple of a circuit as possible. The simplest circuit for ion conduction through a material with ion-blocking electrodes is shown in the middle of Figure 5.4 and contains four circuit elements. R_e is the parasitic resistance of the setup and the IDE and is typically around 100 *ohms*. C_{DL} is the capacitance of the double layer that is formed at the electrode polymer interface due to the lack of a redox reaction at the electrode. R is the resistance of the film and C is the capacitance of the film placed in parallel. The circuit shown in Figure 5.4 is a common interpretation that does not fully take into account the complexity of measuring the impedance of mixed structures. In contrast, Figure 5.5a shows the proposed equivalent circuit model for impedance in a mixed structure with two different types of transport pathways. In our model, $R_d > R_c$ therefore the impedance elements of the connected domains appear at higher frequencies while the elements associated to R_d appear at lower frequencies. As the value of R_c increases, the signal from the disconnected paths can disappear from the frequency range studied.

The R and C values of individual paths are calculated by first fitting the impedance of the fully connected and disconnected structure impedance using the ECM shown in the inset of Figure 5.5b. The R and C values extracted from the model were then used to calculate the resistance and capacitance of a single connected or disconnected path.

The linear scaling relationship of the R value with the total number of connected paths is verified by first fabricating IDEs with varying numbers of connected pathways between IDEs. The structures did not contain any disconnected paths. Alternatively, the total surface area of the film was altered to accommodate difference numbers of the connected pathways. Figure 5.6 plots the resistance as a function of the total number of connected pathways. In addition, the R_{film} was predicted by taking R value extracted from any of the films shown in the plot and calculating the R_{single} using Equation 5.1 where R_{single} is the R value of a single connected pathway and n is the total number of pathways. The R_{single} was used to predict the resistance at different n values by using the Equation 5.2. The resulting R_{film}

and R_{model} values are plotted in FIgure 5.6. From observation it can be seen that the R simply scales as the inverse linear of the R_{single}. With this understanding of the R scaling rule, we move to the more complex case with mixed structures.

$$R_{single} = R_{film}n \tag{5.1}$$

$$R_{model} = \frac{R_{single}}{n} \tag{5.2}$$

With this verification, the R and C values of single ion pathways were calculated using simple linear and inverse linear scaling models and used to predict the circuit elements in the mixed structures. The single path resistance was calculated using the equation:

$$R_{single} = R_{total} \cdot 995000 \tag{5.3}$$

Where R_{single} is defined as the resistance of a single connected domain $R_{single,c}$ or the resistance of a single disconnected domain $R_{single,d}$, R_{total} is either the resistance of the connected or the disconnected domains extracted from the fully connected and disconnected impedance data.

The single path capacitance was calculated using:

$$C_{single} = \frac{C_{total}}{995000} \tag{5.4}$$

Where C_{single} is defined as the capacitance of a single connected $C_{single,c}$ or disconnected $C_{single,d}$ domain, C_{total} is either the capacitance of the connected or the disconnected domains extracted from the model.

The calculated values were used for each R and C in the model shown in Figure 5.7b where the model is split into two Randles cells in parallel. Each cell represents the hemisphere contributions from the connected domains or the disconnected domains. The resistance value of the connected film was scaled (R_c) using the equation:

$$R_c = \frac{R_{single,c}}{n} \tag{5.5}$$

The disconnected resistance (R_d) using the equation:

$$R_d = \frac{R_{single,d}}{995000 - n} \tag{5.6}$$

The connected capacitance (C_c) using the equation:

$$C_c = C_{single,c} \cdot n \tag{5.7}$$

The disconnected capacitance (C_d) using the equation:

$$C_d = C_{single,d} \cdot (995000 - n) \tag{5.8}$$

The connected double layer capacitance ($C_{dl,c}$) using the equation:

$$C_{dl,c} = C_{single,dl,c} \cdot n \tag{5.9}$$

The disconnected double layer capacitance ($C_{dl,d}$) using the equation:

$$C_{dl,d} = C_{single,dl,d} \cdot (995000 - n) \tag{5.10}$$

The connected electrode resistance ($R_{e,c}$) using the equation:

$$R_{e,c} = \frac{R_{single,c,c}}{n} \tag{5.11}$$

The disconnected electrode resistance ($R_{e,d}$) using the equation:

$$R_{e,d} = \frac{R_{single,e,d}}{995000 - n} \tag{5.12}$$

where n is the total number of connected paths. The resulting values for R_c, R_d, C_c, C_d, $C_{dl,c}$, $C_{dl,d}$, $R_{e,c}$, and $R_{e,d}$ are shown in Table 5.1. The values were determined for each structure with varying numbers of connected pathways and the values were used to predict the impedance and phase shift (solid line) in Figure 5.7b and c.

The reasonable fit of the PEO experimental data to the predicted spectra supports our earlier statement that the resistance scales with the number of connected and disconnected paths. Furthermore, the capacitance of the film is observed to also scale linearly with the total number of ion conducting domains. As the total number of connected ion conduction paths decreases, the total film capacitance approaches zero, while the capacitance of the second peak reaches the highest value.

The method demonstrated in this work enables us to observe impedance signal from both the connected and disconnected paths. This allowed us to demonstrate that the impedance signal from the connected path and the disconnected paths are simply linear sums of the total number of each connected pathway. This validity of the concept is demonstrated by the good fit of the predicted to the experimental impedance spectrum. The interpretation is unique to dielectric charge carriers, however in most cases the resulting scaling behavior can look very similar to a metal electron conductor. For an example, in a common impedance spectrum of a membrane, the impedance signal from the disconnected pathways is typically outside of the frequency range studied. The resulting impedance measured in such a system only shows the signal from the connected ion conduction pathways. From our understanding gained through this work, we can provide further insight in work done by others in the community where the structure information was less understood.

Note: In comparison to the PEO, the PSS did not fit the experimental spectra as well at lower frequencies. This is likely attributed to two factors: 1) at high RH conditions, the electric field distribution is complex due to the order of magnitude larger relative permittivity of hydrated PSS and 2) R_d has a larger error associated, therefore variability in $R_{singlepath,d}$ may be affecting the fitting of the spectra. It is important to note, that the resistance of the

Variable \# of connected pathways	Units	995000	746250	497500	248750	0
R_c	ohm	1.85E+03	2.46E+03	3.70E+03	7.39E+03	0.00E+00
R_d	ohm	0.00E+00	1.16E+05	5.78E+04	3.85E+04	2.89E+04
C_c	F	5.70E-10	4.28E-10	2.85E-10	1.43E-10	0.00E+00
C_d	F	0.00E+00	1.03E-10	2.06E-10	3.09E-10	4.12E-10
$C_{dl,c}$	F	6.24E-09	4.68E-09	3.12E-09	1.56E-09	0.00E+00
$C_{dl,d}$	F	0.00E+00	1.56E-09	3.12E-09	4.68E-09	6.24E-09
$R_{e,c}$	ohm	4.39E+02	5.85E+02	8.78E+02	1.76E+03	0.00E+00
$R_{e,d}$	ohm	0.00E+00	1.82E+03	9.11E+02	6.07E+02	4.56E+02

Table 5.1: Predicted equivalent circuit values for PEO impedance obtained at 90 $^{\circ}C$

Variable \# of connected pathways	Units	995000	746250	497500	248750	0
R_c	ohm	2.02E+03	2.70E+03	4.05E+03	8.09E+03	0.00E+00
R_d	ohm	0.00E+00	1.60E+07	8.01E+06	5.34E+06	4.00E+06
C_c	F	4.98E-10	3.74E-10	2.49E-10	1.25E-10	0.00E+00
C_d	F	0.00E+00	1.16E-10	2.33E-10	3.49E-10	4.65E-10
$C_{dl,c}$	F	5.47E-08	4.10E-08	2.73E-08	1.37E-08	0.00E+00
$C_{dl,d}$	F	0.00E+00	1.37E-08	2.73E-08	4.10E-08	5.47E-08
$R_{e,c}$	ohm	2.74E+02	3.65E+02	5.48E+02	1.10E+03	0.00E+00
$R_{e,d}$	ohm	0.00E+00	1.10E+03	5.50E+02	3.67E+02	2.75E+02

Table 5.2: Predicted equivalent circuit values for PSS impedance obtained at 25 $^{\circ}C$ 95 $\%RH$

film.

5.4.5 Determination of Resistance from Simple Peak Analysis

In the above discussion, it was demonstrated that the two-peak impedance scales with the total number of connected and disconnected films. We recognize that ion transport pathways are not bimodal and that a range of ion conduction pathways exist. However, the findings from this study are critical in understanding how to interpret complex impedance in heterogeneous systems. As evidenced in our previous work,[**?**] the disconnected pathways in BCE systems are significantly higher in resistance and capacitance in comparison to the connected domains. In most membrane scale studies, the disconnected pathways may be even higher, resulting in the impedance of the disconnected paths not being in the frequency range studied (i.e. 1 MHz to 0.01 Hz) in typical EIS measurements. In such cases, information about the connectivity a mixed morphology film can still be estimated by simply investigating the higher frequency peak associated with connected systems. If only the conductivity of the

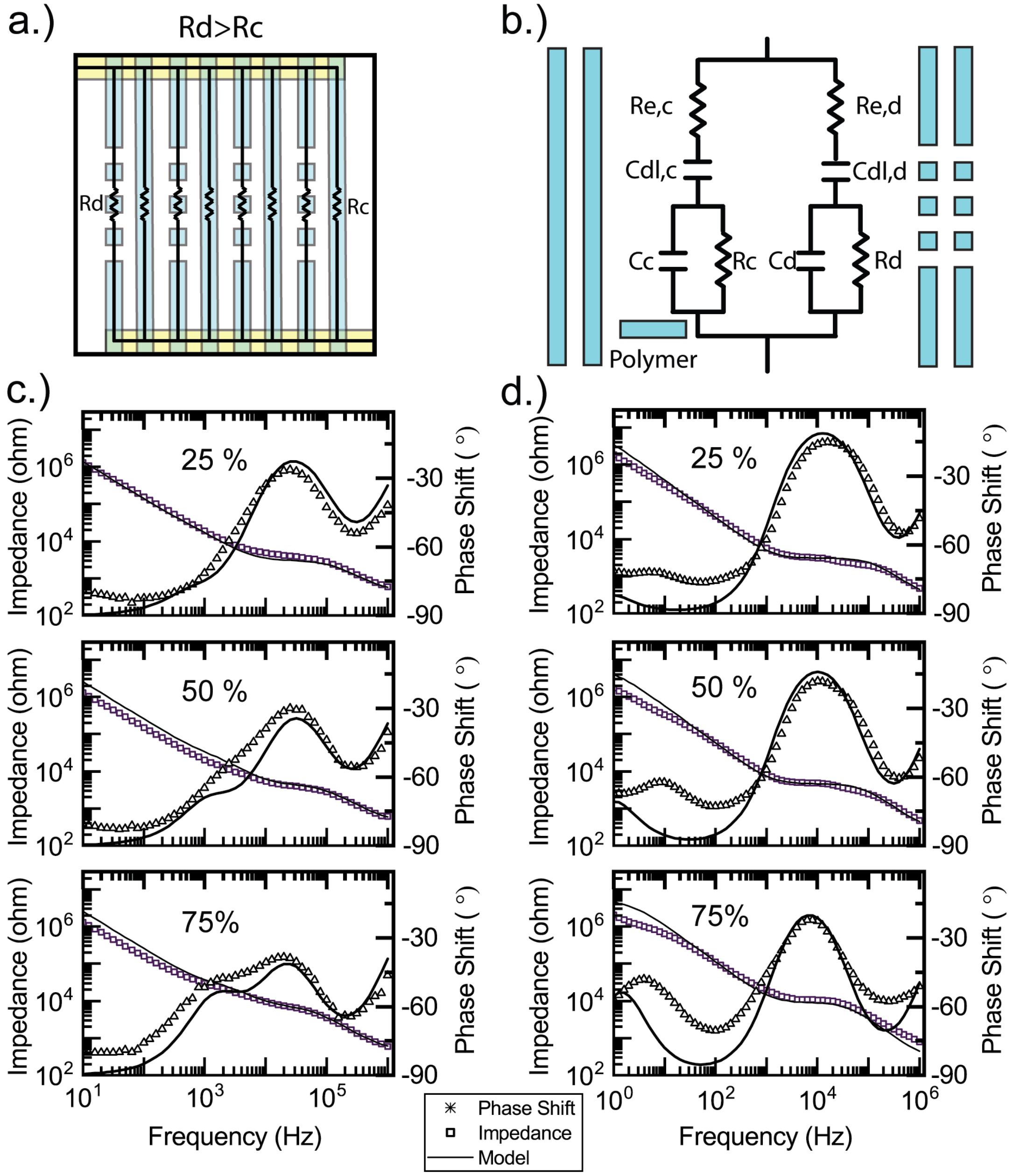

Figure 5.5: Prediction of impedance spectra using extracted resistance and capacitance values. a.)Equivalent circuit used to predict the impedance spectra mixed structures. b.) Alternative equivalent circuit of the resistors demonstrating that EIS probes all of the film but in the frequency range studied, only the signal from the *Rc* is shown. Experimental (scatter) and predicted spectra (line) for the mixed structures with c.) PEO and d.) PSS.

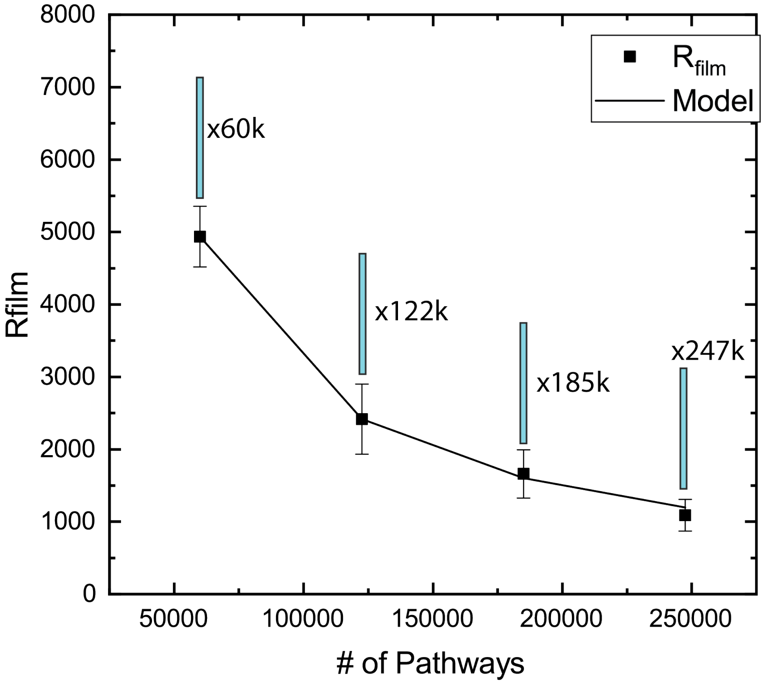

Figure 5.6: Plot showing resistance calculated from extracting the value from the ECM shown in Figure 5.4 and the model based off of Equation 5.2

film based off of the percolated pathways is of interest, this can still be extracted by simply modeling the high frequency (i.e. connected) impedance data. To demonstrate this, the resistance of the film was extracted by extracting the resistance from the higher frequency peak and plotting this data along with the resistance calculated from our previous sections discussion.

The calculated values of resistance and conductivity are plotted in Figure 5.4. The reproducibility of the impedance data across multiple samples is shown in Figure 5.5 along with the impedance response of the PEO ($90\ ^{\circ}C$) and PSS ($25\ ^{\circ}C$, $95\ \%RH$) with varying numbers of connected ion conduction pathways. To extract the resistance, the impedance and phase shift values were taken at the smallest absolute value of the phase shift where the impedance plateaus. The resistance was calculated using the Equation:

$$R = ZCos(Y) \tag{5.13}$$

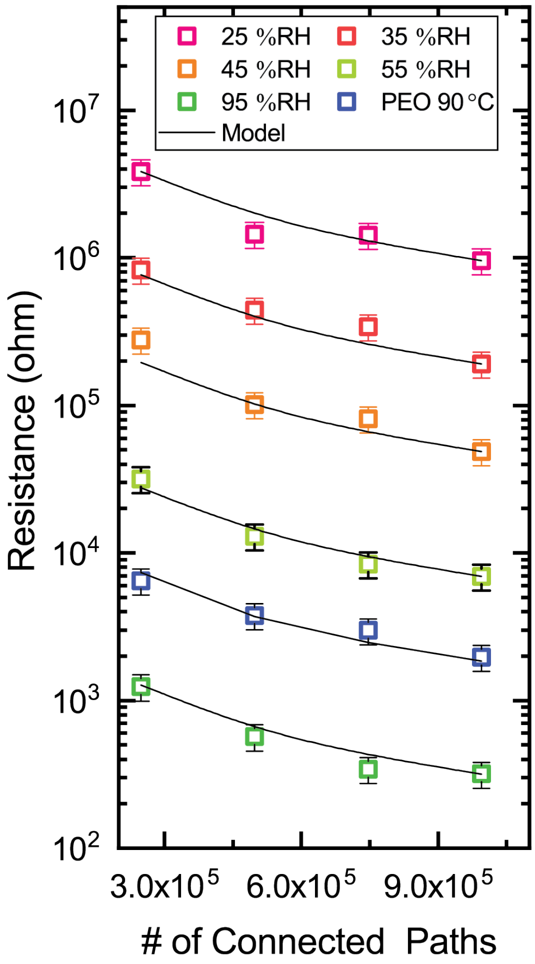

Figure 5.7: Combined electrochemical plots. Semi-log plot of the resistance of the PSS, PEO, and model (line) as a function of the total number of connected conduction pathways.

Where R is the resistance in ohms and Y is the phase shift in degrees. The calculated resistance values from the higher frequency peak in addition to the predicted resistance based off of Equation 5.5 are plotted in Figure 5.7. From inspection, the overlap of the two approaches to extracting the resistance of the film suggests that the conductivity value calculated by the community using the first peak / hemisphere analysis in EIS is characterizing the conductivity based off of only the connected domains and remains a viable strategy going forward.

Evidenced by the quality of model fits, we further justify an approximation made in our previous work [1] where conductivity of a complex ion transport pathway was calculated by using the fully connected ion conduction pathway similar to the fully connected structure demonstrated in this study. In this study, the conductivity of the fully connected BCP morphology similar to the structures studied here were used to predict the conductivity of a fingerprint morphology with tortuous pathways and a fraction of paths connected. In the study, two approximations were made for the calculation 1) only fully connected ion conduction paths contributed to the conductivity and 2) the conductivity decreased inversely with increases in tortuosity. This study confirms the first approximation.

The findings of this study can also provide additional insight into studies conducted by the broader BCE community on thick film BCEs. It is common for the BCE community to supplement statistical structure information such as small angle X-ray scattering (SAXS) with conductivity data to demonstrate different degrees of connectivity of ion conduction pathways in a thick film.[7–12] For example, Majewski et al [13] aligned a Liquid crystal-b-PEO BCE using magnetic fields and measured how the ion conduction changed as a function of degree of alignment and orientation. Structure of the 10 μ m thick membrane was characterized using SAXS and determined to have a very high degree of anisotropy. However, the highest conductivity of the aligned BCE was still a factor of 10 below the homopolymer conductivity. From our findings, we know that only connected paths contribute to conductivity. Therefore, as the ion conduction pathways become increasingly aligned, pathways become more isolated enabling a smaller concentration of insulating defects to fully block ion conduction in a path. If fully disconnected can be captured in frequency range, devices ECMs can be used to predict connectivity of any thin film conduction pathway network.

5.5 Conclusion

In conclusion, we demonstrate a method of isolating structural effects of ion conduction paths by fabricating nanoscale ion conduction pathways on top of IDEs. Using ebeam lithography to precisely pattern dielectric trenches, we designed IDEs with nanoscale pathways that could be connected or disconnected from one electrode to the other by designing nanoscale blockades within the path. For two different polymer electrolyte systems we used EIS to characterize the complex impedance response of the films on device sets with varying ratios of connected to disconnected pathways. By designing and fitting a simplified equivalent circuit model for devices containing one type of conduction pathway, we extracted the resistance and capacitance values pertaining to each component of the charge conduction path of individual connected and disconnected pathways. Using these values, we calculated the resistance and capacitance values for individual pathways. The impedance of the mixed structures were demonstrated to simply be a sum of the pathways by taking the resistance and capacitance values of single connected and disconnected pathways and scaling them by the total number of each path and showing that the values result in a impedance responses that fit well with the experimental values. From simple peak analysis of all EIS data, the extracted resistance was nearly identical to the connected pathway resistance, implying that the simplest interpretations of EIS data often only capture the resistance of the connected conduction pathways but is sufficient if calculating the conductivity of a membrane based off of connected pathways. Using precisely fabricated devices and our simple yet robust ECMs for extraction of resistance values from EIS, we provide a method for determining the connectivity of any ion conducting thin film polymer electrolyte system.

5.6 References

[1] Y. Kambe, C. G. Arges, D. A. Czaplewski, M. Dolejsi, S. Krishnan, M. P. Stoykovich, J. J. de Pablo, and P. F. Nealey, Nano Letters (????).

[2] N. Agmon, Tech. Rep. (1995).

[3] Z. Lu, M. Lanagan, E. Manias, and D. Macdonald, ECS Transactions **28** (2010).

[4] B. Dong, Y. Kambe, M. Dolejsi, P. F. Nealey, and S. N. Patel, in *Meeting Abstracts* (The Electrochemical Society, 2018), 39, pp. 2295–2295.

[5] D. K. Paul, R. McCreery, and K. Karan, Journal of the Electrochemical Society **161**, F1395 (2014), ISSN 0013-4651.

[6] G. Song, Cement and concrete research **30**, 1723 (2000).

[7] P. W. Majewski, M. Gopinadhan, and C. O. Osuji, Journal of Polymer Science, Part B: Polymer Physics **50**, 2 (2012), ISSN 08876266.

[8] P. Deshmukh, M. Gopinadhan, Y. Choo, S. K. Ahn, P. W. Majewski, S. Y. Yoon, O. Bakajin, M. Elimelech, C. O. Osuji, and R. M. Kasi, ACS Macro Letters **3**, 462 (2014), ISSN 21611653.

[9] M. Gopinadhan, P. W. Majewski, E. S. Beach, and C. O. Osuji, ACS Macro Letters **1**, 184 (2012), ISSN 21611653.

[10] P. W. Majewski, M. Gopinadhan, and C. O. Osuji, Soft Matter **9**, 7106 (2013), ISSN 1744-683X, URL `http://xlink.rsc.org/?DOI=c3sm50320h`.

[11] M. J. Park and N. P. Balsara, Macromolecules **43**, 292 (2010), ISSN 00249297.

[12] L. Ramõn-Gimenez, R. Storz, J. Haberl, H. Finkelmann, and A. Hoffmann, Macromolecular Rapid Communications **33**, 386 (2012), ISSN 10221336.

[13] P. W. Majewski, M. Gopinadhan, W.-S. S. Jang, J. L. Lutkenhaus, and C. O. Osuji, Journal of the American Chemical Society **40**, 17516 (2010), ISSN 1520-5126.

CHAPTER 6

QUANTITATIVE ANALYSIS OF TORTUOSITY ON ION TRANSPORT IN POLYMER ELECTROLYTES

6.1 Abstract

Ebeam lithography was used to fabricate nanoscale channels out of insulating SiO_2 between the counter electrodes of an interdigitated electrode and homopolymers were reflowed into the channels to form nanoscale ion conduction channels. The ion conduction paths were then sequentially rotated to investigate the role of path and electric field and tortuosity on the impedance of the film. The study investigated the behavior of tortuosity and relative orientation of the conduction pathway to the applied electric field through experiment and finite element modeling. The resistance of the connected pathways increased faster than what would have been expected from the increase in ion transport pathways. This suggests that ion transport behavior is affected by the orientation of conduction pathways and the tortuosity of the path can increase the resistance of the path beyond a linear scaling with the increase in transport path length. This study suggests that conductivity values calculated in thick film systems with well phase separated morphologies may be resulting in significantly lower conductivity values than what should be expected from the conduction pathways.

6.2 Introduction

In our previous work,[1] we demonstrated that nanofabricated pathways can be used to study effects on nano-scale transport through two different types of ion-conducting polymer systems. Through this study, we found that the conductivity of the BCE film scales with the total number of connected domains and the tortuosity of the connected domains. In the previous chapter, we investigated the effect of the connected and disconnected domains on the impedance response of the system and determined that the complex impedance and the resistance of the film scale linearly or inverse linearly with the total number of connected and disconnected domains.

Here we expand on the previous chapter's work by investigating the second factor that governed the resulting impedance response in the BCE film, tortuosity. Tortuosity was studied by fabricating periodic nanoscale trenches on top of interdigitated electrodes (IDEs) and rotating the ion conduction pathways relative to the applied electric field of the IDEs to model tortuosity. We find that the resistance of the films deviate from the expected results at high degrees of rotation or tortuosity. The behavior, however is shown to disappear with high rotation resistance values converging to simply the length increase in transport path at high degrees of rotation. The results demonstrated in this chapter sheds light on the complex impedance behavior from ion conduction pathways exhibiting high levels of tortuosity.

6.3 Methods

6.3.1 Materials

The polymers used for this study included a poly(styrene-rand-styrene sulfonate) (PSS, Mn 24.7 kg/mol with 88 % sulfonation of styrene repeat units) and poly(ethylene oxide) (PEO, Mn 20 kg/mol with dimethyl-terminated end groups) with a lithium bis(trifluoromethanesulfonyl) imide (LiTFSI) salt, the same systems from our previous study in Chapter (cite blocked). PSS, PEO, and LiTFSI were all from Polymer Source, Inc. and all other chemicals (N,N-dimethyl formamide (DMF, regular and 99 % anhydrous for the glovebox), Acetone, 2-propanol (IPA), and Anisole) were received from Sigma-Aldrich or Fisher Scientific and used without further purification. PSS was used as is while PEO and LiTFSI were dried at 60 $^{\circ}C$ under vacuum for 48 and 72 hours respectively in an inert glovebox antechamber before being brought into the glovebox. Solutions of PEO in DMF and LiTFSI in DMF both with concentrations of 20 mg/mL were prepared and placed on a shaker in the glovebox for at least 24 hours before combining in a ratio of Li cation to EO units in PEO of $r = 0.05$, which was subsequently shook for an additional 24 hours prior to sample preparation.

The Pt interdigitated electrodes with dielectric walls were fabricated on semiconducting polished silicon wafers (1 μm thermally grown oxide) obtained from WRS materials. The spin-on-glass was received from Desert Silicon and used with no further filtration. GL2000 ebeam resist was received from MicroChem Corporation and diluted 1:1 by volume in anisole prior to spin coating. The poly(dimethoxysiloxane) (PDMS) mix kit (Sylgard 184) was purchased from Sigma Aldrich and used as instructed. 10:1 by weight of the base and crosslinker were mixed respectively and poured on top of a petri dish with a taped down Si wafer. After degassing, the PDMS was crosslinked at 75 $^{\circ}C$ for 4 hours.

6.3.2 Fabrication of the Interdigitated Electrodes

Figure 6.1 shows the fabrication process of the IDE with nanoscale dielectric trenches on top. The interdigitated electrodes were comprised of a 5 nm Titanium (Ti) adhesion layer and a 20 nm thick Platinum (Pt) layer, which were fabricated using conventional photolithography on top of a silicon (Si) wafer with 1 μm of thermal oxide grown on the surface. The IDE contained a total of 40 electrodes that were separated from each counter electrode by 8 μm. The overlap between each counter electrode was 1 mm, and each of the electrode teeth was 2 μm wide. 120 nm of spin-on-glass (SOG) was spin coated on top of the IDEs, annealed at 95 $^{\circ}C$ for 1 min, 115 $^{\circ}C$ for 1 min, then 180 $^{\circ}C$ for 15 $mins$. The device was treated with an O_2 plasma descum process (50 W 50 $sccm$) and spin coated with 205 nm of GL2000 ebeam resist and baked on a hotplate at 180 $^{\circ}C$ for 3 $mins$. The ebeam resist was patterned using the JEOL 9500 electron beam writer with an effective ebeam dosage of 350 $\mu C/cm^2$. The film was then developed in Amyl Acetate without agitation for 45 sec, quenched in IPA, and dried with Nitrogen. The devices were etched using a Fluorine etcher. Following the Fluorine etch, the excess ebeam resist was removed using an O_2 plasma etch (50 W forward bias, 50 $sccm$ O_2) for 2 $mins$ in the same chamber without any prior conditioning. The resulting film was removed from the Fluorine etcher and placed inside the YES downstream asher and exposed to a descum process (500 W, 50 $sccm$ O_2) for 3 $mins$. The resulting IDEs had periodic 200 nm wide and 120 nm high walls that, when multiple walls were placed in parallel, formed trenches that spanned from one electrode to the other.

6.3.3 Polymer sample preparation on IDEs

One hydrated and one anhydrous polyelectrolyte were studied for different applications. First, the 24.7 k MW poly(styrene-rand-styrenesulfonate) (PSS) with 80 % of the repeat units functionalized was studied under humidified conditions. When in humid conditions, the water infiltrates the film, dissociates the protons from the static sulfonate groups, and forms a water conduction path for proton transport. The higher polarizability of the water is known to increase the dielectric permittivity of the PSS film. [2, 3] Following an oxygen plasma functionalization, PSS was uniformly deposited on top of the IDEs via spin coating. PDMS cubes with surfaces cured on top of the atomically flat Si wafer were placed on top of the IDE with the PSS coated on top then annealed at 155 $°C$. The annealing process thermally reflowed the PSS into the trenches and the PDMS reacted with the hydroxyl groups on the dielectric walls forming a hydrophobic coating of PDMS on top of the trenches when the PDMS was peeled off. The thickness of the polymer films in the trenches was determined by AFM of the bare IDE then of the IDE after the PSS was reflowed into the film and the PDMS removed. The identical PSS polymer was also deposited onto the control IDE via spin coating. The thickness was determined by ellipsometry on a witness wafer to be 28 nm and 56 nm.

Second, the 20k MW PEO with LiTFSI (PEO/LiTFSI) was studied in anhydrous conditions at 90 $°C$. Following an oxygen plasma functionalization, a solution of PEO/LiTFSI in DMF ([Li:EO] = r = 0.05) was uniformly deposited by spincoating on top of the IDEs. Samples were heated at 100 $°C$ for 5 hours to thermally reflow most of the PEO/LiTFSI into the trenches. Samples were heated at 120 $°C$ for 20 minutes before PDMS was used to press remaining PEO on top of trench walls into trenches. PDMS was peeled off then

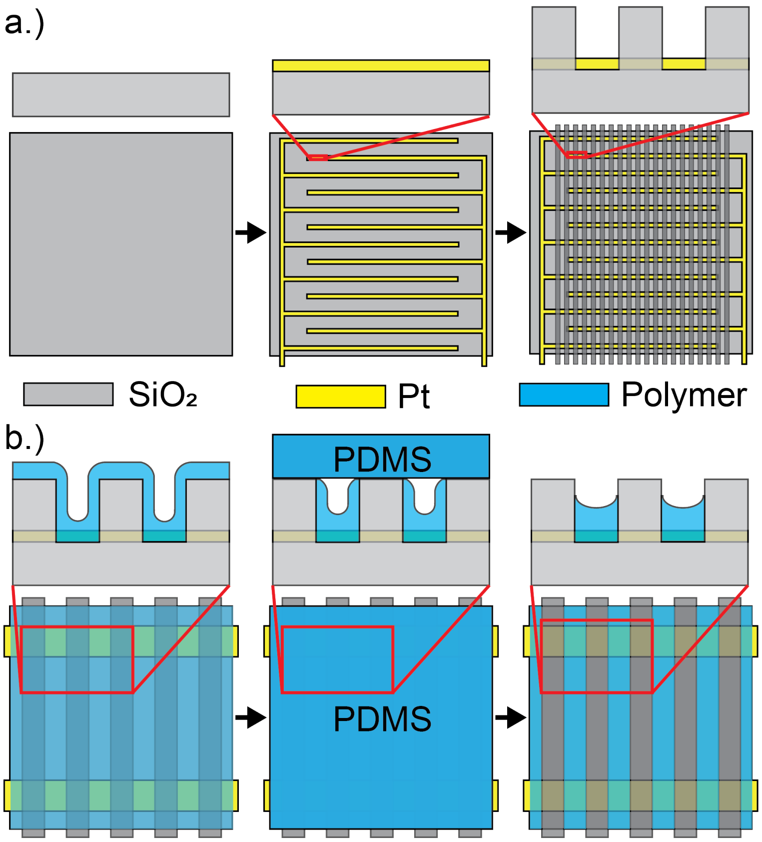

Figure 6.1: Fabrication schematic of the a.) Pt interdigitated electrodes fabricated via photolithography and the dielectric trenches patterned using ebeam lithography and b.) the ion conducting polymer reflow process using PDMS and thermal reflow.

AC impedance measurements were made using a setup within the inert glovebox conditions. The identical PEO solution was also deposited onto a witness wafer via spin coating. The thickness was determined by ellipsometry and confirmed by scratch test and AFM to be 46 nm. Note: the PEO thickness in the trench is subject to a higher degree of error when characterized in the trench using AFM at ambient conditions due to the extremely hygroscopic nature of PEO. Therefore, the thickness of the PEO in the trench was estimated to be double the spin coat thickness at 92 nm. This is a reasonable value considering the PSS reflow also doubled the spin coat thickness.

6.3.4 Structure Characterization

Top-down images of the dielectric trenches were taken with the Carl Zeiss – Merlin field emission scanning electron microscope. The acceleration voltage was 1.0 *kV* with a working distance of 4 *mm* using an in-lens detector. 1 *nm* of Pt/Pd was sputtered onto the surface of the device using the Cressington 108 Auto Sputter Coater to reduce charging due to the electron beam. Topography of the film was characterized by the Bruker Atomic Force Microscope.

6.3.5 Controlling Ion Conduction Pathways

Figure 6.2 shows the different dielectric topologies that were patterned on top of the IDEs using ebeam lithography. The SEM and AFM micrographs shown are taken after all of the polymer sample preparation and electrochemical characterization was completed. Ion conduction pathways were designed as periodic trenches that were 200 *nm* wide and oriented orthogonal to the electrodes, resulting in the shortest and most direct path. The width of the wall between trenches was also 200 *nm* wide. A trench that spans from one electrode to the other along the shortest path possible is referred to as the "0° rotation path", as shown in Figure 6.2a. The ion conduction paths were then sequentially rotated to 30°, 45°, 60°, and 75°. 45° and 75° while maintaining the 200 *nm* channel width. Rotated conduction paths are shown in Figures 6.2 b and c respectively.

Additional control IDEs were fabricated with 8, 12, and 16 *μm* electrode separation distances. On top of the IDEs, ebeam lithography was used to fabricate the 0° rotation path. In this study, only the PSS was studied.

6.3.6 Electrochemical Characterization

The AC impedance measurements for the PSS samples were made under humidified and controlled temperature conditions. After the devices with PSS were prepared, the samples were placed inside of the relative humidity chamber and conditioned at 25 $^{\circ}C$ 25 $\%RH$ for 6 hours prior to measurement. The samples were then measured from 1 MHz to 0.1 Hz with a perturbation voltage of 10 mV. After all the devices were measured, the relative humidity was raised to the next value and the devices were conditioned for a minimum of 3 hrs. In this study, the samples were measured at 25, 35, 45, 55, 65, 75, 85 and 95 $\%RH$ all at 25 $^{\circ}C$.

The AC impedance measurements for the PEO samples were made under inert conditions with temperature control. Samples were placed on the heated stage of the probe station for 10 $mins$ before making AC impedance measurements from 1 MHz to 1 Hz with a perturbation voltage of 100 mV. Each sample was measured at 90, 100, 110, 120, and 130 $^{\circ}C$, well above the melt temperature of 20k MW PEO (70 $^{\circ}C$).

To extract out the resistance and the capacitance for comparison, an equivalent circuit model (ECM) was utilized. The ECM can be seen in Figure 6.4a where each component is defined by a physical element in the ion transport pathway. The justifications of the circuit elements are explained in detail in the work by Sharon et al [4] where similar ion conduction pathways were studied on top of IDEs.

6.3.7 Finite Element Modeling

Finite element modeling was used to simulate the resistance of specific ion conduction pathways as a function of rotation. The resistance near the SiO_2 and polymer interface was reduced to simulate interfacial effects. First, the interfacial effect was held constant as a function of rotation. In the second simulation, the intefacial width was shown to increase as a function of the amount of the electric field being applied orthogonal to the interface.

We developed the mathematical model to investigate the impedance of symmetric cell with blocking electrodes. If there is no electrochemical reaction due to the blocking electrode and there is an applied AC potential, the mass transfer in the polymer can be neglected. With this assumption, the potential in the polymer electrolyte is governed by Laplace's

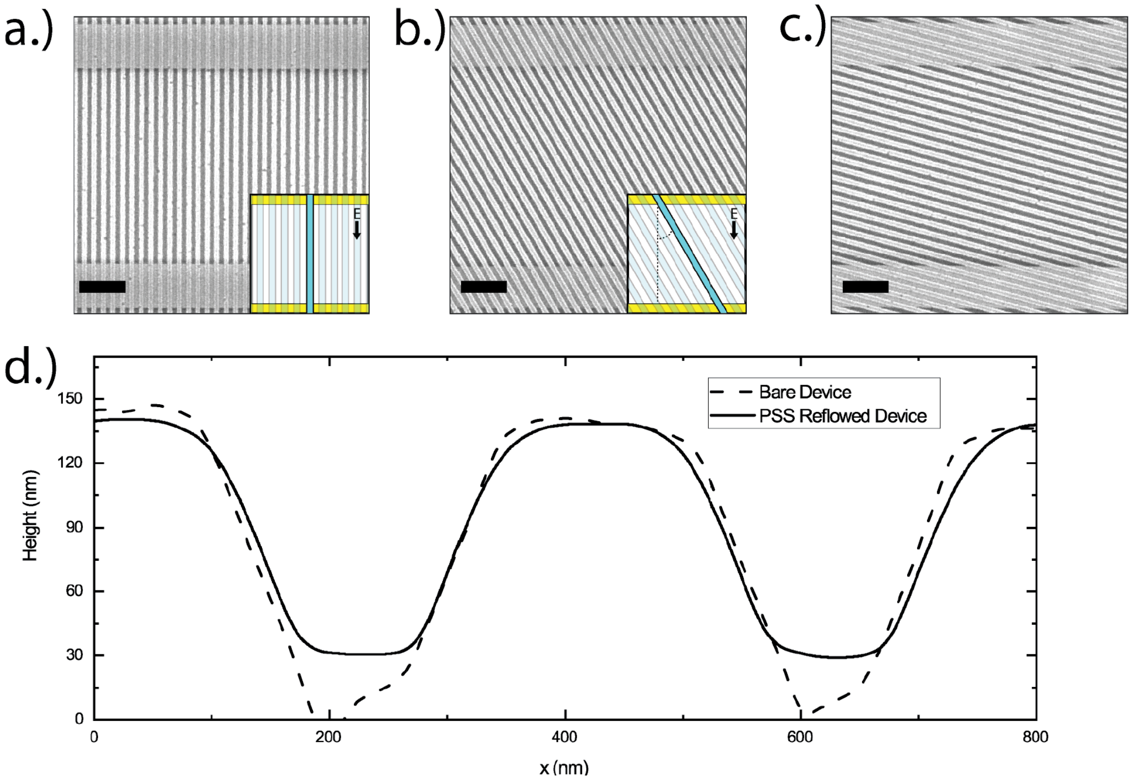

Figure 6.2: Micrographs of the fabricated trenches with reflowed PSS homopolymer. Top down SEM micrographs of the device with a. 0° rotation, b. 45° rotation, and c. 75° rotation. The scale bars are 2 μm. d. AFM cross section topological trace of two trenches before (dotted line) and after (solid line) the deposition and reflow of homopolymer for the PSS system.

equation as below.

$$\nabla^2\phi = 0 \tag{6.1}$$

The system responses to the applied sinusoidal signal can be separated into the steady-state term and the perturbing signal term:

$$\phi = \bar{\phi} + \tilde{\phi}Sin(\omega t) \tag{6.2}$$

where $\bar{\phi}$ is the steady state potential and $\tilde{\phi}$ is perturbation component. For Perturbations of $\tilde{V}Sin(\omega t)$ at open circuit, steady state potential can be neglected.

$$\phi = \tilde{\phi}Sin(\omega t) \tag{6.3}$$

With Euler's relationship, the potential response and perturbing voltage are described as:

$$\phi = Re(\tilde{\phi}exp(j\omega t) \tag{6.4}$$

$$V = Re(\tilde{V}exp(jwt) \tag{6.5}$$

The current density at the blocking electrode surface is expressed as:

$$-\kappa\frac{d\phi}{d\tau}|_s = i = C_0\frac{V - \phi_s}{dt} \tag{6.6}$$

where κ is electrolyte conductivity, C_0 is the double layer capacitance. The current at the electrode surface can be converted to the frequency domain from time domain.

$$-\nabla\phi|_s = j\frac{\omega C_0}{\kappa}V - \phi_s \tag{6.7}$$

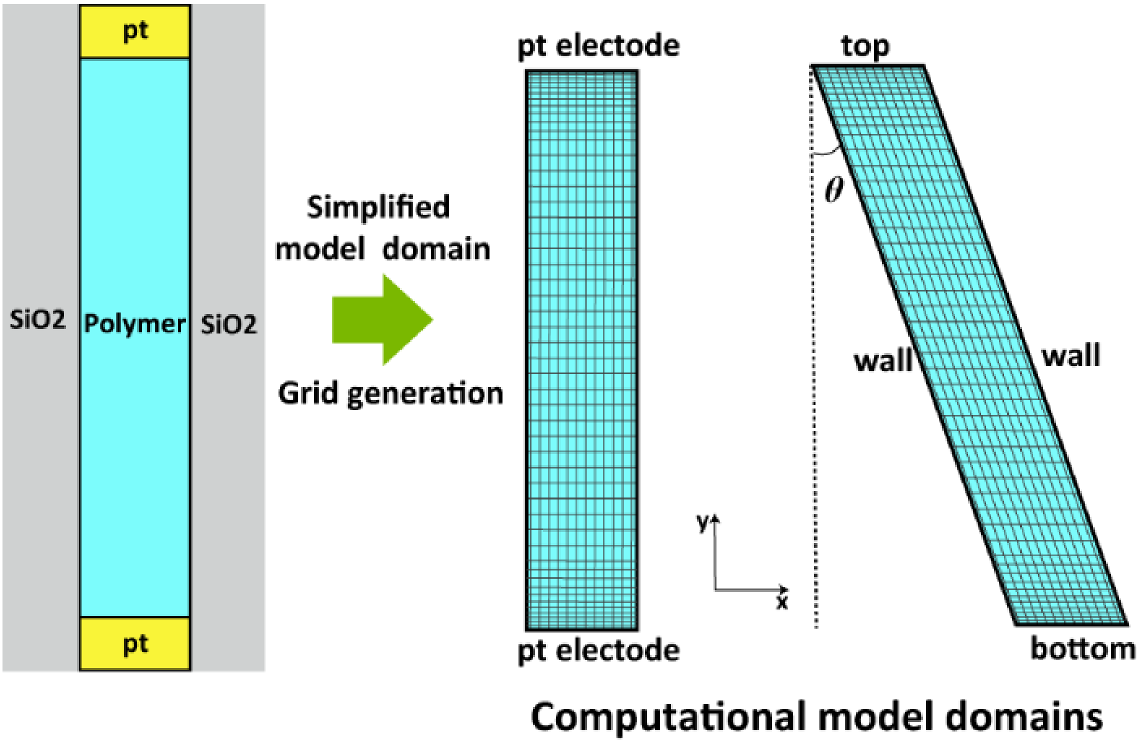

Figure 6.3: Schematic of symmetric cell and computational domains at the different angle 0 to 75.

Figure 6.3 shows the schematic of symmetric cell and the two-dimensional (2-D) computational domain. The adaptive boundary layer near both electrodes was applied by the stretching factor for the structures ranging from 0 to 75 degrees. Note that the only the polyelectrolyte is considered as the model domain without the thickness of the blocking electrode. We used the finite element method to solve the Equation 6.1 using COMSOL Multi-physics ver.5.3. For boundary condition, perturbation voltage as presented in Equation 6.7 is applied to the top and bottom surface and the insulated wall conditions are applied to both side interfaces between SiO_2 and polymer.

6.4 Results and Discussions

6.4.1 Rotation of Ion Conduction Pathways on Resistance and Capacitance

Figure 6.4 shows the resistance and the capacitance changes for PSS as a function of the angle rotation and relative humidity while Figure 6.5 shows the resistance and the capacitance changes for PEO as a function of the angle rotation and relative humidity. Two observations are made. First, the resistance of the film increases with increasing rotation. Second the absolute capacitance is shown to not change significantly with rotation. The model overlaid on the two Figures are calculated by the equation:

$$R_{rot,RH,T} = R_{0^\circ,RH,T} \cdot Cos(\theta) \tag{6.8}$$

Where $R_{rot,RH,T}$ is the resistance of the PSS or PEO films at given degrees of rotation, $R_{0^\circ,RH,T}$ is the resistance of the PSS or PEO at 0° for each measurement condition, and θ is the degree of rotation. For the PSS system, the model fit improves at higher RH values and for the PEO system, the model fit improves at higher temperatures.

Figure 6.6 shows the normalized resistance and capacitance values for the PSS and PEO systems. The resistance was normalized by the equation:

$$R_{n,rot} = \frac{R_{rot,RH,T}}{R_{0^\circ,RH,T}} \tag{6.9}$$

Where $R_{n,rot}$ is the normalized resistance at each rotation and $R_{rot,RH,T}$ is the resistance for PSS or PEO at each given measurement condition and rotation.

The capacitance was normalized using a similar equation:

$$C_{n,rot} = \frac{C_{rot,RH,T}}{C_{0^\circ,RH,T}} \tag{6.10}$$

Where $C_{n,rot}$ is the normalized capacitance at each rotation, $C_{rot,RH,T}$ is the capacitance for PSS or PEO at each given measurement condition and rotation, and $C_{0^\circ,RH,T}$ is the

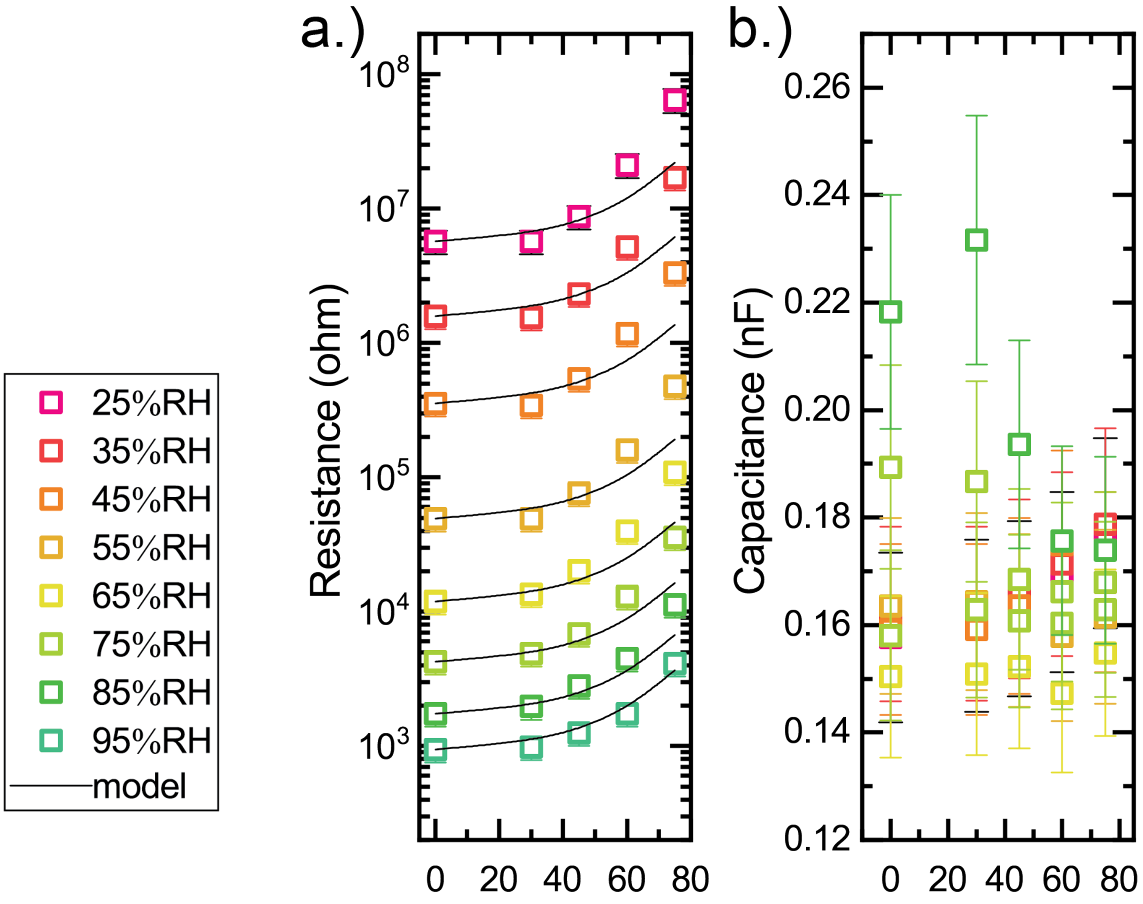

Figure 6.4: a.) Resistance and b.) capacitance data for the PSS ion conduction channels as a function of rotation and RH. Model (line) from Equation 6.8

capacitance of the PSS or PEO at 0° for each measurement condition. The comparison of the normalized resistance and capacitance of the PSS and PEO systems reveals two interesting trends. First, in both PSS and PEO systems, with increasing RH for PSS and increasing temperature for PEO, we see a convergence of the higher rotation resistance values to the trend of $1/cos(\theta)$. Second, the capacitance of the PSS seems to very at high degrees of rotation singificantly more in comparison to PEO which stays constant throughout the range of rotations.

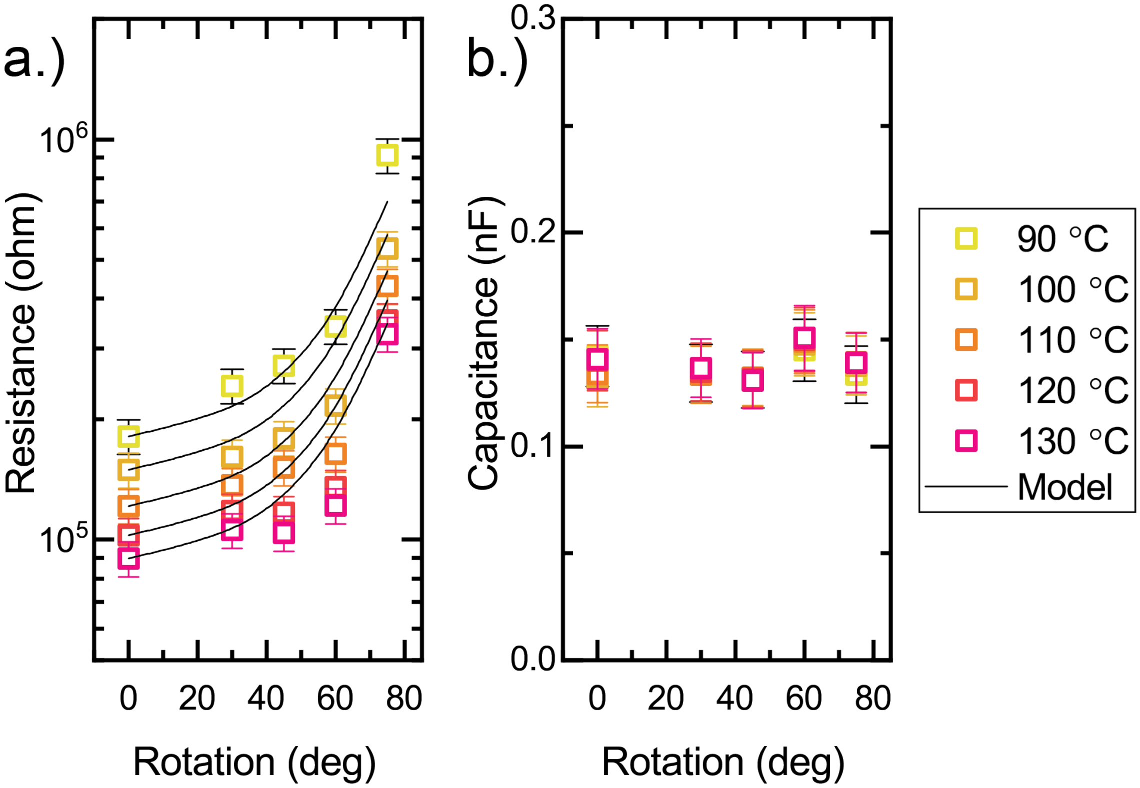

Figure 6.5: a.) Resistance and b.) capacitance data for the PEO ion conduction channels as a function of rotation and temperature. Model (line) from Equation 6.8

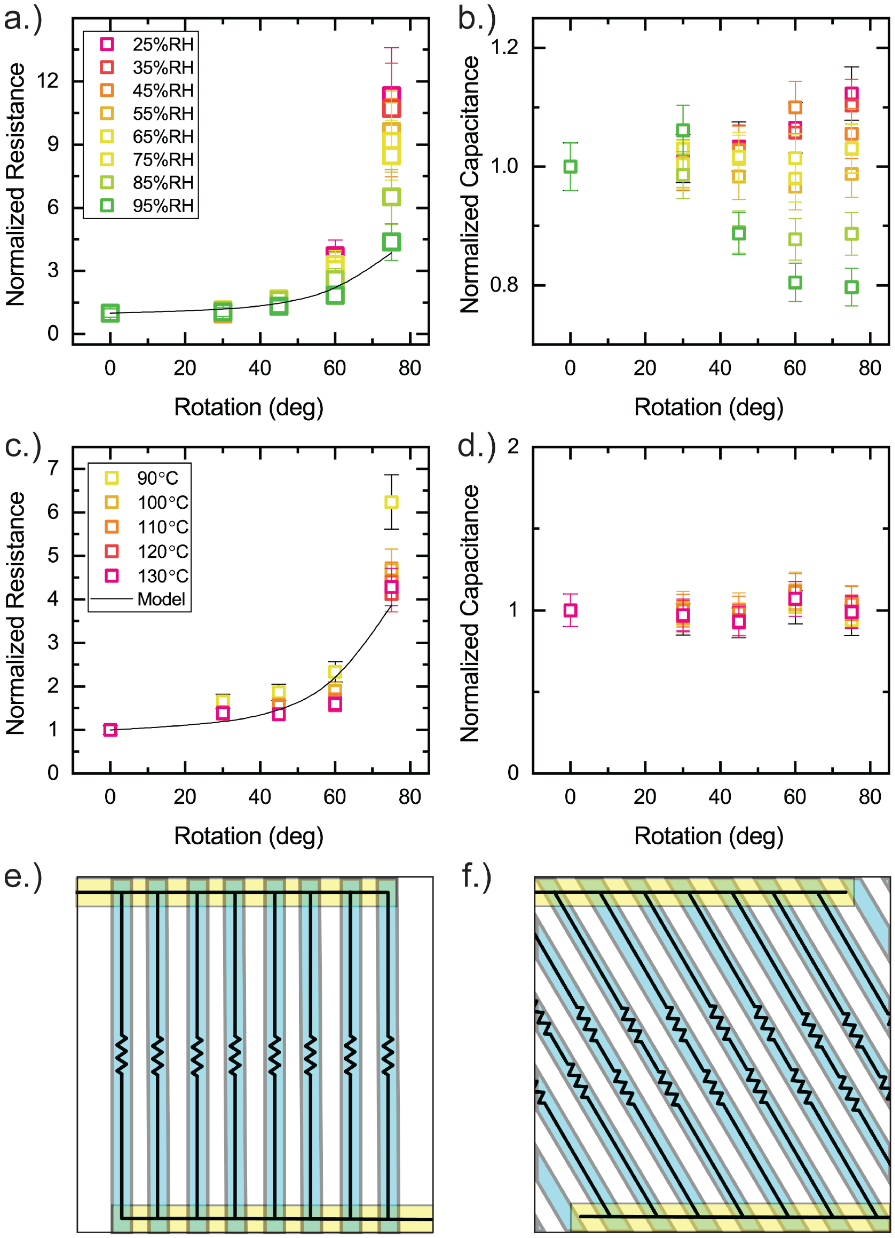

Figure 6.6: Normalized a.) resistance and b.) capacitance as a function of rotation and RH for the PSS. Normalized c.) resistance and d.) capacitance as a function of rotation and temperature for PEO. Equivalent circuit diagram demonstrating the equivalent circuit used for the models for the e.) 0° and f.) 45°.

6.4.2 Resistance Change with Rotation

In the rotation study, we hypothesize that the resistance of the charge conduction path would linearly increase with the increase in path length. As the ion conduction path is rotated, the conduction path increases as a function of the hypotenuse, or $1/cos$. With the rotation study, we see a deviation from our hypothesis in in the resistance. To understand the behavior of the resistance change relative to the simple wire approximation, in Figure 6.6a and c we also plot the $1/cos$ as a reference point. Up to 45° of rotation, the resistance seems to follow the $1/cos$ trend which remains constant with our initial hypothesis. At 60° rotation and above, we begin to see a deviation from the $1/cos$ behavior, suggesting that tortuosity in a ion conducting dielectric cannot be approximated simply as a resistor of increasing length.

The normalized resistance for the 75° morphology at 25 $\%RH$ for PSS is nonetheless still a factor of 4 lower than the normalized resistance calculated for the 100 % blocked morphology in the previous study. This suggests that a highly tortuous but connected pathway can exhibit an intermediate resistance that is higher than what would be expected from a simple pathlength increase, but still lower than what would be expected from a blocked path. This observation may help shed light on how well phase separated BCE thick films report f values that are an order of magnitude lower compared to values predicted by EMT.[5, 6] Our results suggest that the highly tortuous domains will exhibit a resistance that is higher than what would be expected by a simple increase in path length. It is therefore likely that the effective conductivity of BCE films may be significantly higher than what is currently reported in the literature. We will attempt to quantitatively disseminate the normalized resistance deviation from $1/cos$ at high angles of rotation. For an example, Irwin et al, [7] showed a shift in the conductivity of the lamellae phase forming PS-b-PEO with LiTFSI salt. After crossing the Ordered Disordered transition, the conductivity increased, suggesting that the lamellae forming BCE contained disconnected domains. In light of our study, an alternative explanation could be that the ion conduction pathways are highly tortuous therefore the crossing over of the ODT improved tortuosity of the connected domains reducing the compounding effects of tortuosity.

We propose one possible hypothesis to describe the normalized resistance increasing rapidly non-linearly with respect to the angle. It is based on the evidence that the ion mobility near the wall is lower compared to the mobility near the center of the channel due to the adsorption of ions near interface.[8] Under the assumption that κ is constant in all domain regions, the normalized resistance is increased considering only the conduction path as the angle increases, resulting in the following the 1/cos curve. Even though there is the wall effect due to adsorption regardless of the angle, the normalized resistance may be the same as the 1/cos curve. Thus, it can be assumed that there is a wall effect related to the angle. The angle relationship may be interpreted as the difference in the applied electric field and the magnitude of the electric field applied normal to the wall interface. At higher degrees of rotation, assuming the electric field remains constant, a larger magnitude of the field applies a force normal to the wall.

As shown in Figure 6.7, the applied electric filed force E, consists of the electric force toward the wall, E_{wall} and the electric force parallel to hypotenuse of polyelectrolyte, E_{act}. This hypothesis follow two assumptions. One may assume that magnitude of the E_{wall} is related to electrolyte conductivity at the wall $\kappa wall$ because of the ion adsorption near wall. As the angle increases, the effect of the E_{wall} becomes dominant, and there is no amount of conductivity loss κ_{loss}, compared to bulk conductivity, κ_{bulk}, if the E_{wall} is zero at zero degrees. The second variable is that the magnitude of the E_{act} may affect the total distance from the wall that exhibits a lower ion mobility.

Similar to the relationship between displacement thickness and velocity in microchannel flow, the wall effect thickness may be inversely proportional to E_{act}.

Above assumptions can be expressed as:

$$\kappa_{wall} = \kappa_{bulk}(1 - \alpha sin(\theta)) \tag{6.11}$$

$$\delta = d\frac{\beta}{Cos(\theta)} \tag{6.12}$$

where α is absorption fraction constant and β is wall effect constant, which corresponds to how much conductivity decreases near wall and the wall effect boundary layer is grown. Note that it is assumed that the varying between the κ_{wall} and κ_{bulk} is linear as presented in Figure 6.7.

Figure 6.8 shows the finite element analysis simulated resistance as a function of rotation. In Figure 6.8a, the change in resistance was studied in the case where the resistance of the ion conduction channel was higher near the interface of the SiO_2 and the polymer. The effect was shown for three cases where the interface covered 10, 20, and 30 % of the ion conduction channel starting from the interface which contains a resistance that is a factor of 5 larger in comparison to the middle of the channel. The result shows that the normalized resistance of the film did not change as a function of rotation much beyond $1/cos$. This study is further verified through the control experiment shown in Figure 6.9 where the resistance is shown to scale simply with the increase in length of the ion transport pathways. The simulation and the confirmation through the electrode separation study suggests that a constant interface cannot account for the deviation in resistance observed for the high rotations at low RH for PSS and low temperature for PEO.

The second simulation shown in Figure 6.8b shows the resistance change as a function of rotation when a θ dependence is considered. As the pathway is rotated and the electric field remains constant, a higher fraction of the electric field will apply a field orthogonal to the pathway wall. Ions in the connected paths likely experience an increasing force from the field pushing the ions against the walls, reducing the total number of mobile ions. The simulation in Figure 6.8b closely represents the resistance at low RH for the PSS and low temperatures for the PEO.

Evidenced by the convergence of the resistance to $1/cos$ behavior for PEO at high temperatures as well as PSS at high RH, the θ dependence is likely correlated to ion mobility

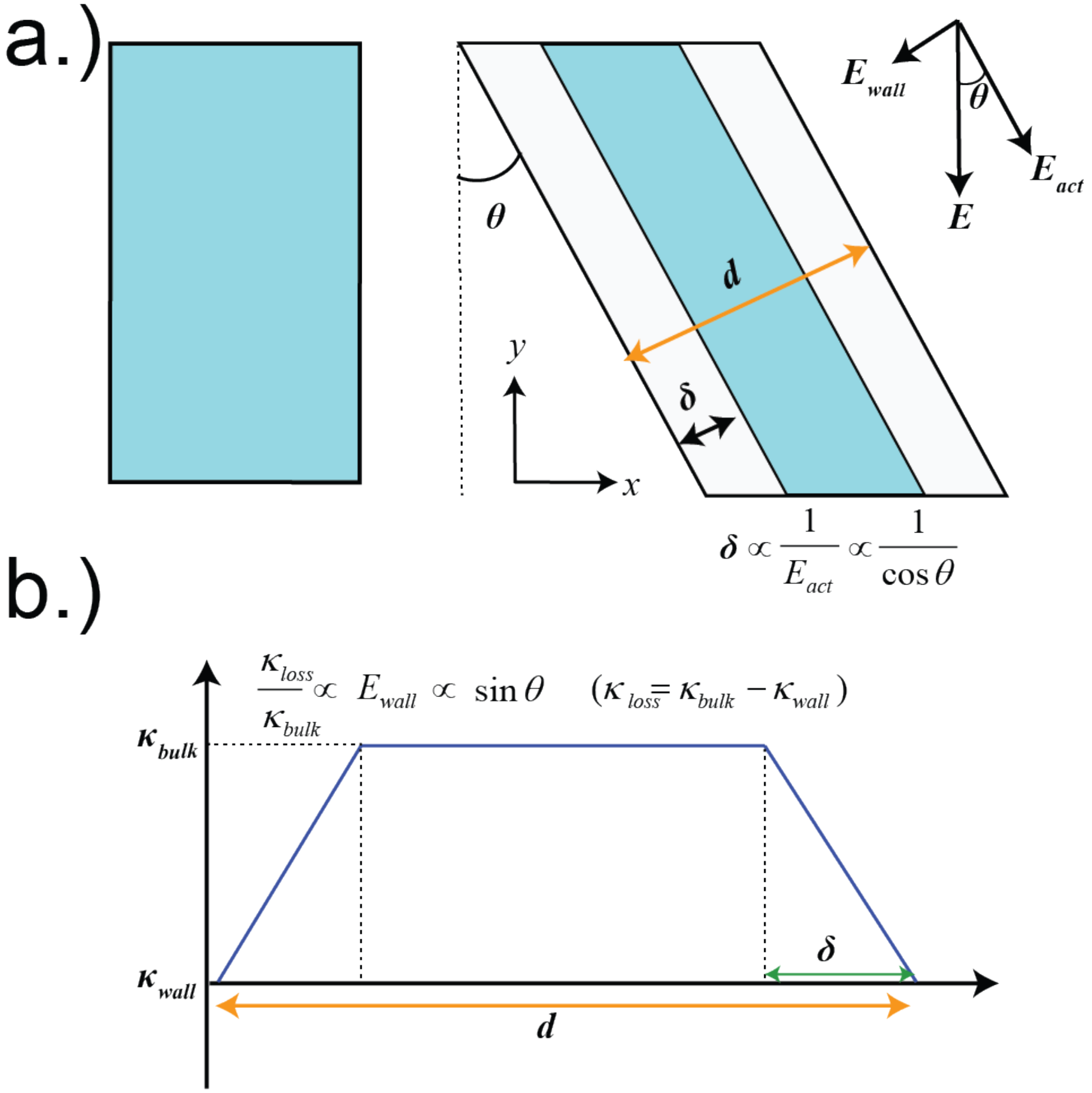

Figure 6.7: Schematic showing the reduction in the mobility of ions near the interface a.) as a top down image and b.) as a cross section.

or the average distance traveled at given frequencies.

6.4.3 Capacitance Change with Rotation

For the PSS system, the normalized capacitance seems to follow an inverse trend to the normalized resistance values of the film. At lower RH values, the capacitance increases with rotation. This is counter to what is expected with an increase in rotation. As shown in equation 6.13:

$$C = \frac{\epsilon \epsilon_0 A}{d} \tag{6.13}$$

Where C is capacitance, ϵ is the relative permitivity, ϵ_0 is the vacuum permitivity, A is the cross sectional area, and d is the ion conduction path distance between electrodes. As the distance of the ion conduction path (d) increases, the capacitance of a film with identical permitivity should decrease. The trend at 25 $\%RH$ and 45 $\%RH$ however goes up. The reduction in the capacitance however does appear at higher RH values where 75° rotation resulted in a decrease in capacitance below the 0° rotation film. This trend appearing for the hydrated PSS and not for PEO while the trend begins to follow the trend of Equation 6.13 suggests that that the addition of water is effectively modulating the electric field. This is well known in literature due to the highly polarizable nature of water enabling the hydrated polymer to reach relative permitivity values near 88 while the rest of the dielectric materials remain at a low 2.4.[9] However, the capacitance for the 75° film should have decreased to a value of 0.25 while the experiment only showed a reduction to 0.8. This suggests that the modulation of the electric field is not complete at 95 $\%RH$ due to the extreme rotation angles relative to the original electric field.

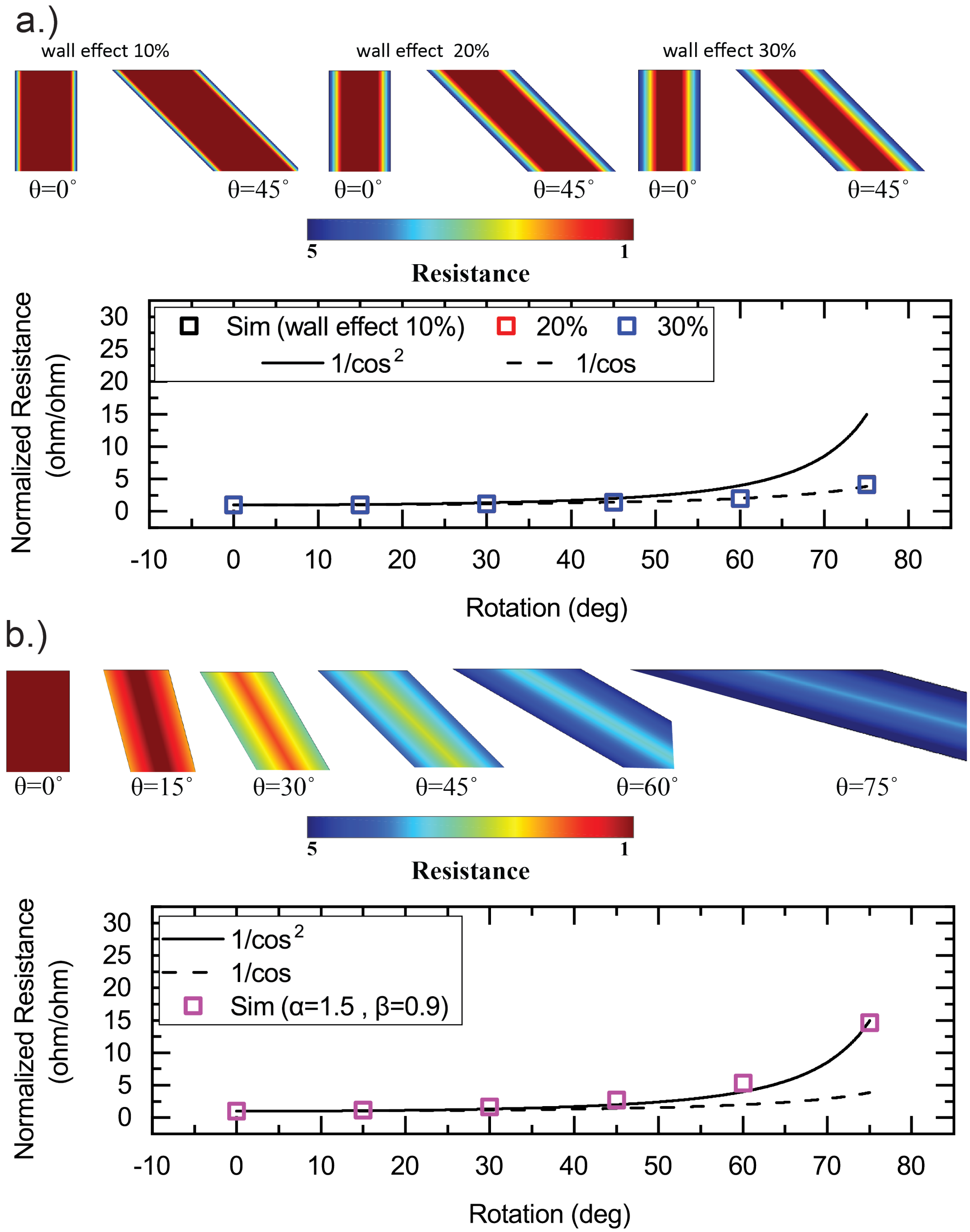

Figure 6.8: Finite element model simulation results for the case where a.) interfacial influence as constant and b.) interfacial influence varies as a function of incident electric field normal to the interface.

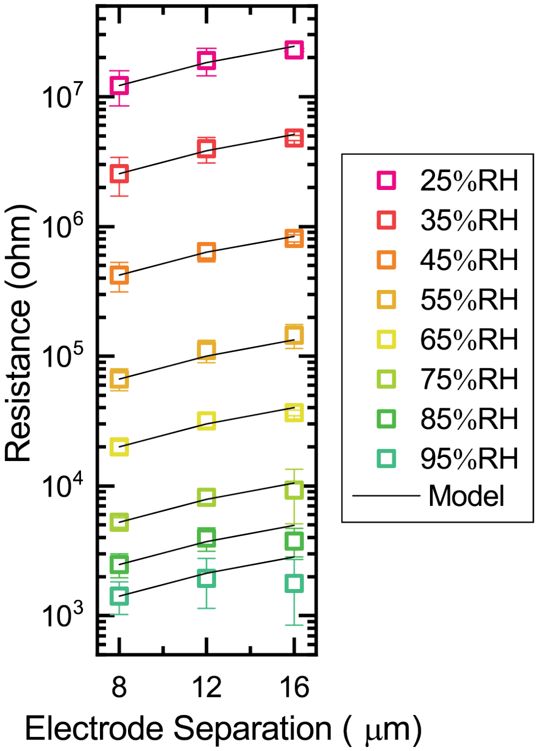

Figure 6.9: Resistance change and the linear fit as a function of electrode separation distance and RH.

6.5 Conclusion

In summary, periodic nanoscale conduction pathways with ion conducting homopolymer channels connecting electrodes were rotated relative to the shortest connected path to simulate tortuosity. It was shown that the resistance at high degrees of rotation demonstrated resistance values as large as a factor of 4 bigger than what would have been expected by the increase in ion conduction length. This behavior was observed in both hydrated and dry materials and disappeared at higher ion mobilities. This suggests that the mean free path length of the film can have an effect on how tortuous of a path can still be accounted as a connected path from one electrode to another. This serves as a critical deviation point between dielectric charge carriers and the equivalent circuit models used to date to demonstrate charge transport in polymer conductors and metal wires.

6.6 References

[1] Y. Kambe, C. G. Arges, D. A. Czaplewski, M. Dolejsi, S. Krishnan, M. P. Stoykovich, J. J. de Pablo, and P. F. Nealey, Nano Letters (????).

[2] N. Agmon, Tech. Rep. (1995).

[3] Z. Lu, M. Lanagan, E. Manias, and D. Macdonald, ECS Transactions **28** (2010).

[4] D. Sharon, P. Bennington, C. Liu, Y. Kambe, B. X. Dong, V. F. Burnett, M. Dolejsi, G. Grocke, S. N. Patel, and P. F. Nealey, Journal of The Electrochemical Society **165**, H1028 (2018), ISSN 0013-4651.

[5] J. Sax and J. M. Ottino, Polymer Engineering and Science **23**, 165 (1983), ISSN 0032-3888.

[6] D. T. Hallinan Jr. and N. P. Balsara, Annual Review of Materials Research **43**, 503 (2013), ISSN 1531-7331.

[7] M. T. Irwin, R. J. Hickey, S. Xie, S. So, F. S. Bates, and T. P. Lodge, Macromolecules **49**, 6928 (2016).

[8] B. X. Dong, P. Bennington, Y. Kambe, D. Sharon, M. Dolejsi, J. Strzalka, V. F. Burnett, P. F. Nealey, and S. N. Patel, Molecular Systems Design & Engineering (2019).

[9] Z. Lu, M. Lanagan, E. Manias, and D. Macdonald (2010), pp. 95–105.

CHAPTER 7

MOLECULAR CONTRIBUTIONS TO REDUCED ION TRANSPORT IN MICRO PHASE SEPARATED ION CONDUCTING BLOCK COPOLYMERS

7.1 Abstract

Lamellae forming poly(styrene-block-2-vinylpyridine) block copolymer was assembled with lamellae domains parallel to the interdigitated electrode surface, the poly(2-vinyl pyridine) was converted into an ion conductor, and the ion transport properties of the film were compared as a function of water content, volume expansion, and glass transition temperature. By forming parallel lamellae structure, the interfacial contributions to ion conduction were isolated from supramolecular contributions enabling us to isolate solvation site percolation and segmental mobility as the dominant mechanisms for transport.

7.2 Introduction

In our previous work,[1] the poly(styrene-block-2-vinylpyridine) (PS-b-P2VP) BCP morphology was controlled on top of IDEs and the AC impedance response was probed while varying the morphology. Orders of magnitude differences in both the ionic conductivity and the capacitance were observed and ion conductivity of complex and tortuous morphologies could be predicted within error if the ion conductivity of the direct and shortest BCP ion conduction path is known. However, it was clear that even when all of the morphology could be characterized, it was impossible to quantitatively decouple the effects of the morphology from the impedance responses that resulted from the existence of a soft BCP interface. The calculated value of the direct and connected path f was 0.63, which is well below the expected value of a direct and fully connected pathway. The discrepancy was attributed to the lower ion concentration near the interface and the influence of the glass poly(styrene) increasing the effective Tg of the P2VP/NMP+ I-.

Here, we report a study of BCE morphologies with a f of 1 by forming parallel lamellae of the PS-b-P2VP/NMP+ I- BCP on top of passivated IDEs. BCP and homopolymers were studied and the effects to the conductivity and capacitance due to the PS/P2VP interface were elucidated. It was demonstrated that the difference of ion conductivity at the interface of the PS and P2VP is influence by only two factors 1) the reduced number of functional sites near the interface due to the presence of PS and 2) the increased glass transition temperature of the P2VP/NMP+ I- backbone due to the presence of the glassy PS. (Further analysis)

7.3 Methods

7.3.1 Materials

The poly(2-vinylpyridine) (Mn 22 kg/mol) homopolymer and the poly(styrene)-block-poly(2vinylpyridine) (Mn 25-25 kg/mol) BCPs were received from Polymer Source and used as is. All other chemicals (Methyl Iodide (MeI), N,N-dimethylformamide (DMF), Acetone, 2-propanol (IPA), and Anisole) were received from Sigma-Aldrich or Fisher Scientific and used without further purification. The Pt interdigitated electrodes with dielectric walls were fabricated on semiconducting polished silicon wafers (1 μm thermally grown oxide) obtained from WRS materials.

7.3.2 Fabrication of Interdigitated Electrodes

Figure 1 demonstrates how the Interdigitated electrodes (IDEs) were fabricated on top of a silicon (Si) wafer with a micron thick thermal oxide growth on the surface. 5 nm titanium (Ti) adhesion layer followed by a 15 nm platinum (Pt) layer were deposited on top of the Thermal Oxide layer using conventional photolithography. The IDEs consisted of 200 electrode teeth, 2 μm wide electrode teeth, 8 μm electrode separation, and 2 mm of electrode overlap per teeth. Following the fabrication of the IDEs, 1 nm thick SiO_2 layer was grown

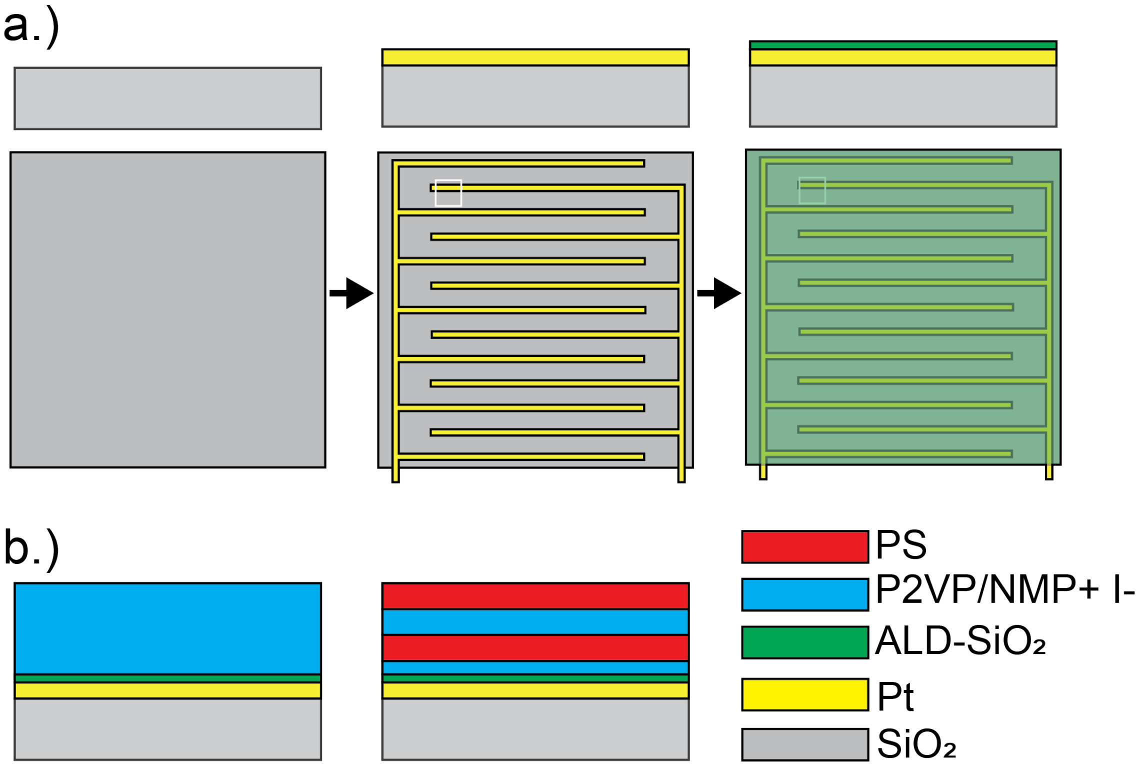

Figure 7.1: Fabrication schematic of the a.) passivated Pt interdigitated electrodes fabricated via photolithography and b.) the structures of the homopolymer and the BCP on top of the device.

on the surface using atomic layer deposition (ALD). The thin film of dielectric grown on the surface allowed for the homogenization of all of the surfaces eliminating homopolymer dewetting sites and increasing the range of temperatures that could be studied.

7.3.3 Deposition of P2VP/ NMP+ I- Homopolymer

22k molecular weight P2VP homopolymer was spin coated onto the IDEs and a Si wafer. The P2VP coated IDE was placed in a vapor chamber with a vial of iodomethane (MeI) for 48 hours. At 48 hours, the MeI vapor converted 50 % of the repeat units into P2VP/NMP+ I- confirmed through FT-IR. This reaction scheme has been reposted in detail previously. [2] The P2VP coated on the Si wafer was used to measure the thickness using ellipsometry.

7.3.4 Deposition of PS-b-P2VP/NMP+ I- Lamella

25k-25k PS-b-P2VP was spin coated onto the IDEs and a Si wafer. The Thickness was controlled by conducting a hole-island test. In the hole-island test, a range of thicknesses were coated onto the substrate and annealed at 250 $°C$ for 10 $mins$ inside the glove box. The samples were characterized under the AFM to determine a MW and composition dependent periodicity (L_0) for the BCP. L_0 was determined to be 28 nm for 25k25k. This matches our previous experimental data on the same material system. [1, 2] To form a parallel lamellar film with no hole-islands, the thickness multiples of 1, 1.5, and 2 of L_0, were spin coated onto the IDEs, annealed then functionalized in the vapor chamber. At 250 $°C$, the P2VP domain preferentially wetted the IDE surface while the PS domain preferentially wetted the free surface. With an asymmetric wetting behavior, the 1.5 L_0 thickness resulted in a smooth film with no hole islands.

7.3.5 Water Weight Added

The mass of water introduced into the 22k P2VP/NMP+ I- domain of the homopolymer was determined by first functionalizing uniform size P2VP powder in MeI for 48 hours and measuring the functionalized powder using the Dynamic Vapor Sorption (DVS) analysis. The water content in the 25k25k PS-b-P2VP/NMP+ I- was measured by drop casting a 5 $wt\%$ solution of the PS-b-P2VP on top of a 1 cm by 1 cm piece of Si wafer that was weighed previously. The dry thickness was 100 μm. After the BCP film was dry, it was placed in the thermal chamber and annealed with the identical protocol to the thin film. The prepared thick film was a solid loading of 30 mg without the Si wafer. The homopolymer and BCE samples were measured in the DVS at 25 $°C$ across 0, 15, 25, 35, 45, 55, 65, 75, 85, 95 $\%RH$. The $\%RH$ was changed after the rate of change of mass at each measurement condition was reduced to 2 mg/min. The samples were conditioned from 0 $\%RH$ up to 95 $\%RH$ then dehumidified down to 0 $\%RH$. The dehumidification cycle was used for the water weight calculations shown in Figure 7.2.

7.3.6 Characterization of Volume Expansion with Hydration

The volume expansion with hydration was estimated by first coating the 42 *nm* thick 22k P2VP homopolymer and 42 *nm* thick 25k25k PS-b-P2VP BCPs on top of a Si wafer. The BCP was then annealed at 250 °*C* in the glove box. The homopolymer and BCP films were then annealed in a sealed chamber with excess MeI vapor for 24 *hrs*. The samples were then dried inside of a vacuum chamber over nigh prior to immediately being transported to the ellipsometer and measuring the thickness. The two samples were then placed inside of the RH chamber and conditioned at 25 °*C* and 25, 35, 45, 55, 65, 75, 85, and 95 %*RH* values for 2 hours per condition prior to being measured immediately using the ellipsometer.

7.3.7 Glass Transition Temperature

The glass transition temperatures (T_g) of the homopolymers were determined by first functionalizing the homopolymer powder that was mechanically ground inside a mortar and pestle. The functionalized powder was placed in individual sample pans for Dynamic Scanning Calorimetry (DSC). The open pans were placed inside of the relative humidity (*RH*) chamber at 25 °*C* and 25 %*RH* and conditioned for 4 hours prior to raising to the %*RH* of interest and conditioned for 2 hours. The pan was then immediately taken out and hermetically sealed and stored for DSC measurements. DSC was run from -90 °*C* to 160 °*C* to -90 °*C* to 160 °*C* and back to 0 °*C* for samples conditioned at 0, 25, 35, 45, 65 %*RH*. DSC was run from -90 °*C* to 90 °*C* to -90 °*C* to 90 °*C* and back to 0 °*C* for samples conditioned at 75, 85, and 95 %*RH*. The 0 %*RH* sample was obtained by drying the P2VP/NMP+ I- inside a vacuum oven overnight and immediately sealed in the same hermetically sealed DSC pans. One sample of the 22k P2VP/NMP+ I- was placed as a power inside of a transparent glass vial with the top open and conditioned for 2 hours at 25 °*C* an 25 %*RH*. The sample was photographed then placed back into the chamber and conditioned at a higher %*RH*. The image of the powder was collected from 25, 35, 45, 55, 65, 75, and 85 %*RH*.

7.3.8 Simulation

To gain insight into the volume fraction of the PS-b-P2VP/NMP+ I- that contributes to conduction in the BCE, we make use of a coarse grain molecular dynamics (MD) simulation. The MD simulation allows us to look at the distribution of the water in the BCE to see its effect on hydration and plasticization. The simulated system is a lamella forming PS-b-P2VP/NMP+ I- with 50 % of the P2VP repeat units functionalized with MeI and hydrated. The water mass in the simulation is 23 $wt\%$ of the P2VP/NMP+ I-, equivalent to that measured experimentally in the BCE at 25 $°C$ 95 $\%RH$ using dynamic vapor sorption analysis. The resulting lamellar morphology is shown in Figure 7.3a. The normalized concentration of the simulated PS, P2VP/NMP+ I-, water, and ions is plotted in Figure 7.3b as a function of position in the direction orthogonal to the PS-P2VP interface.

The theoretically informed coarse-grained (TICG) model was used to generate a lamella morphology. The model treats polymers as bead-spring chains and the Hamiltonian is described with bonded, intra-molecular interactions and non-bonded, intermolecular interactions. The bond energy, $\frac{H_b}{K_B T}$, is modeled as a harmonic potential energy written as:

$$\frac{H_b}{k_B T} = \frac{3}{2b^2} \sum_{m=1}^{M} \sum_{i=2}^{N} (R_{m,i} - R_{m,i-1})^2 \tag{7.1}$$

where M is the number of polymer chains, N is the number of beads on each chain, $R_{m,i}$ are the bead position vectors, $\frac{3}{2b^2}$ is the effective spring constant for Gaussian chains, and b is the statistical segmental length representing chain flexibility. The nonbonded energy, $\frac{H_{nb}}{k_B T}$, is described in terms of one of the blocks:

$$\frac{H_{nb}}{k_B T} = \sum_{\alpha\beta} \chi_{\alpha\beta} \int dr \phi_\alpha(r) + \frac{\kappa}{2} \int dr (\sum_{\alpha} \phi_\alpha(r) - 1)^2 \tag{7.2}$$

where $\chi - \alpha\beta$ are Flory-Huggins parameters quantifying the thermodynamic incompatibility between beads of type α and β, and κ denotes the compressibility of the material. The non-bonded energy is expressed in terms of density fields of the coarse-grained beads,

$\phi_\alpha(r)$, the number density of α beads at position r defined by:

$$\frac{1}{\rho}\sum_{i}^{\alpha}\sigma(R_i - r) \tag{7.3}$$

where ρ is the average bead number density, i runs over all beads of type α and the Dirac delta function is regularized by assigning the bead mass onto the nearest lattice site. This work uses the PM1 scheme to map each bead onto any of the 8 neighboring sites using linear interpolation. (reference 1 and 2 from the paper)

The simulation box used was $4x1.3x1.3R_e^3$, where R_e is the average end-to-end distance of polymer chains. The box is divided into $12x12x12$ lattice sites. The invariant degree of interdigitation is $N = 256$. The Flory-Huggins parameter $\chi_{\alpha\beta}$ N was set to 30 and the compressibility κN is set to 1000. The number of polymer chains is 102. Each chain contained 8 A-type beads and 8 B-type beads.[3] These parameters are chosen according to previous reports that successfully applied the TICG framework to model neutral block copolymers. The model is solved in a Monte Carlo (MC) simulation. The moves used were single-bead translation, chain-flipping, and chain-reptation with 20 %, 40 %, and 40 % probability respectively. The system ran for 1,600,000 MC steps.

Once a lamella morphology is obtained using the TICG model, we proceeded to map atomistic detail onto the lamella. 70% of the chains were randomly selected. Each bead of the chains corresponds to a Kuhn length segment of a polymer (8-10 monomers for PS and P2VP). So, the distance between the beads was scaled to match the size of the monomers and an average of 8 monomers of PS or P2VP were placed onto each bead of their corresponding type. As the monomers are placed, the hydrogen atom on the chiral carbon of the backbone is randomly assigned a direction to ensure the chains are atactic. Additionally, as the P2VP block is mapped, each monomer has a 50 % probability of being functionalized. If it is functionalized, an NMP+ is mapped and the I- required to neutralize the charge is randomly placed in the simulation box.

Once generated, the PS-b-P2VP/NMP+ I- lamella system is minimized using a conjugated gradient algorithm. Then, the system is equilibrated over 20 ns at 500 K and 1 atm, using a timestep of 0.8 fs and a velocity rescale thermostat and Berendsen barostat. Then, a prescribed number of water molecules are randomly inserted into the system and the system is equilibrated over 25 ns using the same conditions as the previous system. Once equilibrated, we simulate for an additional 50 ns at 500 K and 1 atm, using the Nose-Hoover thermostat and MTTK barostat.

All simulations were performed using GROMACS-GPU 5.0.1.4, 5 Particle-Mesh Ewald (PME)6 with a cut-off of 0.9 nm and a Fourier spacing of 0.33 nm was used for the electrostatics. Equations of motion were integrated using Velocity Verlet and a time step of 0.8 fs. Nonbonded interactions were modeled by a Lennard-Jones plus Coulomb potential and cross-terms were calculated using Lorentz-Berthelot mixing rules.

7.3.9 Electrochemical Characterization

The ion transport properties of the 22k P2VP/NMP+ I- homopolymer and the 25k25k PS-b-P2VP/NMP+ I- BCE were characterized on top of the IDEs with AC electrochemical impedance spectroscopy (EIS). The prepared IDEs were clamped to extended electrodes and conditioned inside of the RH chamber at 45 $°C$ 95 $\%RH$ for one hour then at 25 $°C$ 25 $\%RH$ for five hours prior to collecting data. The samples were conditioned for 1 hour at each temperature and RH value prior to measurement. The homopolymers and BCEs were characterized at 25 $°C$ at 25, 35, 45, 55, 65, 75, 85, and 95 $\%RH$ values. Two measurements were made per condition with 20 minutes in between measurements to verify that stable state values were being probed for each parameter. The samples were probed using EIS from 1 MHz to 0.1 Hz using a probing potential of 10 mV. The impedance results were then fitted to an equivalent circuit diagram to extract the resistance and constant phase elements to calculate the conductivity and capacitance values.

The equivalent circuit diagram is shown in the inset of Figure 7.5. The model is identical to the one demonstrated in our previous work with IDEs [4]) where R_e extracts the resistance of the Pt electrodes, W_{dl} extracts the Warburg elements of the double layer formed at the interface of the Pt electrodes and the polymer, R_{film} extracts the resistance of the polymer film, and CPE_{film} extracts the constant phase element parameters necessary for calculating the capacitance. The extracted values of the 25k25k PS-b-P2VP/NMP+ I- film and the 22k P2VP/MP+ I- are shown as tables in a supplementary table.

Conductivity was calculated by using the equation:

$$\sigma_{film} = \frac{d}{R_{film} t l (N-1)} \tag{7.4}$$

Where σ_{film} is the conductivity of the film with the units of mS/cm, d is the separation distance of the electrodes, t is the thickness of the polymer films, l is the length of overlap between individual electrodes, and N is the total number of electrodes.

Capacitance was calculated from the constant phase element variables using the equation:

$$C_{film} = \frac{(R_{film} Q)^{1/a}}{R_{film}} \tag{7.5}$$

Where Q and a are fitting parameters of CPE_{film}. It is critical to note that the variable a was consistently above 0.85 suggesting that the CPE_{film} is close to a perfect capacitor and can be used to extract and interpret the capacitance values.

7.4 Results and Discussion

7.4.1 Water Weight as a Function of RH

Figure 7.2a plots the water content as a function of RH for the 22k homopolymer and the 25k25k BCP as cast and annealed. Two observations area made from this figure: first, the 22k homopolymer film is shown to be consistently higher in comparison to the BCP film and second, the two BCP water concentrations overlap. Figure 7.2b plots the amount of water added into the P2VP/NMP+ I- domain of the homopolymer and the BCP. The value for the annealed and unannealed BCP films were clauclated by taking the water fraction at reach RH value and dividing by 0.6, the mass fraction of the P2VP/NMP+ I- domain of the BCP. It can be seen from the plot that the same amount of water was introduced into the P2VP/NP+ I- domain for the homopolymer and BCP films.

7.4.2 Volume Expansion

Figure 7.2c shows the thickness of the homopolymer and BCP as a function of $\%RH$. There are a number of observations to be made about the trend shown in the graph. First, the volume expansion of the homopolymer is consistently higher in comparison to the BCP system. Second, the thickness reaches a maximum at 65 $\%RH$ then begins to decrease. This transition point occurs for both the homopolymer and the BCP films. Third, the majority of the film expansion for the BCP occurs during the methylation process. Following methylation, the BCP film thickness increased by 10 nm while the hydration process only increased the film thickness by at most 2 nm. The homopolymer increased in thickness by 14 nm when methylated but only by 6 nm after hydration. Fourth, thickness of the homopolymer film and the BCP film were within error at 25 $\%RH$ following the hydration process up to 95 $\%RH$.

Figure 7.2d also shows the normalized volume expansion between the BCP and the homopolymer systems. The normalized volume expansion of the BCP was calculated by using the equation:

$$V_{n,BCP} = \frac{t_{RH} - t_{0RH}}{t_{0RH} - t_{PS}} \tag{7.6}$$

Where $V_{n,BCP}$ is the normalized volume of the BCP, t_{RH} is the thickness at the given RH, $t - 0RH$ is the thickness at 0 $\%RH$, and t_{PS} is the PS thickness determined to be 21 nm from the PS-b-P2VP thickness. The homopolymer volume expansion was determined simply by taking the difference in thickness due to water absorption and dividing by the thickness of the P2VP/NMP+ I- at 0 $\%RH$.

The volume expansion of the homopolymer is noticeably larger in comparison to the P2VP/NMP+ I- domain of the BCP.

7.4.3 Molecular Dynamics Simulations

Figure 7.3 plots the molecular dynamics simulation results of the BCP system at 25 $wt\%$ of water that correlates to the experimental film conditioned at 95 $\%RH$. The concentration distribution shown in Figure 7.3b shows that the PS concentration is non-zero through the majority of the P2VP/NMP+ I- domain. The concentration in the z-direction shows that the water concentration scales with the P2VP domain and that the PS concentration is non-zero through the majority of the P2VP domain. The coordination number and radial distribution function of the water as a function of distance away from the interface of the PS and P2VP/NMP+ I- is shown in Figure 7.3c. The distribution can be seen to overlap regardless of the region of the lamellae or PS concentration.

7.4.4 Glass Transition Temperature of Homopolymer

Figure 7.4 plots the T_g of the 22k P2VP/NMP+ I- as a function of the water fraction in the film. The plot compiles the T_g data as a function of the RH and the water fraction as a function of the RH. The T_g of the homopolymer crosses the experimental temperature at 25 $^\circ C$ between 75 $\%RH$ and 85 $\%RH$. The experimental data is fit to the Fox equation:

$$\frac{1}{Tg} = \frac{1-w}{Tg_{P2VP}} + \frac{w}{Tg_{water}} \tag{7.7}$$

Where T_g is the combined T_g of the film, Tg_{P2VP} is the T_g of the dry P2VP/NMP+ I-, Tg_{water} is the T_g of the water modeled to be 135 K from previous literature [5] , and w is the weight fraction of the water. The Fox equation model seems to fit the experimental data at all but the highest water fraction in the system. Using the Fox equation, the water

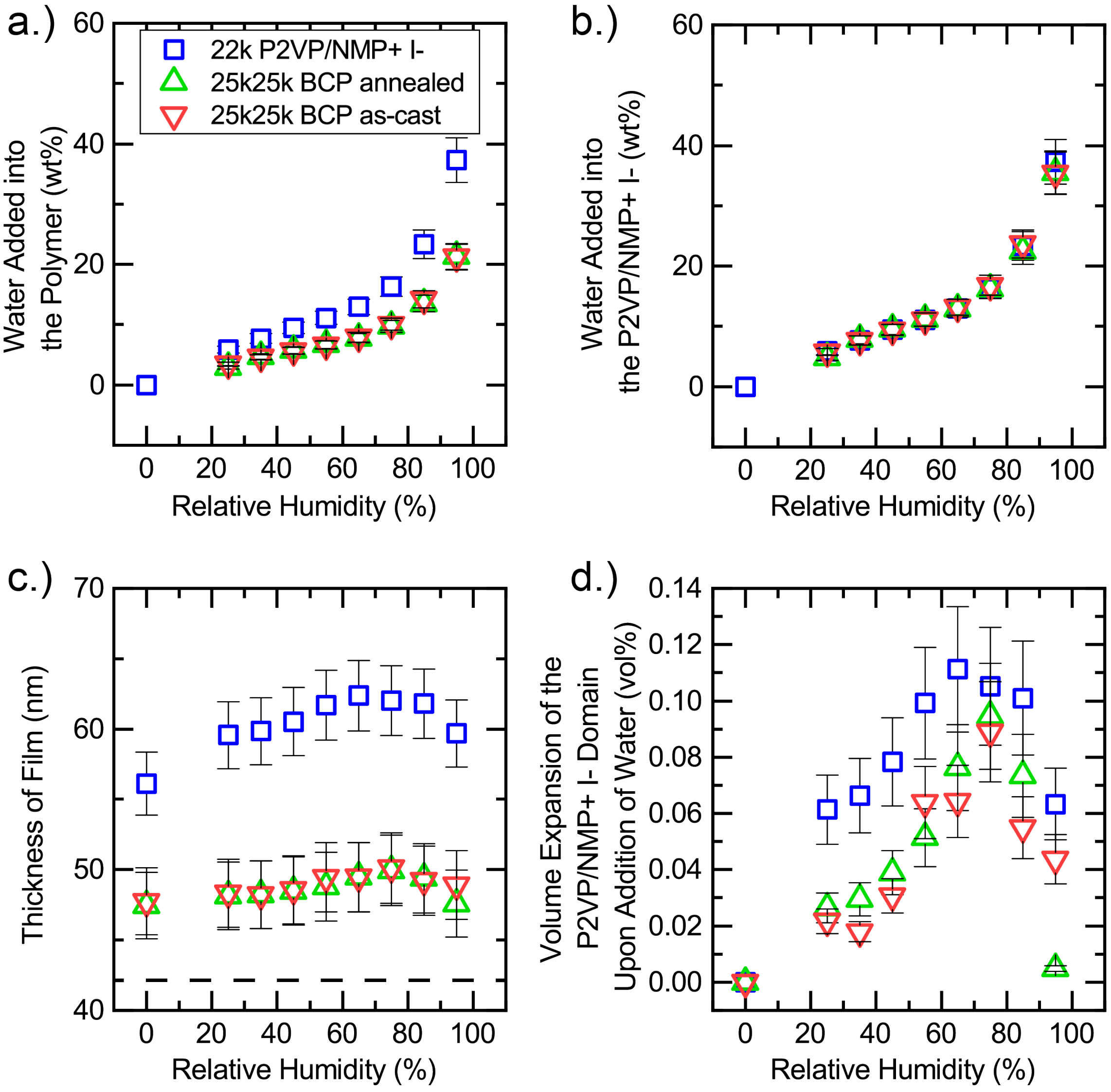

Figure 7.2: Water content, comparisons, and expansion. a.) water wt fraction in homopolymer, BCP annealed, and BCP unannealed as a function of *RH*, b.) the fraction of water added into the P2VP/NMP+ I- component of the homopolymer and the BCP films, c.) thickness change in the homopolymer, annealed BCP, and unannealed BCP films as a function of *RH*, dotted line shows the thickness of the pre-methylation thickness of 42 nm for both homopolymer and BCP and d.) volume expansion of the P2VP/NMP+ I- domain of the homopolymer, annealed BCP, and as-cast BCP films.

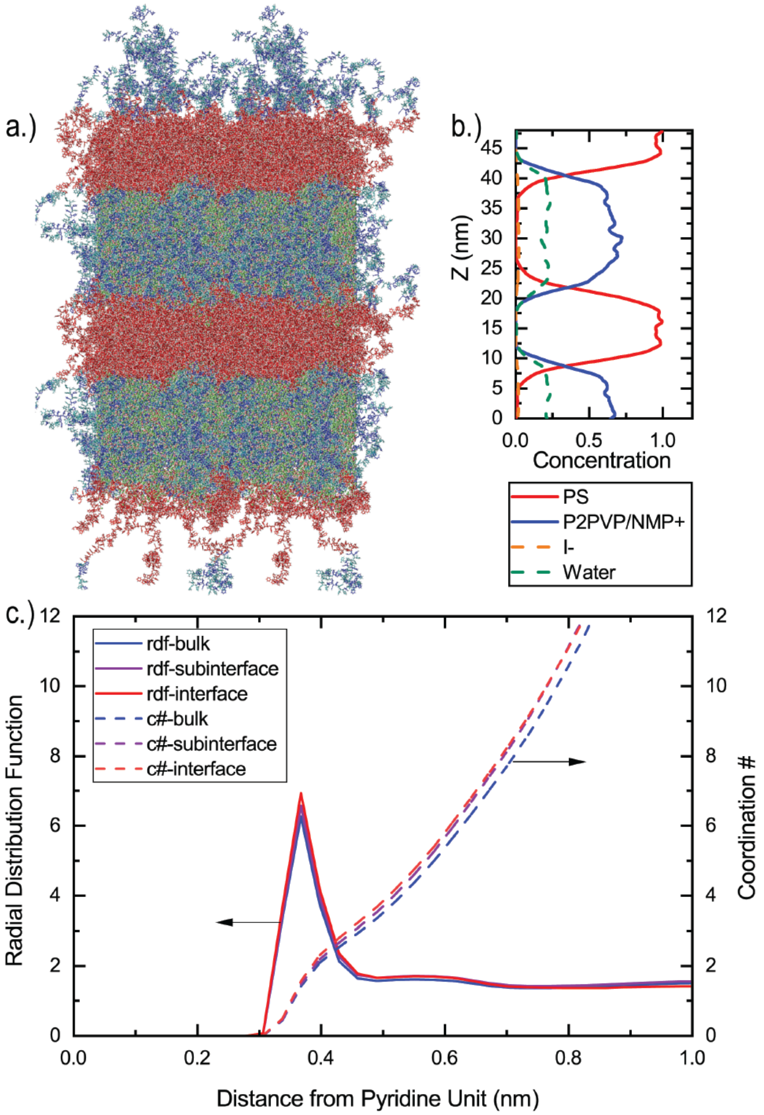

Figure 7.3: Molecular Dynamics simulations. a.) the graphic rendering of the phase separated BCP lamellae film, b.) concentration distribution of PS, P2VP/NMP+, I-, and water as a function of depth, c.) radial distribution function and coordination numbers of the water molecule to the P2VP/NMP+ I- active site as a function of distance from active site at the interface, sub-interface, and P2VP/NMP+ I- bulk.

concentration at which the T_g of the film is 25 $°C$ is calculated to be 17 $wt\%$. The DSC data for lower water fractions and the highest water fraction are shown in a zoomed in graph. It can be observed that the curve of the data transitions from the slope shape that suggests a T_g transition to a peak shape that suggests the film is undergoing a melting transition. This value was interpreted to be the T_g for the plot.

7.4.5 Electrochemical Properties

The conductivity and capacitance values of the homopolymer and the Parallel LAM BCP are plotted as a function of RH in Figure 7.5. The thickness value determined for the different $\%RH$ values were used to derive the thickness used for the conductivity calculation. The conductivity of the homopolymer is consistently higher in comparison to the BCP film. Conductivity is shown to increase quickly at lower water concentrations then increases slowly at higher water concentrations. The two slope regions are well bisected by the water concentration at which the T_g of the film reached 25 $°C$. (talk about the conductivity)

7.4.6 Water Uptake

The interface of the PS and P2VP/NMP+ I- domain is a gradient where the PS concentration approaches one near the PS domain while it approaches zero near the P2VP/NMP+ I- domain. It was hypothesized in our previous work that the water content in the interface may decrease as a function of the PS concentration fraction in the interface. To determine if the presence of the PS reduced the water content at any condition, the difference in water fraction between the BCE and the homopolymer was divided by the homopolymer water weight fraction at each RH. It was determined that the normalized water weight fraction of the BCE was 0.61 ± 0.2. This value of 0.61 ± 0.2 can be understood by calculating for the weight fraction of the P2VP/NMP+ I- and the PS backbone of the 25k25k BCE. The MW of the styrene is 104.15 g/mol, the 2-vinyl pyridine is 105.14 g/mol, and the MeI is 141.94 g/mol. It has been reported previously, at 48 hours reaction time, the degree of

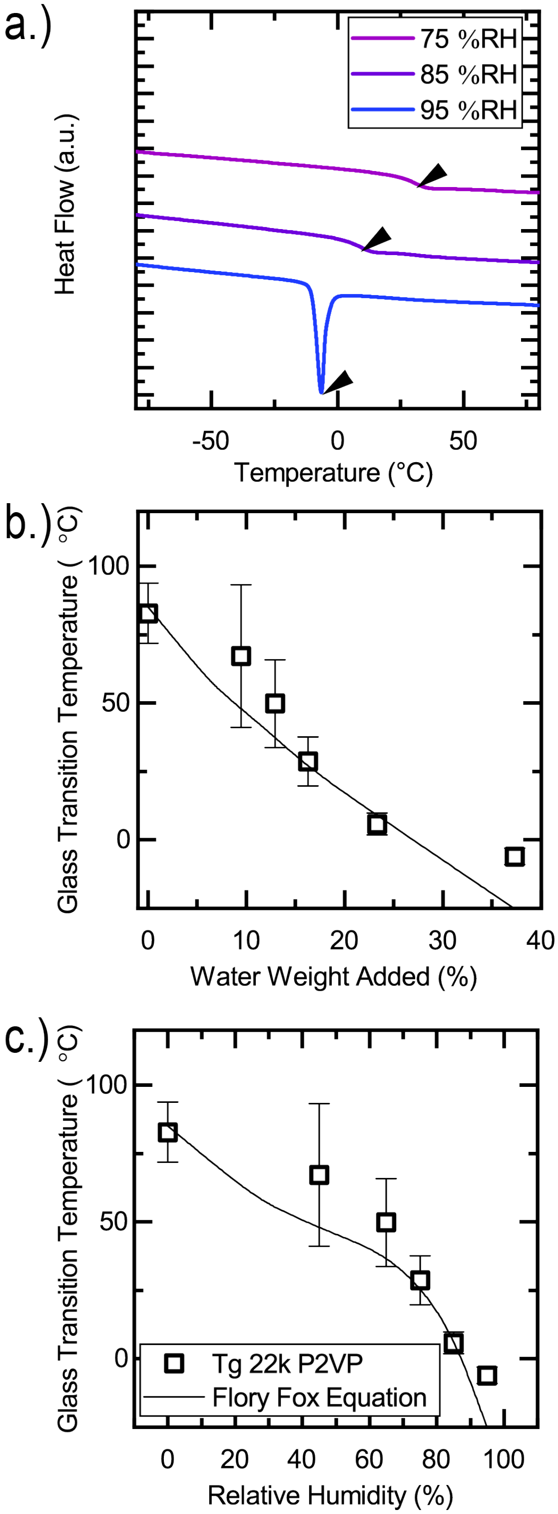

Figure 7.4: Glass transition temperature. a.) experimental T_g and the FOX equation model fit as a function of the RH for the P2VP/NMP+ I- homopolymer and b.) zoomed graph of the DSC data demonstrating the shift from T_g to T_m at 95 $\%RH$.

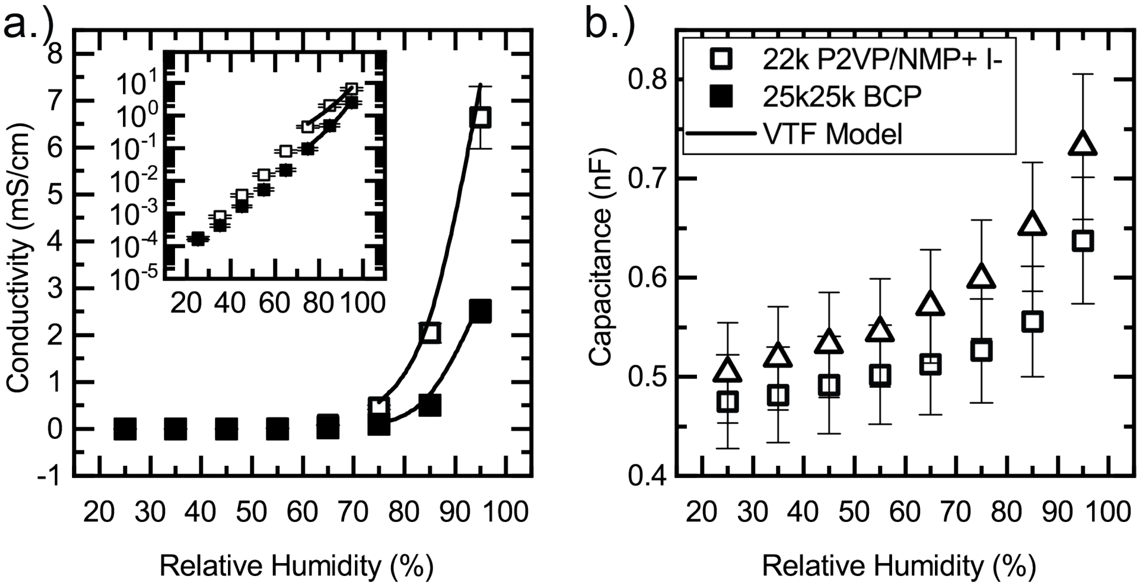

Figure 7.5: Electrochemical properties. a.) conductivity and b.) capacitance of the BCP and homopolymer as a function of RH. VTF model fit is depicted as a line for the conductivity data above 75 $\%RH$

functionalization is 50 % of the P2VP backbone. Taking this increased mass of the P2VP into account, the weight fraction of the P2VP/NMP+ I- domain is determined to be 0.62 which within the error of the normalized water weight fraction. This suggests that the hydrophobic PS does not reduce the degree of hydration in a BCP film. This point is further complimented by the fact that the water concentration of the film does not change when the BCP film is annealed or unannealed. If the PS did affect the degree of hydration, then the water concentration should be lower in the as-cast state. This corroborates the MD simulation of the interface. Figure 7.3c shows the radial distribution function and the coordination numbers of water molecules to the NMP+ active sites as a function of distance. Each function is collected at different distances from the PS-P2VP interface. If hydration is affected by the hydrophobic PS molecules then the RDF and the coordination function would shift to lower coordination when closer to the interface. This observation is not made from the simulation. The data virtually overlaps suggesting that the degree of hydration is not affected by the hydrophobic PS. Considering the importance of hydration of the transport behavior of an ion transport film, it is important to note that the comparison of the 25k25k BCP to the 22k homopolymer can be done across a wide range of water weights without concern for different water fractions affecting the performance of the film. This is because the water weight fraction of the two systems are consistent throughout the range of RH values studied.

7.4.7 T_g to T_m Transition at High RH

In Figure 7.4, the Fox equation is shown to model the T_g curve of the homopolymer within experimental error for the majority of the range of water concentrations except for the highest water concentration at 95 $\%RH$. The model does not fit the of the T_g at 95 $\%RH$. This is likely due to a reduction in the degree of association of the water to the NMP+ sites. Fox equation assumes that the plasticizing agent interacts with the polymer consistently throughout the range of the model fit. At higher degrees of hydration, water becomes less associated to the P2VP/NMP+ I- and begins to form clusters of water. This water is more associated with itself compared to the polymer. When the film is cooled below 260 K, the water molecules can cluster together forming nanoscale ice crystals resulting in a transition from a T_g slope to a T_m peak in the DSC data. Previously, this behavior of the water has been studied by Smith et al [6] where PMMA was hydrated and the transition from T_g to a T_m curve was observed. At high degrees of hydration, Smith also observed an deviation in the T_g. This was attributed to only a fraction of the water interacting with the polymer system. At high hydration limits, the water has been observed to associate less with the polymer forming water clusters. The T_m also exhibits a characteristic depression in the T_m to -7 $°C$.

7.4.8 Volume Change of Homopolymer and BCP with Hydration

It is interesting to note that the maximum thickness occurs where the T_g of the P2VP/NMP+ I- reaches 25 $°C$. At lower RH, it is reasonable to see the increase in the water weight qualitatively follow the thickness change. However, the moment the system enters the rubbery regime, the film begins to shrink. This suggests that the same amount of water incorporated into the film is expanding the film less. It is important to take this into consideration when comparing effects on the ion transport. We hypothesize that if the film enters the rubbery regime, the freedom of movement in the P2VP/NMP+ I- allows the P2VP/NMP+ I- to reconfigure into a more packed structure. This would suggest that the methylation process introduces significant free volume. It is important to note that following the dehydration of the film to 25 $\%RH$, the film thickness measured returns to its original thickness therefore we can assume the effect is reversible and not due to dewetting or the outgassing of volatile reactants. It is also possible that water clusters are denser in comparison to water closely associated with the NMP+ I- sites. This is supported by the shift in the DSC data from a T_g to a T_m.

7.4.9 Effective Conductive Volume $\phi_{effective}$ Deviates from Domain Volume Expansion

From inspection, homopolymer conductivity is consistently higher in comparison to the ion conductivity of the BCP. For the quantitative comparison, we will revisit the equivalent medium theory (EMT).[7, 8] With the use of parallel LAM morphology, we will approximate that the ion conduction path is fully connected without PS blocks, hence f is one. Using the conductivity of the homopolymer and the BCP at each specific RH condition, the effective volume fraction of the film is determined using the equation:

$$\phi_{effective} = \frac{\sigma_{BCP}}{\sigma_{homopolymer}} \tag{7.8}$$

In comparison, the volume fraction of the P2VP/NMP+ I- domain was calculated by taking the thickness of the BCP film and using the equation:

$$\phi_{real} = \frac{t_{BCP,RH} - t_{PS}}{t_{BCP,RH}} \tag{7.9}$$

Where ϕ_{real} is the actual volume fraction of the P2VP/NMP+ I- domain at given RH conditions, $t_{BCP,RH}$ is the BCP thickness at given RH conditions, and t_{PS} is the thickness of the PS domain. We will assume that the PS film does not significantly increase in volume with increasing RH conditions and is considered a constant value of 21 nm.

The resulting values for $\phi_{effective}$ and ϕ_{real} are overlaid on the same plot in Figure 7.6. First, it is important to note that the $\phi_{effective}$ of 0.37 is well within error of the $\phi_{effective}$ of 0.36 calculated in our previous work [1]. This comparison verifies the consistency in materials behavior for morphologies that are aligned parallel and perpendicular to the substrate surface and confirms that the morphology studied in this work behaves like fully connected ion conduction pathways. Second, the ϕ_{eff} is very different from ϕ_{real} when compared as a function of RH. Evidenced from the lack of hole islands and the fact that the conductivity of this study matches well with the conductivity of the previous study, we can state with a high degree of certainty that there are little to no disconnected domains in this study. Therefore, the lack of overlap between the ϕ_{eff} and ϕ_{real} are due to molecular differences in the P2VP/NMP+ I- domain.

In the rubbery regime, the $\phi_{effective}$ increases with increasing hydration likely due to the depression of the T_g far below experimental temperature of 25 $°C$. The increase exhibits a $T - T_g$ like behavior that may be modeled through the Vogel-Tammann-Fulcher (VFT) model. In the hydrated system, the analysis is very similar to a typical VTF analysis,[9, 10] but instead of the T changing, the Vogel Temperature T_0 changes as a function of RH.

The VFT equation is written as:

$$\sigma = Aexp(\frac{-E_a}{R(T - T_0)}) \tag{7.10}$$

Where σ is the conductivity, A is the charge carrier concentration, E_a is a factor related to

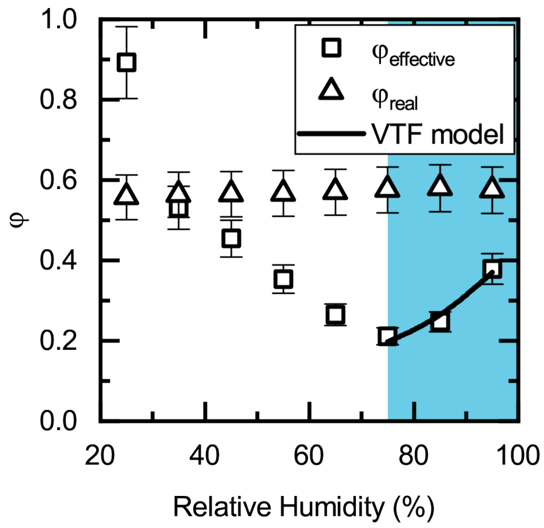

Figure 7.6: Further analysis of electrochemical properties. ϕ_{eff} (square), ϕ_{real} (triangle), and models as a function of RH. Region labeled in blue is the glassy regime.

the activation energy of transport, R is the gas constant, T is the experimental temperature and T_0 is the Vogel Temperature, commonly associated to the T_g of the film subtracted by 50 $^{\circ}C$. In our system, the T value is a constant at 298 K, while the T_0 changes with the RH.

The ϕ_{eff} can be calculated by dividing the BCP VFT equation by the homopolymer VFT equation. The resulting equation is:

$$\phi_{eff} = aExp(\frac{-\delta E}{R(T - T_0)}) \tag{7.11}$$

Where $a = \frac{A_{BCP}}{A_{homopolymer}}$ and $\delta E = E_{BCP} - E_{homopolymer}$. The factors were condensed into a total of two fitting parameters to reduce the the number of solutions.

The VTF equation 7.10 is fit to the homopolymer and BCP conductivity data above 65 $\%RH$ to extract out information about A and E_a. The modified VTF equation 7.11 is fit to the ϕ data above 65 $\%RH$ in Figure 7.6 and the resulting fit is shown as the line. A multivariable regression fit was used to fit both equations and the resulting values are tabulated in Table 7.1.

Comparing the variables, we note three observations: 1) the VTF model fit's the conduc-

Variable	Value	Unit
A_h	0.14	mS/cm
A_{bce}	0.0196	mS/cm
E_{ah}	610	J/mol
$E_{a,bce}$	760	J/mol
a	0.14	-
δE	150	J/mol

Table 7.1: Extracted values from the VTF equation and the modified VTF equation.

tivity and ϕ_{eff} data and 2) a value of 0.14 suggests that a significantly smaller concentration of mobile ions. First, VTF model fits the data in the rubbery regime suggesting that the ion transport is associated to viscoelastic properties such as segmental mobility. Second, A is a factor that is associated to the charge carrier concentration. By having an A_{BCE} value that is close to an order of magnitude smaller in comparison to A_h suggests that the P2VP/NMP+ I domain in the BCP has a lower carrier concentration. The reduced carrier concentration in the BCP film may be explained by the presence of trace concentrations of PS reducing the coordination site concentration causing a reduction in mobile ions.

In the glassy regime, with increasing RH, the $\phi_{effective}$ decreases, reaching the lowest value and the largest deviation from ϕ_{real} at approximately 75 $\%RH$. The presence of a RH dependence on phi_{eff} in the glassy region may be attributed to differences in the free volume change of the film under compression. In Figure 7.2c the volume expansion of the P2VP/NMP+ I- domain upon addition of water is consistently higher in comparison to the PS-b-P2VP/NMP+ I-. The overlap of homopolymer and BCP water uptake data in Figure 7.2b demonstrates the same amount of water is incorporated into the films. The difference in volume expansion with the incorporation of the same mass of water suggests that the BCP film has a consistently lower free volume. The reduced free volume is likely caused by the rigid PS domain preventing the free expansion of the P2VP/NMP+ I- volume under increasing hydration.

Following the elimination of the degree of hydration as a potential factor (see previous discussion), supported by the VTF model fit analysis and the free volume argument in the glassy regime, the ϕ_{eff} may be notably different compared to the phi_{real} in the rubbery regime due to the modulation of P2VP/NMP+ I- segmental mobility near the interface by the glassy PS. Primarily, the PS containing P2VP/NMP+ I- interface is transporting ions slower due to the glassy PS reducing the local segmental mobility of the P2VP/NMP+ backbone. This is supported by the Fox equation where the incorporation of the glassy PS into the P2VP/NMP+ I- domain increases the T_g.

Additionally, the presence of a large difference in the A prefactor for the VTF equation suggests that the PS reduces the percolation of solvation sites affecting the hopping probability of ions from one side to the other. This is supported by work done by Webb et al [11] and Pesko et al [12] where experiment and MD simulations were used to determine that the solvation site connectivity in a PEO system can explain well the changes in ion conductivity observed for polyester based polymer electrolytes with ethylene oxide units. It was also determined, that a very small concentration of non-conductive materials can be used to significantly reduce the percolation of these solvation sites and the overall conductivity in the film. This effect is likely dominant in our system as well, where the trace PS domains are causing reductions in the total number of percolated solvation sites, resulting in a lower A_{BCP}.

7.5 Conclusion

In this work, the PS-b-P2VP/NMP+ I- BCE was assembled parallel to the surface of passivated IDEs and characterized via EIS across a range of humidified environments. The resulting ion transport and dielectric properties were compared to the P2VP/NMP+ I- homopolymer that closely resembles the ion conducting domain of the BCE. The BCE was determined to behave similarly to the homopolymer system, however the conductivity of the BCE was consistently lower even though the same amount of water was introduced into the homopolymer and the BCE systems when normalized for the P2VP/NMP+ I- domain. This was attributed to the reduction in segmental mobility and the solvation site connectivity near the interface due to the presence of the glassy PS domain. Additionally, the study corroborated our previous work and further demonstrated the utility of studying parallel lamellae system to better understand the interfaces and better engineer them for higher conductivity compared to the homopolymer system.

7.6 References

[1] Y. Kambe, C. G. Arges, D. A. Czaplewski, M. Dolejsi, S. Krishnan, M. P. Stoykovich, J. J. de Pablo, and P. F. Nealey, Nano Letters, Submitted (2019).

[2] C. G. Arges, Y. Kambe, H. S. Suh, L. E. Ocola, and P. F. Nealey, Chemistry of Materials **28**, 1377 (2015), ISSN 0897-4756.

[3] A. Panday, S. Mullin, E. D. Gomez, N. Wanakule, V. L. Chen, A. Hexemer, J. Pople, and N. P. Balsara, Macromolecules **42**, 4632 (2009), ISSN 0024-9297.

[4] D. Sharon, P. Bennington, C. Liu, Y. Kambe, B. X. Dong, V. F. Burnett, M. Dolejsi, G. Grocke, S. N. Patel, and P. F. Nealey, Journal of The Electrochemical Society **165**, H1028 (2018), ISSN 0013-4651.

[5] R. P. Kambour, C. L. Gruner, and E. E. Romagosa, Journal of Polymer Science: Polymer Physics Edition **11**, 1879 (2003), ISSN 00981273.

[6] L. Smith and V. Schmitz, Polymer **29**, 1871 (1988).

[7] D. T. Hallinan and N. P. Balsara, Annual Review Mater Res **43**, 503 (2013), ISSN 1531-7331, 1545-4118.

[8] J. Sax and J. M. Ottino, Polymer Engineering and Science **23**, 165 (1983), ISSN 0032-3888.

[9] M. Videa, W. Xu, B. Geil, R. Marzke, and C. A. Angell, Journal of The Electrochemical Society **148**, A1352 (2001), ISSN 00134651.

[10] F. M. Gray, *Solid Polymer Electrolytes: Fundamentals and Technological Applications* (VCH, New York, NY, 1991).

[11] M. A. Webb, Y. Jung, D. M. Pesko, B. M. Savoie, U. Yamamoto, G. W. Coates, N. P. Balsara, Z. G. Wang, and T. F. Miller, ACS Central Science **1**, 198 (2015), ISSN 23747951.

[12] D. M. Pesko, M. A. Webb, Y. Jung, Q. Zheng, T. F. Miller, G. W. Coates, and N. P. Balsara, Macromolecules **49**, 5244 (2016), ISSN 15205835.